INVESTIGATION OF ELLIPTIC FLOW AND CHIRAL MAGNETIC EFFECT WITH THE STAR DETECTOR

A THESIS

Submitted to the

PANJAB UNIVERSITY, CHANDIGARH

For the Award of

DOCTOR OF PHILOSOPHY

2023

in

FACULTY OF SCIENCE

BY
JAGBIR SINGH

GUIDE

Dr. M.M. Aggarwal **Dr. A.K. Bhati**

DEPARTMENT OF PHYSICS
PANJAB UNIVERSITY
CHANDIGARH, INDIA

June 2023

DECLARATION

I declare that the thesis entitled "INVESTIGATION OF ELLIPTIC FLOW AND CHIRAL MAGNETIC EFFECT WITH THE STAR DETECTOR" has been prepared by me under the guidance of Dr. M. M. Aggarwal and Dr. A. K. Bhati, Department of Physics, Panjab University, Chandigarh. No part of this thesis has formed the basis for the award of any degree or fellowship previously.

Jagbir Singh,
Department of Physics, Panjab University
Chandigarh.

DATE :

CERTIFICATE

We certify that Jagbir Singh has prepared his thesis entitled “INVESTIGATION OF ELLIPTIC FLOW AND CHIRAL MAGNETIC EFFECT WITH THE STAR DETECTOR” for the award of PhD degree of the Panjab University, Chandigarh under our guidance. He has carried out the work at Department of Physics, Panjab University, Chandigarh.

Dr. M. M. Aggarwal
Department of Physics,
Panjab University, Chandigarh.

Dr. A. K. Bhati
Department of Physics,
Panjab University, Chandigarh.

DATE :

Dedicated to my Parents

and loved ones

Acknowledgments

I would like to express my deepest gratitude to all those who have supported me throughout my academic journey.

First of all, I am extremely grateful to my supervisors, Dr. M. M. Aggarwal and Dr. A. K. Bhati, for their esteemed guidance and all the useful discussions. I will remain beholden to their understanding and support throughout the period and to their efforts to provide me with the best guidance. I really appreciate their willingness to always help me despite their busy schedule.

I am extremely grateful to Prof. Rajeev K. Puri, Chairperson, Department of Physics, and Ex-Chairpersons Prof. Navdeep Goyal and Prof. Devinder Mehta for providing me with all the facilities required for my research work. Dr. Lokesh Kumar deserves special thanks for his unwavering support and insightful physics discussions. My sincere thanks to Dr. Natasha Sharma and Dr. Navneet Kumar Pruthi for their invaluable suggestions and help at every point.

I am appreciative of the financial help provided by the University Grants Commission and the Department of Science and Technology. I'd like to take this opportunity to thank Dr. Zubayer Ahmed, ALICE-STAR India Collaboration Spokesperson, and former Spokespersons Prof. Bedangadas Mohanty and Prof. Subhasish Chattopadhyay for their warm words of encouragement and invaluable assistance. I'd also like to express my gratitude for the regular collaboration meetings, which provided me with an excellent opportunity to discuss my research findings. I would like to express my sincere thanks to Dr. Lijuan Ruan and Dr. Frank Geurts, STAR Spokespersons, and Ex-Spokespersons Dr. Zhangbu Xu, Prof. Helen Caines, and

Dr. Nu Xu, for all the help and support for my research work and the financial assistance for my visits to STAR. A vote of thanks to the STAR collaboration for providing me with several opportunities to interact with the experts, especially the conveners of the Flow Chirality and Vorticity (FCV) group of STAR, namely Dr. Shinichi Esumi, Prof. Jiangyong Jia, Dr. Prithwish Tribedy, Dr. Shubash Singha, Dr. Zhenyu, and the CME-Focus group conveners of STAR, namely Dr. Evan Finch and Dr. Aihong Tang.

I would like to thank the staff of the purchase section, Department of Physics, Panjab University, especially Mr. Dinesh Kumar, Mr. Satish Kumar, Mr. Sanjeev Pathania, Mr. Udham, Mr. Rajiv, and Mr. Gurhimmat. Many thanks to Mr. Govind, Mr. Vishal, Ms. Meena, and Ms. Sapna of the Grants and Planning division, Panjab University Chandigarh's Administration Block.

I extend my heartfelt gratitude to my esteemed colleagues and lab mates, Dr. Sonia Parmar, Dr. Anjali Attri, Dr. Anjali Sharma, Dr. Sandeep Dudi, Mr. Navneet Kumar, Ms. Ankita, Mr. Aditya, Ms. Arushi, and Ms. Ishu. Their unwavering cooperation and support have played an instrumental role in my journey.

I would like to express my heartfelt gratitude to my dear friends for their unwavering support and boundless love. A special mention goes to Mohd. Tauheed Ilyas, Karan Kindra, Rustam Bir Singh, Gurinder Sahota, Geetanjali Chaudhary, Bharti Rohilla, Dr. Aseem Vashisht, Ashpreet Kaur, Anu Rathi, Isha Sihmar, Kailash, Vikas, Rahul Goel, and Tanvi. Your friendship has been a constant source of inspiration, laughter, and encouragement. You have stood by my side through both the ups and downs, offering unwavering support and understanding. I would also like to extend my gratitude to Dr. Dukhishyam Mallick, Mr. Krishan Gopal, Dr. Ashish Pandav, Mr. Vivek Singh, Mr. Ashwini Kumar, and Mr. Rishab Sharma whom I had the pleasure of meeting during collaboration meetings and various conferences. The bonds we formed during these encounters have transcended professional connections and become friendships I will cherish forever. Since this thesis endured COVID-19, this post-COVID time was less depressing in the hostel because of Mr.

Karan Kaushal, Ravi Kumar, Neeraj Chauhan, Harpreet Singh, and Sandeep Kumar (open eyes foundation).

I would like to express my heartfelt appreciation and immense gratitude to my caring, loving, and supportive family. Words truly fall short of conveying the depth of my gratitude towards my parents, Mr. Gurcharan Singh and Ms. Jasbir Kaur. Their unwavering love, constant encouragement, unwavering trust, and boundless support have been the pillars of my life's journey. I am eternally grateful for your presence in my life.

I wish to continue seeking blessings and love from everybody named here or missed to be named in person.

Thank you all for your contributions to my education and personal growth.

Abstract

The Chiral Magnetic Effect (CME) has been extensively studied in heavy-ion collisions. In non-central collisions, P-odd meta-stable states are formed, and the strong magnetic field generated by highly energetic spectator protons leads to the separation of oppositely charged particles along the system's angular momentum direction and perpendicular to the reaction plane.

To probe the existence and properties of the CME, extensive theoretical and experimental efforts have been made, particularly by experimental collaborations at the Relativistic Heavy Ion Collider (RHIC) and the Large Hadron Collider (LHC). These experiments involve analyzing azimuthal correlations of 2- and 3-particle correlations to search for charge separation patterns indicative of the CME.

This thesis focuses on exploring the charge separation effect and investigating potential events displaying characteristics similar to the CME. A novel method called the Sliding Dumbbell Method (SDM) has been developed to identify potential CME-like events with higher back-to-back charge separation on an event-by-event basis in heavy-ion collisions. The SDM scans the azimuthal plane of each event, calculating the maximum value of the fractional charge separation across the dumbbell (f_{DbCS}).

Two- and three-particle correlators, denoted as δ and γ, respectively, are analyzed using different charge separation classes (or f_{DbCS} bins). The Q-cumulant method is used to compute these correlators and the elliptic flow. To extract the fractional CME signal in the top f_{DbCS} bins, two types of backgrounds were considered. The Charge Shuffle background (ChS) involved random shuffling of charges while keeping their momenta unchanged, providing insight into the level of charge

correlations that can occur by chance. The correlated background involved recovering correlations among particles from the original events within a specific f_{DbCS} bin.

To validate the SDM, a CME-like signal is externally injected by flipping charges of particles in an event generated by the AMPT model. The percentage of the externally injected signal varies across different collision centralities. The AMPT events, both with and without injected CME-like signals, are analyzed in a similar way as the experimental data, including the consideration of background effects.

The AVFD model is also analyzed for different collision systems, such as Au+Au, Ru+Ru, and Zr+Zr, for 30-40% collision centrality at the center of mass energy 200 GeV per nucleon with different levels of CME signal injection (i.e., different values of n_5/s) with 33% LCC (local Charge Conservation). The fraction of CME contributions (f_{CME}) is calculated by computing $\Delta\gamma$ using the top f_{DbCS} bins while also taking into account above mentioned backgrounds.

In the experimental study using the STAR detector in Au+Au collisions, approximately 465 million minimum bias events were obtained after event and track selection cuts. The values of δ and γ correlators in the top f_{DbCS} bins showed a significant increase compared to the average values in a given centrality. Same-sign charge pairs exhibited negative γ correlators and positive δ correlators in the top bins, while opposite-sign charge pairs displayed the opposite trend. Out-of-plane correlations were observed for both same-sign and opposite-sign charge pairs due to the out-of-plane charge separation, indicating the potential CME-like nature of events in the top f_{DbCS} bins. The charge shuffled background exhibited a similar trend with reduced magnitude, while the correlated background had approximately the same values for all f_{DbCS} bins within each centrality. Glimpses of fractional CME were observed in the top 20% charge separation across the dumbbell in the given centrality range of 10-50% collision centralities.

For the isobaric collisions (Ru+Ru and Zr+Zr $\sim$1.7B events each), no significant differences were observed when comparing the background-scaled $\Delta\gamma$ between the two collision systems in the top 20% f_{DbCS} bins. However, CME-like events were observed in the top 20% f_{DbCS} bins in both isobars, representing approximately 2-5% CME signal individually. The expected enhancement in Ru+Ru collisions due to the increased magnetic field may not be distinguishable due to the small multiplicities (or not enough increase in the magnetic field) in these isobar systems.

Overall, the research described in the thesis aims to understand and identify the CME phenomenon in heavy-ion collisions, develop methods for detecting CME-like events, and utilize theoretical models to study the effects of the magnetic field and axial charge density on the QGP's evolution.

Contents

List of Figures

List of Tables

Chapter 1

Introduction

The field of High-Energy Physics (HEP) focuses on investigating the fundamental constituents of matter and their behavior at both the smallest and the largest scales. Researchers in HEP aim to make discoveries that span from understanding the tiniest particles to unraveling the mysteries of the vast cosmos. This field of study is essential not only for our understanding of matter on Earth but also for comprehending the nature of the universe itself.

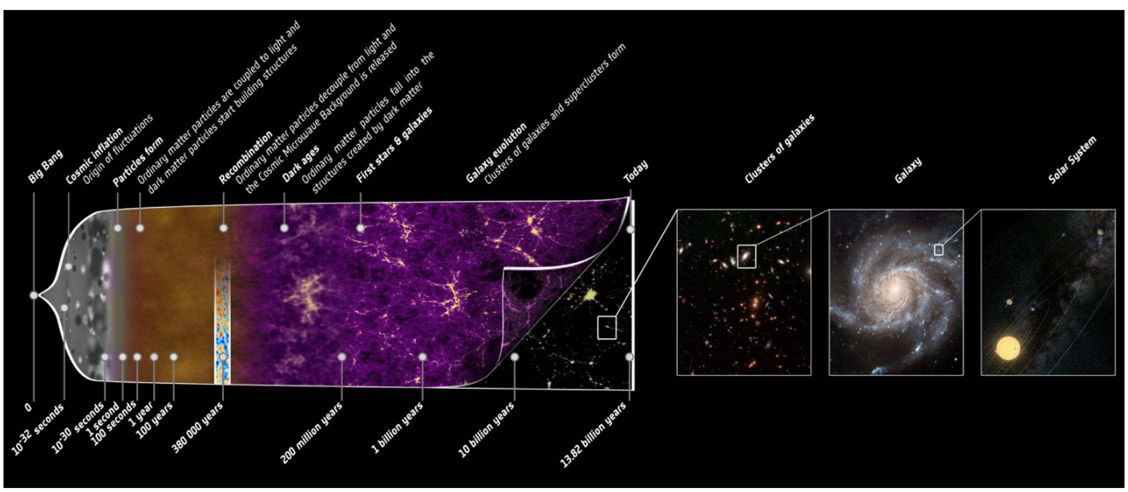

Figure 1.1: A timeline of the universe's evolution, from the big bang through present day [6].

The study of elementary particles lies at the core of High-Energy Physics (HEP), as these particles are regarded as the fundamental constituents of matter.

Through research in this field, scientists have gained insights into the dense and hot state of matter that existed shortly after the Big Bang. Over time, various particles that we are familiar with today emerged from this primordial soup. The expansion and cooling of the universe led to phase transitions, resulting in the formation of hadrons (bound states of quarks and gluons), atoms, and molecules [1–5] as illustrated in the Fig. 1.1 [6]. Despite decades of efforts, many fundamental rules in particle physics are still not fully understood. To probe the matter in the early moments after the Big Bang, enormous particle accelerators have been constructed. These accelerators simulate the conditions of the universe's matter at increasingly smaller time scales.

Experimental investigations of high-energy heavy-ion collisions have the primary goal of studying the fundamental properties of matter and radiation. Matter is composed of molecules, which, in turn, consist of atoms. Atoms comprise a nucleus at the center and electrons are orbiting around it. Protons [7] and neutrons [8] were later discovered to be components of the nucleus, providing an explanation for various nuclear properties. Deep Inelastic Scattering experiments revealed the composite nature of protons and the presence of fractionally charged quarks known as partons [9, 10]. Quarks, due to the interquark potential, are not considered free particles but are confined within hadrons.

The discovery of gluons [11] in 1979 confirmed their role in strong interactions. According to current scientific theories, all components of matter can be broken down into their constituent quarks and leptons, which are elementary particles. The Standard Model [12] of particle physics is a well-established theoretical framework that explains the interactions between these elementary particles. It describes the exchange of bosons, such as photons, W and Z bosons, and gluons, to explain these interactions. The Standard Model has made predictions about the existence of these bosons, and experimental evidence has verified these predictions. The discovery of the Higgs boson confirmed one of the most important predictions of the Standard Model, as it provides mass to other particles through their interactions with it [13–15].

The Standard Model of particle physics incorporates various quantum numbers associated with the particles, such as spin, charge, baryon number, lepton number, and others. The Standard Model includes both matter particles (quarks and leptons) and force-carrying particles (bosons). Figure 1.2 illustrates a schematic

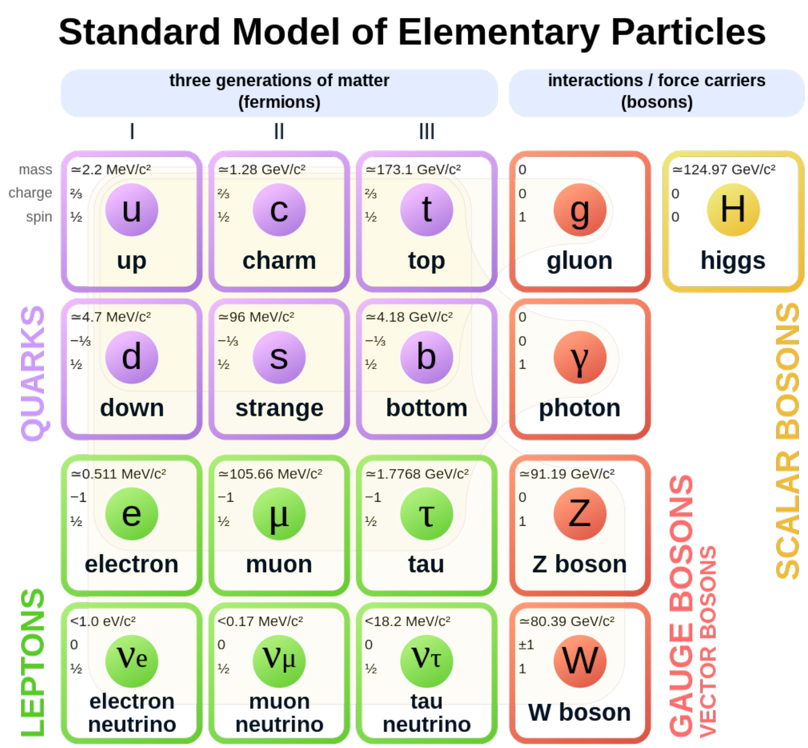

Figure 1.2: A summary of Standard Model particles. Three columns list quarks and leptons. A colored background shows gauge boson pairings with fermions [12].

representation of the particles in the Standard Model, showing the quarks, leptons, and bosons that make up this theoretical framework. Quarks and leptons are both classified as fermions with a spin of 1/2, but they have distinct properties. The lepton family comprises three charged particles (electron, muon, and tau) and three neutral particles (electron neutrino, muon neutrino, and tau neutrino). Leptons and their antiparticles have opposite quantum numbers, although they have the same mass. Quarks are categorized into six flavors: up, down, charm, strange, top, and bottom. The up, charm and top quarks have a charge of $\frac{2}{3}$e, while the down, strange, and bottom quarks have a charge of $\frac{-1}{3}$e. Quarks carry color charges, which come in three varieties: red, green, and blue. Each quark has one of these colors, and their combinations lead to the formation of color-neutral particles such as protons and neutrons. Anti-quarks have corresponding anti-colors, such as anti-red, anti-green, and anti-blue. The bosons in the Standard Model are responsible for mediating the fundamental interactions. The photon is the mediator of the electromagnetic interaction, while gluons mediate the strong interaction. The W and Z bosons are responsible for the weak interaction. Additionally, the model includes the Higgs boson, which is a spin-0 particle.

1.1 Quantum ChromoDynamics and Quark-Gluon Plasma

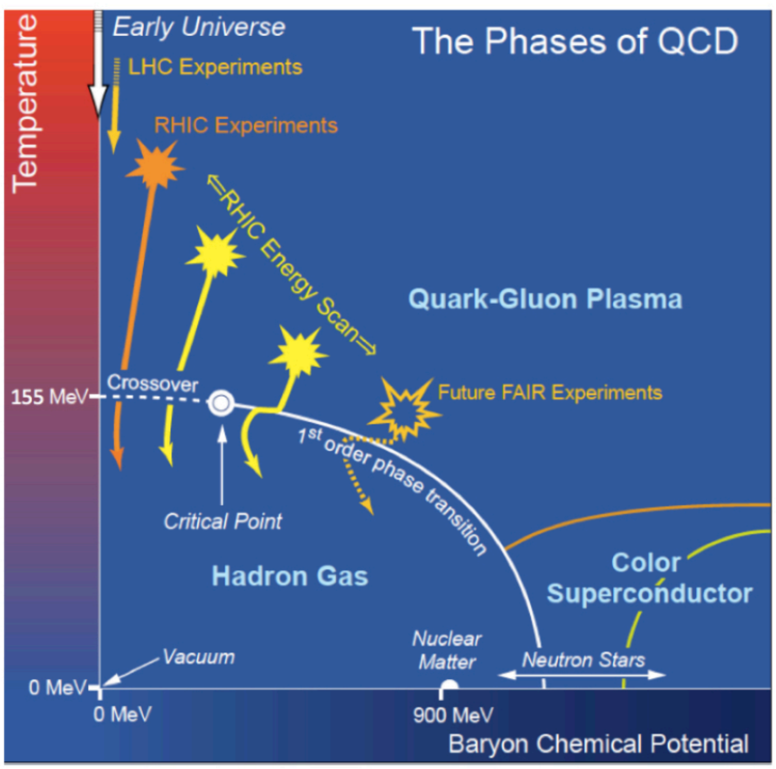

Figure 1.3: A schematic illustration of the QCD phase diagram [27].

QCD [16–19] is a gauge field theory of the strong interaction that describes the interactions between quarks and gluons, with the latter being distinguished from the former by their color quantum numbers. Mesons and baryons are colorless subatomic particles that are made up of both quarks and gluons. Each baryon is made up of three quarks (qqq) while each meson is made up of a pair of a quark and an antiquark ($q\bar{q}$). T.D. Lee [20], suggested in 1974 that dense nuclear matter with asymptotically unbound quarks and gluons may be created by applying a high nucleon density across a large volume. A nuclear state with such a high density is referred to as the "Quark-Gluon Plasma" (QGP) [21,22]. The experimentally observed state of matter known as QGP is described as "a (locally) thermally equilibrated state of matter in which quarks and gluons are deconfined from hadrons, such that color degrees of freedom become manifest over nuclear, rather than just nucleonic volume". Calculations using QCD (Latice-QCD) may also be used to estimate the QGP state at high temperatures [23–26].

A phase diagram, similar to the one used for water, can be used to map the different phases of QCD matter. This diagram indicates at what value of temperature (T) and the baryon chemical potential (μ_{B}), a transition occurs from a normal hadron phase into a deconfined QGP phase. The several phases of QCD matter are depicted in the figure 1.3 [27]. It is possible for quarks and gluons to exist in a deconfined form when the temperature is high and the μ_{B} value is low. Quarks and gluons are contained within hadrons when the temperature is low and the μ_{B} value is low. At high T and low μ_{B}, Lattice-QCD calculations predict that the transition from the hadronic to the QGP phase will be a smooth one, but at high μ_{B}, the phase transition is anticipated by numerous models to be a first-order phase transition. The energy ranges covered by the RHIC at BNL (i.e., Beam Energy Scan-I & II) and the LHC at CERN, which corresponds to μ_{B}, are suitable for the investigation of QGP as well as the phase transition from hadrons to QGP.

1.2 Relativistic Heavy-Ion Collisions

The experiments, such as the STAR [28] experiment at RHIC (Relativistic Heavy Ion Collider) at Brookhaven National Laboratory (BNL) and the ALICE [29] ex-

Year	Accelerators	Location	Species	s_{NN} Energy(GeV)
1986	AGS	BNL	^{16}O, ^{28}Si	5.4
1992			^{197}Au	4.8
1986	SPS	CERN	^{16}O, ^{32}S	19.4
1994			^{208}Pb	17.4
2000	RHIC	BNL	^{197}Au	130
2001			^{197}Au	200
2003			d+^{197}Au	200
2004			^{197}Au	200, 62.4
2005			^{63}Cu	200, 62.4, 22.4
2007			^{200}Au	200
2008			d+^{197}Au	200, 62.4
2010			^{197}Au	200, 62.4, 39, 11.5, 7.7
2011			^{197}Au	200, 19.6, 27
2012			^{238}U	193
2012			^{63}Cu+^{197}Au	200
2014			^{197}Au	200, 14.6
2014			^{3}He+^{197}Au	200
2015			p+^{197}Au	200
2015			p+^{197}Al	200
2016			^{197}Au	200
2016			d+^{197}Au	200, 62.4, 19.6, 39
2017			^{197}Au	54
2018			^{96}Zr,^{96}Ru	200
2018			^{197}Au	27
2010	LHC	CERN	^{208}Pb	2760
2011			^{208}Pb	2760
2013			p+^{208}Pb	5020
2015			^{208}Pb	5020
2016			p+^{208}Pb	5020, 8160
2017			^{129}Xe	5440
2018			^{208}Pb	5020

Table 1.1: Summary of relativistic heavy-ion collisions [32].

periment at the LHC (Large Hadron Collider) at CERN, are designed to create and study the Quark-Gluon Plasma (QGP). These experiments involve the collision of two relativistic heavy ions, aiming to simulate the conditions that prevailed shortly after the Big Bang, leading to the formation of QGP. This unique state of matter is often referred to as the "Little Bang" [30,31] as it mimics the high-energy and dense environment of the early universe. These experiments allow scientists to investigate the properties of QGP, such as its temperature, density, and collective behavior. By studying the QGP, researchers hope to gain insights into the fundamental properties of matter and the strong nuclear force that binds quarks and gluons within hadrons. The experiments involve sophisticated detectors and analysis techniques to measure various observables, such as particle yields, momentum distributions, and correlations. The data collected from these experiments provide valuable information for understanding the behavior of matter under extreme conditions and testing theoretical models, such as the Standard Model of particle physics. The heavy-ion collision experiment's timeline is displayed in table 1.1 [32].

1.2.1 Space-Time Evolution

The hypothesis of the Quark-Gluon Plasma (QGP) suggests that it was present in the early universe shortly after the Big Bang. To study and understand this state of matter, scientists conduct experiments involving relativistic heavy-ion collisions. These collisions generate extremely hot and dense matter that evolves through different stages.

Figure 1.4 illustrates the space-time evolution resulting from heavy-ion collisions [33]. At the moment of collision (t, z) = (0, 0), where "t" represents time and "z" represents space, two nuclei collide. Due to their relativistic speeds, the nuclei are Lorentz-contracted. To facilitate the analysis of relativistic heavy-ion collisions, it is useful to utilize kinetic variables that maintain a simple form or remain invariant under Lorentz transformations. One such variable is the proper time of particles, denoted by τ, which is defined as $\tau = \sqrt{t^2 - z^2}$. In Figure 1.4, regions where

$\sqrt{t^2 - z^2} < 0$ are referred to as space-like regions, while regions where $\sqrt{t^2 - z^2} > 0$ are referred to as time-like regions. Particle production predominantly occurs in the top half of the time-like region.

During the collision, the overlapping region of the approaching nuclei experiences compression, leading to a significant amount of kinetic energy being expelled within a confined space for a short period of time. If the energy density is high enough, the quarks and gluons become deconfined after the collision. However, the resulting state may not be in thermal equilibrium immediately after deconfinement. It takes approximately 1 femtosecond (1 fm/c) for the matter to reach local thermal equilibrium, forming what is commonly known as the QGP. This time is often referred to as the pre-equilibrium stage. Throughout this process, the matter be-

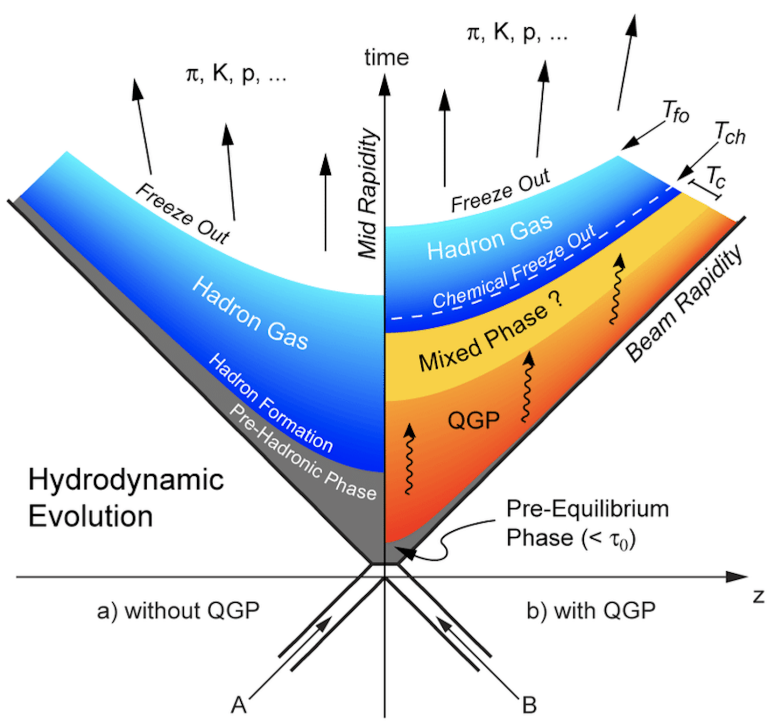

Figure 1.4: Schematic of heavy-ion collision space-time evolution, plotted as a function of t and z, considering a scenario without (left panel) and with (right panel) the creation of a QGP [33].

haves like a fluid, and the characteristics of a plasma are assumed to apply to the QGP. In the QGP, the pressure gradient plays a crucial role in the expansion of the matter. As the QGP expands, it undergoes a cooling process. At a critical temperature (T = T_c), the quarks and gluons present in the QGP undergo a process called hadronization or hadron freeze-out. During hadronization, the quarks and gluons combine to form a hadron gas composed of various types of particles, such as protons, neutrons, pions, and other hadrons. As the hadron gas continues to expand, it reaches a temperature known as the chemical freeze-out temperature (T = T_{ch}). At this temperature, the inelastic interactions between the hadrons cease. This means that the abundance and chemical composition of the particles remains unchanged beyond this point. In other words, the relative ratios of different types of particles are frozen, and no new particle production or changes in the composition occur.

However, elastic interactions between the hadrons can still occur below the chemical freeze-out temperature. These elastic interactions continue until the system reaches the freeze-out temperature (T_{fo}). The freeze-out temperature is the point at which the mean free path of the hadrons becomes large compared to the dynamical size of the system. At this stage, the hadrons are no longer strongly interacting with each other, and they flow freely without further significant interactions. This process of expansion, hadronization, and freeze-out is an important aspect of the evolution of the QGP and helps in understanding the transition from the deconfined quark-gluon matter to the hadronic phase.

1.2.2 Relativistic kinematics

In a typical collider, the coordinate system is designed in such a way that the beam axis is aligned parallel to the Z-axis. The term “primary vertex” refers to the point at where the two nuclei come into contact with one another. The primary vertex of the collision can be determined by using the tracking information that is provided by the data.

1.2.2.1 Transverse Momentum

The particle's total momentum can be split into two distinct components: the longitudinal component (p_z), which describes the part of the momentum parallel to the beam direction, and the transverse component (p_T), which describes the part of the momentum perpendicular to the beam direction. The Z-axis is often the direction of the beam in heavy-ion collisions. Therefore, the value of the transverse momentum (p_T), can be calculated as:

$$p_\mathrm{T} = \sqrt{p_\mathrm{x}^2 + p_\mathrm{y}^2} \tag{1.1}$$

where, p_x and p_y are components of total momentum along the X and Y direction. The p_T is Lorentz invariant quantity.

1.2.2.2 Rapidity

The dimensionless quantity known as rapidity (y), is defined in terms of the particle's energy, E, and its longitudinal momentum, p_z. The rapidity is defined as:

$$y = \frac{1}{2} ln \frac{E + p_\mathrm{z}}{E - p_\mathrm{z}} \tag{1.2}$$

In the non-relativistic limit, the rapidity is equivalent to the particle's velocity where the momentum (p) has a value comparable to or smaller than its mass (m_0) under the Lorentz transformation, rapidity possesses the advantageous property of additivity, providing a distinct benefit in analysis and calculations. In high-energy particle physics, the rapidity (y) of a particle serves as a measure of its relativistic velocity [34–36]. However, at the relativistic limit, the concept of velocity no longer maintains an additive nature.

1.2.2.3 Pseudorapidity

Particle identification is essential for measuring a particle's rapidity, which requires knowledge of its energy and longitudinal momentum. In cases where only the angle relative to the beam axis can be measured, pseudo-rapidity serves as a useful approximation of rapidity. Pseudorapidity can be defined independently of particle mass and momentum, enabling analyses of angular distributions in high-energy experiments [34–36]. Thus, pseudo-rapidity (η) can be defined as:

$$\eta = \frac{1}{2} ln \frac{p + p_z}{p - p_z} = -ln \left[tan \left(\frac{\theta}{2} \right) \right] \tag{1.3}$$

where θ is the angle between the direction of the created particle and the beam.

1.2.2.4 Collision centrality

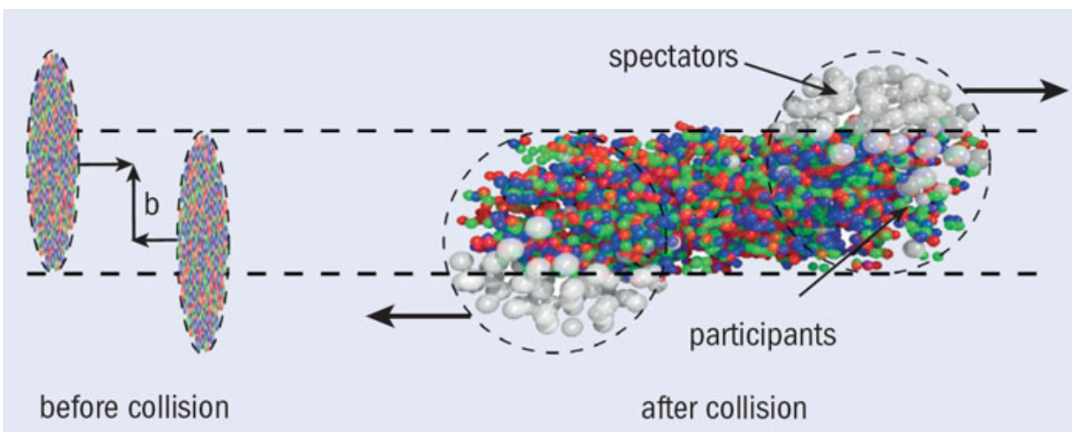

Figure 1.5: A geometric view of relativistic heavy-ion collision with impact parameter. The spectator nucleons remain unaffected while particle production takes place in the participants' zone [38].

The initial geometric overlap of two heavy ions meeting at a particular collision energy dictates the initial energy density and geometry of the medium created in a collision, hence determining the evolution of the medium and their interactions with the particles produced in the collisions [37]. Typically, the initial collision geometry is described by three geometrical factors (or centrality variables): the impact parameter (b), the number of participating nucleons (N_{part}), and the number of binary nucleon-nucleon collisions (N_{coll}). The impact parameter (b) is the distance between the centers of two heavy ions that are colliding in a plane that is perpendicular to the direction of the beam, as demonstrated in Fig. 1.5 [38]. However, these geometrical variables cannot be directly measured by experiments; rather, they are derived by mapping to other observable physics quantities, notably the number of charged particles produced in a collision, which increases monotonically with the occurrence of more central collisions. Under the centrality determination framework of Glauber Model simulations [39–41], this mapping is realizable. Figure 1.6 depicts the rela-

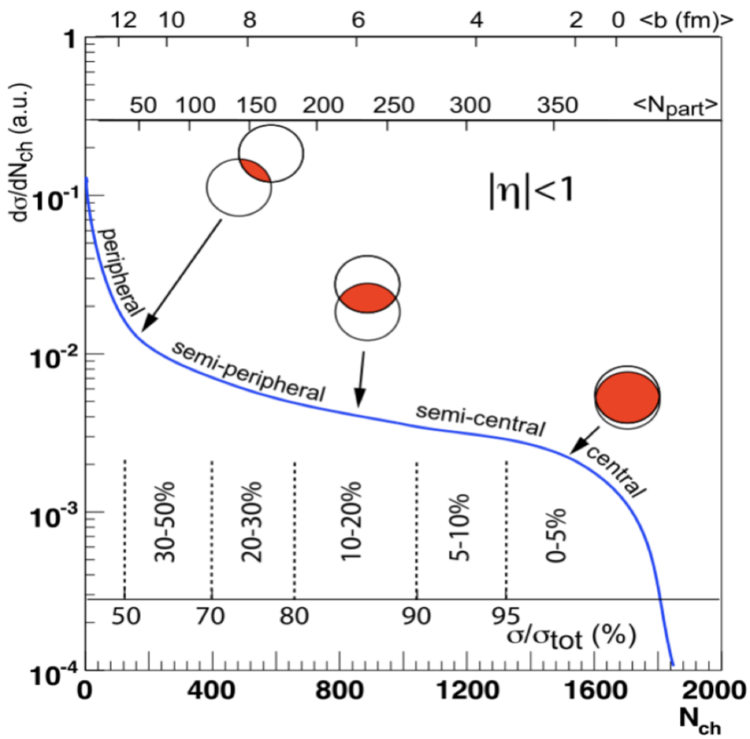

Figure 1.6: An illustration of the relationship between charged particle multiplicity N_{ch}, impact parameter b, average participating nucleons N_{part}, and centrality in percentage [42].

tionship between the measured charged particle multiplicity N_{ch}, the average impact parameter b, the average number of participating nucleons N_{part}, and the percentage centrality in Au+Au collisions at $\sqrt{s_{\mathrm{NN}}} = 200$ GeV [42]. The average value of b and N_{part} is used because they are obtained by averaging inside a particular centrality bin (e.g., 0-5%, 5-10%, ...). The lowest value of N_{part} (i.e., large impact parameter b) corresponds to the most peripheral collisions, whereas increasing N_{part} corresponds to semi-peripheral, semi-central, and central collisions (which have a small impact parameter), respectively.

1.3 Signatures of QGP

Experiments conducted at the Relativistic Heavy Ion Collider (RHIC) and the Large Hadron Collider (LHC) have aimed to investigate and characterize the high energy density state of matter, known as the Quark-Gluon Plasma (QGP), which is expected to be formed in heavy-ion collisions. In these experiments, the particles that emerge from the collision zone are measured and analyzed to infer the presence of the QGP. However, it's important to note that direct detection of the QGP phase during a high-energy physics experiment is not possible due to various interactions that occur during and after the freeze-out process. Instead, the existence of the QGP is inferred indirectly through the observation of specific signatures or signals that are believed to be associated with its formation. These signals serve as evidence for the existence and properties of the QGP.

Some of the conventional and significant QGP signals that have been studied and observed in experiments include elliptic flow, jet quenching, strangeness enhancement, direct photons, and dilepton radiation. These are just a few examples of the various signals and observables that have been studied to characterize the QGP. Each of these signals contributes to our understanding of the properties and behavior of the QGP and helps to build a comprehensive picture of the high-energy density state of matter created in heavy-ion collisions. It's important to note that the field of heavy-ion physics is continuously evolving, and new experimental techniques and observables are being explored to further enhance our understanding of the QGP. Some of the signatures are discussed below:

1.3.1 Azimuthal Anisotropy

It is expected that the azimuthal distribution of the particles created in heavy-ion collisions would give information regarding the reaction dynamics and the equation of state (EOS) at extremely high temperatures and energy densities. There is a vacuum surrounding the heavy-ion collision system. This creates a pressure gradient

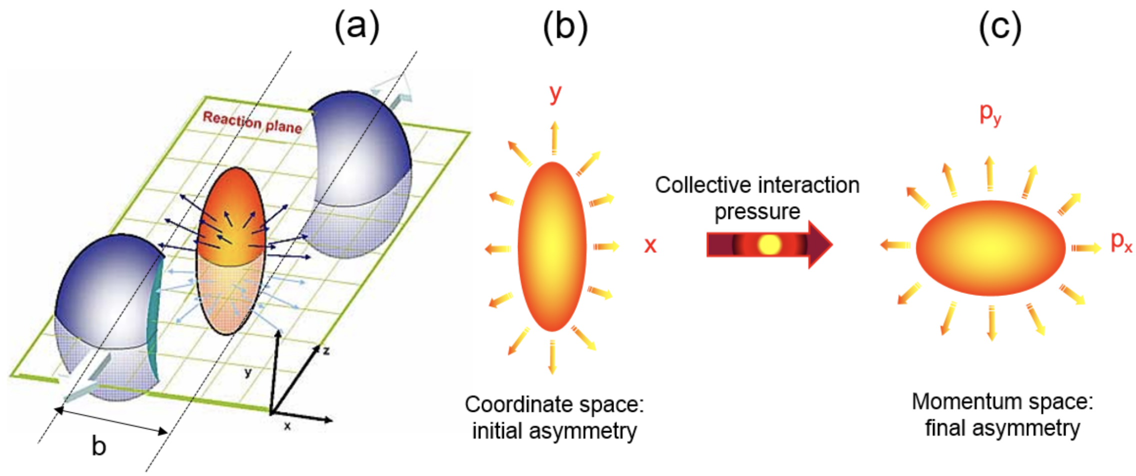

Figure 1.7: A representation of initial-state anisotropy being converted into momentum anisotropy in the overlap zone of a collision geometry with non-central collisions.

from the dense center to the system's periphery. For head-on heavy-ion collisions, this pressure gradient is radially symmetric and boosts all newly generated particles radially outward. The spectra of heavy particles' transverse momentum are influenced by this. The shape of the interaction region for non-central collisions is influenced significantly by the collision's impact parameter. As seen in figure 1.7, the reaction volume has an elliptical shape immediately following the collision.

The almond-shaped spatially asymmetric zone is generated in the case of non-central collisions due to the partial overlap of target and projectile nuclei. Due to the non-zero impact parameter, the flow of particles is anticipated to occur along the transverse plane (x-y plane), where the convention takes the beam's (longitudinal) direction to be along the z-axis. The x-z plane is described as a reaction plane formed by the impact parameter vector and the beam direction. Multiple collisions occur due to the spatial asymmetry, and as a result of a larger pressure gradient along the minor axis, the spatially asymmetric distribution transforms to momentum anisotropy. The geometry of non-central heavy-ion collisions is shown in figure 1.7.

Fourier harmonics [43,44] have been utilized to characterize different patterns of anisotropic flow.

$$E\frac{d^3N}{dp^3} = \frac{1}{2\pi}\frac{d^2N}{p_T dp_t dy}(1+\sum_{n=1}^{\infty}2v_n\cos(n(\phi-\psi_{RP}))+\sum_{n=1}^{\infty}2a_n\sin(n(\phi-\Psi_{RP}))) \quad (1.4)$$

where E, p, p_t, ϕ, y, and Ψ_{RP} correspond to the energy, momentum, transverse momentum, azimuthal angle, rapidity, and the reaction plane angle. Because the sine term vanishes due to reflection symmetry with respect to the reaction plane, the above equation only includes the cosine term. The flow coefficients can be written as,

$$v_n = \langle\cos(n(\phi-\Psi_{RP}))\rangle \quad (1.5)$$

where, v_n is the n^{th} harmonic coefficient. The angle brackets denote the average over all particles in a given event, followed by the average over all events. The various harmonics of Fourier coefficients represent various types of flow. The first two harmonics, i.e., n=1 and 2, play a significant role in anisotropic flow and are referred to as “Directed Flow (v_1)” and “Elliptic Flow ($v_2 = \langle\cos(2(\phi-\Psi_{RP}))\rangle$)” [45, 46]. v_3 and v_4 are “Triangular Flow” and “Quadrilateral Flow” [45], respectively, and are associated with the early heterogeneities. Flow analysis sheds light on numerous characteristics, including beginning circumstances, EOS, thermal equilibrium, system evolution, and freeze-out properties.

1.3.1.1 Elliptic flow

The measurements of the elliptic flow (v_2) constrain the equation of state and transport parameters of QGP. The magnitude of v_2 is related to the initial anisotropy in the geometry of the colliding system and also depends on the characteristics of the medium that it is interacting with. Since it is anticipated that elliptic flow will arise at an early time and persist until hadronization, the measurement provides information on the partonic and hadronic level interactions. RHIC and LHC determined v_2 and compared the results to hydrodynamic models. The results demonstrated that the QGP was generated during the initial stages of the interaction and behaves as

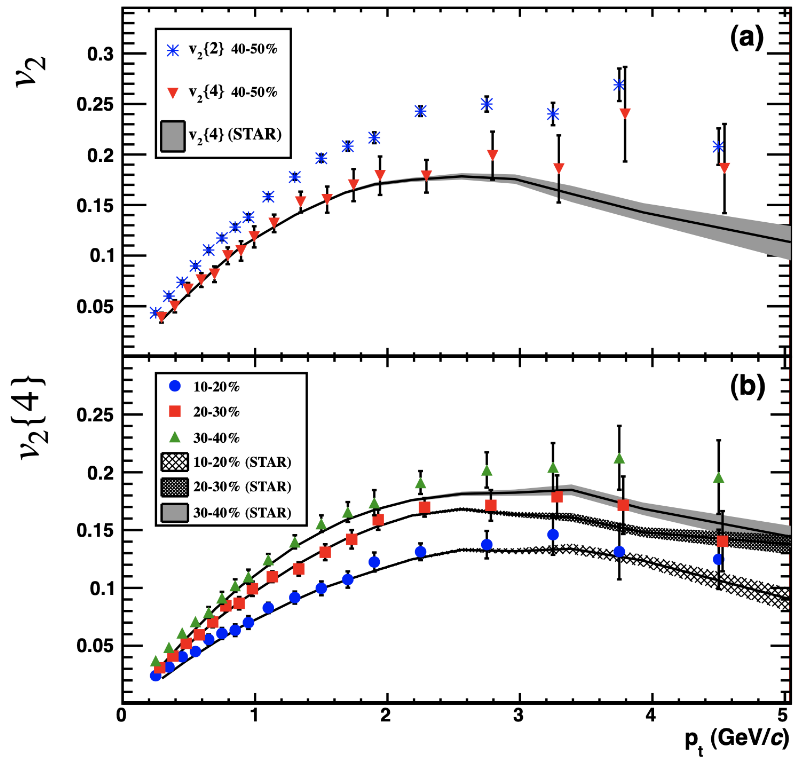

Figure 1.8: Transverse momentum p_T dependence of v_2 in Pb-Pb collisions at $\sqrt{s_{\rm NN}}$ = 2.76 TeV for centrality 40-50% (top) and $v_2\{4\}$ (p_T) for different centralities (bottom) are compared with the STAR v_2 measurements at $\sqrt{s_{\rm NN}}$ = 200 GeV shown in shaded bands.

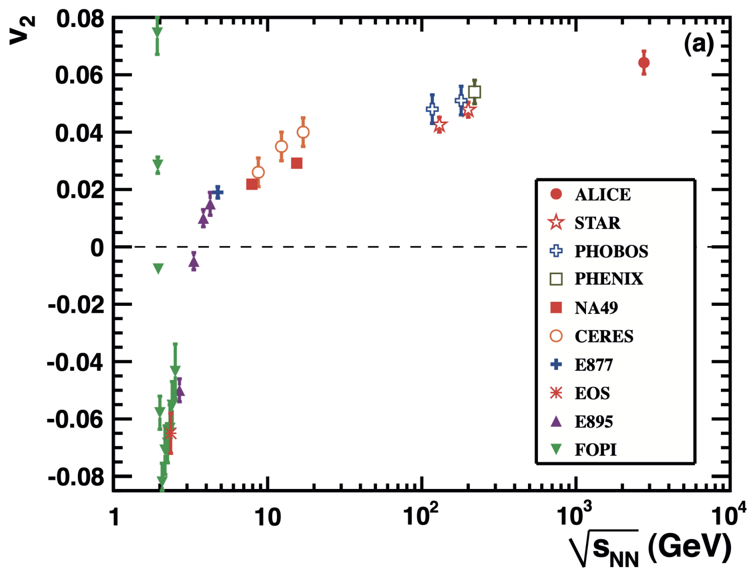

Figure 1.9: The energy dependence of integrated elliptic flow (v_2) is compared with the results for similar centrality from various experiments conducted at different energies [45].

an ideal fluid. Numerous approaches have been developed to examine elliptic flow, including the event-plane method [47,48], the Q-cumulant method [49], the probability p(v_2) [50], etc. The v_2 has been measured by the STAR [51,52], PHENIX [53], PHOBOS [54], and ALICE [55,56] using different approaches and for different systems.

During the first run of heavy ions at LHC, the ALICE collaboration measured elliptic flow in Pb-Pb collisions at $\sqrt{s_{\rm NN}} = 2.76$ TeV [55]. Using the 2- and 4-particle cumulant method [49], the p_t differential elliptic flow as a function of collision centrality has been estimated. Figure 1.8 (top) depicts $v_2(p_t)$ for 40-50% centrality, and

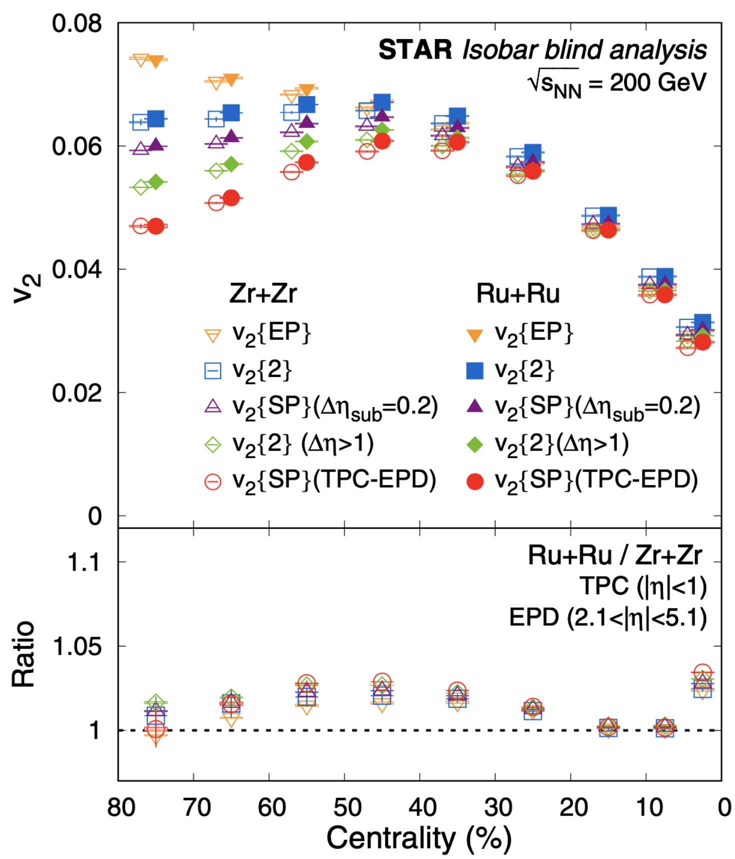

Figure 1.10: Measurements of elliptic anisotropy (v_2) employing a variety of methods in isobar collisions at $\sqrt{s_{\rm NN}} = 200$ GeV using TPC and EPD detectors as a function of the collision centrality [58].

the shaded area reflects the STAR measurement for the same centrality in Au+Au collisions at $\sqrt{s_{\rm NN}} = 200$ GeV [57]. For both ALICE and STAR, the $v_2(p_t)$ values do not vary within uncertainties. Figure 1.8 (bottom) compares $v_2\{4\}(p_t)$ produced using cumulant technique for three different centralities at LHC with STAR results at RHIC. In both measurements, a reasonable degree of consistency is seen.

Additionally, the energy dependence of integrated v_2 has been investigated. The calculations of the ideal hydrodynamic model projected a rise in v_2 with increasing beam energy. Figure 1.9 demonstrates a consistent rise in v_2 as energy increases, showing an increment of 10-30% when energy increases from $\sqrt{s_{\mathrm{NN}}} = 200$ GeV (at RHIC) to 2.76 TeV (at LHC). A rise in the mean p_T ($\langle p_T \rangle$) of charged hadrons is responsible for the bigger integrated v_2 at the LHC.

Figure 1.10 shows latest results of elliptic flow (v_2) from isobaric ($^{96}_{44}Ru +^{96}_{44} Ru$ and $^{96}_{40}Zr +^{96}_{40} Zr$) collisions at $\sqrt{s_{\mathrm{NN}}} = 200$ GeV [58]. The upper panel of Fig. 1.10 presents a summary of the v_2 results obtained by several analysis groups employing a variety of techniques. The v_2 ratio for collisions between Ru+Ru and Zr+Zr are displayed in the lower panels of Fig. 1.10. The ratios are greater than one by 2% to 3% for the mid-central collisions, but they begin to decrease as they move toward the central and peripheral collisions, with the exception of the top 5% centrality bin, in which the ratio is greater than one. It may be concluded from these v_2 ratios that the Chiral Magnetic Effect (CME) backgrounds in the two isobar systems are different.

1.3.2 Jet quenching

Parton hard scattering produces highly energetic particles that lose energy by radiating gluons in the hot dense matter created in heavy-ion collisions, resulting in the suppression of high transverse momentum particles. This is known as jet quenching. This energy loss provides fundamental information about the medium's thermodynamic and transport properties [59]. During the traversal of these energetic partons through the dense medium, it is expected that the energy loss is proportional both to the initial density of gluons [60, 61] and to the lifetime of dense matter. The jet quenching is characterized by an observable known as Nuclear Modification Factor

(R_{AA}) [62], which is defined as the ratio of high p_T hadronic yield in AA collisions to nucleon-nucleon (e.g. pp) collisions scaled by the number of elementary nucleon-nucleon collisions.

$$R_{\mathrm{AA}} = \frac{d^2N^{AA}(dp_T d\eta)^{AA}}{T_{AA}d^2\sigma^{NN}(dp_T d\eta)^{NN}} \tag{1.6}$$

where $T_{AA} = \langle N_{bin}\rangle/\sigma_{inel}^{NN}$ and the σ_{inel}^{NN} are the number of binary collisions and the inelastic cross-section, respectively. Jet quenching is observed at both RHIC and LHC energies. Hard scattering produces back-to-back di-jets due to momentum conservation. There is a possibility that a jet can be produced at the edge of the

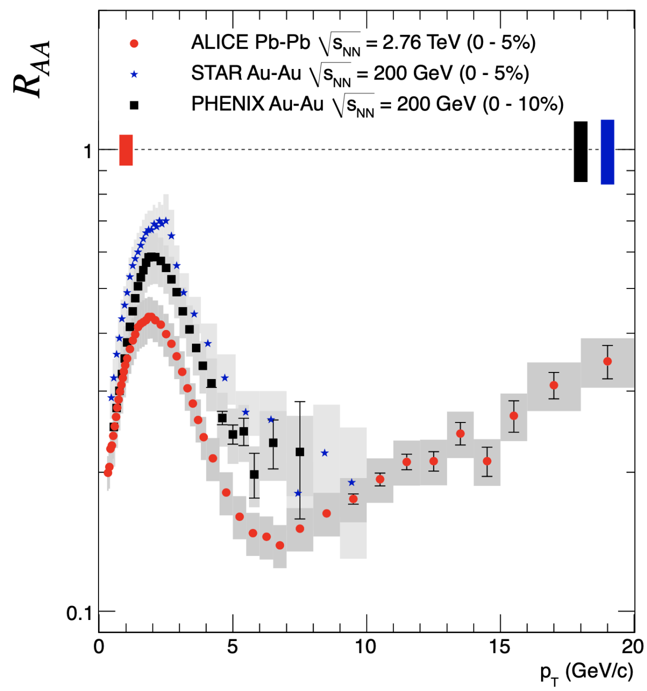

Figure 1.11: The R_{AA} yield for central Pb-Pb collisions at LHC at $\sqrt{s_{\mathrm{NN}}}$ = 2.76 TeV is compared to the same measurement at RHIC in Au+Au collisions at $\sqrt{s_{\mathrm{NN}}}$ = 200 GeV and observed a strong suppression at LHC energy [65].

medium, called the "near-side jet", but due to momentum conservation, another jet will be produced inside the medium, called the "away-side jet". Due to its greater propagation through the medium, the away-side jet would be quenched more than the near-side jet.

The STAR [63] and PHENIX [64] experiments at RHIC reported the results of R_{AA} measurements in more central (0-5% and 0-10%) Au+Au collisions at $\sqrt{s_{\mathrm{NN}}}$ =

200 GeV. They observed strong suppression of high p_T hadron yields. ALICE also measured the nuclear modification factor R_{AA} for charged hadrons in central Pb-Pb collisions at $\sqrt{s_{\rm NN}} = 2.76$ TeV [65] and compared the results to those of STAR and PHENIX in figure 1.11. According to the results, R_{AA} is less than unity. At $p_T =$ 6-7 GeV/c, a smaller drop in the R_{AA} value is seen for ALICE than for RHIC. When compared to RHIC, a strong suppression at LHC suggests that a lot of energy is lost at LHC. For high p_T ($>$ 7GeV/c), a significant increase in R_{AA} is seen, which shows that high p_T hadrons lose a small amount of energy. Another tool for measuring jet

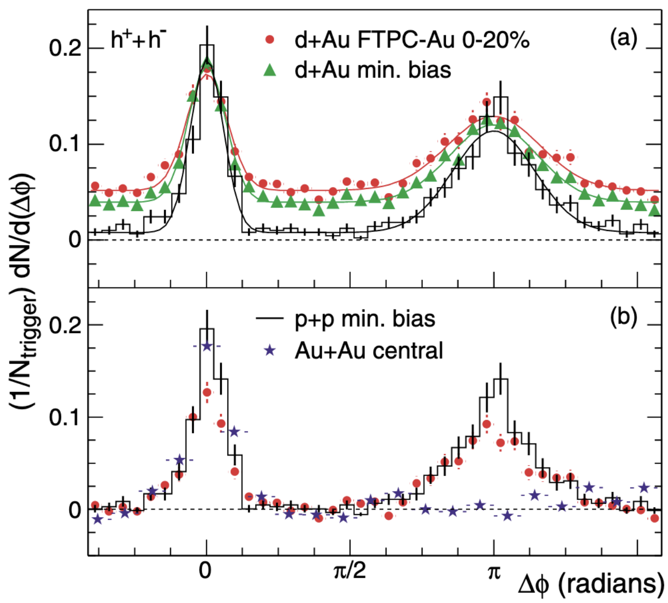

Figure 1.12: Jet azimuthal correlations for pp, d+Au and Au+Au collisions at $\sqrt{s_{\rm NN}} = 200$ GeV measured with STAR experiment [66].

quenching in heavy-ion collisions is the dihadron angular correlation measurement. The STAR measured the dihadron angular correlations for Au+Au, d+Au, and p+p collisions at $\sqrt{s_{\rm NN}} = 200$ GeV. The upper plot in Fig. 1.12 depicts the jet azimuthal correlation distributions for central and minimum bias d+Au collisions, whereas the bottom plot depicts the correlation for central Au+Au and minimum bias pp collisions. From the figure it is observed that in Au+Au collisions the away side peak (around 3.14 radians) is suppressed with respect to the near side peak (around 0 radians). The away side correlations in Au+Au data are quenched, indicating significant suppression, but no away side quenching effect has been observed in d+Au and pp collision systems [66, 67]. This suggests that jet-quenching effects are absent in small collision systems.

1.3.3 Strangeness enhancement

Enhanced formation of strange particles in heavy-ion collisions is considered to be a primary sign of QGP production [68–70]. At first, there are no strange (s) quarks because the nuclei that are colliding only have "u" and "d" quarks. This reveals that strange quarks are generated by the process of thermalization in a hot and dense medium during the strong interaction. The production of strange quarks is mainly due to two types of processes, gg $\rightarrow s\bar{s}$ and $q\bar{q} \rightarrow s\bar{s}$, whose dominance depends on whether the QGP medium is gluon rich or quark rich. Since QGP has a high gluon density, the formation of the $s\bar{s}$ pair from the channel gg $\rightarrow s\bar{s}$ dominates the annihilation of light quarks ($q\bar{q} \rightarrow s\bar{s}$). In pp collisions, where the QGP medium formation is not expected, the strange quarks are mainly produced through annihilations of light quarks. The strangeness enhancement factor (E) is defined as the ratio of yield of a strange particle per participating nucleon in the heavy-ion collisions to that in pp collisions.

$$E = \frac{(Yield/N_{part})^{AA}}{(Yield/N_{part})^{NN}} \tag{1.7}$$

Where N_{part} corresponds to the number of participants in a collision. If the value of "E" is greater than unity, it can attribute to strangeness enhancement. The strangeness enhancement factor (E) in Cu+Cu and Au+Au collisions at $\sqrt{s_{\mathrm{NN}}}$ = 62.4 and 200 GeV for K, ϕ, λ and Ξ particles is shown in Fig. 1.13 [71–74]. The observation of an enhanced ϕ meson production in Cu+Cu and Au+Au collisions indicates a formation of a dense partonic medium, which is responsible for strangeness enhancement. The observed enhancement in the strange hadron production is likely to be the result of similar effects rather than only the results of canonical suppression. Different systems and energies have also been investigated by NA57 [75, 76], STAR [77–79], and ALICE [80]. Figure 1.14 (a, b) shows the enhancement for the

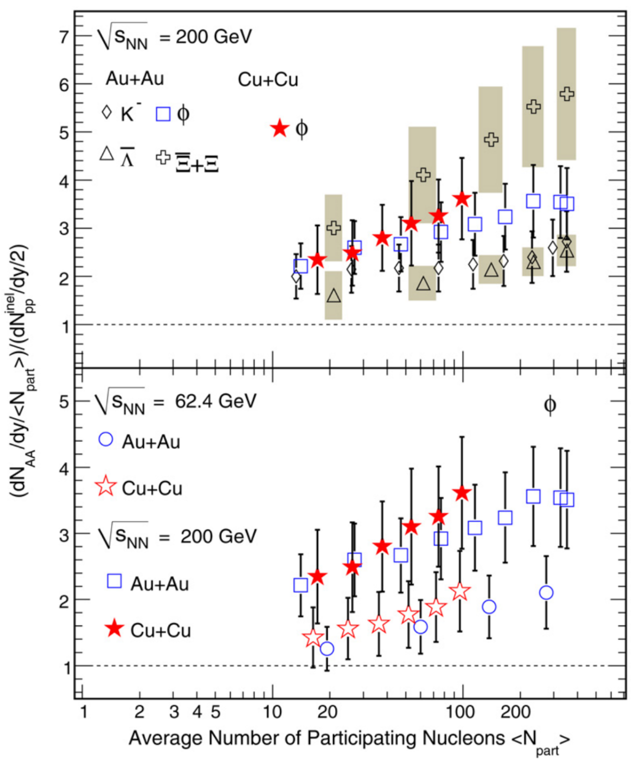

Figure 1.13: Strangeness enhancement factor (E) as a function of $< N_{\text{part}} >$ for K, ϕ, λ and Ξ in Cu+Cu and Au+Au collisions at $\sqrt{s_{\text{NN}}}$ = 200 GeV measured with STAR experiment [72].

strange particles Ξ^-, $\bar{\Xi}^-$, Ω^-+$\bar{\Omega}^+$, in Pb–Pb collisions at $\sqrt{s_{NN}}$ = 2.76 TeV, as a function of the mean number of participants ($\langle N_{part}\rangle$) [80]. The enhancements are larger than the unity for all the particles. The enhancement increases with an increase in the strangeness content of the particle, which is already observed for lower energies and is consistent with enhanced $s\bar{s}$ pair production in a hot and dense partonic medium. The hyperon-to-pion ratios Ξ/π (Ω/π) for A+A and pp collisions both at LHC [81–83] and RHIC [84, 85] energies, are shown in Fig. 1.14 (c) as a function of $\langle N_{part}\rangle$. In pp collisions, strangeness is produced at a higher rate than in low-energy collisions. The figure demonstrates a considerable increase in strangeness production relative to pp, rising with centrality up to around $\langle N_{part}\rangle$ ~150 and seemingly reaching a saturation point thereafter. For the most central collisions, a little decrease in the ratio is seen. Recent thermal model estimates are found to be con-

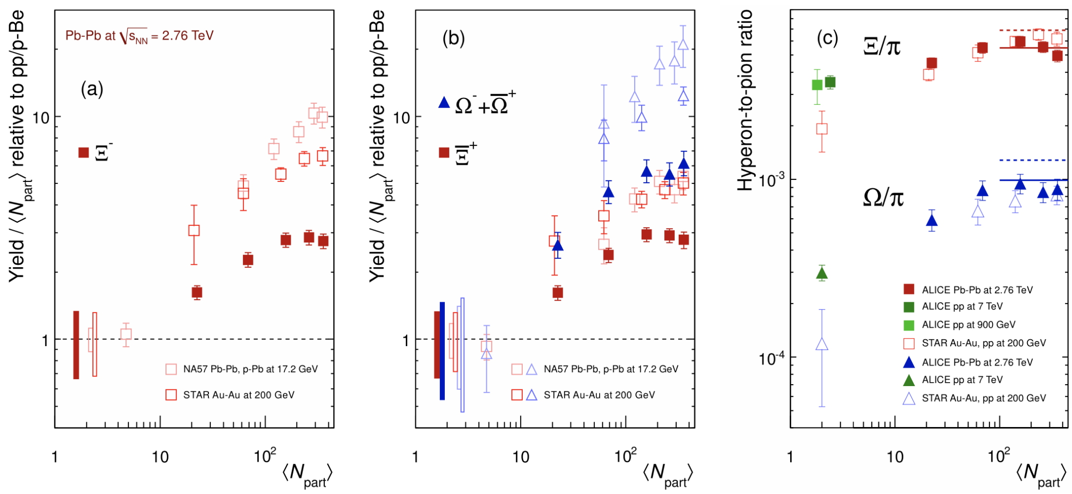

Figure 1.14: (a), (b) Enhancements in the rapidity range $| y |< 0.5$ as a function of the $\langle N_{part}\rangle$, displaying data from the ALICE (solid symbols), RHIC, and SPS (open symbols). The statistical and systematic uncertainties on the pp or p–Be reference are shown by the boxes on the dashed line at unity. (c) The ratio of hyperons to pions in A+A and pp collisions at the LHC and RHIC energies, expressed as a function $\langle N_{part}\rangle$ [80].

sistent with these ratio values for central collisions [86]. The enhancement increases with an increase in the strangeness content of the baryon and its centrality rise as compared to pp.

1.3.4 J/ψ suppression

Suppression of quarkonia (forms of $c\bar{c}$ and $b\bar{b}$ mesons) is an anticipated signal of the QGP. The J/ψ ($c\bar{c}$) meson is a bound state formed by the coupling of a charm quark and its antiquark. Due to the large charm mass, charm quarks are almost exclusively created during hard partonic scattering processes [87]. Because quarkonia survive for such an extended period of time, they experience all phases of the medium's development after collisions [88]. On the other hand, the presence of a QGP medium has the potential to have an impact on the hadronization of the quark-antiquark pairs. In the presence of a dense material that has been deconfined, the bonding between quarks and anti-quarks weakens. As a direct consequence of this, the quarkonium contained within the QGP dissociates, which causes a reduced yield after nuclei collide with one another [89]. Figure 1.15 shows the Nuclear Mod-

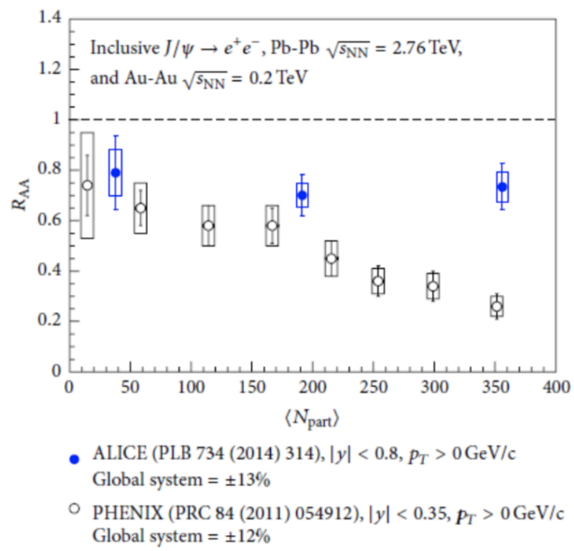

Figure 1.15: Nuclear Modification Factor (R_{AA}) of J/ψ at mid-rapidity as a function of $< N_{part} >$ in Pb-Pb collisions at $\sqrt{s_{NN}}$ = 2.76 TeV, compare with PHENIX measurement at $\sqrt{s_{NN}}$ = 200 GeV [94].

ifiaction Factor (R_{AA}) of J/ψ meson as a function of $\langle N_{part} \rangle$ in Pb-Pb collisions at $\sqrt{s_{NN}}$ = 2.76 TeV in ALICE experiment at the LHC [90–92]. These measurements are compared with PHENIX [93, 94] results at the RHIC energies. From the plot, it is clear that the (R_{AA}) is less than unity, which refers to the suppression of J/ψ at both RHIC and LHC energies. The suppression is increasing at PHENIX [93, 94] as we go from lower $\langle N_{part} \rangle$ (peripheral collisions) to higher $\langle N_{part} \rangle$ (central collisions). In the case of R_{AA} at LHC energy, no centrality dependence is found. The measured J/ψ suppression is decreased (i.e., R_{AA} value increased) from RHIC to LHC energies. At LHC energy, these observations support the formation of a QGP medium that suppresses J/ψ production while a fraction of $c\bar{c}$ pairs combine and enhances J/ψ production.

1.4 Direct Photons and dileptons

The creation of prompt photons is one of the direct signatures of the plasma phase that is created as a result of ultra-relativistic heavy-ion collisions. The term "direct photon" refers to photons that emerge directly from a particle collision. This is different from "decay photons", which emerge out as the daughters of long-lived secondaries that decay electromagnetically, like $\pi^0 \to \gamma\gamma$ or $\Sigma^0 \to \Lambda\gamma$ [95].

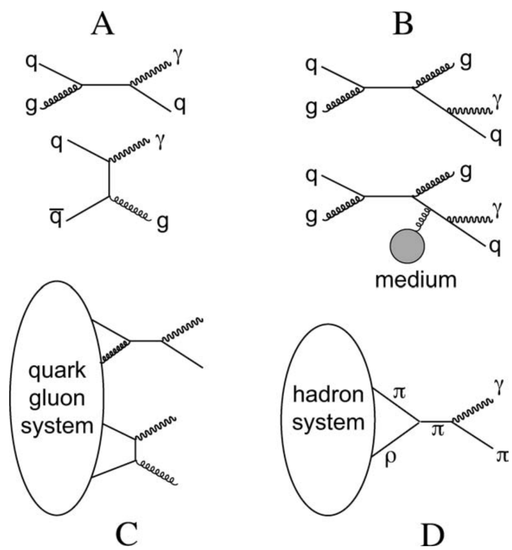

Figure 1.16: A visual representation of the many different mechanisms that can result in the production of direct photons during hadron collisions [95].

Figure 1.16 shows different mechanisms for direct photon production i.e., (A) Scattering between the incoming partons; (B) Photons radiated by outgoing scattered partons, as part of the jet fragmentation process; (C) Scattering between gluons and quarks from a multi-collisional quark/gluon system; (D) Scattering between hadrons from a hadron system [95]. The dominant processes for photon production in QGP are the annihilation ($q\bar{q} \to g\gamma$) and Compton processes (q($\bar{q}$) $\to$ q($\bar{q}$)γ [96]. However, the disadvantage with direct photons is the substantial background from various processes (thermal and non-thermal).

The question is: "What dominates the photon spectra – QGP radiation or hadronic sources?". This can be addressed experimentally by investigating the centrality dependency of the photon yield. It is anticipated that the QGP contribution

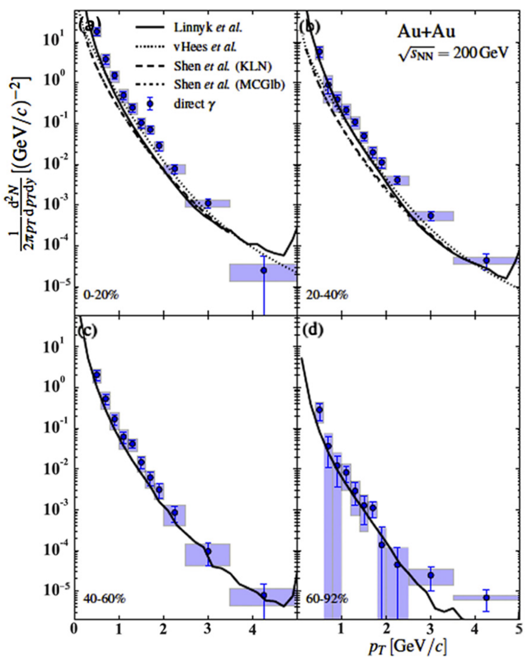

Figure 1.17: The centrality dependence of the direct photon p_T spectra for 0–20%, 20–40%, 40–60%, and 60–92% for Au+Au collisions at $\sqrt{s_{\mathrm{NN}}} = 200$ GeV (model predictions versus the PHENIX data) [97].

will diminish as one move from central to peripheral collisions, which are characterized by a dominance of hadronic channels. Figure 1.17 shows the centrality dependence of the direct photon p_T-spectra for 0–20%, 20–40%, 40–60%, 60–92% for Au+Au collisions at $\sqrt{s} = 200$ GeV [97]. The solid dots stand for the recent PHENIX data [98, 99] whereas the lines indicate the model predictions: solid line – PHSD (denoted as 'Linnyk et al.') [100], dashed and dashed–dotted lines ('Shen et al. (KLN)' and 'Shen et al. (MCGib)') are the results from viscous (2+1)D VISH2+1 and (3+1)D MUSIC hydro models. For the central collisions, the models vary from the data and from each other by up to a factor of 2, because of the varying dynamics and included sources. On the other hand, for the (semi-) peripheral collisions, the PHSD findings which are dominated by meson–meson (mm) and meson–Baryon (mB) bremsstrahlung are more consistent.

Dileptons (lepton pairs, e^+e^- and $\mu^+\mu^-$) have an advantage over direct photons because it is possible to determine the mass of the meson that decayed into the lepton pair. It was proposed [101] that with the presence of quark matter, there would be an enhancement of dileptons of approximately an order of magnitude in the mass region between 200 MeV and 600 MeV. Different hadronic sources of dileptons in pp, p+A, and A+A collisions are given as follows: (i) For low invariant masses (M<1 GeV/c): the Dalitz decays of baryons and mesons (π^0, η, Δ,...) and the direct decay of vector mesons (ρ, ω, ϕ). (ii) For intermediate invariant masses (1<M<3 GeV/c): leptons from correlated $D + D^-$ pairs. (iii) For high invariant masses (M>3 GeV/c): The direct decay of vector mesons (J/Ψ, Ψ) and quark–antiquark annihilation into dileptons ($q + \bar{q} \rightarrow l^+ + l^-$). Also, "Thermal" QGP dileptons are emitted from the partonic interactions in heavy-ion A+A collisions, and they are the primary contributors to the intermediate masses (i.e., "thermal" $q\bar{q}$ annihilation and Compton scattering). At SPS energies, the CERES [102] and NA60 [103] Collaborations have conducted measurements in recent decades to determine the production of dileptons from heavy-ion collisions. The PHENIX Collaboration has successfully measured the dileptons, which consist of pairs of e^+e^- particles for pp and Au+Au at $\sqrt{s}$ = 200 GeV [104].

1.5 Event-by-Event net charge Fluctuations

It is anticipated that the fluctuations of conserved variables within a finite phase space window, such as the system's net charge, will be one of the most sensitive indications of QGP production and phase transition. Furthermore, these fluctuations may provide additional insight into strong interactions. While the particles in a hadron gas (HG) have a unit charge, the charge carriers in the QGP phase are quarks with fractional charges. The oscillations in the system's net–charge are related to the squares of the particles' charges. As a consequence of this, the net–charge variations that occur during the QGP phase are noticeably less pronounced in comparison to those that occur during the HG phase [105]. At the same time, if the initial phase of the QGP is strongly dominated by gluons, the fluctuations per entropy may be reduced even further; this is because the hadronization of gluons raises the entropy [106]. Thus, the net-charge fluctuations are heavily influenced by the phase they originate from.

The charge ratio is used to reduce the influence of uncertainty produced by volume fluctuations, $R = N_+/N_-$, where N_+ and N_- are the number of positive and negative charge particles, respectively. The term "$\nu_{+-,dyn}$" is used to quantify the resulting net charge variations, and it is defined as follows:

$$\nu_{+-,dyn} = \frac{\langle N_+(N_+-1)\rangle}{\langle N_+\rangle^2} + \frac{\langle N_-(N_--1)\rangle}{\langle N_-\rangle^2} - 2\frac{\langle N_-N_+\rangle}{\langle N_+\rangle\langle N_-\rangle} \tag{1.8}$$

This $\nu_{+-,dyn}$ is related to the quantity "D" which is the variance of ratio of N_+ and N_- scaled by the total charged particle multiplicity, as follows:

$$\langle N_{ch}\rangle \nu_{+-,dyn} \approx D - 4 \tag{1.9}$$

ALICE studied net charge fluctuations for Pb-Pb collisions at $\sqrt{s_{\rm NN}} = 2.76$ TeV

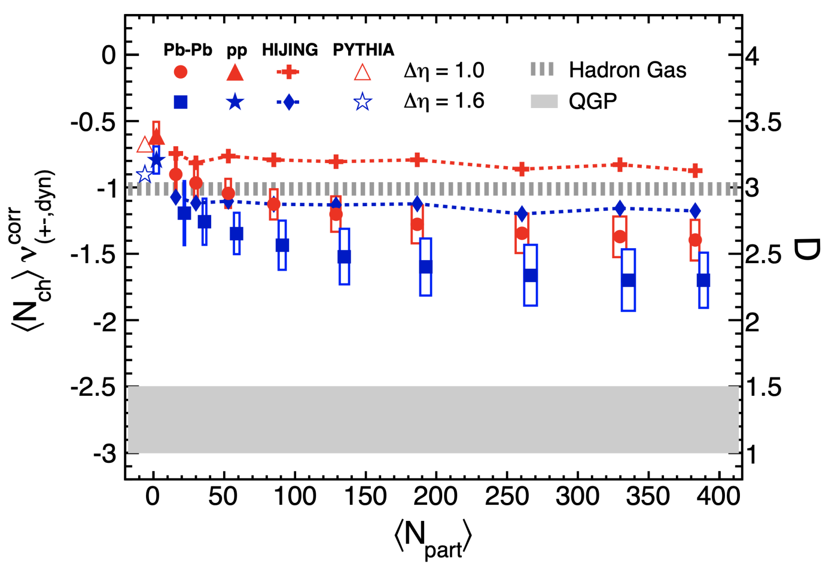

Figure 1.18: $\langle N_{ch}\rangle \nu^{corr}_{+-,dyn}$ (left axis) and D (right axis) as a function of the number of participants for $\Delta\eta = 1$ and 1.6 in Pb–Pb at $\sqrt{s_{\rm NN}} = 2.76$ TeV and pp collisions at $\sqrt{s} = 2.76$ TeV along with results from the HIJING and PYTHIA event generators [107].

and pp collisions at $\sqrt{s} = 2.76$ TeV [107] along with event generators i.e., HIJING and PHYTHIA [107, 108]. Figure 1.18 shows $\langle N_{ch}\rangle \nu^{corr}_{+-,dyn}$ (left axis) and D (right axis) dependence on the number of participants along with theoretical prediction

for QGP and hadron gas. Net charge fluctuations are also studied in reference [107] with dependence on the collision energy, with PHENIX and STAR energies (Au+Au at 200, 130, 62.4 and 19.6 GeV) [109,110] along with ALICE energies.
The measurements from the net charge fluctuation $\nu^{corr}_{+-,dyn}$ (corrected for charge conservation and finite acceptance effect) for pp and Pb-Pb collisions at the same center–of–mass energy ($\sqrt{s} = 2.76$ TeV) are found to be in agreement with hadron gas prediction. Negative values of $\nu^{corr}_{+-,dyn}$ show dominance from the correlation of positive and negative charges. A decreasing trend in fluctuations and D (charge fluctuation per entropy) is observed while going from peripheral to central collisions.

1.6 Thesis Motivation

In the context of high-energy heavy-ion collisions, the primary objective is to create and study the Quark-Gluon Plasma (QGP), a state of matter that is believed to have existed in the early universe just after the Big Bang. This QGP is formed at extremely high energy densities and temperatures and subsequently undergoes expansion and cooling, eventually transitioning into a gas of hadrons. To better understand the properties and characteristics of the QGP, researchers also conduct experiments with asymmetric collision systems, such as proton-nucleus (p+A) and deuteron-nucleus (d+A) collisions. These collisions serve as control experiments where the formation of the QCD medium (which includes the QGP) is not expected. By comparing the results obtained from nucleus-nucleus (A+A) collisions, where the QGP is formed, with those from p+A and d+A collisions, it becomes possible to isolate and investigate the effects of cold nuclear matter (nuclear effects) separately from the hot and dense matter produced in A+A collisions.

In the specific context of the mentioned thesis work, the focus is on studying the event-by-event charge separation effect that occurs in heavy-ion collisions. This effect is investigated through the analysis of charge-dependent multi-particle azimuthal correlations. By examining the correlations between particles with different charges and their azimuthal angles, we can gain insights into the collective behavior and the properties of the QGP, as well as the mechanisms that lead to the separation of positive and negative charges in the collision system.

This analysis technique allows for the investigation of charge-dependent observables that are sensitive to the presence of the QGP and related phenomena. By studying these correlations on an event-by-event basis, our objective is to understand the origin and dynamics of charge separation in heavy-ion collisions and further contribute to our understanding of the QGP and its properties.

1.6.1 Chiral Magnetic Effect

When heavy ions collide, there is an interesting prospect that regions may temporarily form in which the charge-parity (CP) and parity (P) symmetries will be locally violated by the strong interaction. This would result in an imbalance in the number of right-handed and left-handed (anti-)quarks. It has been demonstrated that the net effect would be a separation of charges along the direction of the magnetic field if a sufficiently strong (electro-)magnetic field exists in such a region (as it may be in off-center heavy-ion collisions, generated principally by the protons in the two nuclei), known as the Chiral Magnetic Effect (CME) [111–115].

In this thesis, a new technique for investigating the CME called the Sliding Dumbbell Method (SDM) has been developed. This approach looks at each individual event to determine the back-to-back charge separation. The SDM facilitates the selection of events corresponding to various charge separations (f_{DbCS}) across the dumbbell. The events with back-to-back charge separation of CME kind are isolated and analyzed.

1.7 Organization of Thesis

The thesis is organized as follows:

Chapter 1: Introduction

Provides an introduction to the field of high-energy heavy-ion collisions and the study of the Quark-Gluon Plasma (QGP). It offers an overview of the thesis's motivation and objectives.

Chapter 2: Experimental Set-up

In this chapter, the experimental set-up, particularly the STAR detector at RHIC (Relativistic Heavy Ion Collider), is described in detail.

Chapter 3: Chiral Magnetic Effect and Development of Sliding Dumbbell Method

This chapter focuses on the Chiral Magnetic Effect and the development of the Sliding Dumbbell Method as a tool for analysis.

Chapter 4: Testing on Monte Carlo Models: AMPT and AVFD

The application of the sliding dumbbell method on Monte Carlo models (AMPT and AVFD) is discussed. The results obtained from applying the method to these models are presented.

Chapter 5: Chiral Magnetic Effect in Au+Au collisions at $\sqrt{s_{\mathrm{NN}}} = 200$ GeV using SDM

The sliding dumbbell method is applied to experimental data from Au+Au collisions at a center-of-mass energy of $\sqrt{s_{NN}} = 200$ GeV. This chapter describes the experimental setup, data acquisition, and data analysis procedures. The results obtained from applying the method to the experimental data are presented.

Chapter 6: Chiral Magnetic Effect in isobaric collisions at $\sqrt{s_{\mathrm{NN}}} = 200$ GeV using SDM

The sliding dumbbell method is applied to experimental data from isobaric collisions (Ru+Ru and Zr+Zr) at a center-of-mass energy of $\sqrt{s_{NN}} = 200$ GeV. This chapter describes the experimental setup, data acquisition, and data analysis procedures specific to the isobaric collisions. The results obtained from applying the method to the experimental data from isobaric collisions are presented.

Bibliography

[1] J. C. Collins and M. J. Perry, "Superdense Matter: Neutrons Or Asymptotically Free Quarks?", Phys. Rev. Lett. 34, 1353 (1975).

[2] S. Weinberg, "The First Three Minutes. A Modern View of the Origin of the Universe" (1993).

[3] S. A. Chin, "Transition to Hot Quark Matter in Relativistic Heavy Ion Collision", Phys. Lett. B 78, 552 (1978).

[4] F. Halzen and A. D. Martin, "QUARKS AND LEPTONS: AN INTRODUCTORY COURSE IN MODERN PARTICLE PHYSICS", ISBN: 978-0-471-88741-6 (1991).

[5] G. L. Kane, "MODERN ELEMENTARY PARTICLE PHYSICS", Published in: REDWOOD CITY, USA: ADDISON-WESLEY (1987).

[6] Jay M. Pasachoff, "Big bang theory", https://doi.org/10.1036/1097-8542.080900

[7] E. Rutherford, "Collision of a Particle with Light Atoms. IV. An Annomalous Effect in Nitrogen", Phil. Mag. 37, 581 (1919).

[8] J. Chadwick, "Possible Existence of a Neutron", Nature 129, 312 (1932).

[9] E. D. Bloom *et al.*, "High-Energy Inelastic $e-p$ Scattering at 6° and 10°", Phys. Rev. Lett. 23, 930 (1969).

[10] M. Breidenbach *et al.*, “Observed Behavior of Highly Inelastic Electron-Proton Scattering”, Phys. Rev. Lett. 23, 935 (1969).

[11] R. Brandelik *et al.* [TASSO Collaboration], “Evidence for planar events in e^+e^- annihilation at high energies”, Phys. Lett. B 86, 243 (1979).

[12] Standard Model of Elementary Particles. https://en.wikipedia.org

[13] J. Woithe *et al.*, “Let’s have a coffee with the Standard Model of particle physics!”, Phys. Educ. 52, 034001 (2017).

[14] G. Aad *et al.*, [ATLAS collaboration], “Observation of a new particle in the search for the Standard Model Higgs boson with the ATLAS detector at the LHC”, Phys. Lett. B 716, 1 (2012).

[15] W. Adam *et al.* [CMS collaboration], Phys. Lett. B 716, 30 (2012).

[16] S. Bethke, “Experimental Tests of Asymptotic Freedom”, Prog. Part. Nucl. Phys. 58, 351 (2007).

[17] H. Ding *et al.*, “Thermodynamics of strong-interaction matter from lattice QCD”, Int. J. Mod. Phys. E 24, 1530007 (2015).

[18] U. Heinz *et al.*, “Exploring the properties of the phases of QCD matter - research opportunities and priorities for the next decade”, arXiv:1501.06477 [nucl-th] (2015).

[19] D. H. Perkins, “Introduction to High Energy Physics”, Cambridge University Press (2012).

[20] T. D. Lee and G. C. Wick, “ Vacuum stability and vacuum excitation in a spin-0 field theory”, Phys. ReV. D 9, 2291 (1974).

[21] Adams *et al.* [STAR collaboration], “Experimental and theoretical challenges in the search for the quark–gluon plasma: The STAR Collaboration’s critical assessment of the evidence from RHIC collisions”, Nucl. Phys. A 757, 102 (2005).

[22] D. H. Rischke, “The Quark gluon plasma in equilibrium” , Prog. Part. Nucl. Phys. 52, 197-296 (2004).

[23] F. Karsch, “Lattice results on QCD thermodynamics”, Nucl. Phys. A 698, 199 (2002).

[24] F. Karsch, “Lattice QCD at Non-Zero Chemical Potential and the Resonance Gas Model”, Prog. Theor. Phys. Suppl. 153, 106 (2004).

[25] R. C. Hwa and X. N. Wang, “Quark–Gluon Plasma 3”, vol. 3, World Scientific (2004).

[26] R. V. Gavai and S. Gupta, “On the critical end point of QCD”, Phys. Rev. D 71, 114014 (2005).

[27] “Studying the Phase Diagram of QCD Matter at RHIC”, $https://drupal.star.bnl.gov/STAR/files/BES_WPII_ver6.9_Cover.pdf$ (2014).

[28] K. H. Ackermann *et al.*, “STAR detector overview”, Nucl. Instrum. Meth., vol. A499, pp. 624–632, 2003.

[29] B. Alessandro *et al.* [ALICE Collaboration], “ALICE: Physics Performance Report, Volume II”, J. Phys. G 32, 1295 (2006).

[30] R. S. Bhalerao, “Relativistic Heavy-Ion Collisions”, “https://cds.cern.ch/record/1695331/files/p219.pdf”

[31] John Ellis., “From little bangs to the big bang”, Journal of Physics: Conference Series. Vol. 50, 1, IOP Publishing (2006).

[32] T. SUGIURA, “Exploring the QCD phase diagram measured by cumulants of net-charge distributions in Au+Au collisions at the STAR experiment”, [Thesis] (2018).

[33] B. Betz, “Jet Propagation and Mach-Cone Formation in (3+1)-dimensional Ideal Hydrodynamics”, [Dissertation] (2009).

[34] E. Daw, "Lecture 7 - Rapidity and Pseudorapidity", (2012).

[35] R. Sahoo, "Relativistic Kinematics", Lecture in IX SERC School on Experimental High Energy Physics, IIT Madras, India (2013).

[36] C. Y. Wong, "Introduction to High-Energy Heavy-Ion Collisions", World Scientific Publishing Co. Pte. Ltd. (1994).

[37] B. B. Back, "Studies of multiplicity in relativistic heavy-ion collisions", Journal of Physics: Conference Series 5, 16 (2005).

[38] A. Toia, "Participants and spectators at the heavy-ion fireball", CERN Courier (2013).

[39] R. J. Glauber *et al.*, "Lectures in Theoretical Physics", New York: Interscience (1959).

[40] R. L. Ray and M. S. Daugherity, "Applicability of Monte Carlo Glauber models to relativistic heavy-ion collision data", J. Phys. G: Nucl. Part. Phys. 35, 125106 (2008).

[41] T. W. Ludlam, A. Pfoh, A. Shor, "HIJET, "A Monte Carlo event generator for p nucleus and nucleus nucleus collisions"", BNL-37196 (1986).

[42] M. L. Miller *et al.*, "Glauber modeling in high energy nuclear collisions", Ann. Rev. Nucl. Part. Sci. 57, 205 (2007).

[43] R. S. Bhalerao, "Radial Flow, Anisotropic Flow and Relativistic Hydrodynamics for the Beginners", 3rd SERC School on Nuclear Physics (2009).

[44] S.A. Voloshin and Y. Zhang, "Flow study in relativistic nuclear collisions by Fourier expansion of Azimuthal particle distributions", Phys. Rev. C 70, 665 (1996).

[45] R. Snellings, " Elliptic flow: a brief review " , New J. Phys. 13 055008 (2011).

[46] M. M. Aggarwal, “Elliptic Flow in Relativistic Heavy-Ion Collisions”, Advances in Nuclear Physics 257, 161 (2019).

[47] A. M. Poskanzer, S. A. Voloshin, “Methods for analyzing anisotropic flow in relativistic nuclear collisions”, Phys. Rev. C 58, 1671–78 (1998).

[48] J.Barrette *et al.* [E877 Collaboration], “Energy and charged particle flow in 10.8 AGeV/c Au+Au collisions”, Phys. Rev. C 55, 1420–1430 (1997).

[49] A. Bilandzic, R. Snellings, “Flow analysis with cumulants:direct calculations”, Phys. Rev. C 83, 044913 (2011).

[50] G. Aad *et al.* [ATLAS Collaboration], “Measurement of the distribution of event-by-event flow harmonics in lead-lead collisions at $\sqrt{s_{NN}}$=2.76 TeV with the ATLAS detector at the LHC”, JHEP 11, 183 (2013).

[51] K. Ackermann *et al.* [STAR collaboration], “Elliptic Flow in Au+Au Collisions at $\sqrt{s_{NN}}$=130 GeV”, Phys. Rev. Lett. 86, 402 (2001).

[52] C. Adler *et al.* [STAR collaboration], “Elliptic flow from two- and four-particle correlations in Au+Au collisions at $\sqrt{s_{NN}}$=130 GeV”, Phys. Rev. C 66, 034904 (2002).

[53] K. Adcox *et al.* [PHENIX collaboration], “Flow Measurements via Two-Particle Azimuthal Correlations in Au+Au Collisions at $\sqrt{s_{NN}}$=130 GeV”, Phys. Rev. Lett. 89, 212301 (2002).

[54] B. Back *et al.* [PHOBOS collaboration], “Pseudorapidity and Centrality Dependence of the Collective Flow of Charged Particles in Au+Au Collisions at $\sqrt{s_{NN}}$=130 GeV”, Phys. Rev. Lett. 89, 222301 (2002).

[55] K. Aamodt *et al.* [ALICE Collaboration], “Elliptic flow of charged particles in Pb-Pb collisions at 2.76 TeV”, Phys. Rev. Lett., Vol. 105, 252302 (2010).

[56] J. Adam *et al.* [ALICE Collaboration],“Anisotropic flow of charged particles in Pb-Pb collisions at $\sqrt{s_{\mathrm{NN}}} = 5.02$ TeV”, Phys. Rev. Lett. 116, no.13, 132302 (2016).

[57] K.H. Ackerman *et al.* [STAR collaboration], “Elliptic flow of charged particles in Au+Au collisions at 130 GeV”, Phys. Rev. Lett. 86, 402 (2001).

[58] M.S. Abdallah *et al.* [STAR collaboration], “Search for the chiral magnetic effect with isobar collisions at $\sqrt{s_{\mathrm{NN}}}$= 200 GeV by the STAR Collaboration at the BNL Relativistic Heavy Ion Collider”, Phys. Rev. C 105, 014901 (2022).

[59] I Edmond *et al.*, “Jet quenching parameter in an expanding QCD plasma”, Phys. Lett. B 786, 288 (2018).

[60] D. H. Perkins, “Introduction to High Energy Physics”, Cambridge University Pres (2000).

[61] J. D. Bjorken, “Energy Loss of Energetic Partons in Quark-Gluon Plasma: Possible Extinction of High p(t) Jets in Hadron - Hadron Collisions”, FERMILAB-PUB-82-59-THY (1982).

[62] R. Pasechnik and M. Sumbera, “Phenomenological Review on Quark-Gluon Plasma: Concepts vs. Observations”, Universe 3, 7 (2017).

[63] L. Adamczyk *et al.* [STAR collaboration], “Measurements of jet quenching with semi-inclusive hadron+jet distributions in Au+Au collisions at $\sqrt{s_{\mathrm{NN}}} =$ 200 GeV”, Phys. Rev. C 96, 024905 (2017).

[64] S.S. Adler *et al.* [PHENIX collaboration], “High p_T charged hadron suppression in Au+Au collisions at $\sqrt{s_{\mathrm{NN}}} = 200$ GeV”, Phys. Rev. C 69, 034910 (2004).

[65] K. Aamodt *et al.* [ALICE collaboration], ”Suppression of Charged Particle Production at Large Transverse Momentum in Central Pb-Pb collisions at $\sqrt{s_{\mathrm{NN}}} = 2.76$ TeV”, Phys. Lett. B 696, 30 (2011).

[66] J. Adams *et al.* [STAR collaboration], "Evidence from d+Au measurements for final state suppression of high p(T) hadrons in Au+Au collisions at RHIC", Phys. Rev. Lett. 91, 072304 (2003).

[67] C. Adler *et al.* [STAR collaboration], "Disappearence of back-to-back high-p_T correlations in central Au+Au collisions at $\sqrt{s_{\rm NN}} = 200$ GeV", Phys. Rev. Lett 90, 082302 (2003).

[68] J. Rafelski and B. Muller, "Strangeness Production in the Quark-Gluon Plasma", Phys. Rev. Lett. 48, 1066 (1982).

[69] P. Koch, J. Rafelski and W. Greiner, "Strange hadrons in hot nuclear matter", Phys. Lett. B 123, 151 (1983).

[70] P. Koch, B. Muller and J. Rafelski, "Strangeness in Relativistic Heavy Ion Collisions", Phys. Rep. 142, 167 (1986).

[71] K. Redlich *et al.*, "Strangeness enhancement and energy dependence in heavy ion collisions", Eur. Phys. J. C 24, 589 (2002).

[72] B. I. Abelev *et al.* [STAR Collaboration], "Energy and system size dependence of ϕ meson production in Cu+Cu and Au+Au collisions", Phys. Lett. B 673, 183 (2009).

[73] J. Adams, *et al.* [STAR Collaboration], "ϕ meson production in $Au + Au$ and $p + p$ collisions at $\sqrt{s_{\rm NN}} = 200$ GeV", Phys. Lett. B 612, 181 (2005).

[74] T. Akesson *et al.* [AFS Collaboration], "Inclusive vector-meson production in the central region of pp collisions at $\sqrt{s} = 63$ GeV", Nucl. Phys. B 203, 27 (1982).

[75] F. Antinori *et al.* [NA57 Collaboration], "Enhancement of hyperon production at central rapidity in 158 A GeV/c Pb-Pb collisions", J. Phys. G, 427 (2006).

[76] F. Antinori *et al.* [NA57 Collaboration], "Strangeness enhancements at central rapidity in 40 A GeV/c Pb-Pb collisions", J. Phys. G 37, 045105 (2010).

[77] B. I. Abelev *et al.* [STAR Collaboration], "Enhanced strange baryon production in Au + Au collisions compared to p+p at $\sqrt{s_{NN}} = 200$ GeV", Phys. Rev. C 77, 044908 (2008).

[78] J. Adams *et al.* [STAR Collaboration], "Scaling Properties of Hyperon Production in Au+Au Collisions at $\sqrt{s_{NN}} = 200$ GeV", Phys. Rev. Lett. 98, 062301 (2007).

[79] J. Adams *et al.* [STAR Collaboration], "Multistrange baryon production in Au+Au collisions at $\sqrt{s_{NN}} = 130$ GeV", Phys. Rev. Lett. 92, 182301 (2004).

[80] B. Abelev *et al.* [ALICE Collaboration], "Multi-strange baryon production at mid-rapidity in Pb-Pb collisions at $\sqrt{s_{NN}} = 2.76$ TeV", Phys. Lett. B 728, 216 (2014).

[81] B. Abelev, *et al.* [ALICE Collaboration], "Multi-strange baryon production in pp collisions at $\sqrt{s} = 7$ TeV with ALICE", Phys. Lett. B 712, 309 (2012).

[82] B. Abelev, *et al.* [ALICE Collaboration], "Centrality dependence of π, K, and p production in Pb-Pb collisions at $\sqrt{s} = 2.76$ TeV", Phys. Rev. C 88, 044910 (2013).

[83] K. Aamodt, *et al.* [ALICE Collaboration], "Strange particle production in proton-proton collisions at$\sqrt{s} = 0.9$ TeV with ALICE at the LHC", Eur. Phys. J. C 71, 1594 (2011).

[84] B.I. Abelev, *et al.* [STAR Collaboration], "Strange particle production in p+p collisions at $\sqrt{s} = 200$ GeV", Phys. Rev. C 75, 064901 (2007).

[85] B.I. Abelev, *et al.* [STAR Collaboration], "Systematic measurements of identified particle spectra in pp, d+Au, and Au+Au collisions at the STAR detector" , Phys. Rev. C 79, 034909 (2009).

[86] E. Schnedermann, J. Sollfrank, U. Heinz, "Thermal phenomenology of hadrons from 200A GeV S+S collisions", Phys. Rev. C 48, 2462 (1993).

[87] M. L. Mangano, “Two lectures on heavy quark production in hadronic collisions”, Proc. Int. Sch. Phys. Fermi 137, 95 [hep-ph/9711337] (1998).

[88] M. Strickland, “Thermal Bottomonium Suppression”, AIP Conf. Proc. 1520, 179 (2013).

[89] T. Matsui and H. Satz, “J/Ψ Suppression by Quark-Gluon Plasma Formation”, Phys. Lett. B, vol. 178, 416 (1986).

[90] K. Aamodt *et al.* [ALICE Collaboration], “Coherent J/Ψ photoproduction in ultra-peripheral Pb-Pb collisions at $\sqrt{s_{NN}} = 2.76$ TeV”, Phys. Lett. B 718, 1213 (2013).

[91] B. Abelev *et al.* [ALICE Collaboration], “Centrality, rapidity and transverse momentum dependence of J/Ψ suppression in Pb–Pb collisions at $\sqrt{s_{NN}} = 2.76$ TeV“, Phys. Lett. B 734, 314 (2014).

[92] B. Abelev *et al.* [ALICE Collaboration], “J/Ψ Suppression at Forward Rapidity in Pb-Pb Collisions at $\sqrt{s_{NN}} = 2.76$ TeV”, Phys. Rev. Lett. 109, 072301 (2012).

[93] A. Adare *et al.* [PHENIX Collaboration], “J/Ψ suppression at forward rapidity in Au+Au collisions at $\sqrt{s_{NN}}= 200$ GeV”Phys. Rev. C 84, 054912 (2011).

[94] A. Kurepin *et al.*, “ Solving the problem of anomalous J/Ψ suppression by the MPD experiment on the NICA collider* “, Eur. Phys. J. A 52, 260 (2016).

[95] P. Stankus, “Direct photon production in relativistic heavy-ion collisions”, Ann. Rev. Nucl. Part. Sci. 55 (2005).

[96] Jan-e Alam *et al.*, “Thermal Photons and Lepton Pairs from Quark Gluon Plasma and Hot Hadronic Matter”, Annals of Phys. 286, 159 (2001).

[97] E. Bratkovskaya, “Phenomenology of photon and dilepton production in relativistic nuclear collisions”, Nuclear Phys. A 931, 194–205 (2014).

[98] A. Adare *et al.* [PHENIX Collaboration], "Centrality dependence of low-momentum direct-photon production in Au+Au collisions at $\sqrt{s_{NN}} = 200$ GeV", Phys. Rev. C 91, 6 (2015).

[99] S. Mizuno *et al.* [PHENIX Collaboration], "Centrality dependence of soft photon production and its collective flow in Au+Au collisions at $\sqrt{s_{NN}} = 200$ GeV", Nucl. Phys. A 931, 686 (2014).

[100] O. Linnyk *et al.*, "Photon elliptic flow in relativistic heavy-ion collisions: Hadronic versus partonic sources", Phys. Rev. C 88, 034904 (2013); O. Linnyk, *et al.*, "Centrality dependence of the direct photon yield and elliptic flow in heavy-ion collisions at $\sqrt{s_{NN}} = 200$ GeV", Phys. Rev. C 89, 034908 (2014).

[101] G. Domokos and Joseph I. Goldman, "Quark-matter diagnostics", Phys. Rev. D 23, 203 (1981).

[102] D. Adamova, *et al.* [CERES Collaboration],"Modification of the ρ meson detected by low-mass electron–positron pairs in central Pb-Au collisions at 158 AGeV/c" Phys. Lett. B 666, 425 (2008).

[103] R. Arnaldi, *et al.* [NA60 Collaboration], "First Measurement of the ρ Spectral Function in High-Energy Nuclear Collisions", Phys. Rev. Lett. 96, 162302 (2006).

[104] A. Toia, *et al.* [PHENIX Collaboration], "e^-e^+ pairs: a clock and a thermometer of heavy ion collisions", J. Phys. G 35, 104037 (2008).

[105] S. Jeon and V. Koch, "Charged Particle Ratio Fluctuation as a Signal for Quark-Gluon Plasma", Phys. Rev. Lett. 85, 2076 (2000).

[106] M. Asakawa, U. Heinz, and B. Muller, "Fluctuation Probes of Quark Deconfinement", Phys. Rev. Lett. 85, 2072 (2000).

[107] B. Abelev *et al.* [ALICE Collaboration], "Net-Charge Fluctuations in Pb-Pb Collisions at $\sqrt{s_{NN}}$=2.76 TeV", Phys. Rev. Lett. 110, 152301 (2013).

[108] M. Gyulassy and X. N. Wang, "HIJING 1.0: A Monte Carlo program for parton and particle production in high energy hadronic and nuclear collisions", Comput. Phys. Commun. 83, 307 (1994); W. T. Deng, X. N. Wang, and R. Xu, "Hadron production in p+p, p+Pb, and Pb+Pb collisions with the HIJING 2.0 model at energies available at the CERN Large Hadron Collider", Phys. Rev. C 83 014915 (2011).

[109] J. Adams *et al.* [STAR Collaboration], "Net charge fluctuations in Au+Au collisions at $\sqrt{s_{NN}}$=130 GeV", Phys. Rev. C 68, 044905 (2003).

[110] B. I. Abelev *et al.* [STAR Collaboration], "Beam-energy and system-size dependence of dynamical net charge fluctuations", Phys. Rev. C 79, 024906 (2009).

[111] S. A. Voloshin, "Parity violation in hot QCD: How to detect it", Phys. Rev. C 70, 057901 (2004).

[112] K. Fukushima, D. E. Kharzeev and H. J. Warringa, "Chiral magnetic effect", Phys. Rev. D 78, 074033 (2008).

[113] B. I. Abelev *et al.* [STAR Collaboration], "Azimuthal Charged-Particle Correlations and Possible Local Strong Parity Violation", Phys. Rev. Lett. 103 251601 (2009).

[114] B. I. Abelev *et al.* [ALICE Collaboration], "Charge separation relative to the reaction plane in Pb-Pb collisions at $\sqrt{s_{NN}} = 2.76$ TeV", Phys. Rev. Lett. 110 012301 (2013).

[115] V. Khachatryan *et al.* [CMS Collaboration], "Observation of Charge dependent Azimuthal correlations in p-Pb collisions and its implications for the search for the Chiral magnetic effect", Phys. Rev. Lett 118 122301 (2017).

Chapter 2

STAR experiment at RHIC

To study the formation of the Quark Gluon Plasma (QGP), Brookhaven National Laboratory (BNL) which is situated at Long Island, New York, USA, set up the Relativistic Heavy-Ion Collider (RHIC) [1] to collide heavy-ions, ranging from protons to gold nuclei at relativistic energies. The energy density of the matter made by these collisions is expected to be ten times higher than that of normal nuclear matter. In the sense of a quark matter phase transition, RHIC reverses the process that happened a few microseconds after the Big Bang, when quarks and gluons were in a free state and turned into ordinary nuclear matter. One of this accelerator's strengths is its ability to collide a variety of nuclear species (i.e., gold (Au), uranium (U), copper (Cu), isobar (Ru and Zr), and deuterons) as well as polarized protons at a range of different center-of-mass energies. The research for this thesis was carried out at the RHIC.

2.1 The Relativistic Heavy Ion Collider (RHIC)

The Relativistic Heavy Ion Collider (RHIC) [1,2] began its operations in 2000, while another operational collider facility is the Large Hadron Collider (LHC) at CERN [3], which started operating in 2010. It is currently the sole spin-polarized proton collider. The research carried out at RHIC captivates the attention of physicists from all over the world, particularly those working in the fields of nuclear physics, particle physics, astrophysics, cosmology, and condensed matter physics. One of the most significant goals of RHIC is to investigate the features of Quark Gluon Plasma [4,5] in order to better understand how matter behaved in the early stages of our universe following the Big Bang. Table 2.1 provides an overview of the different kinds of particle collisions that are carried out at the RHIC [6].

Particle species	Total particle energy (GeV/nucleon)
Polarized $p + p$	31.2 – 254.9
Polarized p + ^{27}Au^{13+}	103.9 + 98.7
Polarized p + ^{197}Au^{79+}	103.9 + 98.6
d + ^{197}Au^{79+}	9.9 + 9.8 – 100.7 + 100.0
^{3}He^{2+} + ^{197}Au^{79+}	103.5 + 100.0
^{63}Cu^{29+} + ^{63}Cu^{29+}	11.2 – 100.0
^{63}Cu^{29+} + ^{197}Au^{79+}	99.9 + 100.0
^{96}Zr^{40+} + ^{96}Zr^{40+}	100.0
^{96}Ru^{44+} + ^{96}Ru^{44+}	100.0
^{197}Au^{79+} + ^{197}Au^{79+}	3.85 – 100.0
^{197}Au^{79+} + ^{197}Au (fixed target)	3.85 – 31.2
^{238}U^{92+} + ^{238}U^{92+}	96.4

Table 2.1: Summary of RHIC operations [6]

2.1.1 Different stages of particle acceleration

The RHIC accelerator complex shown in Fig. 2.1 consists of different components in order to accelerate ions up to a maximum energy of 100 GeV per nucleon or protons up to a maximum energy of 250 GeV [8]. The essential subsystems include the Electron Beam Ion Source (EBIS) accelerator, the LINAC (Linear Accelerator), the Boosters, the Alternating Gradient Synchrotron, the beamline, and the RHIC rings.

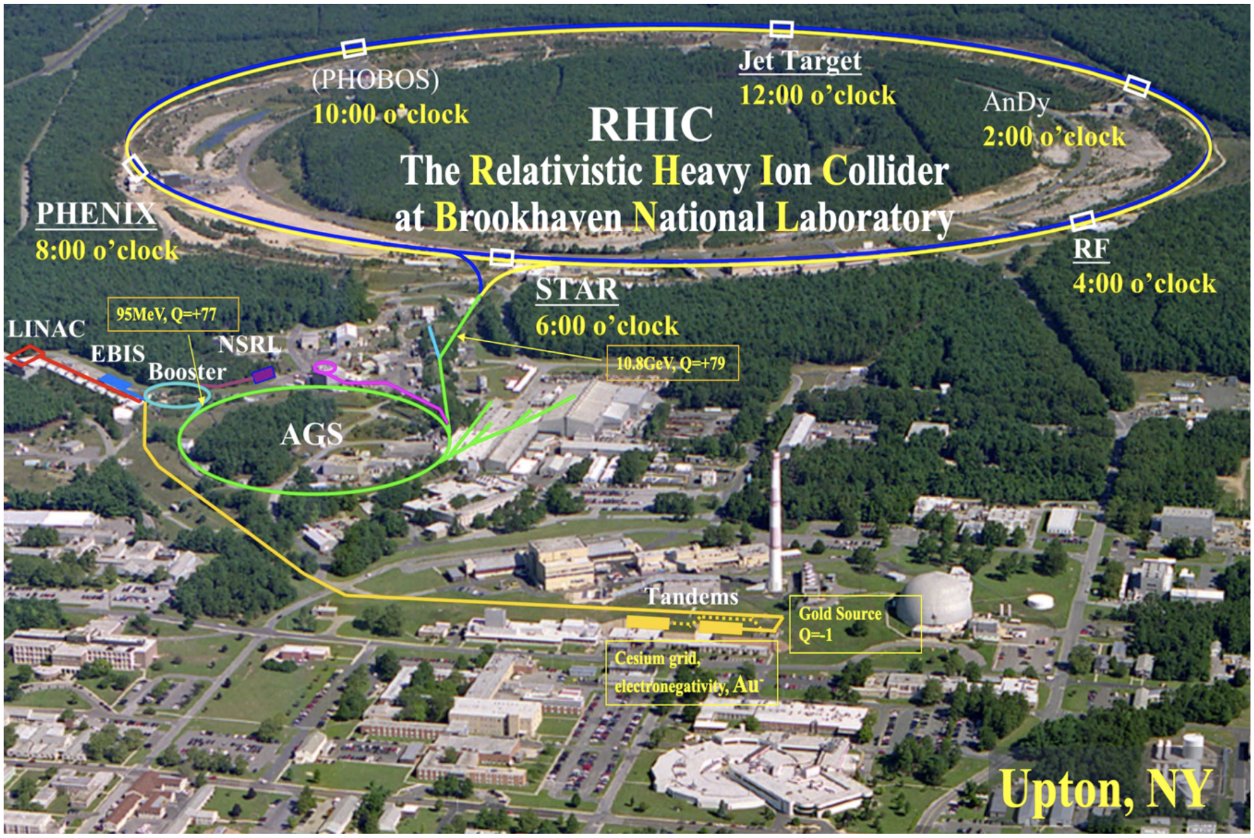

Figure 2.1: Major components of the RHIC accelerator complex, as well as the supporting infrastructure [7].

2.1.1.1 EBIS

Electron Beam Ion Source (EBIS) [9] is a pre-injector system for heavy-ion acceleration in which any element can be used to produce highly charged ion beams. EBIS removes electrons from nuclei using kinetic scattering with electron beams, hence it is not limited by the atom's electronegativity and can offer any stable ion species from deuterons to uranium. EBIS generates +32 charged Au ions with an energy of 2 MeV/nucleon.

2.1.1.2 LINAC

The 200 MeV linear accelerator (LINAC) [10] is made up of nine accelerator radiofrequency cavities, nine ion sources, and a radiofrequency quadrupole. It supplies RHIC experiments with energetic and/or polarised proton beams. Afterwards, the proton beams from the LINAC are transferred to the booster synchrotron.

2.1.1.3 Booster synchrotron

A synchrotron is a type of circular accelerator that has its accelerating voltage synchronized with the period of circulation of the particles that are being accelerated. The Booster has an extremely high vacuum, which makes it feasible to accelerate heavy ions all the way up to uranium. At the point of exit from the booster, gold ions experience an acceleration that results in a nucleon-specific energy of 100 MeV and a charge of +77. After that, the beam is injected into the ring of the AGS.

2.1.1.4 AGS

Ions are collected by the Alternating Gradient Synchrotron (AGS) [11], which also increases the beam's energy to a maximum of 8.86 GeV/nucleon (or about 99.7% the speed of light) in preparation for RHIC injection. At the exit, any electrons that are still present are removed as given in table 2.2.

2.1.1.5 AGS to RHIC

At the beginning of the AGS-to-RHIC transfer line [12], a foil removes the final two electrons from the gold ions. Using the switching magnets [13] at the end of the line, the bunches are directed either clockwise to the left or counterclockwise to the right in the RHIC ring.

Accelerator name	Incoming Ion		Outgoing Ion	
	charge	speed	charge	speed
EBIS			+32	2MeV
Booster Synchrotron	+32	2MeV	+77	100MeV
AGS	+77	100MeV	+79	8.86GeV
RHIC storage ring	+79	8.86GeV		

Table 2.2: Ion movement summary [14].

Accelerator name	Incoming P speed	Outgoing P speed
OPPIS		750KeV
Linac	750KeV	200MeV
Booster	200MeV	2.35GeV
AGS	2.35	24.3GeV
RHIC Ring	24.3GeV	

Table 2.3: Technical information for pp run [14].

2.1.1.6 RHIC ring

The ions are then fed into RHIC after their electrons have been removed. This procedure is repeated for each of the two RHIC rings. As soon as the two rings are filled with ion beams, the beams are accelerated to their maximum working energy of 100 GeV/nucleon per beam, resulting in a maximum center-of-mass energy of 200 GeV/nucleon-pair. Table 2.2 lists a summary of ion movement in the RHIC.

The Optically Pumped Polarized Ion Source, abbreviated as OPPIS, is utilized to produce protons. After then, ions or protons are grouped together in a bunch. In a bunch, there are approximately 10^9 ions or 10^{11} protons. In each storage, there are a number of these bunches that are being accelerated to the target energy of collision with a gap of only a few nanoseconds between each bunch. Technical information for pp run is mentioned in table 2.3. As soon as they reach the target energy (for ions or protons), a collision will take place in either the STAR or the PHENIX detector. Once a collision has occurred, the newly formed particles hit or pass through a number of different sub-detectors. A ".daq" file is used to store information that corresponds to certain data, such as the amount of ionization energy lost, the number of hits, and momenta, etc. There is a dead period of the detector on the order of a nanosecond between every set of events that are recorded.

As seen in Fig. 2.1, there are two distinct rings, the "Blue Ring (clockwise)" and the "Yellow Ring (counterclockwise)". The RHIC accelerator measures 2.4 miles (3.8 km) in circumference and features six "interaction sites" (IRs) where the counter-circulating beams intersect. The RHIC collisions were recorded and analyzed by the four experimental detectors positioned around the ring: STAR (Solenoidal Tracker At RHIC), PHENIX (Pioneering High Energy Nuclear Interaction experiment), PHOBOS, and BRAHMS (Broad Range Hadron Magnetic Spectrometers Experiment). The STAR [15] is positioned at 6 o'clock near the AGS to RHIC injection stations and PHENIX [16] at 8 o'clock. The PHOBOS (10 o'clock) [17] and BRAHMS (2 o'clock) [18] experiments are already decommissioned in 2005 and 2006, while PHENIX (retired in 2016) is now undergoing a thorough redesign as sPHENIX [19]. The STAR detector is specifically designed for the tracking and detection of charged hadrons that traverse a broad solid angle at mid-rapidity in a solenoidal magnetic field [20]. The PHENIX experiment was designed to measure the direct probes of the impact by employing a partial coverage detector system while operating in a superconductively produced axial magnetic field [16]. The PHOBOS detector was designed specifically to monitor the bulk particle multiplicities and has the widest pseudo-rapidity coverage [17]. The BRAHMS experiment was developed with the intention of investigating the physics of small-x through the use of momentum spectroscopy [18].

For high-energy heavy ion collisions, specialized detectors are necessary to detect a wide variety of particles and maintain sensitivity to low-energy particles emitted in the collisions. Historically, four main experiments/detectors have been commissioned at RHIC, however at present, only STAR is operational.

2.2 The Solenoidal Tracker At RHIC (STAR)

One of the four experiments at the RHIC complex is called the STAR, which stands for Solenoid Tracker at RHIC [15]. It consists of many sub-detector systems, with excellent particle identification capabilities, where each detector is specialized in detecting certain kinds of particles or recording kinematic information. These sub-

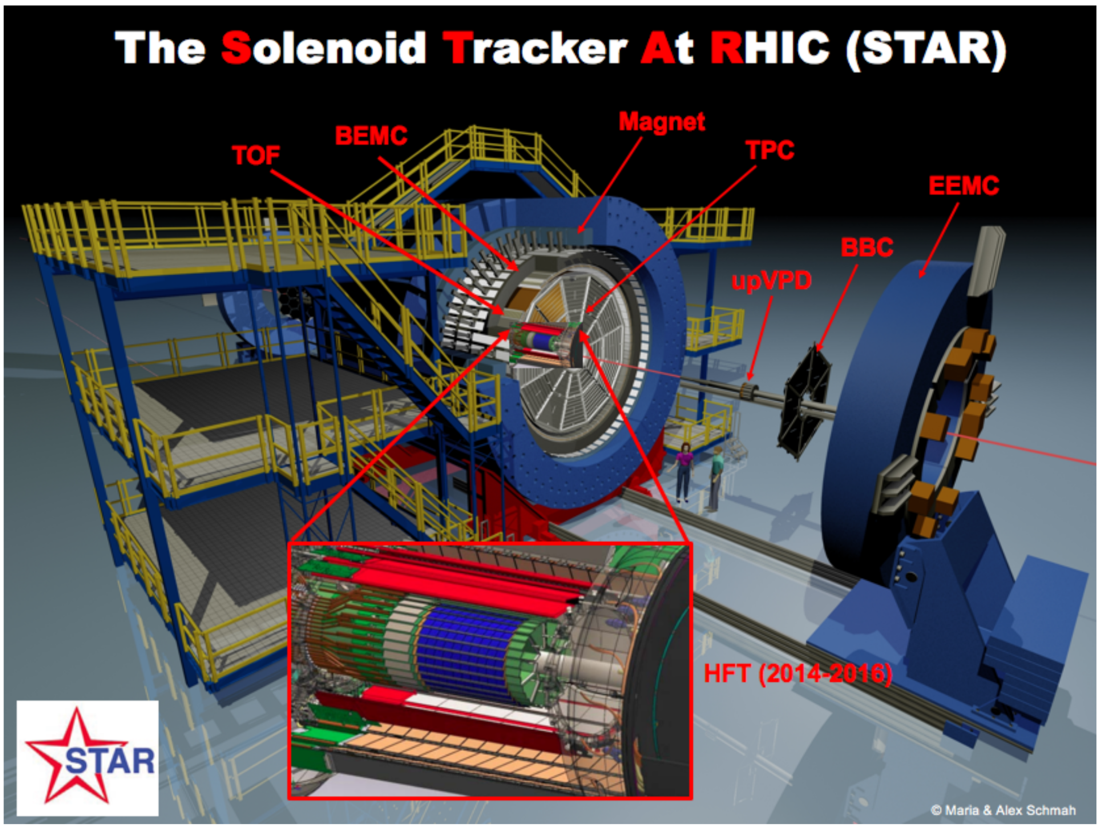

Figure 2.2: STAR detector's three-dimensional view.

detectors of STAR are capable of collecting crucial characteristics of the number of particles created in each heavy-ion collision. The purpose of STAR is to measure the production of hadrons over a big solid angle. Tracking with a high degree of precision, analysis of momentum, and quick identification of particles at the center of mass rapidity are all made possible by the STAR detectors' sub-systems. It is the only experiment at RHIC that can detect the whole azimuth and track particles with energies ranging from 100 MeV/c to 20 GeV/c [15]. The event-by-event characterization of heavy-ion collisions is particularly well suited for STAR in this regard. Figure 2.2 depicts the three-dimensional schematic structure of the STAR detection

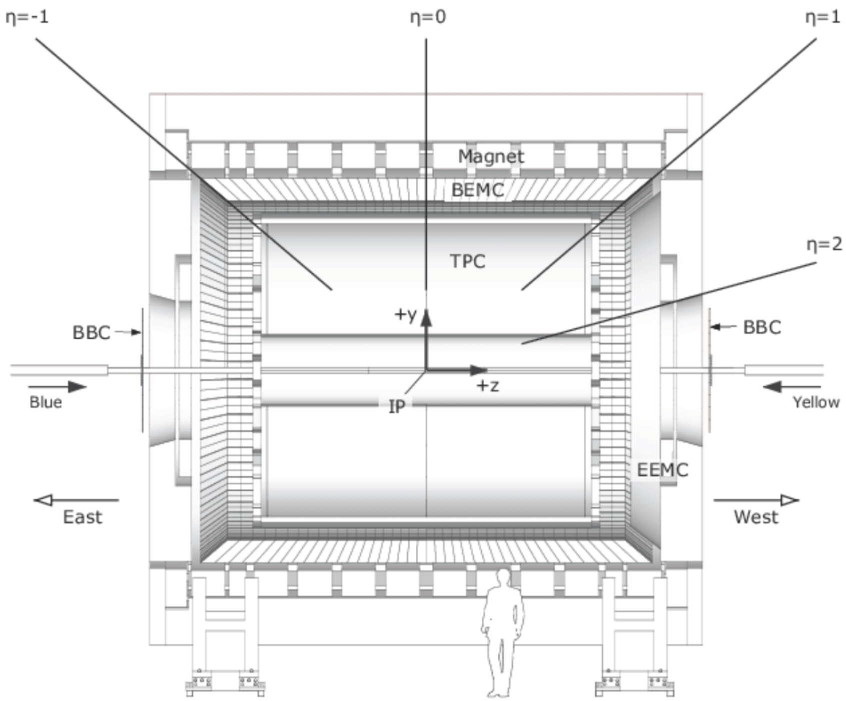

Figure 2.3: A cross-sectional schematic illustration of the STAR detector, highlighting its several sub-detectors [21].

system. As illustrated in Fig. 2.2 and Fig. 2.3, STAR is made up of over ten separate detector subsystems that are used to analyze a wide range of physical observables. Some of the sub-detector systems (TPC: Time Projection Chamber, TOF: Time-of-Flight detector, BEMC: Barrel Electromagnetic Calorimeter, EEMC: End-cap Electromagnetic Calorimeter, MTD: Muon Telescope Detector, HFT: Heavy Flavor Tracker, BBC: Beam Beam Counter, VPD: Vertex Position Detector) are discussed below.

RICH (Ring Imaging CHerenkov detector) [22], CTB (Central Trigger Barrel), FTPC (Forward TPC) [23], SVT (Silicon Vertex Tracker) [24], and PMD (Photon Multiplicity Detector) [25] are among the few detectors that have been employed in the past. Indian group was responsible for the fabrication and maintenance of the Photon Multiplicity Detector (PMD). The PMD was a pre-shower gas detector that detects the photon multiplicity in the forward region. It was installed away from the magnet system at a distance of 550 centimeters from the center of the TPC.

2.2.1 The Time Projection Chamber (TPC)

The Time Projection Chamber (TPC) [26], commonly known as the "heart" of the STAR experiment, is the principal detector utilized in the STAR experiment. The TPC provides good tracking, momentum, and ionization energy loss information of particles. It covers a pseudo-rapidity range of $|\eta| < \mathbf{1.8}$ in the center-of-mass frame with entire azimuthal coverage ($\phi = 2\pi$). Particle momenta can be measured from

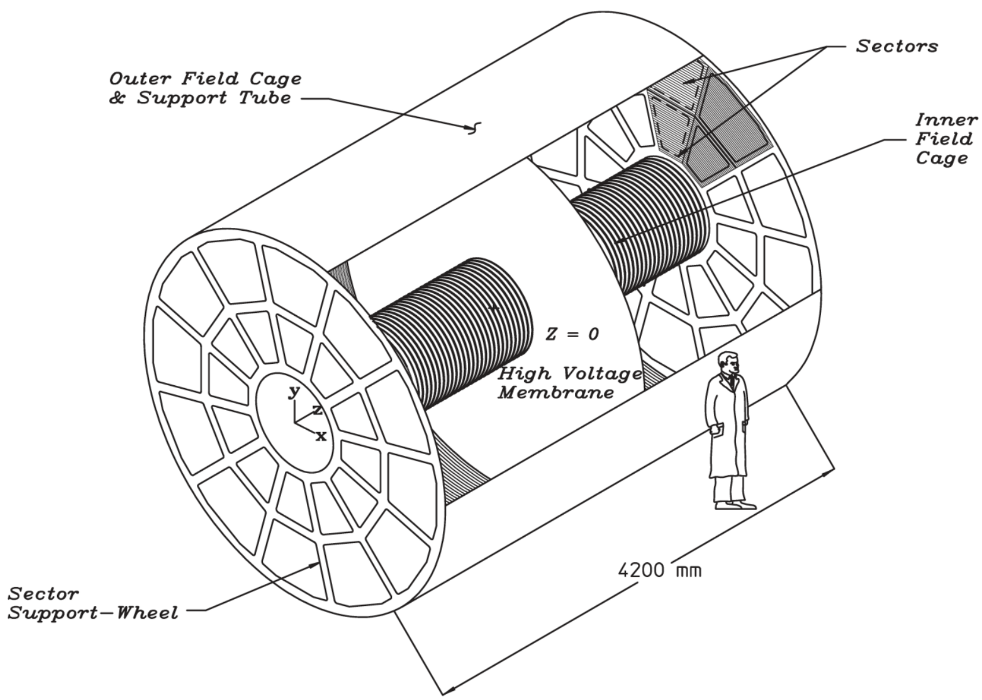

Figure 2.4: A schematic drawing of the Time Projection Chamber [26].

100 MeV/c to 30 GeV/c, and successful particle identification can be achieved for tracks with momenta from 100 MeV/c to 1 GeV/c. The TPC, shown in Fig. 2.4 measures a length of 4.2 meters and a diameter of 4 meters as listed in Table 2.4. Differently charged particles captured by the TPC in Au+Au collisions are shown in Fig. 2.5. This detector is capable of both the reconstruction of the particle

Item	Dimension	Comment
Length of the TPC	420 cm	Two halves, 210 cm long
Outer Diameter of the Drift Volume	400 cm	200 cm radius
Inner Diameter of the Drift Volume	100 cm	50 cm radius
Dist. between Cathode and		
Ground Plane	209.3 cm	Each side
Cathode	400cm diameter	At the center of the TPC
Cathode Potential	28 kV	Typical
Drift Gas	P10	10% methane, 90% argon
Pressure	Atm. + 2mbar	Regulated at 2mbar above Atm.
Drift Velocity	5.45 cm/μs	Typical
Transverse Diffusion (σ)	230 $\mu m/\sqrt{cm}$	140 V/cm & .5 T
Longitudinal Diffusion (σ)	360 $\mu m/\sqrt{cm}$	140 V/cm
Number of Anodes Sectors	24	12 per end
Number of Pads	136,608	
Signal to Noise Ratio	20 : 1	
Electronic Shaping Time	180ns	FWHM
Signal Dynamic Range	10 bits	
Sampling Rate	9.4 MHz	
Sampling Depth	512 time buckets	380 time buckets typical
Magnetic Field	0, ±.25T, ±.5T	Solenoidal

Table 2.4: STAR TPC technical parameters [27].

trajectories (with a 0.5 T magnetic field directed parallel to the beam) and the identification of particles (PID) by observing the energy loss per unit length (dE/dx) in the detection medium. STAR uses the P10 gas because of the high drift velocity of electrons and ions, which consists of 90% argon (Ar) and 10%methane (CH_4) [28]. The Argon gas has a very low affinity for free electrons, while the methane gas

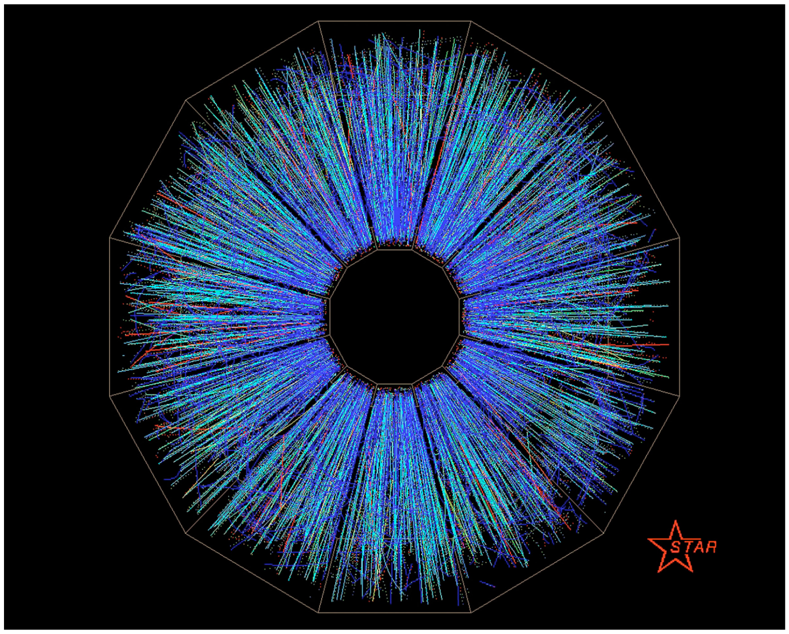

Figure 2.5: Charged particles from central Au+Au collisions at RHIC, captured by the TPC [7].

has the ability to quench the propagation of ultraviolet photons. When a charged particle passes through a TPC gas, it will ionize the TPC gas atoms around every few tens of a millimeters along its route, and it will also leave behind a cluster of electrons. An external electric field, which is supplied by the field cage and the high-voltage central membrane, will act as a driver for these electron clusters, causing them to move toward the anode plane. The field cage includes the outer field cage and inner field cage , which could provide a perfect uniform electric field (approx. 135 V/cm) to drift electrons. Any distortions of the electric field will result in a distortion of the recorded trajectories of these charged particles. The field cage also helps to prevent the TPC gas from being contaminated by the outside air. The high voltage Central Membrane (CM) is placed in the middle of the TPC, perpendicular to the Beamline, held at a high voltage of ∼28 kV. At the end of TPC are the anode and pad planes as shown in Fig. 2.6, where the pads are held at ground potential [29]. Ionization of the gas molecules occurs whenever a charged particle passes through the TPC. The electrons that are liberated in the gas as a result of a high-voltage cathode (operating at 28 kV) are guided through the electric field toward the endcaps, where they are collected by multi-wire proportional counters (MWPC). The TPC is divided into 24 sectors, and each sector has two sub-sectors, one inside and one outside. One TPC sector is depicted in Fig. 2.6, together with

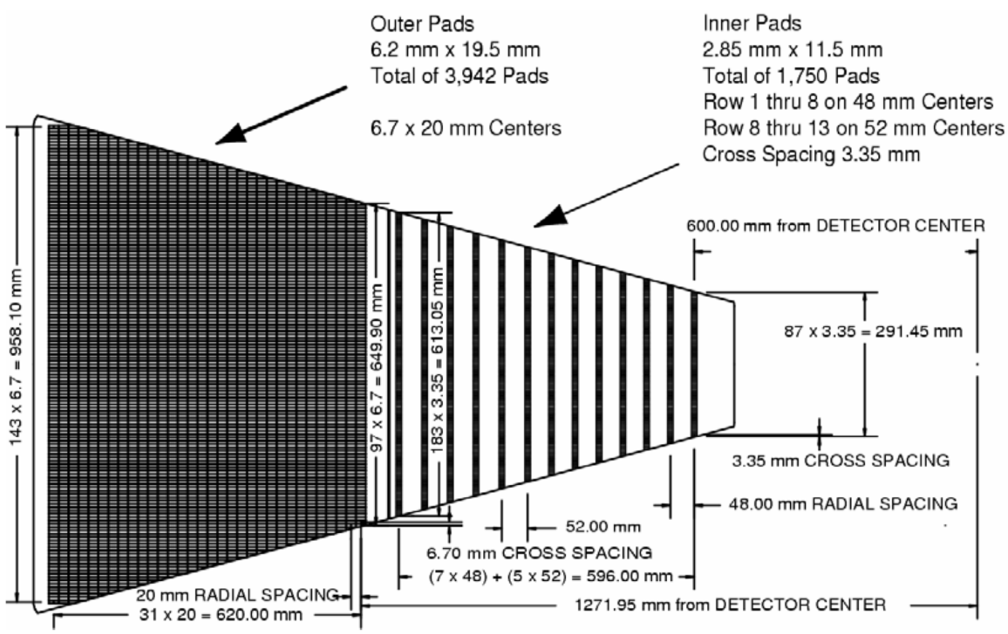

Figure 2.6: A schematic depiction of a TPC anode plane sector highlighting the inner and outer sub-sectors and padrows [29].

its one outer sub-sector and one inner sub-sector component. The outer sub-sector is made up of 3,942 big pads that are continually placed in order to offer a high resolution for the energy loss measurement (i.e., dE/dx). The inner sub-sector, which is located at a larger pseudo-rapidity where track density is significantly higher, is made up of 1,750 tiny pads that provide improved two-hit resolution.

The geometries of the inner and outer sectors are slightly distinct from one another, to emphasize two-track separation at small radii, as well as good dE/dx and a reasonable channel count at large radii [29]. There are 13 pad rows in each inner sector, whereas there are 32 pad rows in each outer sector; hence, a track may provide a maximum of 45 hits. There are three wire planes in the readout chambers: a gated grid, a ground plane, and anode wires. When charged particles come into contact with TPC gas and ionize a significant number of atoms, then electrons and positive ions will get free along the path of these charged particles. These electrons will eventually make their way to the end cap, where they will be gathered by the Multi-Wire Proportional Chamber (MWPC), which is made up of a pad plane, three wire planes (the gating grid, ground plane, and anode wires). When the electrons

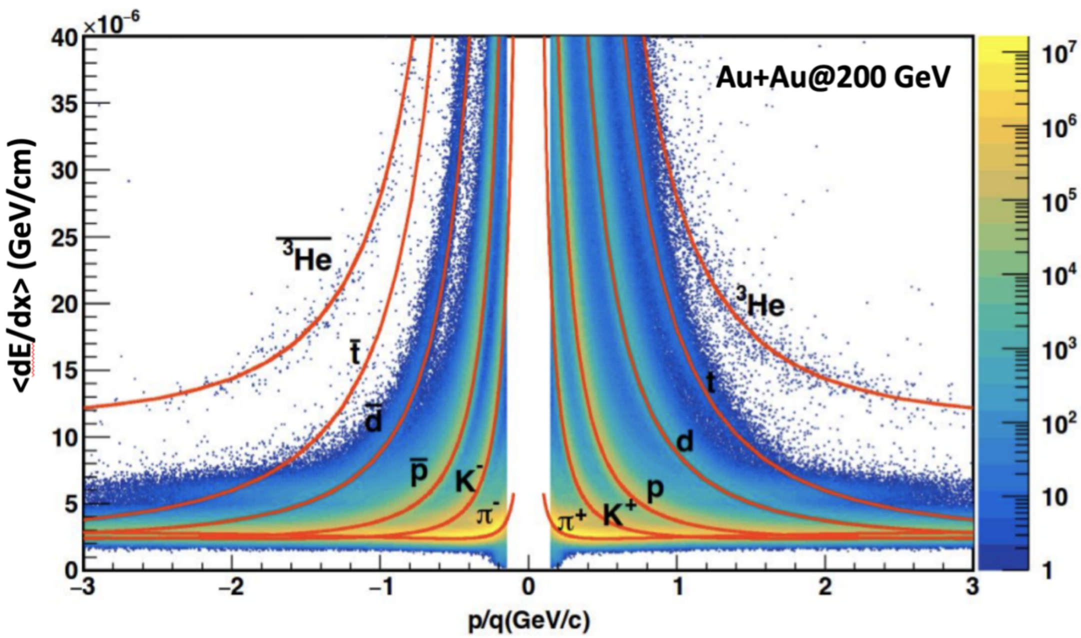

Figure 2.7: The truncated mean of the ionization energy loss, dE/dx, against the rigidity, p/q (where p is the momenta and q is the charge), of various particles determined by TPC in Au+Au collisions at $\sqrt{s_{\rm NN}} = 200$ GeV [32].

reach the region of the MWPC with the strong electric field, an avalanche will be set off, which will result in the production of more electrons, which will subsequently cause a signal to be induced on the readout plane. These generated signals are used to determine the paths traveled by charged particles and the location of ionization clusters along those paths. The distribution of induced signals on the pads are used to calculate the x and y coordinates, while the z coordinate is derived by taking the product of the drift velocity and the drift duration of the cluster as it moves from the ionization point to the anode.Using the Kalman filter technique [30,31], the whole path traveled by a particle is reconstructed. These tracks are known as "global tracks". After the reconstruction of the tracks, we will be able to determine the transverse momenta (p_T) of particles by using the curvatures of the tracks in conjunction with the magnetic field within the TPC volume. Those global tracks that were reconstructed with more than 10 hits are used to fit the initial primary vertex. It is possible to compute the Distance of Closest Approach, often known as DCA, of each global track in relation to the fitted primary vertex. When a new fit is applied to those tracks with a DCA of less than 3 centimeters, another primary vertex position is determined. The above process is repeated until the position of the fitted vertex converges. Finally, the tracks with DCA $<$ 3cm away from the primary vertex have been designated as primary tracks, and the momentum that is connected with these tracks has been re-fitted while taking into account the primary vertex point. The primary vertex resolution is proportional to $1/\sqrt{N_{track}}$ (N_{track} is the total number of available tracks for the fitting), and events with $\sim$1000 tracks may reach a resolution of 350 µm.

One can calculate the ionization energy loss by integrating the induced electrical signal amplitude of each cluster or hit. It is possible to accomplish particle identification using the information obtained from the observed ionization energy loss (dE/dx) of the tracks. This is possible due to the fact that each type of particle exhibits a distinctive pattern of energy loss while interacting with TPC gas. Figure 2.7 provides for instance the truncated mean of the ionization energy loss (represented by dE/dx) vs the stiffness (represented by p/q) of various particles as determined by TPC for Au+Au collisions.

2.2.2 The Time of Flight (TOF) Detector

As shown in Fig. 2.2 and Fig. 2.8, the barrel Time-of-Flight (TOF) detector [33], which comprises 120 trays, is positioned directly outside of the STAR TPC. A pseudo-rapidity range of up to one unit ($|\eta| < 1$) is covered by the barrel TOF detector with a full azimuthal angle. Each tray of the TOF detector covers one unit of η and an azimuthal angle (ϕ) of six degrees. There are 32 Multi-gap Resistive Plate Chamber (MRPC) modules on each TOF tray [34, 35]. The VPD detectors

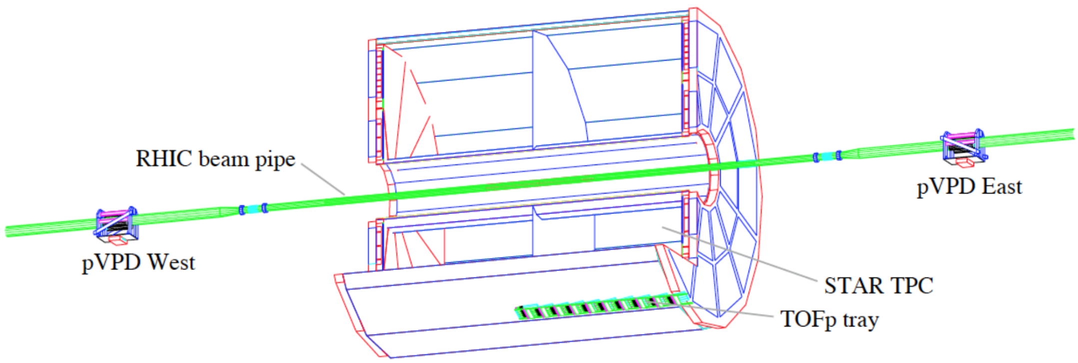

Figure 2.8: In connection to STAR TPC and RHIC beam pipe, the TOF detectors [33].

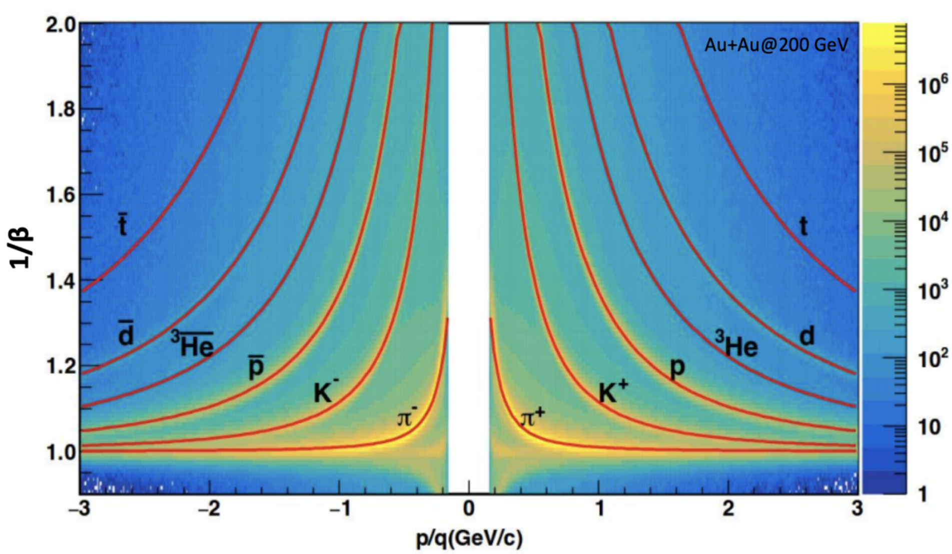

Figure 2.9: The relationship between the inverse velocity $1/\beta$ and the rigidity p/q in Au+Au collisions at $\sqrt{s_{\mathrm{NN}}} = 200$ GeV, as observed by the STAR TOF detector [32].

and the barrel TOF detector are the two components that make up the entire TOF system. The barrel TOF detector is responsible for measuring the "stop time, t_1", while the VPD detector is responsible for measuring the "start time, t_0". The time period known as the "time-of-flight" may be calculated by using the formula $\Delta t = t_1 - t_0$. Thereafter, the impacts that were recorded on the barrel TOF trays are compared to the tracks that were constructed using TPC.

It is possible to compute the inverse velocity $1/\beta$ by using the knowledge of momentum p and track length Δ. It is possible to determine the mass of this charged particle by using the formula $m = \frac{p}{c}\sqrt{1/\beta^2 - 1}$. Therefore, the TOF detector is capable of facilitating particle identification (PID) based on mass. However, as the momentum of a particle grows very high, its velocity will reach extremely near the speed of light; hence, the PID becomes more difficult to implement at larger momentum. In Fig. 2.9, the inverse velocity $1/\beta$ recorded by the STAR TOF detector is plotted against the rigidity p/q in Au+Au collisions. As one can see, the individual particles produce curves that are clearly differentiated from one another.

2.2.3 Barrel Electromagnetic Calorimeter (BEMC)

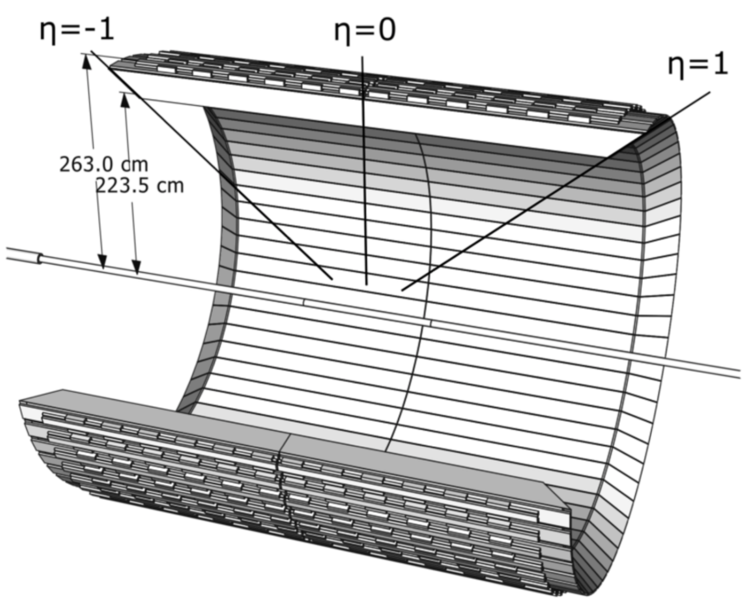

Figure 2.10: The depiction of the Barrel Electromagnetic Calorimeter (BEMC) at STAR [36].

The Barrel Electromagnetic Calorimeter (BEMC) [36] is located on top of the

TOF detector and inside the aluminium coils that form the STAR solenoid. BEMC matches the TPC tracking acceptance perfectly since it has a pseudo-rapidity range that goes up to 1 and it covers the complete azimuthal angle. Figure 2.10 provides a diagrammatic representation of the BEMC. BEMC is made up of a total of 120 calorimeter modules, and each module can be segmented into 40 towers, subtending 6° in azimuthal angle and 1 unit of pseudo-rapidity. Additionally, each module has two towers in the azimuthal direction and twenty towers in the direction of η. There are a total of sixty modules that fall into the ranges of η >0 and η <0. Figure 2.11

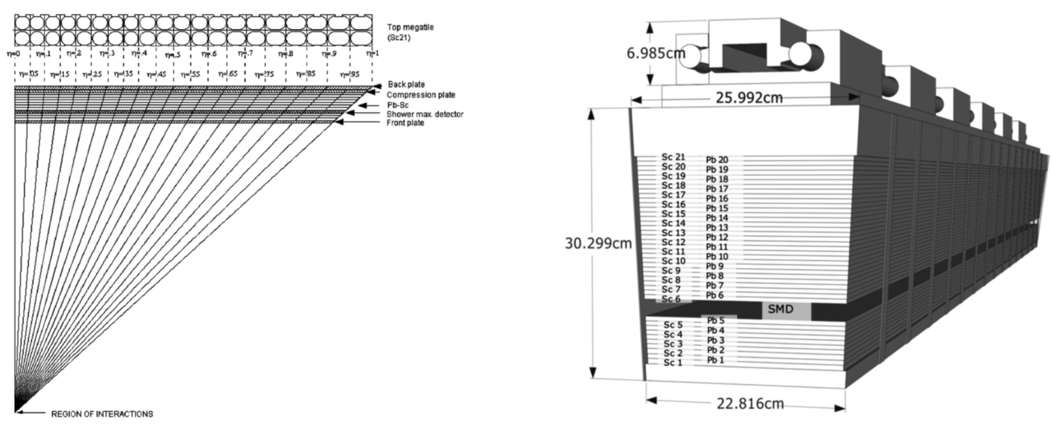

Figure 2.11: The side view (left) and end view (right) of a single BEMC module [36].

shows the side view of a BEMC module on the left panel, and the end view of a BEMC module on the right panel. The full BEMC modules are segmented into 4,800 towers (120 x 40), each of which is pointing to the center of the interaction region. The plastic scintillators are installed in a structure known as a “megatile”, of which the 21^{st} specimen is depicted on the left side of Fig. 2.11. Each module includes a lead scintillator stack in addition to a Barrel Shower Maximum Detector (BSMD). Although BEMC towers demonstrate a good energy resolution for electromagnetic showers, the much larger size of a tower compared to the size of an electromagnetic shower does not allow for a good spatial resolution for these showers. Because the BSMD is capable of providing a significantly improved spatial resolution (a few millimeters), it is of great assistance in the process of identifying electrons, π°'s, and direct photons.

BEMC is employed as a triggering detector at STAR because its readout response rate is quite high; this allows it to keep up with the RHIC collision rate, which is approximately 9.35 MHz. BEMC is able to trigger events that contain particles with high transverse energy, making it a very valuable tool for pre-selecting events throughout the process of collecting online data.

2.2.4 Endcap Electromagnetic Calorimeter (EEMC)

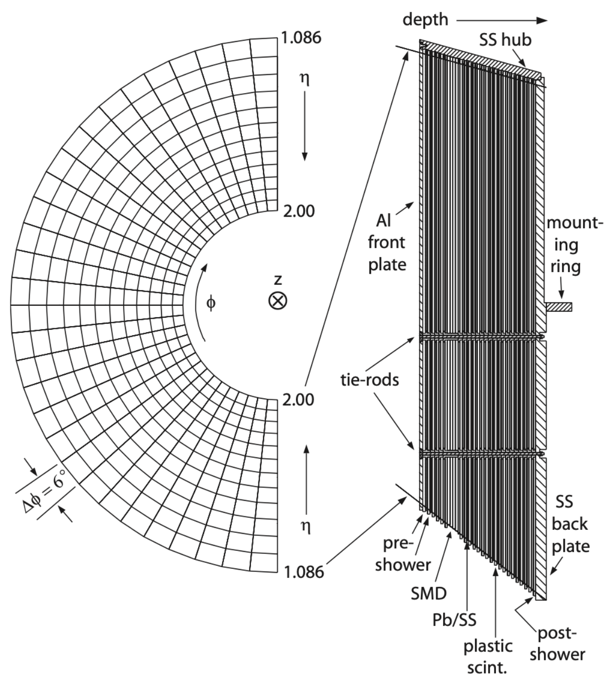

Figure 2.12: A representation, in schematic form, of the tower construction and layers of the Endcap Electromagnetic Calorimeter placed at STAR [37].

The Endcap Electromagnetic Calorimeter (EEMC) [37] is a lead-scintillator sampling calorimeter that consists of 60 azimuthal segments and 12 radial segments. It enables measurements to be taken in the forward direction, with $1 < \eta < 2$, with full azimuthal coverage for high p_T photons, electrons, positrons, and electromagnetically decaying mesons (η, π°). A scintillating-strip shower-maximum detector (also known as an SMD) along with pre-shower and post-shower layers make up the core elements of an EEMC. The detector annulus is divided into two parts and one-half of the detector annulus is depicted in Fig. 2.12. The scintillating-strip SMD provides assistance in distinguishing between γ and π°. Additionally, the pre-shower and post-shower layers contribute to the differentiation of electrons and charged hadrons. EEMC's triggering efficiency and coverage are of critical importance for the spin physics program of polarized pp collisions.

2.2.5 Vertex Position Detector

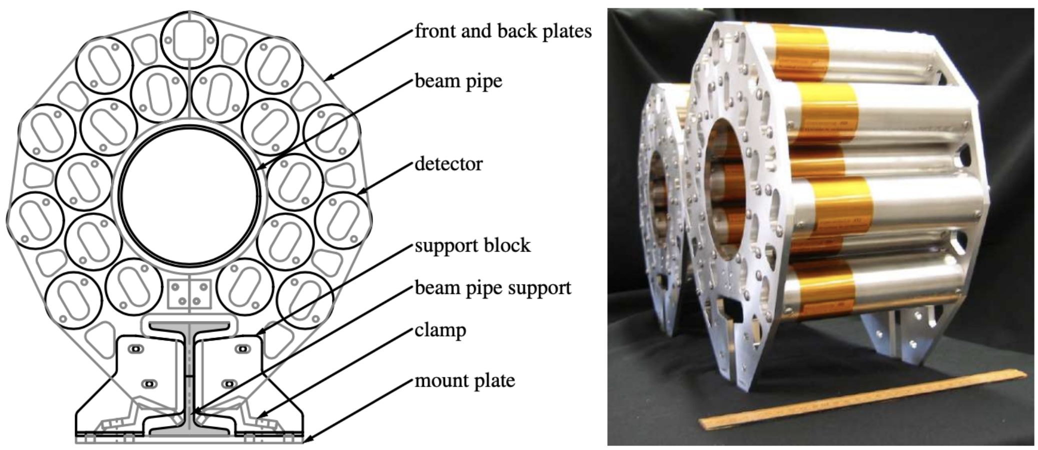

Figure 2.13: On the left is a schematic front view of a VPD assembly and on the right is a photograph of the two VPD assemblies [38].

The Vertex Position Detector (VPD) [38] is able to measure the primary vertex position along the beam direction as well as the "start time" of a collision with high accuracy. The VPD is made up of two different assemblies, both of which are positioned in a symmetrical manner 5.7 meters distant from the center of the interaction region (or center of TPC). The pseudo-rapidity range covered by each of these assemblies is $4.24 < |\eta| < 5.1$. The VPD detector as a whole can achieve timing resolutions of 30 picoseconds on the event start time and a position resolution of 1 cm on the primary collision vertex along the beam direction for Au+Au collisions at $\sqrt{s_{\mathrm{NN}}} = 200$ GeV. There are 19 channels in each VPD assembly, one of them is shown in Fig. 2.13 (Right). VPD is completely integrated into the STAR experiment's trigger system and offers critical information for the minimum-bias trigger in heavy-ion collisions.Additionally, information on the Z component of the primary vertex may be obtained from the VPD. The timing resolution of the VPD is significantly higher than that of the BBC detector.

2.2.6 Beam Beam Counter

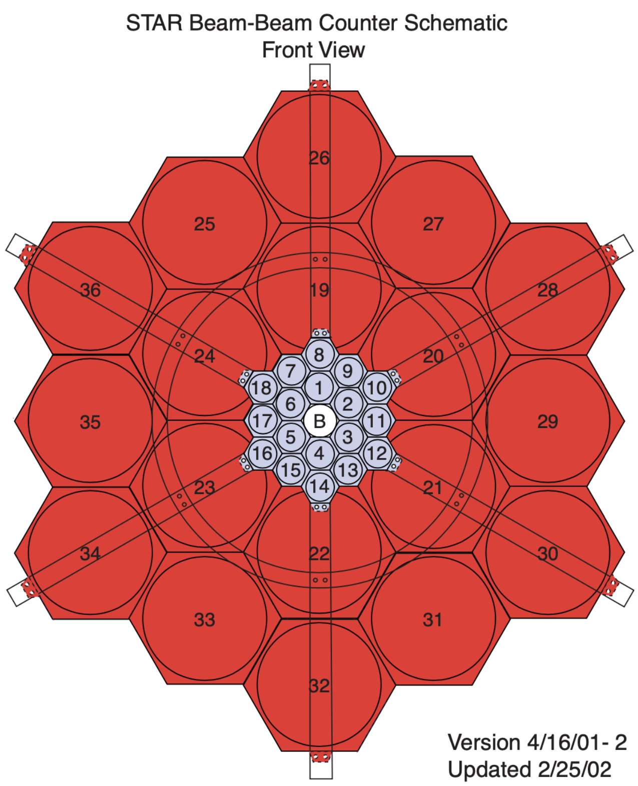

Figure 2.14: Schematic view of STAR Beam Beam Counter (BBC) with inner and outer hexagonal tiles [39].

The Beam Beam Counter (BBC) [39] is positioned on either side of the TPC, encompassing the whole azimuthal angle, and with a pseudo-rapidity range $2.1 < |\eta| < 5.0$. This array of hexagonal scintillators is positioned around the beam pipe at a distance of 3.7 m (along the beam direction) from the center of TPC. The schematic view of STAR BBC is shown in Fig. 2.14 with inner and outer hexagonal tiles. It is necessary to have at least one pair of coincidental hits between the BBC East and BBC West detectors in order to generate a minimum bias (MB) trigger. This coincidence is also used to exclude occurrences involving beam gas. The difference in time between the BBC is utilized to pinpoint the position of the collision vertex. Additionally, the tiny BBC tiles may be utilized to recreate the first-order event plane for flow measurements. In addition to the MB trigger, the relative positions of the particles that are detected by the BBC give important information that is used to estimate the polarizations of proton beams. As a result, this information can be highly helpful for the study of proton spin structure. Internally, each ring is further subdivided into two distinct sub-rings, each consisting of either six or twelve tiles [40]. A BBC coincidence is constituted when a signal from any of the 18 tiles on the east side coincides with a signal from any of the 18 tiles on the west side of the normal interaction region [41].

2.2.7 Zero Degree Calorimeter

The two ZDC detectors [42] are hadronic calorimeters that are placed on both sides of TPC at a distance of approximately 18.25 meters along the beam axis from the center of the TPC. These detectors are designed to measure the amount of energy that is deposited by spectator neutrons at a small angle that is relatively close to zero degrees ($\theta < 2$ mrad). A coincidence between the two ZDCs is necessary for the minimum bias trigger, with the total of the signals being more than 40% of the signal from a single neutron.

2.2.8 Trigger System

The major trigger detectors at STAR are Zero Degree Calorimeters (ZDC), Beam Beam Counters (BBC), Vertex Position Detectors (VPD), and ElectroMagnetic Calorimeters (EMC). Because the readout rates of the various detector subsystems vary, these fast detectors comprise the Level-0 trigger that starts the data acquisition (DAQ) procedure. The STAR trigger system is subdivided into four hierarchic levels. The levels 0, 1, and 2 use fast detectors, e.g. the CTB, BBC, VPD, and the

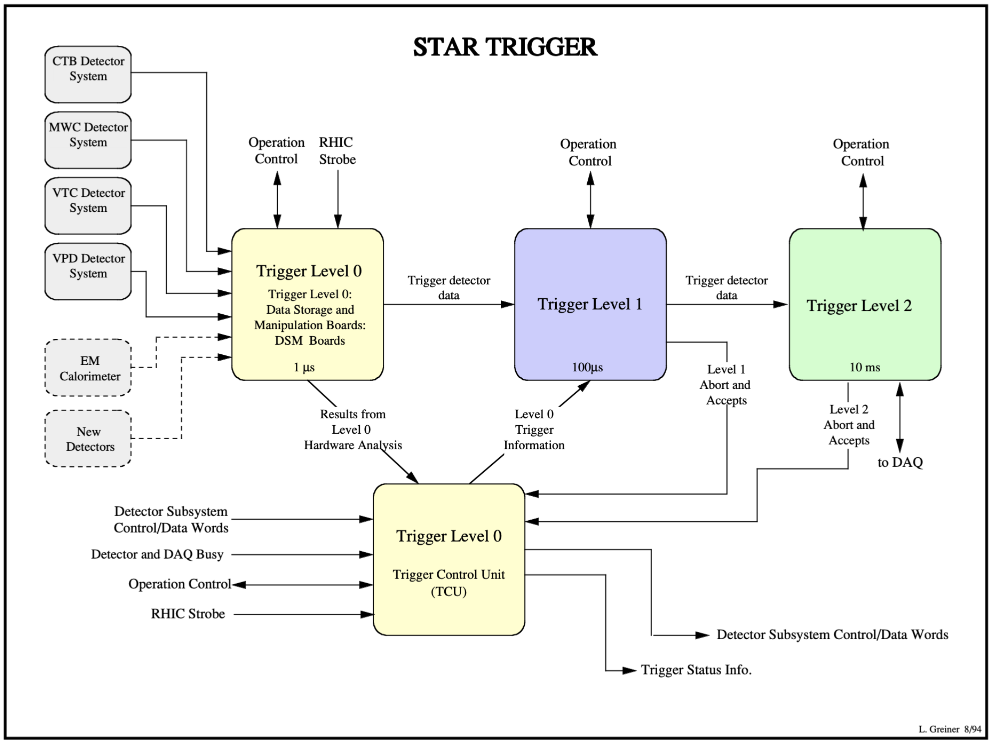

Figure 2.15: A flowchart representation of STAR Trigger system [40].

ZDC [43]. Level-3 [44] is a software trigger that uses data from the slower detectors TPC, SVT, and FTPC. For high-luminance beams, interaction rates at RHIC may exceed 10 MHz [45]. Slow detectors (TPC, SVT, FTPC, EMC) operate at a rate of 200 kHz.

The STAR (Solenoidal Tracker at RHIC) experiment utilizes a trigger system to select events for further analysis based on input from fast detectors. The trigger system plays a crucial role in determining which events are recorded and stored for subsequent analysis by slower tracking detectors. The fast detectors in the trigger system are designed to quickly identify specific signals or events of interest. These signals may be rare or have unique characteristics that make them valuable for scientific study. By using the trigger detectors to identify and select these events, the STAR experiment maximizes the statistics captured for such events, ensuring that a sufficient number of them are recorded for analysis. The trigger system operates by applying predefined selection criteria or algorithms to the data provided by the fast detectors. If an event meets the specified criteria, it is flagged as a trigger event and subsequently recorded by the data acquisition system. This allows for efficient data collection and storage, focusing on events that are most relevant to the scientific goals of the experiment.

There are three stages that include the utilization of the fast trigger detectors as shown in Fig. 2.15. Level 0 is responsible for accepting events and receiving data from the detectors. Level-0 takes in all the information for each bunch crossing and sends a signal to the slow detectors (TPC, SVT, and FTPC) to start the readout. Level-1 can abort an event in the middle of the readout (which takes 40 ms for the TPC). After the data is read, it is converted to a digital format on the front-end electronics. This takes approximately 10 ms for the TPC. During this digitizing time, Level-2 can reject an event before the data is transferred to the DAQ system. DAQ (Data Acquisition) is not informed that an event has taken place [46] until it has first successfully completed all three levels. Instead of storing a random sample of the available collisions, the Level-3 data analysis system has the capability to analyze all the data up to a rate of 50 s^{-1} (50 events per second) and utilize this additional information to make decisions about which events should be stored for further analysis. The Level-3 system processes and analyzes each event in real-time or near real-time, taking into account various criteria and algorithms to evaluate the characteristics and significance of the event. Based on this analysis, the system can make informed decisions about the scientific value and potential of the event. Instead of storing every single event, which could be overwhelming and computationally expensive, the Level-3 system intelligently chooses the most relevant events, ensuring that important scientific information is captured while optimizing storage capacity.

In summary, the Level-3 data analysis system can analyze all the available data up to a certain rate and utilize this information to make informed decisions about event storage. This approach allows for efficient data management while ensuring that important scientific events are captured and available for further analysis.

Bibliography

[1] H. Hahn, E. Forsyth, et al., "The RHIC design overview", Nucl. Inst. Meth. A 499, 245 (2003).

[2] G. Baym, "RHIC: From dreams to beams in two decades", Nucl. Phys., vol. A698, (2002).

[3] "https://cds.cern.ch/record/999421?ln=en"

[4] J. Adams *et al.,* "Experimental and theoretical challenges in the search for the quark–gluon plasma: The STAR Collaboration's critical assessment of the evidence from RHIC collisions", Nucl.Phys.A 757,102 (2005).

[5] John Ellis., "From little bangs to the big bang", Journal of Physics: Conference Series. Vol. 50, 1, IOP Publishing (2006).

[6] R. Esha, "Exploring the critical phenomenon in the QCD phase diagram at STAR", [PhD Thesis] (2019).

[7] "https://www.flickr.com/photos/brookhavenlab/sets/72157613690851651/"

[8] M. Harrison, T. Ludlam, S. Ozaki, "RHIC project overview", Nuclear Instruments and Methods in Physics Research A 499, 235, (2003).

[9] J. G. Alessi, D. Graham *et al.,* "Ion optics of RHIC electron beam ion source", Review of Scientific Instruments 81, 02A509 (2010).

[10] https://www.bnl.gov/rhic/linac.php

[11] H. C. Hseuh and K. M. Welch, "Developments in the vacuum systems of AGS-RHIC", Vacuum 46, 8, 803 (1995).

[12] W. W. MacKay *et al.,* "AGS To RHIC transfer line: Design and Commisioning[1]", "https://www.agsrhichome.bnl.gov/RHIC/Runs/RhicAtr.pdf"

[13] M. Anerella *et al.,* "The RHIC magnet system", Nucl. Instrum. Meth. A 499, 280, 2003.

[14] S. K. Tripathy, "Strange and Deformed: A Study of Strangeness Production in U+U collisions at $\sqrt{(}s_{NN}) = 193$ GeV in STAR" (2019).

[15] K. H. Ackermann *et al.,* "STAR detector overview", Nucl. Instrum. Meth., vol. A499, pp. 624–632, 2003.

[16] K. Adcox *et al.,* "PHENIX detector overview", Nucl. Instrum. Meth., vol. A499, pp. 469–479, 2003.

[17] B. B. Back *et al.,* "The PHOBOS detector at RHIC", Nucl. Instrum. Meth., vol. A499, pp. 603–623, 2003.

[18] M. Adamczyk *et al.,* "The BRAHMS experiment at RHIC", Nucl. Instrum. Meth., vol. A499, pp. 437–468, 2003.

[19] A. Adare *et al.,* "An Upgrade Proposal from the PHENIX Collaboration", "https://arxiv.org/pdf/1501.06197.pdf".

[20] R.L. Brown *et al.,* "The STAR detector magnet subsystem", Nucl. Instrum. Meth. A: Accelerators, Spectrometers, Detectors and Associated Equipment, 499, 2, 633 (2003)

[21] L. Adamczyk *et al.,* "Longitudinal and transverse spin asymmetries for inclusive jet production at mid-rapidity in polarized $p+p$ collisions at $\sqrt{(}s)$=200 GeV", Phys. Rev. D 86, 3, 032006 (2012).

[22] A. Braem *et al.,* "Identification of high p-perpendicular particles with the STAR-RICH detector", Nucl. Instrum. Meth. A 499, 2, 720 (2003) .

[23] K. H. Ackermann *et al.,* "The Forward time projection chamber (FTPC) in STAR", Nucl. Instr. Meth. A, 499, 2, 713 (2003).

[24] R. Bellwied *et al.,* "The STAR silicon vertex tracker: A large area silicon drift detector", Nucl. Instrum. Meth. A 499, 640(2003).

[25] M. M. Aggarwal *et al.,* "The STAR Photon Multiplicity Detector", Nucl. Instr. Meth. A, 499, Issues 2–3, 751 (2003).

[26] M. Anderson *et al.,* "The STAR time projection chamber: a unique tool for studying high multiplicity events at RHIC", Nucl. Instrum. Meth. A 499, 659, (2003).

[27] Liwen Wen, "Probing Quark-Gluon Plasma and Chiral Effects in Heavy-Ion Collisions: Measurements of Strangeness (Ω and ϕ) Production and Identified Particle Correlation in Au+Au Collisions at STAR/RHIC", (2019).

[28] L. Kotchenda *et al.,* "STAR TPC gas system", Nucl. Instrum. Meth. A 499, 703 (2003).

[29] M. Anderson *et al.,* "A readout system for the STAR time projection chamber", Nuclear Instruments and Methods in Physics Research A, 499, 679, (2003).

[30] Kalman, R.E., "A New Approach to Linear Filtering and Prediction Problems", Trans. ASME, J. Basic Eng., vol. 82 D, pp.35–45 (1960).

[31] Kalman, R.E., "Contributions to the Theory of Optimal Control", Bol. Soc. Mat. Mexicana, 5, pp. 102–119 (1960).

[32] Grigory Nigmatkulov (for the STAR collaboration), "STAR Highlights and Future", IV International Conference on Particle Physics and Astrophysics, "https://drupal.star.bnl.gov/STAR/system/files/Nigmatkulov_icppa2018_final.pdf", (2018).

[33] W. J. Llope *et al.,* "The TOFp/pVPD time-of-flight system for STAR", Nucl. Instr. Meth. A 522, 3, 252 (2004).

[34] M. Shao *et al.,* "Beam test results of two kinds of multi-gap resistive plate chambers", Nucl. Instr. Meth. A 492, 344 (2002).

[35] B. Bonner *et al.,* "A single Time-of-Flight tray based on multigap resistive plate chambers for the STAR experiment at RHIC", Nucl. Instr. Meth. A 508, 181 (2003).

[36] M. Beddo *et al.,* "The STAR barrel electromagnetic calorimeter", Nucl. Instrum. Meth. A 499, 725 (2003).

[37] C. E. Allgower *et al.,* "The STAR endcap electromagnetic calorimeter", Nucl. Instrum. Meth. A 499, 740 (2003).

[38] W.J Llope *et al.,* "The STAR Vertex Position Detector", Nucl. Instr. Meth. A 759, 23 (2014).

[39] C. A. Whitten for STAR Collaboration, "The beambeam counter: A local polarimeter at star," AIP Conference Proceedings 980 no. 1, 390–396 (2008).

[40] https://www.star.bnl.gov/public/trg/

[41] J. Kiryluk *et al.,* "Local Polarimetry for Proton Beams with the STAR Beam Beam Counters", arXiv:hep-ex/0501072 (2005).

[42] C. Adler *et al.,* "The RHIC Zero Degree Calorimeter", Nucl. Instrum. Methods Phys. Res., Sect. A 470, 488 (2001).

[43] F.S. Bieser *et al.,* "The STAR trigger", Nucl. Instr. Meth. A 499, 766 (2003).

[44] C. Adler *et al.,* "The STAR level-3 trigger system", Nucl. Instr. Meth. A 499, 778 (2003).

[45] J. M. Landgraf *et al.,* "An overview of the STAR DAQ system", Nucl. Instr. Meth. A 499, 2, 762 (2003).

[46] "https://www.star.bnl.gov/public/trg/runschool/introduction/"

Chapter 3

Chiral Magnetic Effect and Development of Sliding Dumbbell Method

3.1 Introduction

The quantum chromodynamics predicts that meta-stable domains with fluctuating topological charges can change the chirality of quarks and cause CP violation locally [1–3] at very high temperatures and/or densities in the event of quark-gluon plasma (QGP) formation. In relativistic non-central heavy-ion collisions, an observable charge separation in the direction of the magnetic field (B$\sim 10^{15}$ T), created by spectator protons, may arise as a consequence of local parity violation. This phenomenon, characterized by the separation of charges along the magnetic field direction, is commonly known as the Chiral Magnetic Effect (CME), as illustrated in Fig. 3.1 [4–7]. The formation of the CME in heavy-ion collisions requires three essential elements i.e., an external magnetic field created by moving spectators in a heavy-ion collision, a localized non-zero axial charge density, and QGP formation. These prerequisites are satisfied at a very early stage in the process of heavy-ion collisions. The magnetic field's intensity and its duration are other important factors

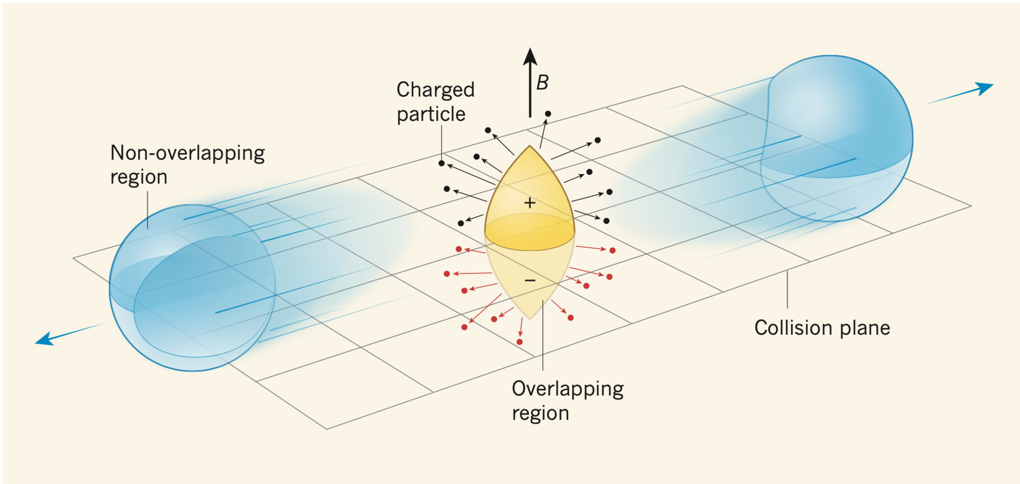

Figure 3.1: A schematic illustration of charge separation in non-central (nuclei that partially overlap) heavy-ion collision. The non-overlapping regions continue undisturbed in the plane of the collision (shown by the blue arrows), and an extraordinarily powerful magnetic field, denoted by B, is formed perpendicular to the plane of the collision. Positively charged particles (black) and negatively charged particles (red) would be emitted from opposite regions of the overlapping zone, a phenomenon known as the chiral magnetic effect [7].

in determining the CME [5]. It is suggested in reference [8] that the strength of the CME signal gradually declines at higher energy as a result of the fact that the magnetic field develops and decays in a relatively short span of time. For the purpose of this thesis, a significant emphasis has been placed on exploring the charge separation effect through the examination of azimuthal correlations involving two and three particles. This analysis plays a pivotal role in identifying potential events that exhibit characteristics similar to the chiral magnetic effect (CME). By employing CME-sensitive methods [9–11], we aim to scrutinize and analyze the event samples that display back-to-back charge separation on an event-by-event basis.

In heavy-ion collisions, the Fourier decomposition of particle azimuthal angle distribution in momentum space is described as follows:

$$\begin{aligned}\frac{dN}{d\phi} \propto 1 + 2v_1 cos(\phi - \psi_{RP}) + 2v_2 cos2(\phi - \psi_{RP}) + ...\\ + 2a_1 sin(\phi - \psi_{RP}) + 2a_2 sin2(\phi - \psi_{RP}) + ...\end{aligned} \tag{3.1}$$

where ϕ and Ψ_{RP} represent the azimuthal angle of the particles and the reaction-plane angle (the angle formed by the impact parameter vector and the beam axis). The parameters, v_1 and v_2, denote the directed flow and the elliptic flow, respectively. Here, a_1 is the parity-violating parameter whose sign changes depending on the topological charge. As a result of the random fluctuations of topological charge that occur from event to event, $< a_1 >= 0$, which implies that the direct detection of the parity violation effect is impossible. The up-down asymmetry of quarks ("A_u") is defined as [11]:

$$A_u = \frac{N_R - N_L}{N_R + N_L} \tag{3.2}$$

where N_R and N_L represent the numbers of right-handed and left-handed quarks, respectively. In the presence of CP violation during hadronization, the previously undetected asymmetry in quarks can manifest as an observable asymmetry in charged pions. This transition is facilitated by the restoration of CP violation and can be quantified by relating the difference between N_R and N_L to the topological charge, denoted as Q.

The asymmetry for $\bar{u}$ antiquarks, denoted as $A_{\bar{u}}$, is related to A_u as $A_{\bar{u}} = -A_u = -\frac{\kappa}{2}$. The asymmetry between u and $\bar{u}$ quarks is not directly observed, if the hadronization process preserves P (Parity) and CP (charge-parity) symmetry, it should result in an observable asymmetry in the production of charged pions. Therefore, we assume that the asymmetry in the production of charged pions, denoted as $A\pi^+ = -A\pi^-$, is equal to A_u. Considering the relationship between N_R, N_L, and Q, the asymmetry in charged pions can be estimated as follows:

$$A_{\pi^+} = -A_{\pi^-} \simeq \frac{Q}{N_{\pi^+}} \tag{3.3}$$

where N_{π^+} represents the pions multiplicity. It is important to note that Q, the topological charge, is a conserved quantity. On the other hand, N_π is highly fluctuating, making it challenging to detect charge separation effects in all interactions. Therefore, an expectation of $A_\pi \approx 10^{-2}$ is proposed [11], considering the complex interplay between the asymmetry, the pion multiplicity, and the topological charge.

3.2 Results from different experiments:

The primary objective of the heavy-ion physics program is to identify any experimental evidence of the chiral magnetic effect (CME). Over the past decade, significant efforts have been made to devise new methods and observables to detect the presence of CME. Unfortunately, most of these methods have only resulted in setting various upper limits of confidence. However, there is some hope, as a hint of the signal was recently reported in Au+Au collisions with a center of mass energy of 200 GeV per nucleon.

The CME sensitive three particle correlator [10,12] is defined as:

$$\begin{aligned} \gamma &= \langle cos(\phi_\alpha + \phi_\beta - 2\Psi_{RP})\rangle \\ &= \langle cos\Delta\phi_\alpha cos\Delta\phi_\beta\rangle - \langle sin\Delta\phi_\alpha sin\Delta\phi_\beta\rangle \\ &= v_{1,\alpha}v_{1,\beta} - a_{1,\alpha}a_{1,\beta} \end{aligned} \tag{3.4}$$

For symmetric rapidity distribution, v_1 and v_2 are zero, so one can measure the parity-violating parameter a_1. Here, ϕ_α, ϕ_β denote the azimuthal angles of the par-

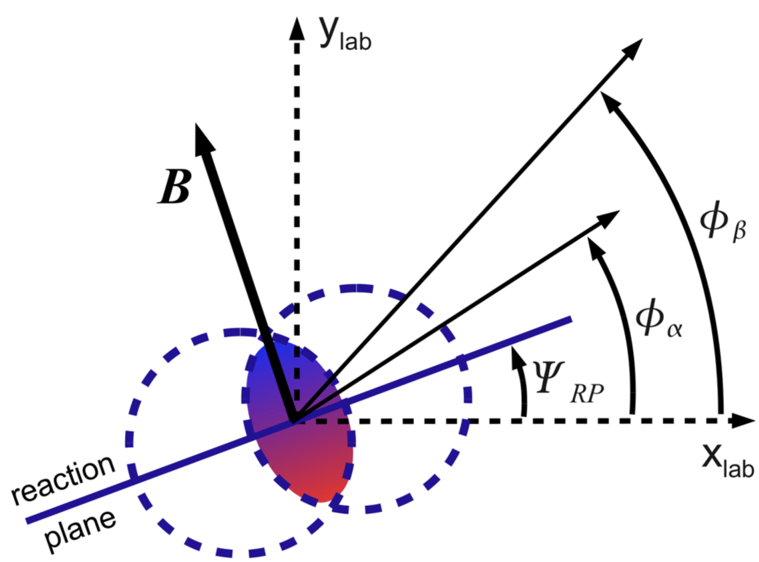

Figure 3.2: A schematic illustration of the geometry of the collisions in non-central nuclear interactions, displaying the azimuthal angles of the particles that are generated in the transverse plane [13].

ticles "α" and "β", respectively. Figure 3.2 shows a simplified diagram of the geometry of non-central collisions. Ψ_{RP} is the reaction plane angle (spanned by the beam axis and the impact parameter vector of the collision), and $\Delta\phi_{\alpha(\beta)} = \phi_{\alpha(\beta)} - \Psi_{RP}$. In eq. 3.4, term $\langle cos\Delta\phi_\alpha cos\Delta\phi_\beta\rangle$ represents in- plane correlations and $\langle sin\Delta\phi_\alpha sin\Delta\phi_\beta\rangle$ represents out-of- plane correlations, and, γ is the difference between in-plane and out-of-plane correlations. These out-of-plane charge correlations are particularly vulnerable to the CME. The angle brackets denote that the calculations were performed over the particles in an event and then over all the events. Experimentally, the reaction plane angle (Ψ_{RP}) cannot be determined. Therefore, the event plane angle (Ψ_{EP}), which is an estimation of the reaction plane angle (Ψ_{RP}), is measured [14]. Thus, eq. 3.4 can be modified as [10]:

$$\gamma = \langle cos(\phi_\alpha + \phi_\beta - 2\phi_c)\rangle / v_{2,c} \tag{3.5}$$

where, the third particle (labeled "c" above) serves to measure the event plane [10], and, $v_{2,c}$ represents the elliptic flow of third particle i.e., "c". The γ correlator is studied for different charge combinations i.e., opposite-sign (OS, $+-, -+$) and same-sign (SS, $++, --$) charge pairs. For CME, γ_{OS} is expected to be positive and γ_{SS} to be negative. The difference between γ_{OS} and γ_{SS} i.e., $\Delta\gamma = \gamma_{OS} - \gamma_{SS}$ is studied to check the CME contribution towards the charge separation.

The charge-dependent two-particle azimuthal correlator is denoted by "$\delta_{\alpha,\beta}$" and its definition is as follows:

$$\delta \equiv \langle cos(\phi_\alpha - \phi_\beta)\rangle = \langle cos\Delta\phi_\alpha cos\Delta\phi_\beta\rangle + \langle sin\Delta\phi_\alpha sin\Delta\phi_\beta\rangle \tag{3.6}$$

Using γ and δ correlator from Eq. 3.4 and Eq. 3.6, one can calculate the in-plane and out-of-plane correlations. The charge-dependent azimuthal correlations have been investigated in order to search for different chiral effects in heavy-ion collisions. Several major collaborations, such as STAR, PHENIX, ALICE, and CMS, have studied the measurement of charge-dependent azimuthal correlations as a function of collision centrality.

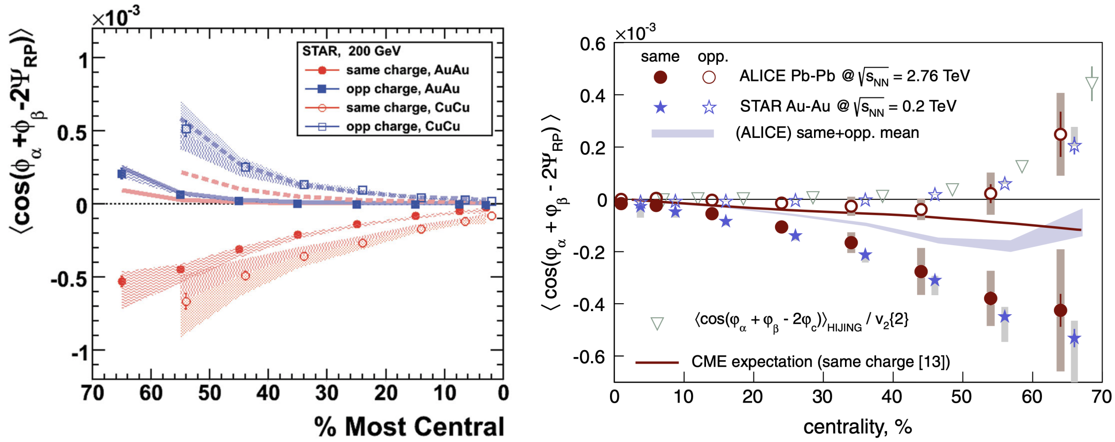

Figure 3.3: (Left) γ-correlator ($\langle\cos(\phi_\alpha + \phi_\beta - 2\Psi_{RP}\rangle$ for Au+Au and Cu+Cu at $\sqrt{s_{\rm NN}}$=200 GeV as a function of centrality. HIJING predictions are shown by the thick solid (Au+Au) and dashed (Cu+Cu) lines, respectively [13]. (Right) The centrality dependence of the three-particle correlator for Pb-Pb collisions at $\sqrt{s_{\rm NN}}$ = 2.76 TeV [17]. The circles show cumulant analysis ALICE results whereas the star symbol displays STAR data taken from [13].

Centrality dependence: STAR collaboration at RHIC measured azimuthal correlations of charged pairs for the first time and observed qualitative agreement with CME expectations. STAR collaboration at RHIC measured γ-correlator in Au+Au and Cu+Cu collisions at $\sqrt{s_{\rm NN}}$ = 200 GeV in the year 2009 [13, 15, 16] for different collision centralities. Figure 3.3 (Left) shows γ-correlator for opposite-sign (OS) which exhibits positive correlations whereas same-sign (SS) correlations are negative, which was consistent with theoretical predictions. As expected, the signal weakens with increasing multiplicity, but at the same centrality, the signal from Cu+Cu collisions is larger than that from Au+Au collisions.

Figure 3.3 (Right) reports the result from ALICE (Pb+Pb at $\sqrt{s_{\rm NN}}$ = 2.76 TeV), which indicates that a strong correlation exists between same sign charge pairs, whereas a very weak correlation exists between the opposite-sign charge pairs. The varying correlation magnitude depending on the charge combination could be understood as the suppression of charge correlations when one of the particles is emitted towards the center of the dense medium formed during a heavy-ion collision [5, 11, 17]. Figure 3.3 (Right) compares ALICE data to HIJING model expectations. Due to the absence of collective azimuthal anisotropy in this model, the

HIJING estimates (same and opposite charge were averaged in the figure) for three-particle correlations are divided by the experimentally determined value of v_2 (i.e. $\langle\cos(\phi_\alpha + \phi_\beta - 2\phi_c)\rangle / v_{2,c}$) [18].

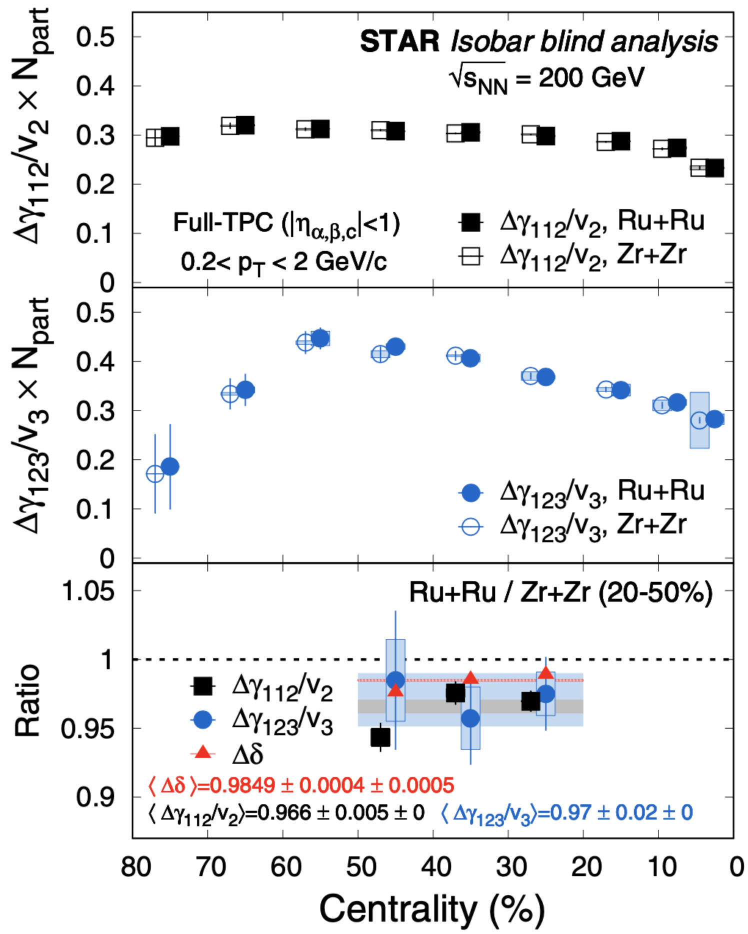

Figure 3.4: The upper and middle panels display the outcomes of scaled charge separation across the second and third harmonic event planes (EPs) divided by the anisotropy coefficient for Ru+Ru (solid marker) and Zr+Zr (open marker) for 0-80% collision centrality. To enhance clarity, the upper two panels incorporate N_{part} scaling. The lower panel presents the ratios of different quantities specifically for the 20-50% centrality range, without N_{part} scaling applied [19].

Figure 3.4 illustrates the results obtained from the analysis of $\Delta\gamma_{112}/v_2$ (CME-sensitive) and $\Delta\gamma_{123}/v_3$ (CME-insensitive) values, multiplied by N_{part}, for each individual isobar species, specifically Ru+Ru and Zr+Zr collisions at $\sqrt{s_{NN}} = 200$ GeV. The upper and middle panels present these values for the respective isobar species. Meanwhile, the lower panel displays the ratios of these quantities specifically for the

20-50% centrality range. It is important to highlight that these ratios do not take N_{part} into consideration, as the values of N_{part} differ between the two isobar systems at the same centrality. Initially, it was anticipated that the ratio $\frac{\Delta\gamma_{112}/v_2{}^{Ru+Ru}}{\Delta\gamma_{112}/v_2{}^{Zr+Zr}}$ would be greater than 1, owing to the larger magnetic field in Ru+Ru collisions compared to Zr+Zr collisions (due to Ru having 4 more protons than Zr). However, the observation pertaining to charge separation in the 20-50% collision centralities does not align with any of the predefined CME signatures [19].

When transitioning from $\sqrt{s_{\rm NN}}$ = 0.2 TeV to 2.76 TeV, the data from both the LHC (Large Hadron Collider) and RHIC (Relativistic Heavy Ion Collider) experiments indicate minimal energy dependence for the three-particle (γ) correlator. This suggests that the behavior of the three-particle correlator remains relatively consistent across this energy range, without significant changes or variations.

Energy dependence: In order to investigate the collision energy dependence of the γ-correlator, Au+Au collisions were conducted at a range of energies, from $\sqrt{s_{\rm NN}}$ = 7.7 GeV to 200 GeV. However, it should be noted that the charge separation is also influenced by the deconfinement process, suggesting the presence of a minimum energy threshold beyond which the chiral magnetic effect (CME) becomes either non-existent or severely limited. Figure 3.5 showcases the γ-correlator for opposite-sign (OS) and same-sign (SS) charge pairs as a function of centrality in Au+Au collisions at various STAR BES-I energies, ranging from 7.7 GeV to 62.4 GeV. The figure reveals that the difference between the OS and SS γ-correlators is close to zero at 7.7 GeV and remains negligibly small at 11.5 GeV, 19.6 GeV, and up to 27 GeV. These findings indicate the absence of a CME-like effect [20]. Interestingly, the γ-correlator exhibits comparable sensitivity at both STAR's 200 GeV and ALICE's 2.76 TeV energies, as discussed previously. This can be attributed to the fact that while the strength of the magnetic effect increases with higher collision energies, its duration becomes shorter.

Small systems: Due to the lower strength of the magnetic field in small system collisions, such as p+p or p+A, compared to heavy-ion collisions (A+A), it

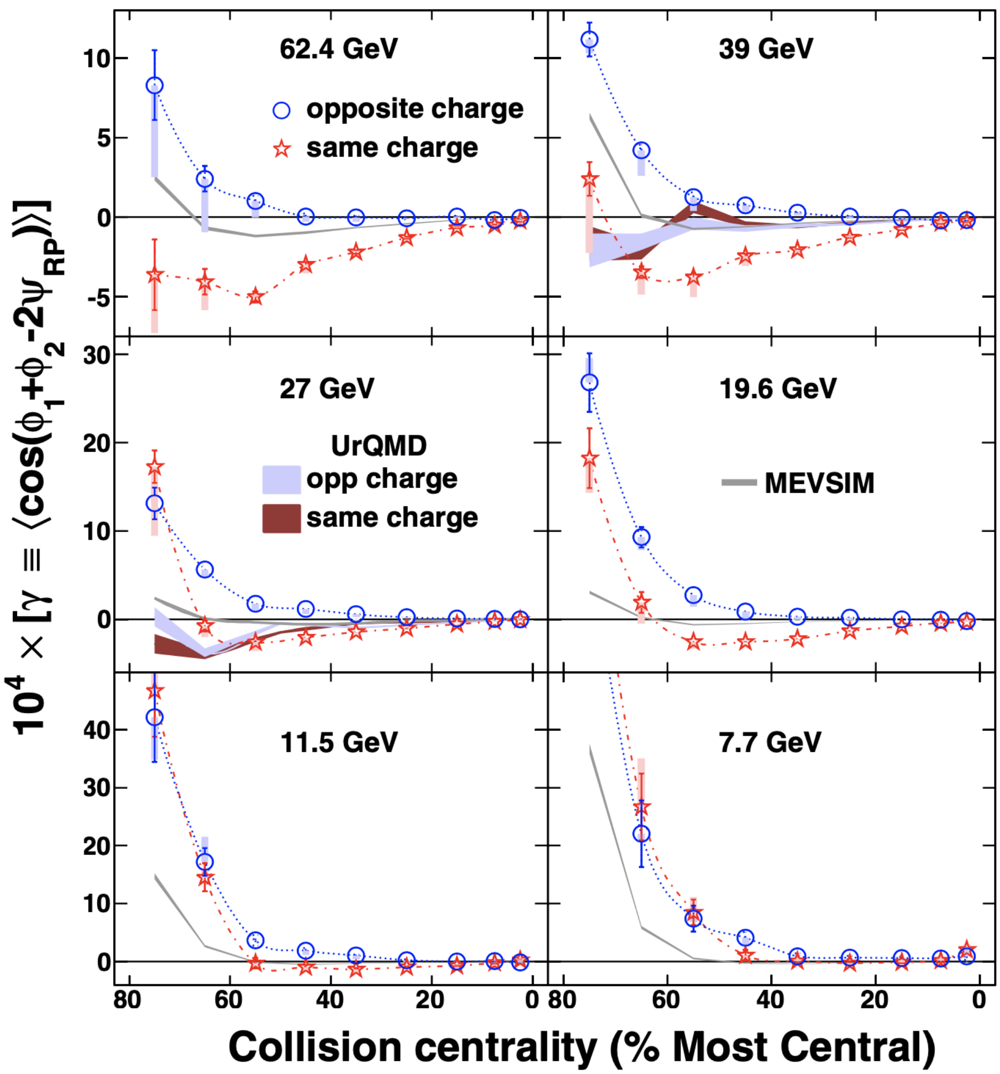

Figure 3.5: The three-point correlator (γ), plotted as a function of centrality for Au+Au collisions with energies ranging from 7.7 to 62.4 GeV, with charge-independent results from the model calculations predicted by MEVSIM (grey curves). Calculations performed using UrQMD are also represented by shaded bands for 27 and 39 GeV [20].

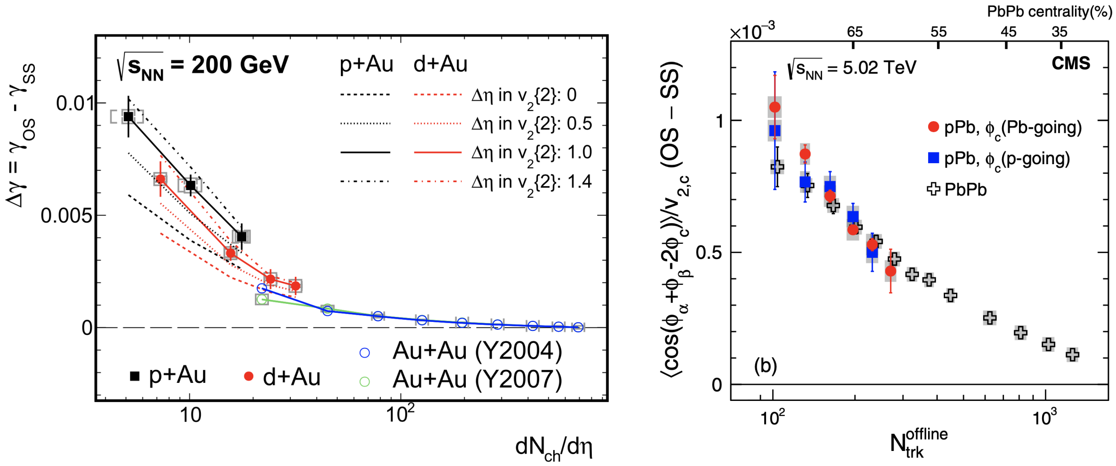

Figure 3.6: (Left) The $\Delta\gamma$ correlator in p+Au and d+Au collisions as a function of multiplicity, compared to that in Au+Au collisions [23]. (Right) The difference of the opposite sign and same sign three-particle correlators as a function of $N_{trk}^{offline}$, averaged over $|\eta_\alpha - \eta_\beta| < 1.6$, in p-Pb and Pb-Pb collisions at $\sqrt{s_{NN}}$= 5.02 TeV [24].

is expected that there will be a significant difference in the correlation values between these two collision types [21,22]. Therefore, small systems have the potential to serve as a baseline for studying heavy-ion collisions. The CMS experiment conducted at the LHC and the STAR experiment at the RHIC have both investigated charge separation in small system collisions. The STAR [23] experiment demonstrates a consistent trend in both p+Au and d+Au systems, as well as in collisions involving heavy ions, as shown in Fig. 3.6 (Left). Similarly, the CMS [24] experiment exhibits the same trend and behavior for the $\Delta\gamma$-correlator in p+Pb and Pb+Pb interactions in regions where multiplicities overlap, as depicted in Fig. 3.6 (right).

Confidence limit: Using the Event Shape Engineering (ESE) method, the ALICE collaboration estimated an upper limit of 26%-33% (depending on the initial-state model) on the contribution of the CME signal in Pb+Pb collisions at $\sqrt{s_{\rm NN}}$ = 2.76 TeV with a confidence level of 95% [25] as shown in Fig. 3.7 (Left). The CMS [26] has put an upper limit on the CME contribution to $\Delta\gamma$ of 7% in Pb+Pb collisions at $\sqrt{s_{\rm NN}}$ = 2.76 TeV at 95% confidence level as shown in Fig. 3.7 (Right). Recently, in another measurement of charge separation, the ALICE [27] has established an upper limit, on the fraction of the CME signal (f_{CME}), of 15-18%(20-24%) at 95%(99.7%) confidence level for the 0-40% collision centralities by utilizing the

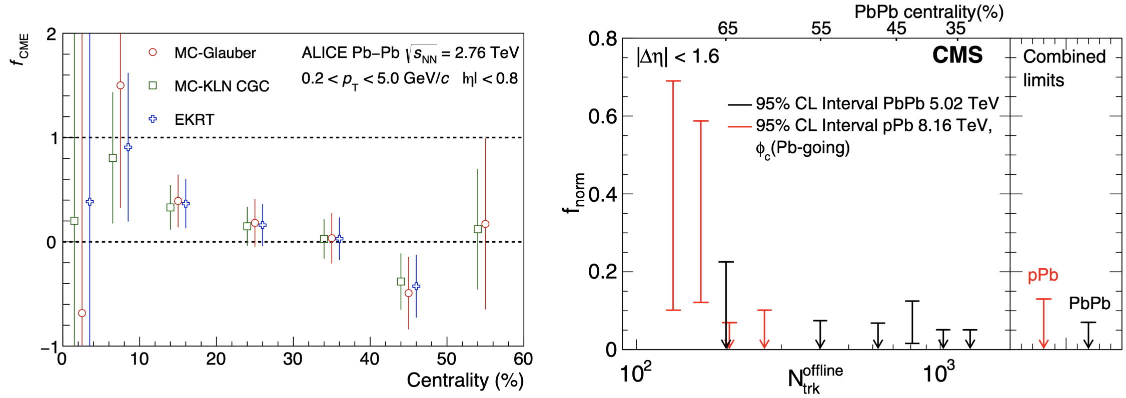

Figure 3.7: (Left) Centrality dependence of the CME fraction extracted from the slope parameter of fits to data and MC-Glauber, MC-KLN CGC and EKRT models, respectively [25]. (Right) The upper limit of the fraction f_{norm} at 95% C.L. as a function of event multiplicity. The combined limits from all presented multiplicities and centralities are also shown in pPb and PbPb collisions [26].

data-driven background.

3.3 Charge Separation Measurements using CME sensitive parameter H

Separating the backgrounds driven by elliptic flow from the effects induced by the magnetic field is currently the most significant challenge in charge separation measurements. Several hypotheses have been proposed as potential solutions. One approach involves examining correlation measurements in different collision systems, such as Cu+Au [28] or U+U [29, 30] collisions, which exhibit distinct patterns of geometric eccentricity and electromagnetic fields compared to Au+Au collisions. Another option is to analyze and differentiate the components in the δ and γ correlations that might indicate a direct dependence on elliptic flow (v_2), as discussed in [12]. The multi-particle correlator is considered the most effective observable for searching for the chiral magnetic effect. The "H-correlator" technique leverages the unique characteristics of both the 2-particle "δ" correlator and the 3-particle "γ" correlator. The δ and γ correlators consist of two components: the flow-independent contribution associated with the CME and the flow-dependent correlations. By examining and separating these components, researchers can better understand and distinguish the different contributions to the observed correlations.

$$\gamma_{\alpha\beta} = kv_2 F_{\alpha\beta} - H_{\alpha\beta},$$
$$\delta_{\alpha\beta} = F_{\alpha\beta} + H_{\alpha\beta}, \tag{3.7}$$

In the equation 3.7, F represents the flow-driven background and H represents the

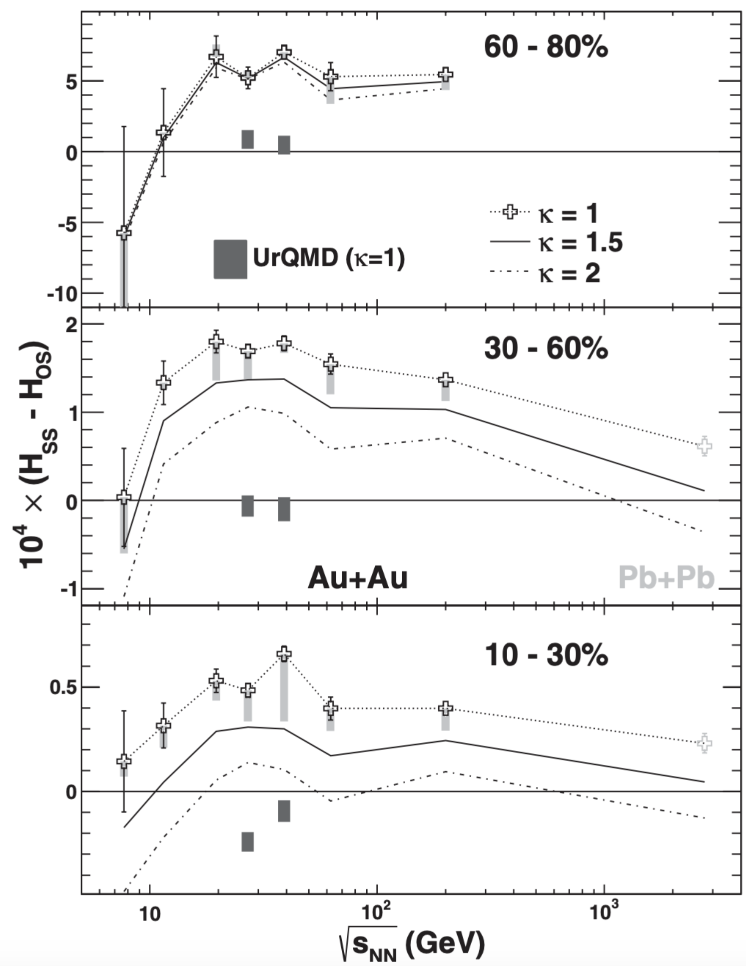

Figure 3.8: $H_{SS} - H_{OS}$ as a function of the center of mass energy for three centrality bins in Au+Au collisions for k=1, 1.5, and 2. Results are compared with Au+Au collisions at 200 GeV and Pb-Pb collisions at 2.76 TeV. The results from UrQMD are shown in the top panel for k=1 for the center of mass energies 27 and 39 GeV [31].

flow-independent CME contribution [12]. To account for acceptance corrections, a constant parameter "k" of order one is introduced. By utilizing data for γ, δ, and v_2, it is possible to extract the F and H signals. Figure 3.8 illustrates the results for $H_{SS} - H_{OS}$ as a function of center-of-mass energy for different collision centrality bins in three panels. These results are compared to UrQMD simulations (for Au+Au collisions at $\sqrt{s_{NN}} = 27$ GeV and 39 GeV) as well as Au+Au collisions at 200 GeV and Pb-Pb collisions at 2.76 TeV. When investigating charge separation along the magnetic field using ($H_{OS} - H_{SS}$), a weak energy dependence is observed until 19.6 GeV, followed by a sharp decline at lower energies. At lower energies where the hadronic phase has a more dominant role compared to the partonic phase, the probability of CME decreases [31].

Another interesting method involves categorizing events belonging to a specific centrality class based on the elliptic flow and observing how the charge separation signal (comparable to the γ correlator) shifts according to the assigned v_2 bins. This method does not require assuming a free parameter like "k" in Eq. 3.7. This study demonstrates a nonzero signal consistent with prior analyses [32].

Recent studies aimed at distinguishing flow backgrounds and isolating potential CME signals provide a compelling argument for the identification and quantification of CME in heavy-ion collisions when considered collectively. To differentiate the signal driven by the magnetic field (along with topological fluctuations) from the background driven by the collective flow determined by collision geometry, it was proposed to compare CME observables in ${}^{96}_{44}Ru + {}^{96}_{44}Ru$ and ${}^{96}_{40}Zr + {}^{96}_{40}Zr$ isobaric collisions. The idea behind this proposal is that both isobaric collisions would exhibit an identical background to CME observables due to the similar size and shape of the colliding nuclei. However, there would be a difference in the magnetic field created by the two isobaric systems, with Ru+Ru collisions having a higher magnetic field intensity by approximately 10% compared to Zr+Zr collisions. This difference in magnetic field would result in approximately a 20% variation in the CME signal in Ru+Ru collisions [19, 33–39]. In addition to the mentioned approaches, a new method has been developed to identify back-to-back charge separation and to identify potential events exhibiting CME-like characteristics.

3.4 The Sliding Dumbbell Method

The previous measurements have reported the existence of the Chiral Magnetic Effect (CME) using multi-particle correlators for different collision centralities. However, it is important to recognize that not every heavy-ion collision environment is suitable for producing the CME. Therefore, it becomes crucial to search for the CME signal in each event individually to isolate potential events that exhibit back-to-back charge separation. A novel method called the "Sliding Dumbbell Method"

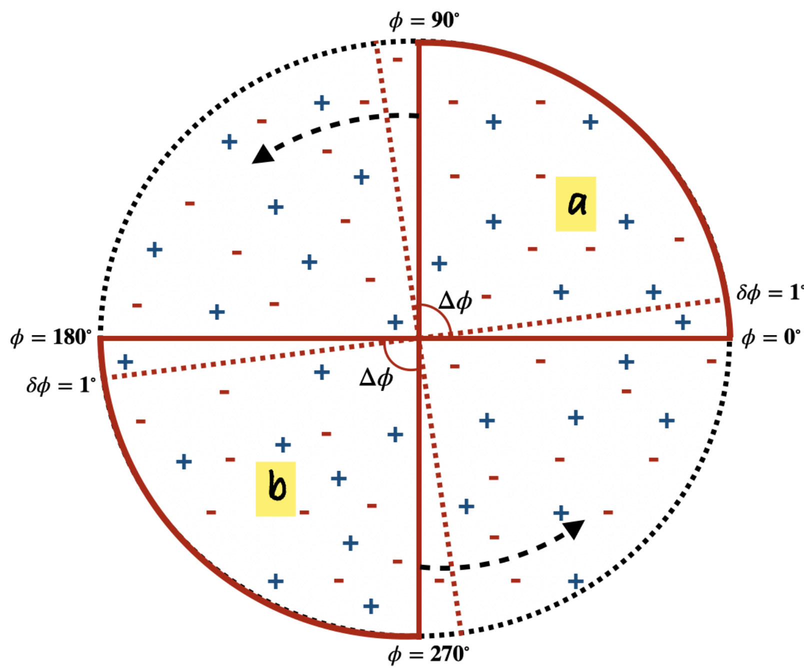

Figure 3.9: A graphical representation of the transverse (azimuthal) plane showing positive (+) and negative (-) particle hits that occur during an event. A red dumbbell of size $\Delta\phi = 90^\circ$ marked with "a" and "b" on either side is also shown. The sliding of the dumbbell in a counterclockwise direction is denoted by the black arrows and the dashed dumbbell that has been moved by one unit ($\delta\phi = 1^\circ$) is also depicted.

(SDM) [40–42] has been developed to identify potential CME-like events with higher back-to-back charge separation on an event-by-event basis in heavy-ion collisions. The SDM is similar to the Sliding Window Method employed by the WA98 collaboration [43,44]. In the SDM, the azimuthal plane of each event is scanned by sliding a dumbbell shape with a size of $\Delta\phi = 90^\circ$ in steps of $\delta\phi = 1^\circ$. During the scan, the maximum value of the charge separation parameter Db_{+-} (denoted as Db^{max}_{+-}) is calculated for each region, with the condition that $\mid Db_{asy} \mid$ is less than 0.25. The dumbbell shape is imaginary and spans 90° in the azimuthal plane perpendicular to the beam direction. Subsequently, a fine-grained scan of the entire azimuthal plane is conducted by sliding the dumbbell in steps of $\delta\phi = 1^\circ$ counterclockwise. Db_{+-} and Db_{asy} are computed for each dumbbell setting.

Db_{+-} represents the charge separation parameter and is defined as follows:

$$\begin{aligned} Db_{+-} &= Db^a_+ + Db^b_- \\ &= \frac{n^a_+}{n^a_+ + n^a_-} + \frac{n^b_-}{n^b_+ + n^b_-} \end{aligned} \tag{3.8}$$

The value of Db_{+-} in the Sliding Dumbbell Method (SDM) is calculated based on the number of positive and negative charge particles on each side of the dumbbell. Specifically, n^a_+ and n^a_- represent the number of positive and negative charge particles in the "a" side of the dumbbell (in a 90° azimuth), while n^b_+ and n^b_- represent the number of positive and negative charge particles in the "b" side of the dumbbell. If Db_{+-} equals 1, it indicates that there is an equal number of positive and negative charge particles on both sides of the dumbbell, resulting in no back-to-back charge separation. Conversely, if Db_{+-} equals 2 (the maximum value), it indicates a 100% back-to-back charge separation. In addition to Db_{+-}, the SDM also calculates the charge excess asymmetry across the dumbbell, denoted as Db_{asy}.

$$Db_{asy} = \frac{Pos^a_{ex} - Neg^b_{ex}}{Pos^a_{ex} + Neg^b_{ex}} \tag{3.9}$$

The charge excess asymmetry across the dumbbell, Db_{asy}, is determined by the difference between the positively charged particle excess ($Pos^a_{ex} = n^a_+ - n^a_-$) on side "a" of the dumbbell and the negatively charged particle excess ($Neg^b_{ex} = n^b_- - n^b_+$) on side "b" of the dumbbell. Figure 3.10 illustrates three different cases with varying Db_{asy} values.

- In Case-I: Pos^a_{ex} is equal to Neg^b_{ex} resulting in $\mid Db_{asy} \mid = 0$, which represents an ideal scenario for a CME-like event.

- In Case-II: Figure 3.10 represents an event with $\mid Db_{asy} \mid = 0.25$, indicating a moderate charge excess asymmetry.
- In Case-III: there is a positive charge excess without a negative charge excess, indicating charge excess on only one side of the dumbbell. A similar case can occur with only a negative charge excess and no positive charge excess.

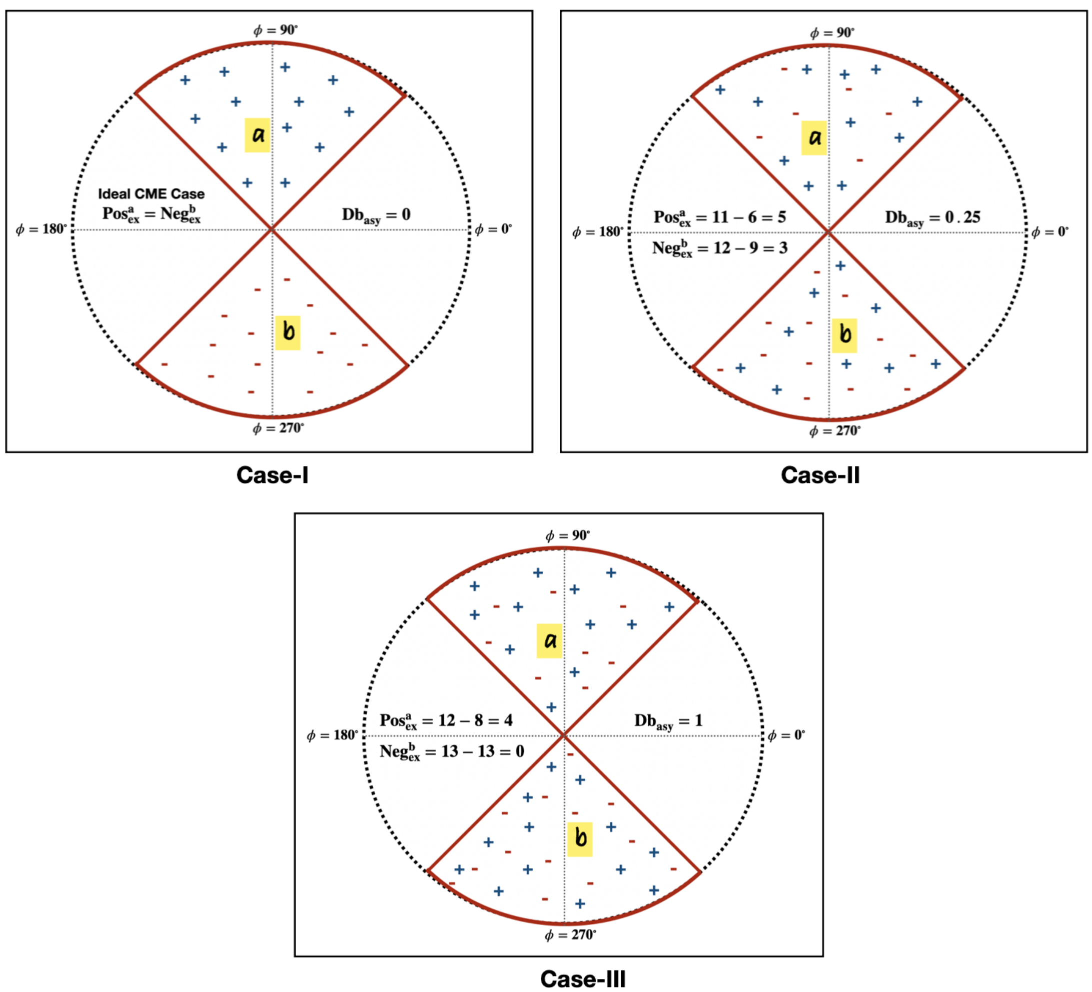

Figure 3.10: Examples exhibiting different charge asymmetry across the dumbbell for different events.

For the analysis, Db^{max}_{+-} is selected with the condition $\mid Db_{asy} \mid < 0.25$, ensuring that there is no significant charge excess on one side of the dumbbell. This selection helps identify events that are CME-like. Using Db_{+-}^{max}, the back-to-back fractional charge separation across the dumbbell, f_{DbCS}, is calculated as follows:

$$f_{DbCS} = Db_{+-}^{max} - 1 \tag{3.10}$$

The f_{DbCS}, which represents the charge separation across the dumbbell, is quantified on a scale from 0 to 1. A value of $f_{DbCS} = 1$ indicates maximum back-to-back charge separation (100% charge separation), while a value of $f_{DbCS} = 0$ corresponds to minimum back-to-back charge separation. To assess the effectiveness of the SDM, the f_{DbCS} distributions are computed for each collision centrality. These distributions are then divided into ten percentile bins, with the first bin representing the top 10% of f_{DbCS} values (highest charge separation) and the tenth bin representing the lowest values of f_{DbCS} (lowest charge separation). Subsequently, the multi-particle correlators are examined using different charge separation classes (or f_{DbCS} bins). The Q-cumulant method is employed to analyze the multi-particle correlators, which are extensively discussed in the subsequent section.

3.5 Multi particle Azimuthal Correlations

The main objective of this thesis is to investigate the charge separation effect induced by the Chiral Magnetic Effect (CME) through the analysis of two- and three-particle azimuthal correlations. Computing multi-particle correlations directly require significant computational resources due to the need to consider all possible particle multiplets. To overcome this challenge and mitigate numerical inaccuracies, the Q-cumulant approach is employed as a computational technique [45]. In the analysis of multi-particle correlations, the Q-vector is defined as:

$$Q_n = \sum_{i=1}^{M} e^{in\phi_i} \tag{3.11}$$

where n represents the harmonic order (e.g., n = 1, 2, 3, ...), ϕ_i is the azimuthal angle of the i^{th} particle and the summation is performed over all particles in the event with a multiplicity of M. The computation of multi-particle correlations involves two steps:

Step-I: The following expression can be used to define the average multi-particle correlations for each event:

$$\langle 2\rangle_{n|n} \equiv \frac{1}{P(M,2)} \sum_{i,j=1(i\neq j)}^{M} e^{in(\phi_i-\phi_j)} \tag{3.12}$$

$$\langle 3\rangle_{n,n|2n} \equiv \frac{1}{P(M,3)} \sum_{i,j,k=1(i\neq j\neq k)}^{M} e^{in(\phi_i+\phi_j-2\phi_k)} \tag{3.13}$$

$$\langle 4\rangle_{n,n|n,n} \equiv \frac{1}{P(M,4)} \sum_{i,j,k,l=1(i\neq j\neq k\neq l)}^{M} e^{in(\phi_i+\phi_j-\phi_k-\phi_l)} \tag{3.14}$$

where $P(n,m)$ is $\frac{n!}{(n-m)!}$

Step-II: After determining the correlations for each event, the final multi-particle azimuthal correlation is determined by taking an average across all events:

$$\langle\langle 2\rangle\rangle_{n|n} \equiv \frac{\sum_{i=1}^{N}(w_2)_i(\langle 2\rangle_{n|n})_i}{\sum_{i=1}^{N}(w_2)_i} \tag{3.15}$$

$$\langle\langle 3\rangle\rangle_{n,n|2n} \equiv \frac{\sum_{i=1}^{N}(w_3)_i(\langle 3\rangle_{n,n|2n})_i}{\sum_{i=1}^{N}(w_3)_i} \tag{3.16}$$

$$\langle\langle 4\rangle\rangle_{n,n|n,n} \equiv \frac{\sum_{i=1}^{N}(w_4)_i(\langle 4\rangle_{n,n|n,n})_i}{\sum_{i=1}^{N}(w_4)_i} \tag{3.17}$$

where double brackets denote an average over all tracks and then over all "N" events. The multiplicity weights, w_2, w_3, w_4, are introduced to get rid of the multiplicity

(M) fluctuations which are defined as:

$$w_2 \equiv M(M-1) \tag{3.18}$$

$$w_3 \equiv M(M-1)(M-2) \tag{3.19}$$

$$w_4 \equiv M(M-1)(M-2)(M-3) \tag{3.20}$$

Thus the Q-cumulants are defined as:

$$c_2\{2\} = \langle\langle 2\rangle\rangle \tag{3.21}$$

$$c_2\{4\} = \langle\langle 4\rangle\rangle - 2 * \langle\langle 2\rangle\rangle^2 \tag{3.22}$$

In terms of flow harmonic, the cumulants can be written as,

$$v_n^2\{2\} = c_2\{2\} \tag{3.23}$$

$$v_n^2\{4\} = (-c_2\{4\})^{1/4} \tag{3.24}$$

The calculation of multi-particle correlations from the Q-cumulants involves several steps. Here are the general steps:

2-Particle Correlator: For example, the 2-particle cumulant ($C_n\{2\}$) represents the correlation between pairs of particles, while higher-order cumulants like $C_n\{3\}$ and $C_n\{4\}$ involve correlations among three and four particles, respectively. Two particle azimuthal correlations are obtained for different charge combinations i.e., Same Sign (SS) and Opposite Sign (OS) charge pairs, which are defined as follows:

Same-Sign: $\mid Q_n \mid^2$ for same-sign is defined as:

$$\mid Q_n \mid^2 = \sum_{i,j=1}^{M} e^{in(\phi_i - \phi_j)} \tag{3.25}$$

- (i $\neq$ j) i.e., the correlation between different types of particles and 2-particle contribution is calculated as:

$$\langle 2 \rangle_{n|n} * P_{M,2} \tag{3.26}$$

- (i = j) i.e., represents the self-correlation (auto-correlation) term which given the contribution:

$$1 * M \tag{3.27}$$

Thus, $\mid Q_n \mid^2$ can be written as follows:

$$\mid Q_n \mid^2 = \langle 2 \rangle_{n|n} * P_{M,2} + 1 * M \tag{3.28}$$

Rearranging the above equation provides the 2-particle correlator for same-sign charge pairs:

$$\langle 2 \rangle_{n|n} = \frac{\mid Q_n \mid^2 - M}{M(M-1)} \tag{3.29}$$

where by using Euler's formula (i.e., $e^{ix} = cosx + isinx$),
$\mid Q_n \mid^2 = Q_n Q_n^* = \cos^2 \phi + \sin^2 \phi$.
Opposite-Sign: The opposite-sign 2-particle correlator is defined as follows:

$$\mid Q_n \mid^2 = q_{\underline{n}} Q_n^* \tag{3.30}$$

where Q_n^* represents the Q-vector for positive charge particles (group A) of multiplicity M, and $q_{\underline{n}}$ represents the Q-vector for negative charge particles (group B) of multiplicity m. In this case, the average is taken over all possible pairs of particles, where one particle is from group A (positive charge) and the other particle is from group B (negative charge). By computing this opposite-sign 2-particle correlator, one can quantify the correlation between particles of opposite charges and investigate the charge separation effect caused by the Chiral Magnetic Effect (CME) in heavy-ion collisions. Two-particle correlator for Opposite-sign is defined as:

$$\langle 2\rangle_{\underline{n}|n} = \frac{q_{\underline{n}} Q_n^*}{m * M} \tag{3.31}$$

where $q_{\underline{n}} Q_n^* = \cos\phi_i \times \cos\phi_j + \sin\phi_i \times \sin\phi_j$.

Three-Particle Correlator: To estimate the three-particle correlator as defined in Eq. 3.4, we decompose the Q-vector ($Q_n Q_n Q_{2n}^*$) compositions. Similar to the 2-particle correlations, we first discuss the same-sign charge pair case and then the opposite-sign case.

Same-Sign: In the case of same-sign charge pairs, the three-particle correlator is computed using the Q-vector defined as follows:

$$Q_n Q_n Q_{2n}^* = \sum_{i,j,k=1}^{M} e^{in(\phi_i+\phi_j-2\phi_k)} \tag{3.32}$$

In the three-particle correlator, denoted as $\langle 3\rangle_{n,n|2n}$, the indices i, j, and k represent different particles. For the same-sign case, particles i and j are from the same group (either positive or negative charges), while particle k can be from any of the two groups.

There are three different cases for the indices i, j, and k:

- When all the 3 indices are different i.e., (i $\neq$ j $\neq$ k), it represents 3-particle correlation contribution as:

$$\langle 3\rangle_{n,n|2n} * M(M-1)(M-2) \tag{3.33}$$

- When any of the two indices are different, i.e., (i $\neq$ j = k) or (i = j $\neq$ k)
  1. (ϕ_i + ϕ_j - 2ϕ_k) = (ϕ_i-ϕ_k) for (i $\neq$ j = k)
  it's a 2-particle correlation with contribution as:

$$\langle 2\rangle_{n|n} * M(M-1)2! \tag{3.34}$$

2. (ϕ_i + ϕ_j - 2ϕ_k) = (2ϕ_i-2ϕ_k) for (i = j $\neq$ k)

Similarly, this is also 2-particle correlation with contribution as:

$$\langle 2\rangle_{2n|2n} * M(M-1) \tag{3.35}$$

- When i=j=k (auto-correlation), the contribution is:

$$1 * M \tag{3.36}$$

Using these equations in Eq. 3.32 we get,

$$Q_nQ_nQ^*_{2n} = \langle 3\rangle_{n,n|2n}*M(M-1)(M-2)+\langle 2\rangle_{n|n}*M(M-1)2!+\langle 2\rangle_{2n|2n}*M(M-1)+M \tag{3.37}$$

Re-arranging the above equation and using $\langle 2\rangle_{n|n}$ in that from Eq. 3.29, we get:

$$\langle 3\rangle_{n,n|2n} = \frac{Q_nQ_nQ^*_{2n} - 2* \mid Q_n \mid^2 - \mid Q_{2n} \mid^2 + 2 * M}{M(M-1)(M-2)} \tag{3.38}$$

After implementing Euler's formula, the following represents what the final 3-particle correlator looks like:

$$\begin{aligned}\langle 3\rangle_{n,n|2n} = (&cos2\phi_k(cos\phi^2_{i(j)} - sin\phi^2_{i(j)}) + sin2\phi_k(2sin\phi_{i(j)}cos\phi_{i(j)})\\ &- (cos2\phi_k cos2\phi_{i(j)} + sin2\phi_k sin2\phi_{i(j)})\\ &- 2.(cos2\phi^2_{i(j)} + sin2\phi^2_{i(j)})\\ &+ 2M)/M(M-1)(M-2)\end{aligned} \tag{3.39}$$

Opposite-Sign: In the opposite-sign scenario of the three-particle correlator, we consider one type of particle (either positive or negative) from one set or group, and another type of particle from a different set. This leads to different possibilities for the indices i, j, and k in the expression (ϕ_i + ϕ_j - 2ϕ_k) representing the azimuthal angles of the particles. There are three different cases for the indices i, j, and k:

- if i $\neq$ j $\neq$ k

  we get (ϕ_i + ϕ_j - 2ϕ_k), which is a 3-particle correlation and its contribution is:

$$\langle 3\rangle_{\underline{n},n|2n} * M(M-1)m \tag{3.40}$$

- if i = k or j = k

  we get (ϕ_i + ϕ_j - 2ϕ_k) = (ϕ_j - ϕ_i), which represent 2-particle correlation and its contribution is:

$$\langle 2\rangle_{\underline{n}|n} * M * m \tag{3.41}$$

Using Eq. 3.40 and Eq. 3.41 in the Eq. 3.32, we get the 3-particle correlator for opposite sign as follows:

$$\langle 3\rangle_{n,n|2n} = \frac{q_{\underline{n}}Q_nQ^*_{2n} - q_{\underline{n}}Q^*_n}{mM(M-1)} \tag{3.42}$$

After applying Euler's formula, the following represents the final 3-particle correlator for the opposite sign:

$$\begin{aligned}\langle 3\rangle_{n,n|2n} = &(cos2\phi_k(cos\phi_i cos\phi_j - sin\phi_i sin\phi_j)\\ &+ sin2\phi_k(cos\phi_i sin\phi_j - sin\phi_i cos\phi_j) - 2*(cos\phi_i cos\phi_j + sin\phi_i sin\phi_j))\\ &/mM(M-1)\end{aligned} \tag{3.43}$$

Four-Particle Correlation: To calculate the 4^{th} order cumulant using the Q-vector, the Q_n is expressed as:

$$\mid Q_n \mid^4 = \sum_{i,j,k,l=1}^{M} e^{in(\phi_i+\phi_j-\phi_k-\phi_l)} \tag{3.44}$$

The equation above can be divided into four different cases based on the indices i, j, k, and l for the Same-Sign (SS) charge pair combination. In this analysis, we focus only on the Same-Sign (+ + or - -) combination, as this correlator is used to calculate the elliptic flow. By considering different combinations of i, j, k, and l within the Same-Sign charge pair, we can study the correlations among particles with the same charge. These correlations help us understand the behavior of the elliptic flow in heavy-ion collisions.

- if i≠j≠k≠l, we get:

$$\langle 4\rangle_{n,n|n,n} M(M-1)(M-2)(M-3) \tag{3.45}$$

- When three of the four indices are different i.e., i=j≠k≠l or i≠j=k≠l or i≠j≠k=l

  1.) If i=j≠k≠l then $(\phi_i + \phi_i - \phi_k - \phi_l\ ) = (2\phi_i - \phi_k - \phi_l)$ i.e., a 3-particle correlation with contribution as:

$$\langle 3\rangle_{2n|n,n} * M(M-1)(M-2) \tag{3.46}$$

  2.) If i≠j≠k=l then $(\phi_i + \phi_j - \phi_k - \phi_k\ ) = (\phi_i + \phi_j - 2\phi_k)$ i.e., Again 3-particle correlation with contribution as:

$$\langle 3\rangle_{n,n|2n} * M(M-1)(M-2) \tag{3.47}$$

  3.) If i≠j=k≠l then $(\phi_i + \phi_j - \phi_j - \phi_l\ ) = (\phi_i - \phi_l)$ i.e., a 2-particle correlation with contribution as:

$$\langle 2\rangle_{n|n} * M(M-1)2!(M-2)2! \tag{3.48}$$

- When any two indices are different i.e., i=j=k≠l or i≠j=k=l or i=j≠k=l

  1.) the two cases i.e., i=j=k≠l or i≠j=k=l give the same results as:

  $(\phi_i + \phi_j - \phi_k - \phi_l\ ) = (\phi_i - \phi_l)$, making it a 2-particle correlation as follows:

$$\langle 2\rangle_{n|n} * M(M-1)2!2! \tag{3.49}$$

2.) If i=j≠k=l then $(\phi_i + \phi_j - \phi_k - \phi_l\ ) = (2\phi_i - 2\phi_k)$, which again give rise to 2-particle correlation as follows:

$$\langle 2\rangle_{2n|2n} * M(M-1) \tag{3.50}$$

3.) If i=k≠j=l, which give rise to the term as:

$$M(M-1) * 2! \tag{3.51}$$

- Only the auto-correlation term remains when all of the indices are the same, i.e., "i = j = k = l", which give Multiplicity "M" as contribution,

$$1 * M \tag{3.52}$$

In order to obtain the four particle correlation term, calculate Eq. 3.44 using the above four cases and their computed values, i.e.,

$$\begin{aligned} \mid Q_n \mid^4 = &\langle 4\rangle_{n,n|n,n} * M(M-1)(M-2)(M-3) \\ &+ [\langle 3\rangle_{2n|n,n} + \langle 3\rangle_{n,n|2n}] * M(M-1)(M-2) \\ &+ \langle 2\rangle_{n|n} * [(M(M-1)2!(M-2)2! + M(M-1)2!2!)] \\ &+ \langle 2\rangle_{2n|2n} * M(M-1) + M(M-1)2 + M \end{aligned} \tag{3.53}$$

Rearranging the above equation gives 4-particle correlator ($\langle 4\rangle_{n,n|n,n}$) as:

$$\begin{aligned} \langle 4\rangle_{n,n|n,n} = &\frac{(\mid Q_n \mid^4 + \mid Q_{2n} \mid^2 - 2 * R[Q_{2n}Q_n^*Q_n^*] - 4(M-2) \mid Q_n \mid^2)}{M(M-1)(M-2)(M-3)} \\ &+ \frac{2}{(M-1)(M-2)} \end{aligned} \tag{3.54}$$

the final four-particle correlator can be obtained by averaging over N number of events and is used to estimate the 4^{th} order cumulant.

After calculating the second and fourth-order cumulants and the three-particle correlator, we can utilize the information of elliptic flow (v_2) to measure the three-particle azimuthal correlations with respect to the reaction plane. The second and fourth-order cumulants obtained previously are employed to calculate the elliptic flow using equations Eq. 3.23 and 3.24, as discussed earlier. These calculations allow us to investigate the relationship between the measured azimuthal correlations and the underlying elliptic flow in the system.

In the previous sections, we have derived cumulants from multi-particle correlations without considering acceptance effects. However, in reality, detectors may have non-uniform acceptance, which can introduce biases in the measured correlations. While the simple cumulant expressions derived earlier are suitable for describing ideal detectors, a more generalized approach is necessary to account for acceptance corrections in the presence of biased detectors.

The topic of acceptance corrections [46–48] due to biased detectors is discussed in detail in Chapter 5. In this chapter, we delve into the specific equations and methods used to correct acceptance effects and ensure accurate measurements of the correlations. The techniques outlined in this chapter, based on previous research, provide a comprehensive understanding of how to correct detector biases and obtain reliable results from experimental data.

Bibliography

[1] D. Kharzeev, R. D. Pisarski and M. H. G. Tytgat, “Possibility of spontaneous parity violation in hot QCD”, Phys. Rev. Lett. 81, 512-515 (1998).

[2] D. Kharzeev and R. D. Pisarski, “Pionic measures of parity and CP violation in high-energy nuclear collisions”, Phys. Rev. D 61, 111901 (2000).

[3] P. D. Morley and I. A. Schmidt, “Strong P, CP, T violations in Heavy Ion Collisions”, Z. Phys. C 26, 6271861 (1985).

[4] D. Kharzeev, L. D. McLerran, and H. J. Warringa, “The Effects of topological charge change in heavy ion collisions: Event by event P and CP violation”, Nucl. Phys. A 803, 227 (2008).

[5] K. Fukushima, D. E. Kharzeev, and H. J. Warringa, “The Chiral Magnetic Effect”, Phys. Rev. D 78, 074033 (2008).

[6] M. Asakawa, A. Majumder, and B. Muller, “Electric Charge Separation in Strong Transient Magnetic Fields”, Phys. Rev. C 81, 064912 (2010).

[7] A. Dobrin, “No sign of asymmetry in the strong force”, Nature 546, 477, “doi:10.1038/nature23086” (2017).

[8] D.E. Kharzeev et al., “Chiral Magnetic and Vortical Effects in High Energy Nuclear Collisions - A Status Report”, Prog. Part. Nucl. Phys. 88, 1 (2016).

[9] S.A. Voloshin, “Estimate of the CME signal in heavy-ion collisions from measurements relative to the participant and spectator flow planes”, Phys. Rev. C 98, 054911 (2018).

[10] S. A. Voloshin, “Parity violation in hot QCD: how to detect it”, Phys. Rev. C 70, 057901 (2004).

[11] D. Kharzeev, “Parity violation in hot QCD: Why it can happen, and how to look for it”, Phys. Lett. B 633, 260 (2006).

[12] A. Bzdak, Volker Koch, and Jinfeng Liao, “Charge-Dependent Correlations in Relativistic Heavy Ion Collisions and the Chiral Magnetic Effect”, Lecture Notes in Physics, 871, 503 (2013) [arXiv:1207.7327v1].

[13] B. I. Abelev *et al.* [STAR Collaboration], “Azimuthal Charged-Particle Correlations and Possible Local Strong Parity Violation”, Phys. Rev. Lett. 103, 251601 (2009).

[14] A. M. Poskanzer and S. A.Voloshin, “Methods for analyzing anisotropic flow in relativistic nuclear collisions”, Phys. Rev. C 58, 1671 (1998).

[15] B. I. Abelev *et al.* [STAR Collaboration], “Observation of charge-dependent azimuthal correlations and possible local strong parity violation in heavy ion collisions”, Phys. Rev. C 81, 054908 (2010).

[16] L. Adamczyk *et al.* [STAR Collaboration], “Fluctuations of charge separation perpendicular to the event plane and local parity violation in $\sqrt{s_{NN}} = 200$ GeV Au+Au collisions at the BNL Relativistic Heavy Ion Collider”, Phys. Rev. C 88, 064911 (2013).

[17] B. I. Abelev *et al.* [ALICE Collaboration], “Charge separation relative to the reaction plane in Pb-Pb collisions at $\sqrt{s_{NN}} = 2.76$ TeV”, Phys. Rev. Lett. 110, 012301 (2013).

[18] K. Aamodt *et al.* [ALICE Collaboration], “Elliptic Flow of Charged Particles in Pb-Pb collisions at $\sqrt{s_{NN}} = 2.76$TeV”, Phys. Rev. Lett. 105, 252302 (2010).

[19] M. S. Abdallah *et al.* [STAR Collaboration], “Search for the chiral magnetic effect with isobar collisions at $\sqrt{s_{NN}}$= 200 GeV by the STAR Collaboration at the BNL Relativistic Heavy Ion Collider”, Phys. Rev. C 105, 014901 (2022).

[20] L. Adamczyk *et al.*, "Beam-Energy Dependence of Charge Separation along the Magnetic Field in Au+Au Collisions at RHIC", Phys. Rev. Lett. 113, 052302 (2014).

[21] K. Dusling, W. Li and B. Schenke, "Novel collective phenomena in high-energy proton–proton and proton–nucleus collisions", Int. J. Mod. Phys. E 25, no.01, 1630002 (2016).

[22] J. L. Nagle and W. A. Zajc, "Small System Collectivity in Relativistic Hadronic and Nuclear Collisions", Ann. Rev. Nucl. Part. Sci. 68, 211 (2018).

[23] J. Adam *et al.* [STAR Collaboration], "Charge-dependent pair correlations relative to a third particle in p+Au and d+Au collisions at RHIC", Phys. Lett. B 798 134975 (2019).

[24] Khachatryan V. *et al.* [CMS Collaboration], "Observation of charge-dependent azimuthal correlations in p-Pb collisions and its implication for the search for the chiral magnetic effect", Phys. Rev. Lett 118, 122301 (2017).

[25] S. Acharya *et al.* [ALICE Collaboration], "Constraining the magnitude of the Chiral Magnetic Effect with Event Shape Engineering in Pb–Pb collisions at $\sqrt{s_{NN}} = 2.76$ TeV", Phys. Lett. B 777, 151 (2018).

[26] A. M. Sirunyan *et al.* [CMS Collaboration], "Constraints on the chiral magnetic effect using charge-dependent azimuthal correlations in pPb and PbPb collisions at the CERN Large Hadron Collider", Phys. Rev. C 97, 044912 (2018).

[27] S. Acharya *et al.* [ALICE Collaboration], "Constraining the Chiral Magnetic Effect with charge-dependent azimuthal correlations in Pb-Pb collisions at $\sqrt{s_{NN}} = 2.76$ and 5.02 TeV" JHEP 09, 160 (2020).

[28] W. T. Deng and X. G. Huang, "Electric fields and chiral magnetic effect in Cu+Au collisions", Phys. Lett. B 742, 296 (2015).

[29] Gang Wang [STAR Collaboration], "Search for Chiral Magnetic Effects in High-Energy Nuclear Collisions", Nucl. Phys A 904, 248c (2013).

[30] S. A. Voloshin, "Testing the Chiral Magnetic Effect with Central U+U Collisions", Phys. Rev. Lett. 105, 172301 (2010).

[31] [L. Adamczyk *et al.* [STAR Collaboration], "Beam-Energy Dependence of Charge Separation along the Magnetic Field in Au+Au Collisions at RHIC", Phys. Rev. Lett. 113 (2014) 052302.

[32] L. Adamczyk *et al.* [STAR Collaboration], "Measurement of charge multiplicity asymmetry correlations in high-energy nucleus-nucleus collisions at $\sqrt{s_{NN}}$ = 200 GeV", Phys. Rev. C 89 (2014) 044908.

[33] D. E. Kharzeev, J. Liao, and S. Shi, "Implications of the isobar run results for chiral magnetic effect in heavy ion collisions", Phys. Rev. C 106, 5 (2022).

[34] S. A. Voloshin, "Testing the Chiral Magnetic Effect with Central U+U collisions", Phys. Rev. Lett. 105, 172301 (2010).

[35] V. Koch *et al.*, "Status of the chiral magnetic effect and collisions of isobars", Chin. Phys. C 41, 0720012106 (2017).

[36] W. Deng *et al.*, "Test the chiral magnetic effect with isobaric collisions", Phys. Rev. C 94, 041901, 2, 110 (2016).

[37] W. T. Deng *et al.*, "Predictions for isobaric collisions at $\sqrt{s_{NN}} = 200$ GeV from a multiphase transport model", Phys. Rev C 97, 044901 (2018).

[38] H. Li *et al.*, "Multiphase transport model predictions of isobaric collisions with nuclear structure from density functional theory", Phys. Rev. C 98, 054907, 2, 125 (2018).

[39] J. Adam *et al.* [STAR Collaboration], "Methods for a blind analysis of isobar data collected by the STAR collaboration", Nucl. Sci. Tech. 32, 48 (2021).

[40] Jagbir Singh, "Search for the Chiral Magnetic Effect using Sliding Dumbbell Method in Isobar Collisions ($^{96}_{44}Ru +^{96}_{44} Ru$ and $^{96}_{40}Zr +^{96}_{40} Zr$) at RHIC", Proceedings of the DAE Symp. Nucl. Phys. 66, 1048, (2012).

[41] Jagbir Singh, Anjali Attri, and Madan M. Aggarwal, "Charge dependent azimuthal correlations using Sliding Dumbbell Method to search CME in Au+Au Collisions with AMPT", Proceedings of the DAE Symp. Nucl. Phys. 64, 830, (2019).

[42] Anjali Attri, Jagbir Singh, Madan M. Aggarwal, "Event-by-Event Charge Separation in Au+Au Collisions at $\sqrt{s_{NN}}$ = 200 GeV Using AMPT", Springer Proc. Phys. 261, 1065 (2021).

[43] M.M. Aggarwal, G. Sood, and Y.P. Viyogi, "Event-by-event study of DCC-like fluctuation in ultra-relativistic nuclear collisions", Phys. Lett. B 638, 39 (2006).

[44] M.M. Aggarwal et al. [WA98 Collaboration], "Event-by-event charged-neutral fluctuations in Pb+Pb collisions at 158 A GeV", Phys. Lett. B 701, 300 (2011).

[45] A. Bilandzic, R. Snellings and S. Voloshin, "Flow analysis with cumulants: direct calculations", Phys. Rev. C 83, 044913 (2011).

[46] N. Borghini, P. M. Dinh and J. Y. Ollitrault, "A new method for measuring azimuthal distributions in nucleus-nucleus collisions", Phys. Rev. C 63, 054906 (2001) [arXiv:nucl-th/0007063].

[47] N. Borghini, P. M. Dinh and J. Y. Ollitrault, "Flow analysis from multiparticle azimuthal correlations", Phys. Rev. C 64 054901 (2001) [arXiv:nucl-th/0105040].

[48] R. Kubo, "Generalized Cumulant Expansion Method*", Journal of the Physical Society of Japan, Vol. 17, No. 7 (1962).

Chapter 4

Testing SDM using event generators: AMPT and AVFD

4.1 Introduction

The Chiral Magnetic Effect (CME) [1–5] has been extensively studied in heavy-ion collisions. In non-central collisions, P-odd meta-stable states are formed, and the strong magnetic field generated by highly energetic spectator protons leads to the separation of oppositely charged particles along the system's angular momentum direction and perpendicular to the reaction plane. The existence of CME relies on the presence of a strong magnetic field from spectator protons and a non-zero axial charge density resulting from high-energy heavy-ion collisions [6,7]. The search for conclusive evidence of the CME signature is a major focus in heavy-ion collision studies. In 2018, the STAR experiment at RHIC performed isobar collisions to validate the formation of CME in heavy-ion collisions, highlighting the significance of this investigation. STAR conducted investigations in Au+Au collisions [8,9] and isobaric collisions [10], ALICE explored Pb-Pb collisions [11,12], and CMS analyzed p-Pb and Pb-Pb collision data [13]. However, despite ongoing research, no definitive evidence for the existence of the Chiral Magnetic Effect (CME) has been reported thus far.

To contribute to the ongoing efforts, the thesis introduces the "Sliding Dumbbell Method" (SDM) as a new approach for detecting localized charge separation. The SDM is specifically designed for this purpose and will be applied to analyze the data from STAR's Au+Au collisions and isobaric collisions. Overall, the thesis aims to advance the understanding of the Chiral Magnetic Effect and provide insights into its existence and significance in heavy-ion collisions, particularly focusing on the experiments conducted by STAR and utilizing the newly developed Sliding Dumbbell Method.

4.2 AMPT

Studies based on perturbative Quantum Chromodynamics (pQCD) [14] have indicated that thermalization can occur in collisions involving very large nuclei and/or at very high energies, despite the asymptotically small value of the strong coupling constant at the saturation scale. However, it is important to note that the dense matter created in heavy-ion collisions at facilities like RHIC (Relativistic Heavy Ion Collider) may not reach full thermal or chemical equilibrium due to limitations in volume and energy. To deal with this kind of non-equilibrium many-body dynamics, A Multi-Phase Transport (AMPT) model [15] has been developed that includes both the initial partonic and final hadronic interactions as well as the transition between these two phases of matter [16, 17]. The AMPT model was developed to describe nuclear collisions from p+A to A+A systems with center-of-mass energies from about $\sqrt{s_{NN}}$ = 5 to 5500 GeV at LHC.

The AMPT model is constructed from four major components: beginning circumstances, partonic interactions, partonic-to-hadronic matter conversion, and hadronic interactions. The HIJING (Heavy Ion Jet INteraction Generator) model is used to determine the initial conditions, which comprise the spatial and momentum distributions of minijet partons and soft string excitations [18–21]. Zhang's Parton Cascade(ZPC) [22] is used to model the scatterings that occur between partons. There are two different versions of AMPT, the Default version, and the String Melting ON version.

Default AMPT: Figure 4.1 (Left) shows the colliding nuclei "A" and "B" with the schematic structures of the default AMPT. The initial conditions for heavy-ion collisions at RHIC are obtained from the HIJING model [18–21]. HIJING is a realistic Monte Carlo (MC) event generator that provides a complete set of created particles at the main vertex. This set includes the produced particles' dynamic properties such as their energy and momentum. It incorporates mechanisms such as soft beamjets and the generation of multiple minijets, as well as a model for jet quenching and a parton structure for the investigation of nuclear shadowing. It is also possible to describe the dependence of the impact parameter on the number of inelastic processes by using the geometry of the nucleus. Following the establishment of the initial state, the minijet partons proceed to Zhang's Parton Cascade (ZPC), where partons are recombined with their parent strings when the interactions among them stops. The AMPT model then uses the Lund string fragmentation model to turn the resulting strings into hadron [15]. The default AMPT effectively described

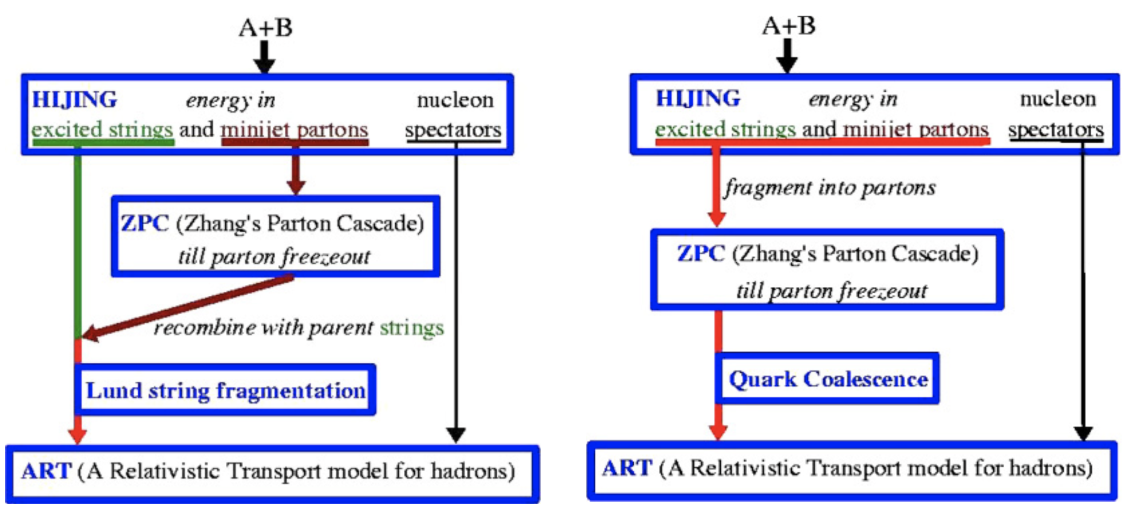

Figure 4.1: (Left) The structure of the Default AMPT. (Right) The structure of the AMPT with String Melting ON [15].

transverse momenta (p_T) of detected particles from the heavy-ion collision at SPS and RHIC while it underestimated the elliptic flow (v_2) at RHIC.

String Melting ON AMPT: In the SM version, all of the excited strings are transformed into partons, and a quark coalescence model is used to combine partons into hadrons as shown in Fig. 4.1 (Right). A hadronic cascade is used to describe the dynamics of the subsequent hadronic matter, which is based on the ART (a relativistic transport model for hadron) model and extended to include additional reaction channels. These channels include the processes of formation and decay of K^* resonance and antibaryon resonances, as well as the production of baryon-antibaryon pairs through meson interactions and their corresponding annihilation reactions. String melting raises parton density, which leads to the overpopulation of partonic matter; on the other hand, quark coalescence enhances the elliptic flow of hadrons. Hence, the string melting AMPT model with a small parton cross-section can successfully depict the elliptic flow in Au+Au collisions at RHIC energies [15]. The string melting version of the AMPT model is capable of accurately characterizing the anisotropic flow and particle correlations in collisions involving both small and large systems when applied to RHIC and LHC energies.

4.2.1 CME-like signal injection in AMPT

AMPT is the most accurate model that can predict the elliptic flow, however, it does not include CME. Hence, in order to analyze the charge separation that is caused by CME, a signal that is similar to CME is injected externally into the events that are generated by AMPT by flipping the charges of the particles in an event. We have generated 16 million AMPT events of Au+Au collisions at a center of mass energy of 200 GeV with the reaction plane angle equal to zero (i.e., Ψ_{RP}=0) while employing the string melting ON configuration. Depending on the signal injection in final state particles, two different sets of AMPTs are made, which are:

- **AMPT:** This is AMPT with string melting ON configuration without any modification i.e., no external CME-like signal.
- **CME:** This sample was produced by randomly inverting the charge of two negatively charged particles into positively charged particles in the ϕ range of 45°-135° and two positively charged particles into negatively charged particles

in the ϕ range of 225°-315°, in an azimuthal plane. This was done perpendicular to the reaction plane (with "$\Psi_{RP} = 0$") in AMPT-generated events. In this manner, a CME-like back-to-back charge separation is injected in the AMPT as expected in the case of the CME, and this sample of events is referred to as the "CME". As the externally injected signal is consistent, however, its percentage varies across different collision centralities, as listed in table 4.1.

Sr. No.	Collision centrality	Percentage of CME-like injected signal
1.	0-5%	~0.4%
2.	5-10%	~0.5%
3.	10-20%	~0.65%
4.	20-30%	~0.95%
5.	30-40%	~1.4%
6.	40-50%	~2.2%
7.	50-60%	~4.0%
8.	60-70%	~6.7%

Table 4.1: The percentage of CME-like injected signal in Au+Au AMPT at $\sqrt{s_{NN}}$ = 200 GeV for various collision centralities.

Two background event samples (i.e., charge shuffled event sample) for "AMPT" and "CME" are also generated. Following are the event samples which are analyzed in a similar way using the Sliding Dumbbell technique.

- AMPT (No CME-like signal injection)
- CME (AMPT with CME-like signal injection)
- Charge shuffled (ChS) background sample obtained using AMPT sample
- Charge shuffled (ChS) background sample obtained using CME sample

4.3 Analysis Details

The charge separation has been measured using a multi-particle correlator for different collision centralities as well as for various charge separations across the dumbbell i.e., f_{DbCS}. Figure 4.2 displays the flow chart describing the various steps involved in the analysis.

- The entire azimuthal plane is scanned in the first stage, and f_{DbCS} distributions are computed for each collision centrality and for each set.

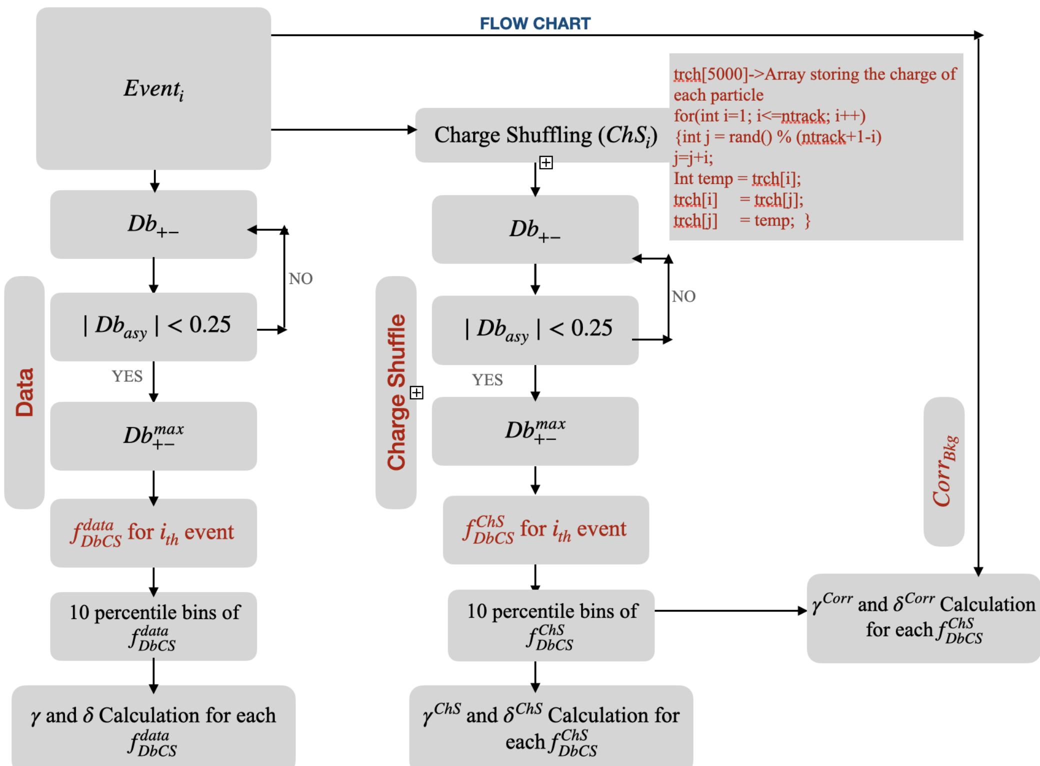

Figure 4.2: A flow chart explaining analysis strategy with data and backgrounds.

- The f_{DbCS} distributions are subdivided into ten percentile bins, ranging from $0-10\%$ (highest charge separation) to $90\%-100\%$ (lowest charge separation) for each collision centrality.

- Afterwards, multi-particle (2-, 3-, and 4-particle) correlators are calculated for each f_{DbCS} bin in each centrality for AMPT, CME, ChS and Correlated background.

- $\Delta\gamma$ $(= \gamma_{OS} - \gamma_{SS})$, $\Delta\delta$, and v_2 are computed for all f_{DbCS} bins in each collision centrality.

- Finally calculate f_{CME} for all collision centralities and for all samples (i.e., AMPT and CME).

The flow chart shows three different samples Data (AMPT/CME), Charge Shuffle (ChS), and Correlated Background (Corr) independently.

4.3.1 Background Estimation

Charge Shuffle background (ChS): It refers to the contribution from random combinations of charges, where the charges of particles are shuffled randomly while keeping their momenta (i.e., θ and ϕ) unchanged. This background estimation helps in understanding the level of charge correlations that can occur purely by chance. The value of γ for the "ChS" events' sample is determined for a specific bin of f_{DbCS} and is referred to as γ_{ChS}.

Correlated background (Corr): This on the other hand, accounts for correlations arising from non-CME effects, such as collective flow or resonance decays. It represents the background signal that is not related to the Chiral Magnetic Effect but can manifest as charge correlations. This is recovered from the corresponding original events in a particular f_{DbCS} bin and termed as correlated background γ_{Corr}.

Thus, the total background contribution to the γ-correlator is given by:

$$\gamma_{TotalBkg} = \gamma_{ChS} + \gamma_{Corr} \tag{4.1}$$

4.4 Error estimation in AMPT

To obtain an estimation of the statistical errors, we employ the "Sub-Sampling" method. This technique involves dividing the entire dataset into "n" samples, each containing an equal number of events. Subsequently, the desired observable "x" is calculated for each sub-sample. The standard deviation (SD) for the overall sample is computed using the following formula:

$$\sigma(SD) = \sqrt{\frac{\sum (x_i - \langle x \rangle)^2}{n-1}} \tag{4.2}$$

where x_n is the value of observable "x" that was calculated for the "i^{th}" sub sample, and $\langle x \rangle$ is the average value of observable "x" for overall sample as given below;

$$\langle x \rangle = \frac{1}{n} \sum_{i=1}^{n} x_i \tag{4.3}$$

Thus, using Eq. 4.2 and Eq. 4.3, one can calculate the final statistical error on the mean value of "x" as follows;

$$\sigma_{\langle x \rangle} = \frac{\sigma(SD)}{\sqrt{n}} \tag{4.4}$$

In order to estimate the statistical errors for the simulations conducted with AMPT, we divided the data sets (AMPT, CME, and ChS) into 10 sub-samples. Each sub-sample was carefully constructed to contain an approximately equal number of events to get the statistical error estimation. In our analysis, we utilized 1σ errors

4.5 Simulation results from AMPT

We generated 16M AMPT events for Au+Au collisions with String Melting ON configuration at the center of mass energy of 200 GeV. Also, CME and ChS samples are obtained by flipping the charges of positive/negative and by shuffling the charges of particles as discussed previously. Depending on the total number of participating nucleons that took part in the collision, these events are categorized into a variety of collision centralities (i.e., 0-5% for the most central events, 5-10% for the next most central, and, 90-100% for the most peripheral events). Experimental track cuts [23,24] were applied i.e., $0.15 < p_T < 2.0$ GeV/c and $|\eta| < 1.0$ having complete azimuthal coverage. The results on 2-particle and 3-particle correlators, as well as their differences, in Au+Au collisions at 200 GeV/nucleon categorized by collision centrality, are discussed in this section.

4.5.1 2-particle (δ) correlator

The Fig. 4.3 illustrates the centrality dependence of the 2-particle $\delta-$correlator ($\delta = \langle \cos(\phi_i - \phi_j) \rangle$) for different charge combinations (same sign (+ +,- -) and opposite sign (+ -,- +))for AMPT, CME, and charge shuffle samples. The correlation values for the default AMPT and charge shuffle samples are relatively low as compared to the CME sample. Only the charge-shuffled points from the CME sample are displayed in the figure as charge-shuffled points obtained from the AMPT sample coincide within the errors. For event sample "CME", stronger correlations are

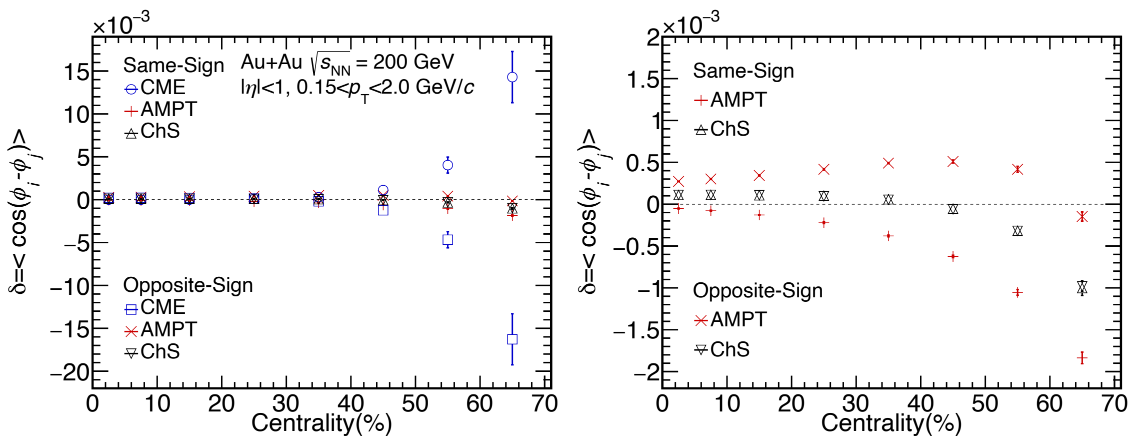

Figure 4.3: (Left) Centrality dependence of 2-particle δ correlator for same and opposite sign charge pairs for AMPT, CME, and charge shuffle (ChS) samples. (Right) A magnified figure for AMPT and ChS.

observed for different charge pairs, the same sign correlations are positive whereas the opposite sign correlations are negative. The amplitude of correlations increases with decreasing centrality, and this holds true for correlations comprising charge pairs with the same as well as opposing signs. AMPT (with no CME signal) shows weaker correlations for both same-sign (SS) and opposite-sign (OS), here SS charge pairs are negative and OS charge pairs are positive. Correlations values for SS and OS charge pairs are approximately zero for the Charge Shuffle (ChS for CME) sample. In Fig. 4.3 (b) magnified scale is shown for AMPT and ChS and, for "ChS" SS and OS charge pairs show similar correlations while AMPT shows very little difference.

4.5.2 3-particle (γ) correlator

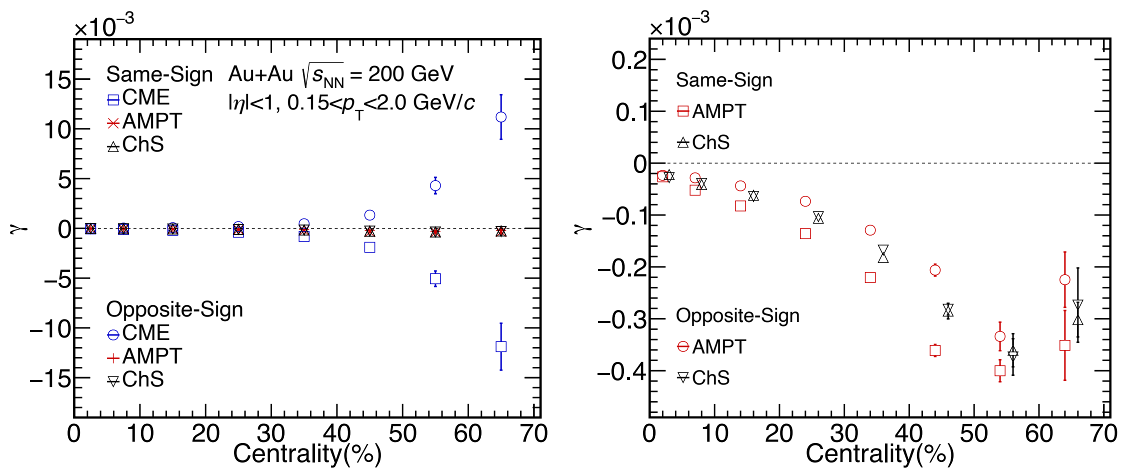

Figure 4.4: (Left) Centrality dependence of γ correlator for same and opposite sign charge pairs for AMPT, CME, and charge shuffle (ChS) samples. (Right) A magnified figure for AMPT and ChS.

Figure 4.4 presents measurements of the centrality dependence of the three particle $\gamma-$correlator ($\gamma = \langle\cos(\phi_i + \phi_j - 2\phi_c)\rangle/v_2$) for various charge combinations i.e., SS (+ +, - -), and OS (+ -, - +) charge pairs. The $\gamma-$correlator for SS charge pairs is negative and exhibits larger correlations while OS charge pairs correlations are positive in the case of the CME sample. In addition to this, the strength of correlations increases as the percentage of injected signal increases. The correlation value decreases with increasing collision centrality i.e., for most central events the correlations are weaker. Small negative values for the AMPT are observed for both OS and SS. ChS also shows negative correlations for both SS and OS and they both agree within uncertainties for all collision centralities as shown in Fig. 4.4 (Right).

4.5.2.1 $\Delta\gamma$ correlator

It can be observed from Fig. 4.5 that the magnitude of $\Delta\gamma$ increases as the percentage of CME-like signal increases, indicating that the $\Delta\gamma$ correlator has a substantial dependence on the percentage of injected signal and is maximum for 60-70% collision centrality ($\sim$6.7% externally injected signal). For the AMPT events, $\Delta\gamma$ is very small ($\sim$close to zero) for all collision centralities because there is no CME in AMPT, whereas $\Delta\gamma$ for ChS event sample is consistently zero within errors for all collision centralities (Fig. 4.5 (b)).

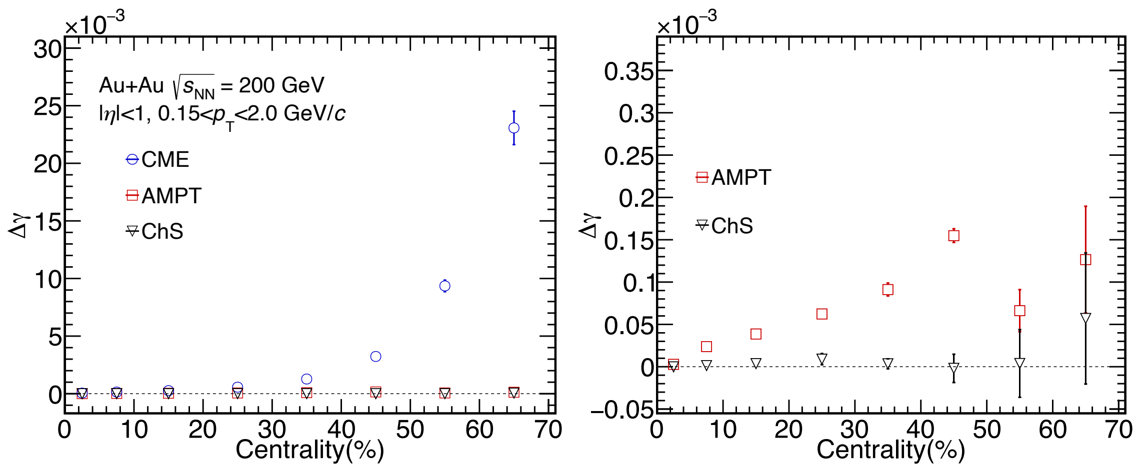

Figure 4.5: (Left) Centrality dependence of $\Delta\gamma$ correlator for AMPT, CME, and charge shuffle (ChS) samples. (Right) Similar to figure (Left) but for AMPT and ChS only with a magnified scale.

4.5.3 Elliptic Flow (v_2)

Since we used the Q-cumulants to get the 3-particle $\gamma-$correlator, Fig. 4.6 displays the centrality dependence of the elliptic flow for AMPT. It is seen that the elliptic flow increases with decreasing collision centrality and reaches a maximum value for 30-50% collision centrality. Also, elliptic flow from 2-particle ($v_2\{2\}$) calculations is higher than the elliptic flow from 4-particle ($v_2\{4\}$) calculations. We have taken the mean of ($v_2\{2\}$) and ($v_2\{4\}$) for our analysis.

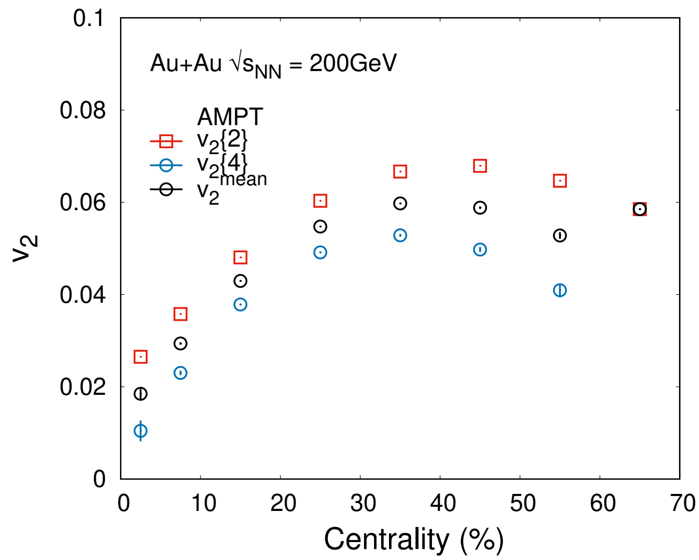

Figure 4.6: Comparing centrality dependence of elliptic flow ($v_2\{2\}$ and ($v_2\{4\}$) for AMPT using cumulant method.

4.5.3.1 In-plane and out-of-plane correlations

The in-plane ($\sim \langle\cos(\Delta\phi_i)\cos(\Delta\phi_j)\rangle$) and out-of-plane ($\sim \langle\sin(\Delta\phi_i)\sin(\Delta\phi_j)\rangle$) correlations can be obtained from δ and γ correlators as given below:

$$\gamma = \langle cos(\phi_i + \phi_j - 2\Psi_{RP})\rangle = \langle cos(\Delta\phi_i)cos(\Delta\phi_j)\rangle - \langle sin(\Delta\phi_i)sin(\Delta\phi_j)\rangle \quad (4.5)$$

$$\delta = \langle cos(\phi_i - \phi_j)\rangle = \langle cos(\Delta\phi_i)cos(\Delta\phi_j)\rangle + \langle sin(\Delta\phi_i)sin(\Delta\phi_j)\rangle \quad (4.6)$$

where, $\Delta\phi_{i(j)} = \phi_{i(j)} - \Psi_{RP}$. The out-of-plane correlations are sensitive to the CME [25]. The out-of-plane correlations for the same-sign (opposite-sign) charge pairs are stronger than the in-plane correlations for the CME event sample as displayed in Fig. 4.7. The out-of-plane correlations increase with the increase in the externally injected signal. For AMPT (without CME signal) and ChS event samples, the in-plane and out-of-plane correlations are very low and are approximately equal within errors.

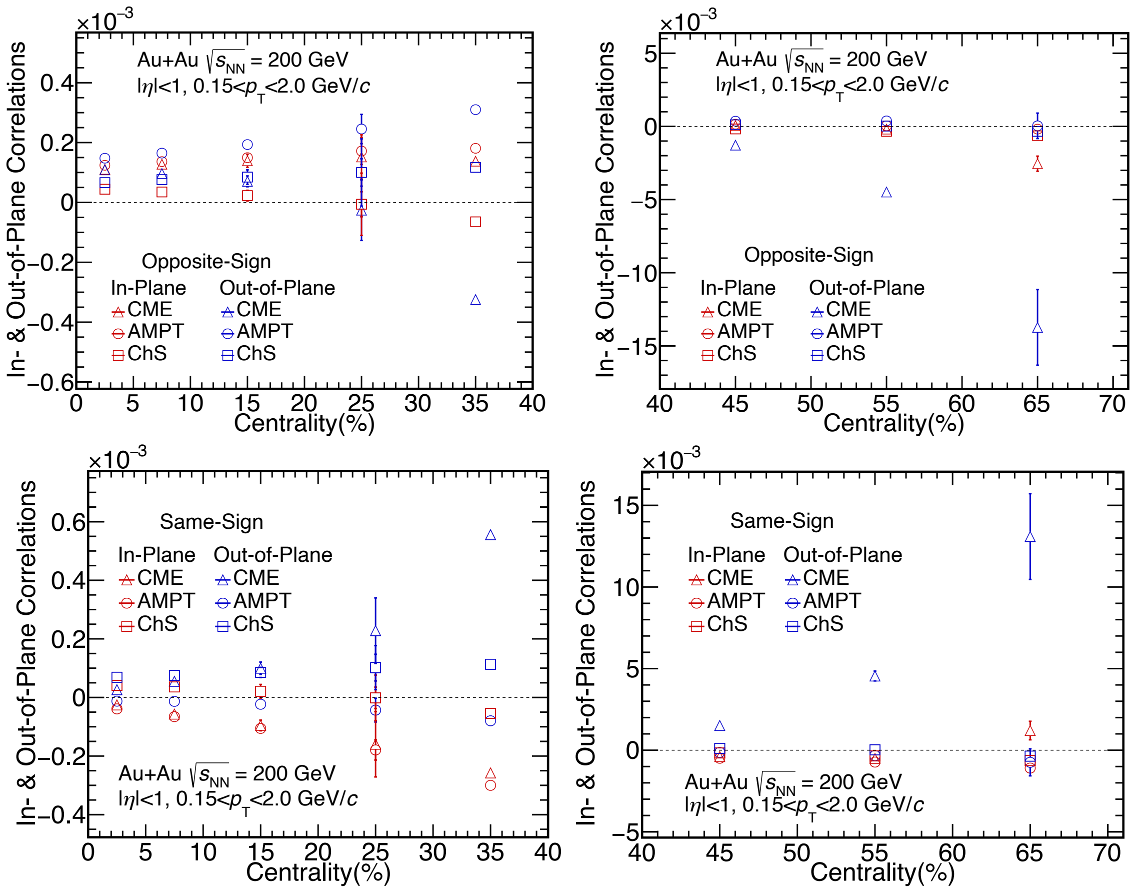

Figure 4.7: The variation of in-plane and out-of-plane correlations with collision centralities for opposite-sign (Top Panels) and same-sign (Bottom Panels) charge combinations for AMPT, CME, and charge shuffle (ChS) samples.

4.6 Results using Sliding Dumbbell Method

The following section presents the results based on the fractional charge separation (f_{DbCS}) obtained using the SDM. These results shed light on the magnitude and centrality dependence of the charge separation effect across the dumbbell in heavy-ion collisions. They provide valuable insights into the nature of charge dynamics and possible indications of the Chiral Magnetic Effect in the studied collision system. By analyzing f_{DbCS}, the thesis aims to characterize and quantify the charge separation across the dumbbell, further contributing to the understanding of the collective behavior and charge dynamics in heavy-ion collisions.

4.6.1 f_{DbCS} distributions

The f_{DbCS} distributions for CME, AMPT, and ChS are compared for different collision centralities in Fig. 4.8. These distributions are indistinguishable for higher collision centralities (i.e., 0-5%, 5-10%, etc.) due to the low percentage of the injected CME-like signal. The distribution move towards a higher value of f_{DbCS} with decreasing collision centrality i.e., f_{DbCS} approaches to 1. The distributions became distinguishable and moved closer to 1 with an increase in the externally injected CME-like signal. The AMPT and charge shuffle both show distributions that are very similar to one another for all collision centralities. It has been observed that f_{DbCS} distributions for an externally injected CME-like signal extend to higher f_{DbCS} values than those of AMPT and charge shuffled (ChS) samples.

These distributions are now divided into 10 percentile bins, beginning from the right. In the top bin (0-10%), f_{DbCS} has the maximum charge separation and contains the potential CME-like events. On the other hand, the bin with a f_{DbCS} of 90-100% contains the lowest charge separation and contains events which are normal. Figure 4.9 displays the scatter plots for f_{DbCS}^{CME} versus f_{DbCS}^{ChS} for 30-40% and 50-60% collision centralities with a vertical red line corresponding to the top 10% f_{DbCS}^{ChS} on the right side of the line. Figure 4.9 shows that there is no correlation

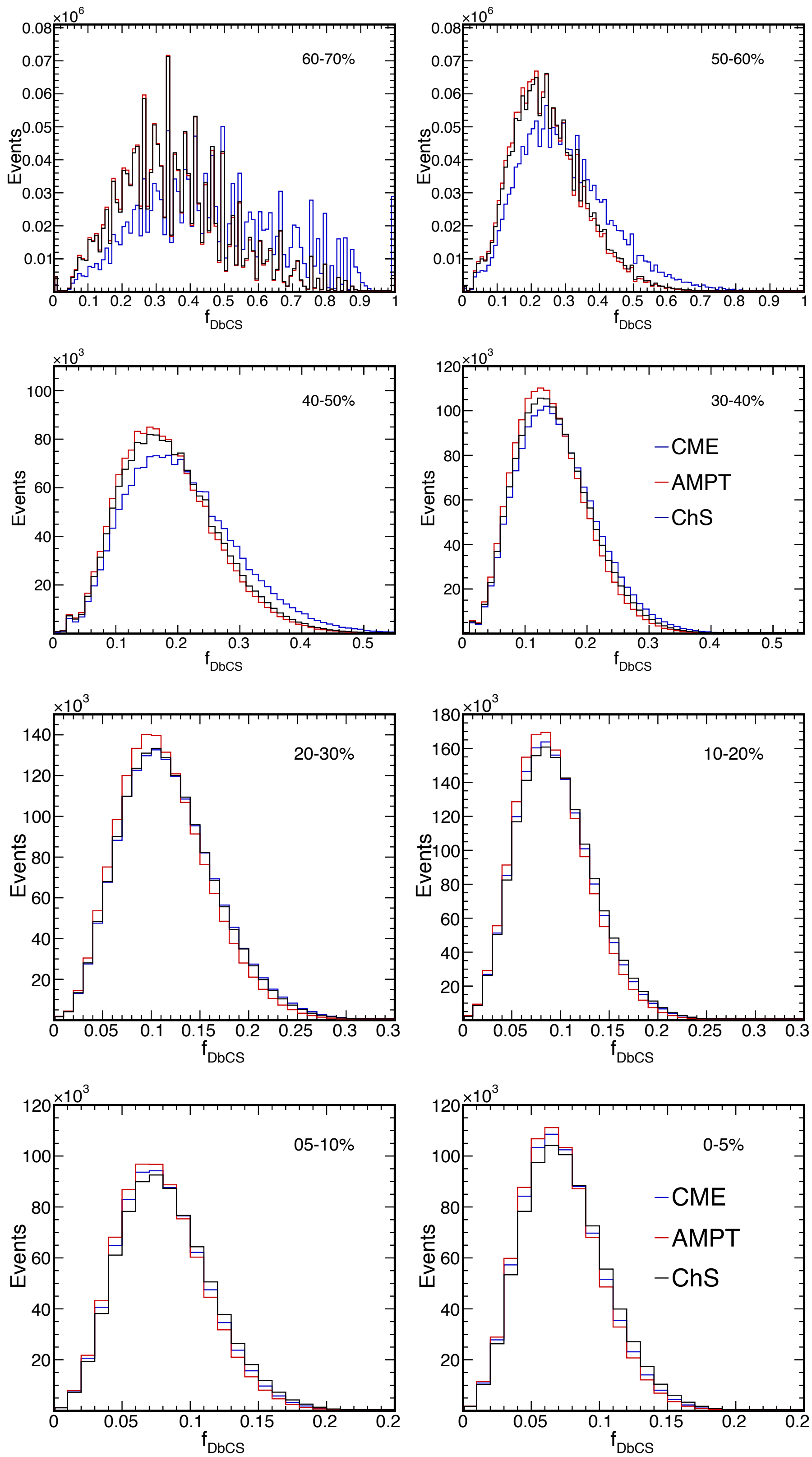

Figure 4.8: Comparison of f_{DbCS} distributions for CME, AMPT, and ChS for 0-70% collision centralities.

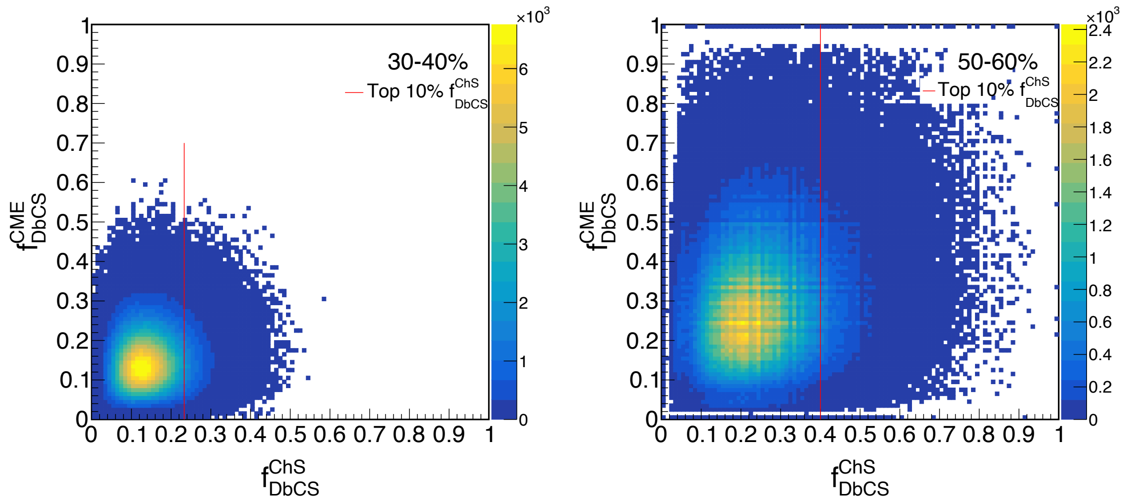

Figure 4.9: The scatter plot f^{CME}_{DbCS} versus f^{ChS}_{DbCS} for 30-40% and 50-60% collision centrality.

between the f^{ChS}_{DbCS} of the charge shuffled event and the f^{CME}_{DbCS} of the CME event. Also, it is noticed that charge shuffled events corresponding to the top 10% f^{ChS}_{DbCS} are spread over 0-100% f^{CME}_{DbCS}.

4.6.2 δ correlator

Figure 4.10 displays the δ-correlator plots for different f_{DbCS} bins within each collision centrality, showing both opposite and same sign charge pairs. It is evident that the δ values are significantly higher in the top f_{DbCS} bins compared to the average value within a given centrality (refer to Fig. 4.3). The top f_{DbCS} bins display negative correlations for opposite sign (i.e., negative for δ (OS)) charge pairs, whereas for same sign charge pairs these bins exhibit positive correlations (i.e., positive for δ (SS)). The magnitude of δ(OS & SS) gets stronger as the percentage of the CME-like signal increases.

4.6.3 Elliptic Flow (v_2)

The charge separation (f_{DbCS}) dependence of mean elliptic flow ($v_2 = \frac{v_2\{2\}+v_2\{4\}}{2}$) for AMPT and CME (externally injected CME-like signal) samples are shown in

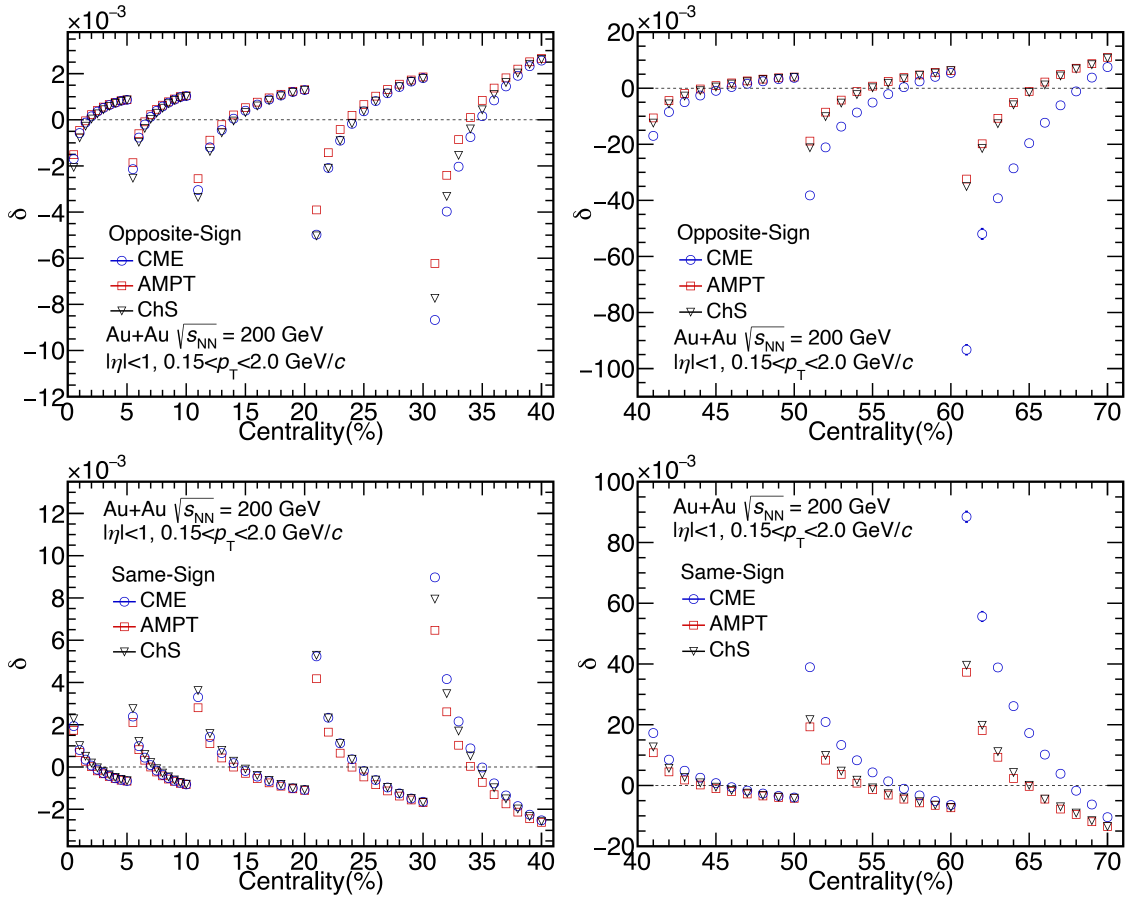

Figure 4.10: The dependence of δ correlator on the charge separation (f_{DbCS}) for OS (top panel) and SS (bottom panel) charge pairs for different collision centralities for CME (externally injected CME-like signal), AMPT, charge shuffled (ChS) event samples. The left panels are for 0-40% collision centralities (with zoomed y-axis) for the sake of clarity and the right panels are for 40-70% collision centralities.

Fig. 4.11 (Left: 0-40% collision centrality and Right: 40-70% collision centrality). It is seen that the elliptic flow increases in the top f_{DbCS} bins while decreasing with the decrease in f_{DbCS} values. Also, it is to be noticed that v_2 $(= \frac{v_2\{2\}+v_2\{4\}}{2})$ is higher for the CME sample in the top f_{DbCS} bins than that of AMPT sample for all collision centralities.

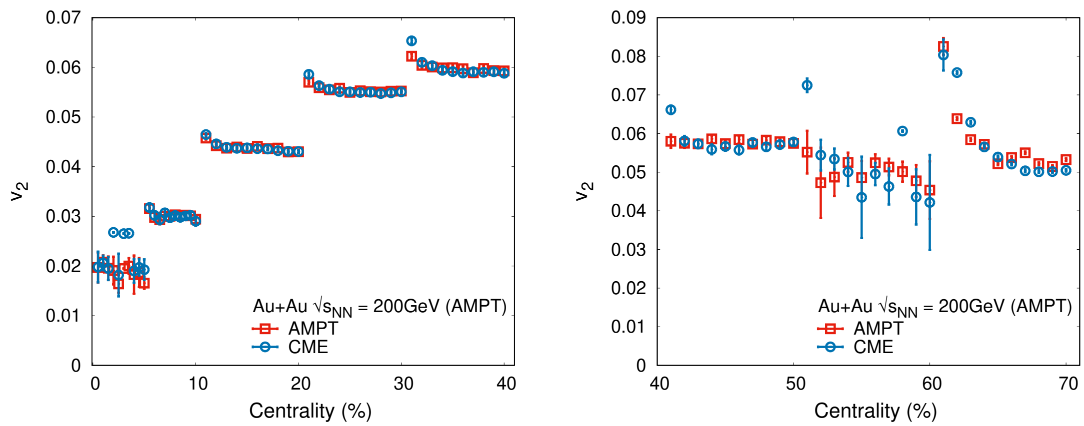

Figure 4.11: The charge separation (f_{DbCS}) dependence of elliptic flow (v_2) for AMPT and CME samples for different collision centralities.

4.6.4 γ correlator

Figure 4.12 presents the γ-correlator for opposite sign (Top) and same sign (Bottom) charge pairs with centrality for 10 percentile bins of f_{DbCS} distribution for CME, AMPT, Charge Shuffle (ChS) and Correlated backgrounds (i.e., $Corr_{CME}$ and $Corr_{AMPT}$). The magnitude of γ enhances many times for both SS and OS charge pairs for the top f_{DbCS} bins as compared to that of the average value for a given collision centrality as shown in Fig. 4.4. It is seen that the opposite sign charge pairs are weakly correlated having positive γ whereas the same sign charge pairs are strongly correlated having negative γ for top f_{DbCS} bins. The correlations increase with an increase in the percentage of externally injected CME-like signal and decrease with an increase in collision centrality. The γ-correlator decreases with deceasing f_{DbCS} values. The highest value of γ-correlator for SS and OS charge pairs are in the top 10% f_{DbCS} bin. The correlations for both OS and SS charge pairs de-

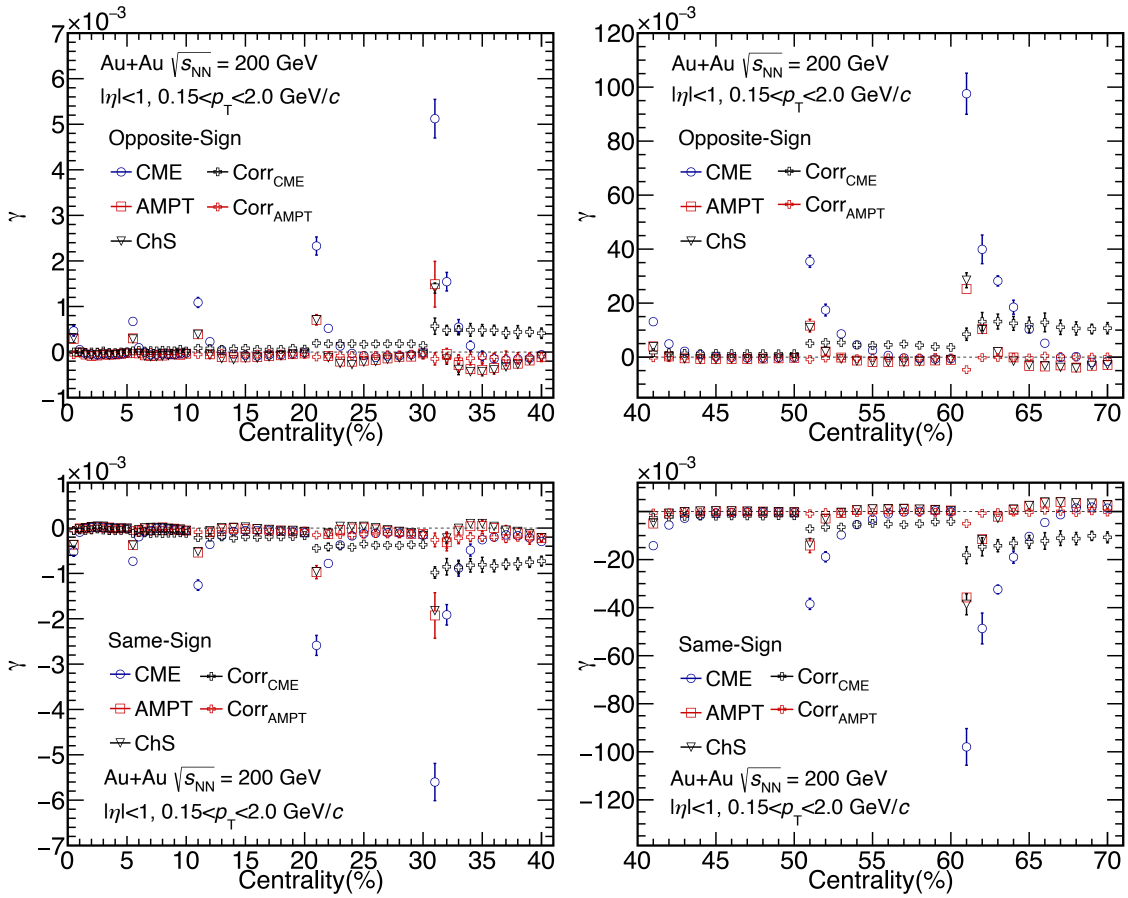

Figure 4.12: The charge separation (f_{DbCS}) dependence of γ-correlator for opposite sign (Top panel) and same sign (Bottom panel) for CME (externally injected CME-like signal), AMPT, charge shuffled (ChS) event samples for different collision centralities. The left panels are for 0-40% collision centralities (with magnified y-axis) and the right panels are for 40-70% collision centralities.

crease with decreasing f_{DbCS} values and become approximately zero for lower f_{DbCS} values. For instance, SS is negative while OS is positive for the top f_{DbCS} (i.e., say 0-30% f_{DbCS} or 0-40% f_{DbCS}) bins, which indicates the increased back-to-back charge separation in these events. On the other hand for the remaining f_{DbCS} bins (say 40-100% f_{DbCS}), signs of OS/SS correlation changes, resulting in the normal trend (i.e., normal events lying in the lower f_{DbCS} bins). The AMPT and charge shuffle background (ChS) match with each other within errors for different f_{DbCS} bins in each collision centrality. The correlated backgrounds (Corr) are independent of f_{DbCS} bins and exhibit a constant value (within uncertainties) for all the f_{DbCS} bins within each collision centrality.

4.6.5 In- and out-of-plane correlations

We have also computed in-plane and out-of-plane correlations for SS and OS charge pairs for different f_{DbCS} bins as well as for different collision centralities as shown in Fig. 4.13. From the figure, it is clear that the out-of-plane (i.e., $\sim \langle \sin(\Delta\phi_i)\sin(\Delta\phi_j)\rangle\rangle$) correlations are stronger than those in-plane (i.e., $\sim \langle \cos(\Delta\phi_i)\cos(\Delta\phi_j)\rangle\rangle$) correlations for SS and OS charge pairs in the top f_{DbCS} bins within each collision centrality. However, the in-plane correlations are weaker in the top f_{DbCS}. The correlations also increase with the increase in the injected CME signal as shown in the figure.

4.6.6 $\Delta\gamma$ correlator

Figure 4.14 presents the $\Delta\gamma$ as a function of f_{DbCS} for different collision centralities for CME, AMPT, ChS, and correlated backgrounds. It has been observed that the data points for charge shuffle and default AMPT agree within the statistical errors for different f_{DbCS} bins, however, the data points that corresponds to the CME sample have higher correlation values. $\Delta\gamma$ for the correlated background (Corr) are independent of f_{DbCS} bins and have a constant value (within uncertainties) for all the f_{DbCS} bins within each collision centrality. It increases with a decrease in collision

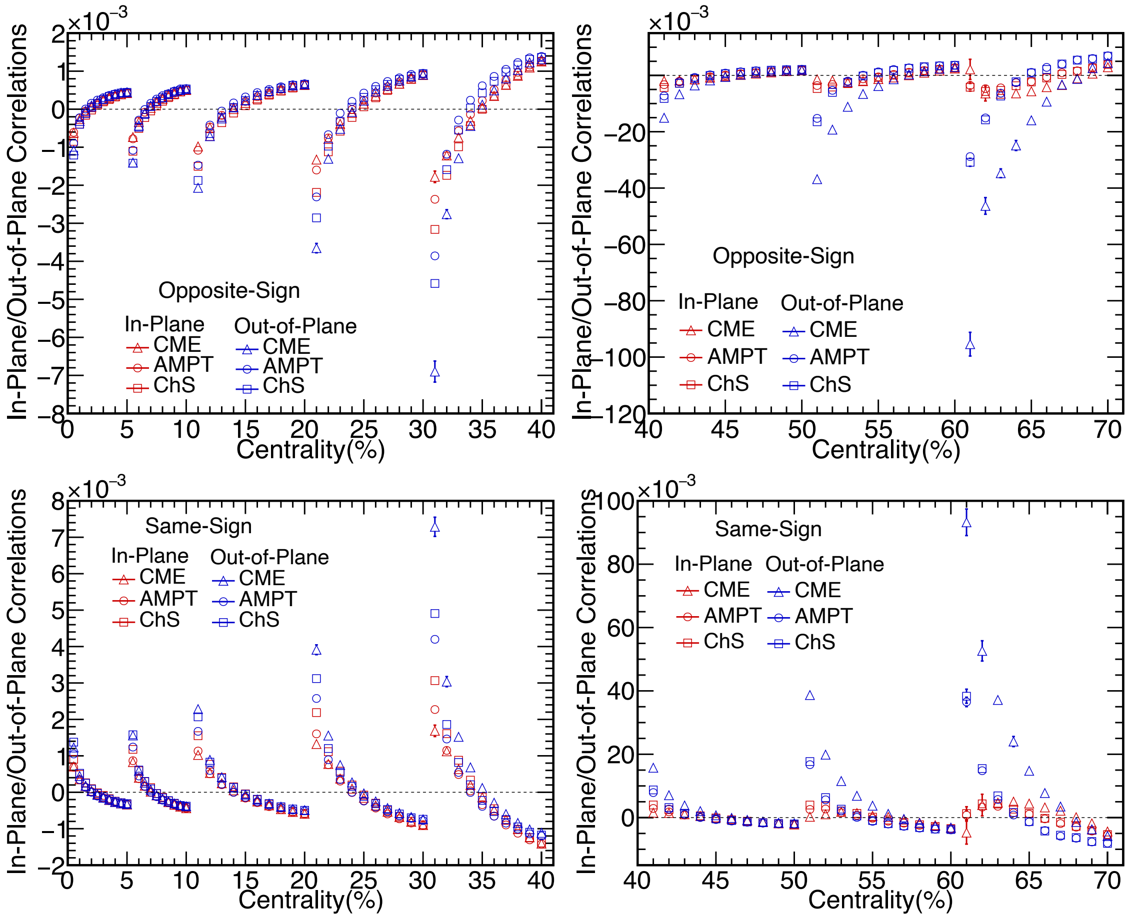

Figure 4.13: Decomposition of the γ and δ correlators into in-plane (red symbols) and out-of-plane (blue symbols) correlations for the opposite-sign (Top panel) and the same-sign (Bottom Panel) charge pairs. The left panels are for 0-40% collision centralities (with zoomed y-axis) and the right panels are for 40-70% collision centralities for the sake of clarity.

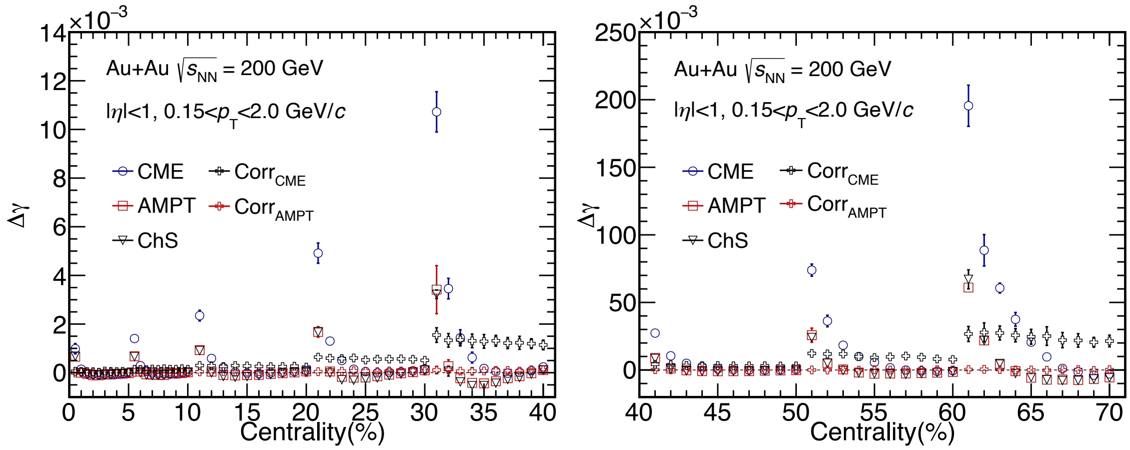

Figure 4.14: The dependence of $\Delta\gamma$ on the charge separation (f_{DbCS}) for different collision centralities for CME (externally injected CME-like signal), AMPT, charge shuffled (ChS) along with corresponding correlated backgrounds for the CME ($Corr_{CME}$) and AMPT ($Corr_{AMPT}$). The figure is splitted into 0-40% (Left) and 40-70% (Right) collision centralities for the sake of clarity.

centrality and increases with an increase in the CME signal. In addition to this, it can be seen that the values for the CME have higher values than the combined values of Charge Shuffle (ChS) and Correlated background ($Corr_{CME/AMPT}$) for the top f_{DbCS} bins. The variation of $\Delta\gamma$ (for f_{DbCS} bins) normalized to the average value

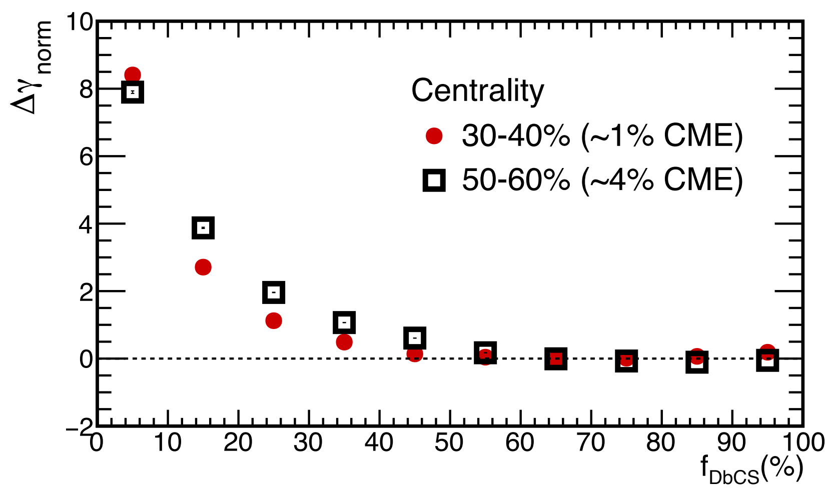

Figure 4.15: $\Delta\gamma_{Norm}$ versus f_{DbCS} for the 30-40% and 50-60% collision centralities.

($\Delta\gamma_{average}$) for a given collision centrality (i.e., $\Delta\gamma_{Norm} = \Delta\gamma_{top10\%}/\Delta\gamma_{average}$) versus charge separation (f_{DbCS}) is displayed in Fig. 4.15. This figure is shown only for two collision centralities i.e., 30-40% (with $\sim$ 1% CME signal injected) and 50-60%

(with $\sim$ 4% CME signal injected). It is seen that for the top 10% f_{DbCS} the $\Delta\gamma_{Norm}$ is $\sim$8 and it decreases rapidly with decreasing externally injected CME signal and $\Delta\gamma_{Norm}$ approaches zero for 90-100% f_{DbCS}. A similar type of enhancement in γ and $\Delta\gamma$ can be seen for AMPT and charge shuffled samples in Fig. 4.12 and Fig. 4.14.

4.6.6.1 CME fraction (f_{CME})

f_{DbCS}	CME				
	50-60% Centrality (∼4% CME)	40-50% Centrality (∼2% CME)	30-40% Centrality (∼1.4% CME)	20-30% Centrality (∼0.9% CME)	10-20% Centrality (∼0.65% CME)
0-10%	0.508±0.079	0.53±0.046	0.555±0.094	0.53±0.0553	0.487±0.070
10-20%	0.533±0.146	0.56±0.085	0.615±0.175	0.54±0.115	0.51±0.15
20-30%	0.354±0.155	0.319±0.154	0.061±0.304	-	-
30-40%	0.010±0.246	-	-	-	-

Table 4.2: The f_{CME} values for different f_{DbCS} bins for 10-60% centralities for the CME sample (i.e., CME signal injected).

Table 4.2 and 4.3 list the fraction of CME contributions for the top f_{DbCS} bins for default AMPT and CME samples. The f_{CME} is calculated for each bin of the f_{DbCS} using Eq. 4.7.

f_{DbCS}	AMPT				
	50-60% Centrality (No CME)	40-50% Centrality (No CME)	30-40% Centrality (No CME)	20-30% Centrality (No CME)	10-20% Centrality (No CME)
0-10%	0.01±0.124	0.003±0.087	0.045±0.081	0.0185±0.045	0.0027±0.06
10-20%	0.07±0.238	-	-	-	-

Table 4.3: The f_{CME} values for different f_{DbCS} bins with for 10-60% centralities for AMPT sample i.e., No CME.

$$f_{CME} = 1 - \frac{\Delta\gamma_{Bkg}}{\Delta\gamma_{AMPT/CME}}$$
$$\Delta\gamma_{Bkg} = \Delta\gamma_{ChS} + \Delta\gamma_{Corr} \tag{4.7}$$

It is observed that fraction is significant in the top f_{DbCS} bins and the number of f_{DbCS} bins exhibiting such a trend decreases with the decreasing percentage of externally injected CME-like signal. However, f_{CME} derived from the default AMPT with no externally injected CME-like signal is essentially zero within statistical errors. In view of these, it is important to point out that in order to verify the presence of the CME in heavy-ion collisions, one needs to investigate the top f_{DbCS} bins which have the largest back-to-back charge separation for a certain collision centrality.

4.7 Anomalous-Viscous Fluid Dynamics (AVFD)

The main challenge in the quest for the Chiral Magnetic Effect (CME) in heavy-ion collisions is effectively distinguishing between the background and the signal of interest. To accurately predict the effects of CME in realistic heavy-ion collision scenarios, it is crucial to develop state-of-the-art modeling tools. In this section, the Anomalous Viscous Fluid Dynamics (AVFD) framework is introduced, which simulates the evolution of chiral fermion currents in the Quark-Gluon Plasma (QGP) on top of the VISHNU bulk hydrodynamic evolution for heavy-ion collisions.

The AVFD model utilizes anomalous fluid dynamics to describe the development of fermion currents in the QGP formed as a result of relativistic heavy-ion collisions [26, 27]. The VISH2+1 hydrodynamics provides a description of the underlying evolution of the bulk medium [28]. The AVFD model combines normal viscous hydrodynamics with anomalous fluid dynamics within a unified framework. It takes into account parameters such as initial conditions, magnetic field, and viscous transport coefficients, allowing for an interplay between the evolution of the axial charge current and the bulk medium. In the simulation, the EBE-avfd Beta1.0 version of the AVFD model is employed, which incorporates event-wise fluctuations in the initial conditions. These events were generated with different CME signals by Yufu Lin, and the simulated events were directly analyzed.

The axial charge plays a crucial role in the formation of the chiral magnetic effect (CME) current, which leads to the observed separation of charges. The resulting charge separation signal is highly sensitive to the initial state of the axial

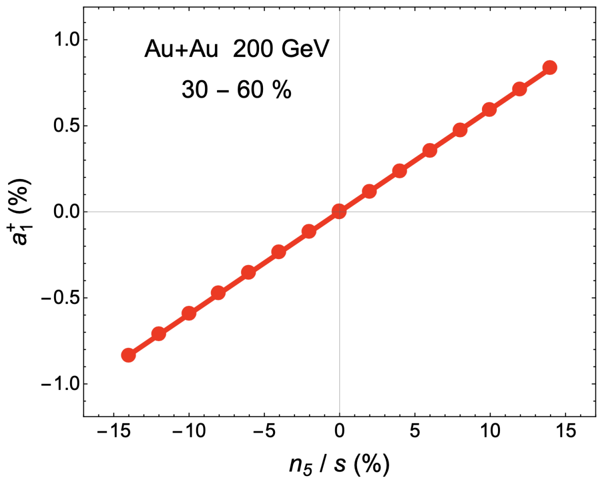

Figure 4.16: Charge separation a_1 versus the axial charge per entropy density n_5/s.

charge. The axial charge density, although small compared to the entropy density, has a linear relationship with the axial chemical potential. This implies that the current density (J_μ) is proportional to the product of the axial chemical potential (μ_5) and the external magnetic field (B_μ), denoted as $J_\mu = CA\mu_5 B_\mu \propto n_5$. Therefore, the final charge separation signal in CME is roughly linearly dependent on the initial amount of axial charge (Fig. 4.16) [29,30].

The AVFD framework controls the CME signal through the axial charge per entropy density (n_5/s), which determines the imbalance between right-handed and left-handed fermions induced at the beginning stage of each event. The value of n_5/s, such as 0.0 (0%), 0.1 (10%), and 0.2 (20%), is used as input to the AVFD. The percentage of local charge conservation (LCC) within an event is a crucial parameter that determines the background. LCC refers to the proportion of positively and negatively charged partners emitted from the same fluid element compared to the overall multiplicity of the event. By considering these factors and analyzing the simulated events using the AVFD framework, this study aims to understand the interplay between the axial charge current and the bulk medium in heavy-ion collisions and investigate the signatures of the Chiral Magnetic Effect (CME). We have analyzed three different data sets for AVFD i.e., Au+Au, Ru+Ru, and Zr+Zr at 200 GeV each comprising three different samples according to different CME signal

AVFD LCC 33%	Au+Au	Ru+Ru	Zr+Zr
n_5/s=0.0	∼95 M	∼58 M	∼48 M
n_5/s=0.1	∼58 M	∼49 M	∼71 M
n_5/s=0.2	∼77 M	∼50 M	∼56 M

Table 4.4: List of number of events for Au+Au, Ru+Ru and Zr+Zr collisions at $\sqrt{s_{NN}} = 200$ GeV for various n_5/s for AVFD generated data sets for 30-40% collision centrality.

injections. The different samples for each data set for 30-40% collision centrality are listed in table 4.4. These data sets have 33% LCC in all the samples.

4.7.1 Three-particle correlator

We have calculated the 3-particle γ correlator for AVFD simulated datasets using the Q-cumulants similar to AMPT simulations. Figure 4.17 (Left) shows γ correlator for opposite and same sign charge pairs for Au+Au and Isobar (Ru+Ru and Zr+Zr) collisions with different axial charge per entropy density (i.e., n_5/s =0.0, 0.1, and 0.2) and having 33% LCC. It is seen that γ is negative for the SS charge pairs while

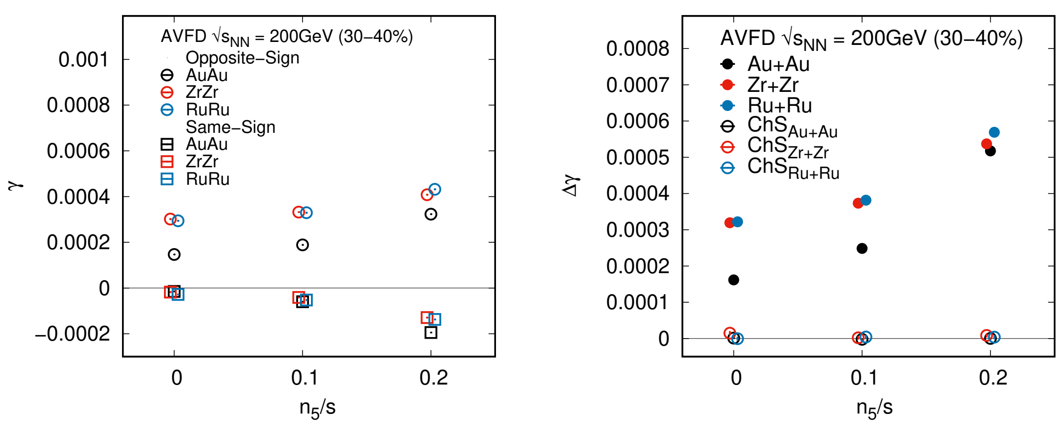

Figure 4.17: γ (Left) and $\Delta\gamma$ (Right) calculated for AVFD generated events for 30-40% collision centrality for Au+Au, Ru+Ru and Zr+Zr collisions at $\sqrt{s_{NN}} =$ 200 GeV as a function of the axial charge per entropy density n_5/s. The points are shifted for Ru+Ru and Zr+Zr for the sake of clarity.

for the OS charge pairs it is positive. The magnitude of the γ increases with an increase in the axial charge per entropy density n_5/s from 0.0 to 0.2. It is also noted that the γ is similar within error for the two isobar (Ru+Ru and Zr+Zr) collisions for both SS and OS charge pairs.

$\Delta\gamma$ correlator is shown in Fig. 4.17 (Right) for three AVFD generated data sets. It is seen that the $\Delta\gamma$ increases with increasing CME signal in AVFD and has the highest value at n_5/s $=$ 0.2 for 30-40% collision centrality. The charge shuffle background is similar for the three different samples (i.e., n_5/s $=$ 0.0, 0.1, and 0.2) of each AVFD dataset (i.e., Au+Au and isobar). The statistical uncertainties are very low and within the markers.

4.7.2 Results for AVFD simulated events using SDM

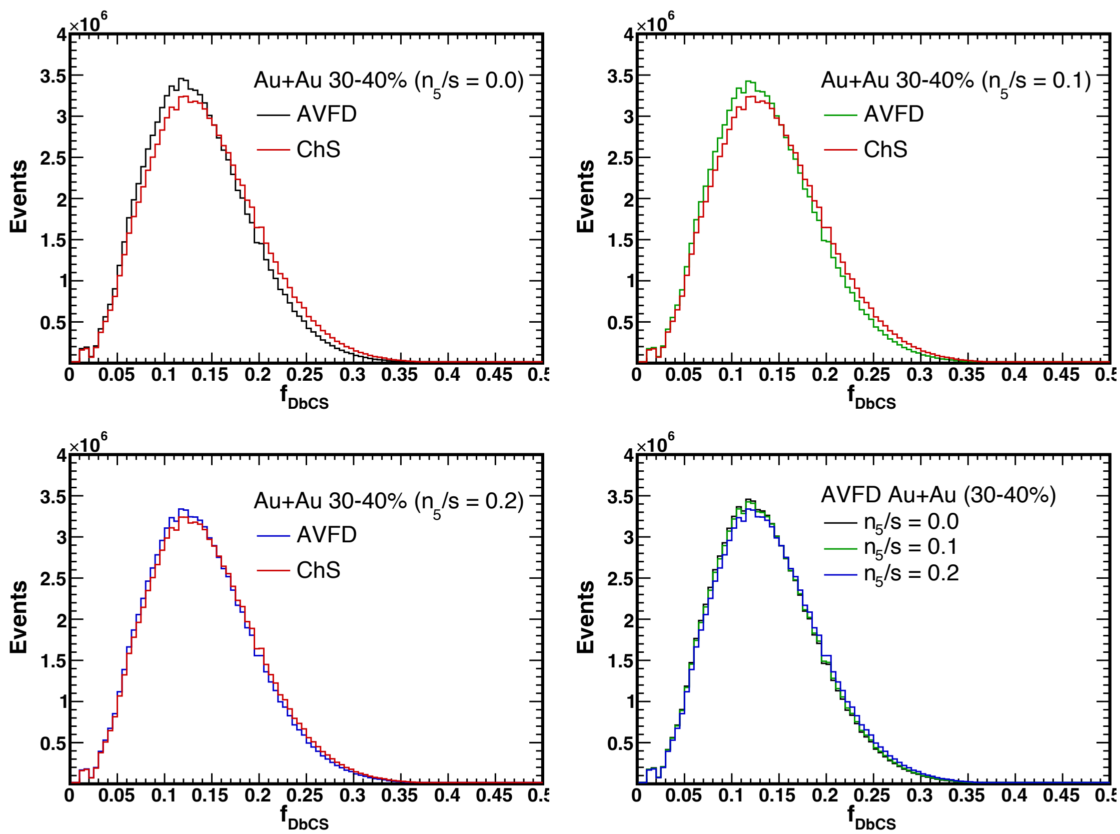

Figure 4.18: Comparison of f_{DbCS} distributions for Au+Au AVFD with corresponding charge shuffle (ChS) background for the three different sets. The three different sets are also compared (Bottom right).

In this section, we will discuss results using the Sliding Dumbbell Method where a dumbbell of 90° scans the whole azimuthal plane and provide the information of fractional charge separation across the dumbbell (i.e., $f_{DbCS} = Db^{max}_{+-} - 1$).

4.7.2.1 f_{DbCS} distribution for AVFD simulated events using SDM

The f_{DbCS} distribution for Au+Au AVFD for 30-40% collision centrality (for $\sqrt{s_{NN}}$ = 200 GeV) having different axial charge per entropy density n_5/s are shown in Fig. 4.18. It is seen that the f_{DbCS} distributions for ChS are ahead of Au+Au AVFD for all three sets. The f_{DbCS} distribution for Au+Au with n_5/s=0.2 is ahead of the other two sets as shown in Fig. 4.18 (Bottom Right) although the difference is very little.

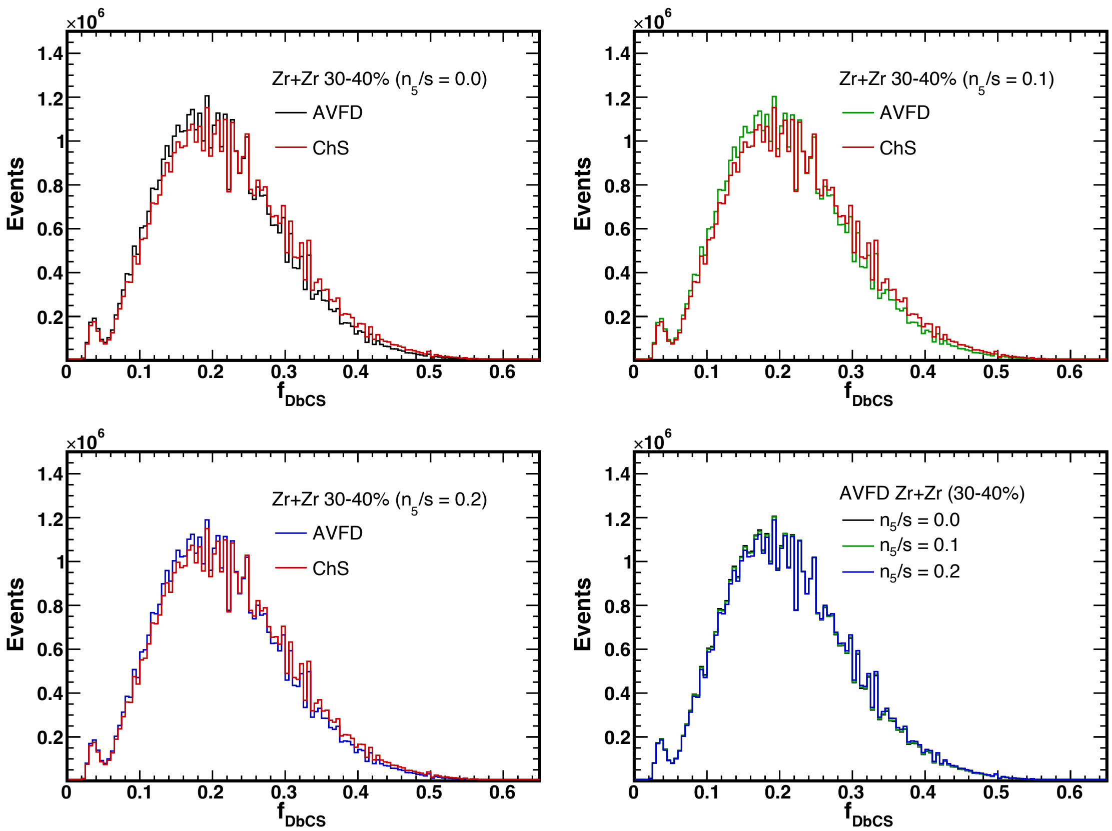

Figure 4.19: Comparison of f_{DbCS} distributions for Zr+Zr AVFD with corresponding charge shuffle (ChS) background for the three different sets. The three different sets are also compared (Bottom right).

The f_{DbCS} distribution for Zr+Zr AVFD and Ru+Ru AVFD having three different sets of the axial charge per entropy density n_5/s for 30-40% collision centrality are shown in Fig. 4.19 and Fig. 4.20, respectively. It is seen that the f_{DbCS} distributions for the AVFD Zr+Zr (Ru+Ru) are trailing the ChS background for the three different sets. The comparison of the three different sets reveals that there is not a significant difference (Bottom right figures). Once we get these f_{DbCS} distribution

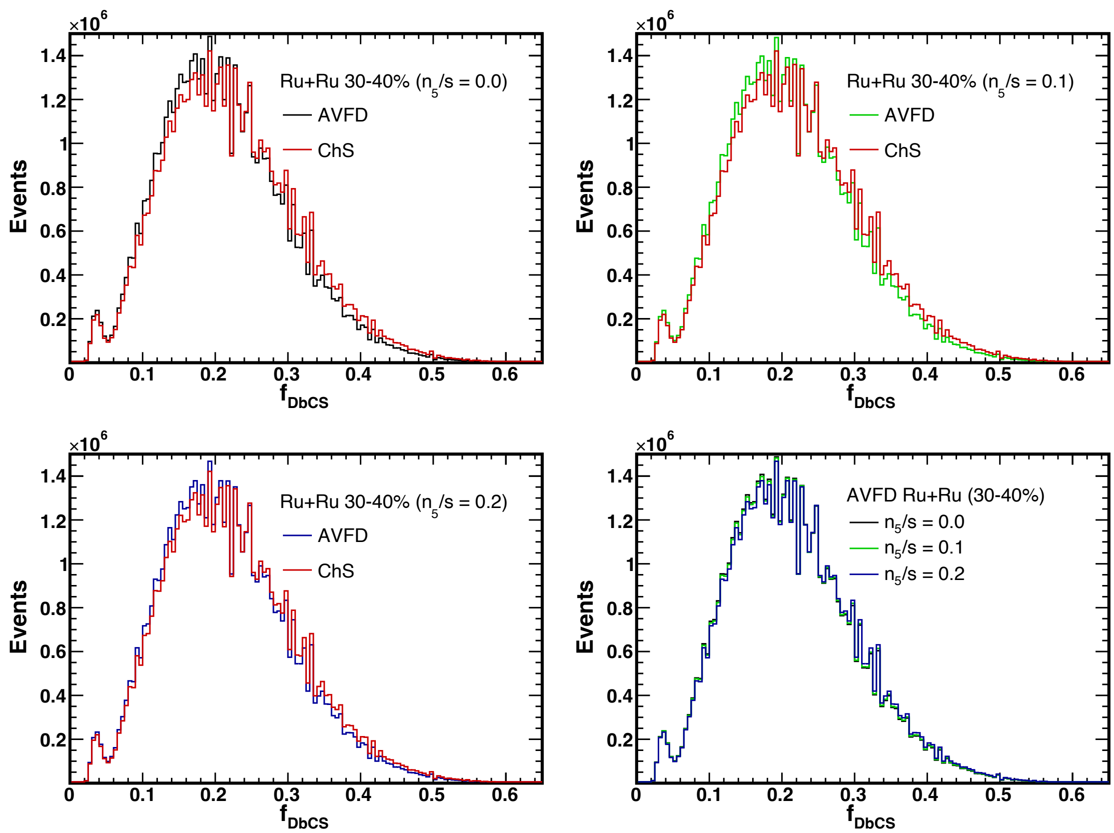

Figure 4.20: Comparison of f_{DbCS} distributions for Ru+Ru AVFD with corresponding charge shuffle (ChS) background for the three different sets. The three different sets are also compared (Bottom right).

for AVFD (Au+Au, Ru+Ru and Zr+Zr) and their corresponding ChS, we make 10 percentile bins for 30-40% collision centrality ranging from highest (0-10% from the right side of distribution) to lowest (90-100% from the left side of distribution). This partitioning of events on the basis of f_{DbCS} helps to get potential CME-like events with the highest back-to-back charge separation across the dumbbell.

4.7.2.2 Elliptic flow (v_2) dependence on charge separation (f_{DbCS})

Figure 4.21 illustrates the dependence of v_2 on f_{DbCS} (10 bins) for 30-40% collision centrality for Au+Au, Ru+Ru and Zr+Zr collisions, simulated using AVFD at $\sqrt{s_{NN}}$ =200 GeV with three different sets of AVFD corresponding to different CME signal (with n_5/s=0.0, 0.1, 0.2). $v_2\{2\}$ is higher than $v_2\{4\}$ in all f_{DbCS} bins. It can be

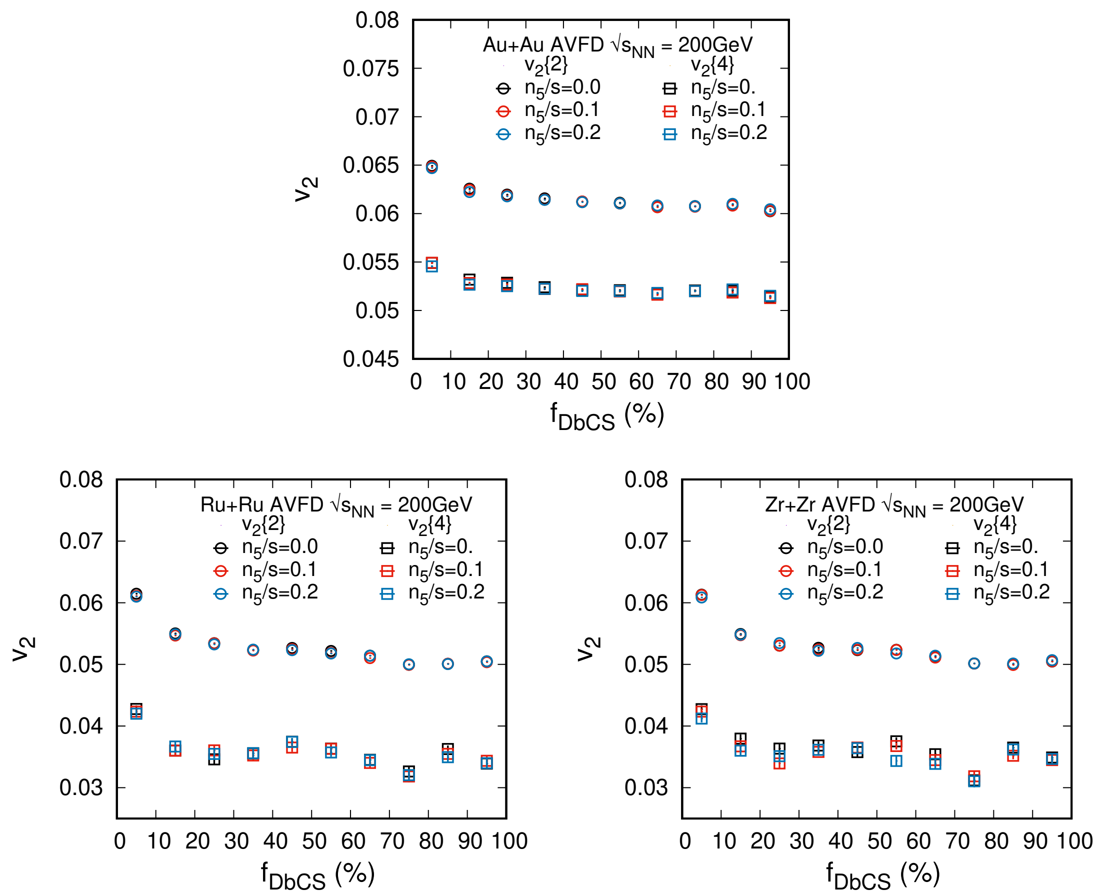

Figure 4.21: Dependence of elliptic flow (v_2) on f_{DbCS} (10 bins) for 30-40% collision centrality for Au+Au, Ru+Ru and Zr+Zr AVFD (with n_5/s=0.0, 0.1, 0.2) at $\sqrt{s_{NN}}$ =200 GeV.

seen that the v_2 is higher for the top 10% f_{DbCS}. In order to compute gamma we have taken the mean of $v_2\{2\}$ and $v_2\{4\}$ as v_2.

4.7.2.3 γ correlator using SDM

Figure 4.22 displays the γ-correlator for opposite-sign (Left) and same-sign (Right) charge pairs with respect to f_{DbCS} percentile bins for Au+Au AVFD, Charge Shuffle (ChS) and Correlated background (i.e., $Corr_{Au+Au}$) for three samples of AVFD, each corresponding to different CME signal injections (i.e., n_5/s=0.0, 0.1, 0.2). It is evident from the figure that the magnitude of γ increases for both same-sign (SS) and opposite-sign (OS) for top f_{DbCS} bins and is highest for the top 10% f_{DbCS}. Furthermore, within each f_{DbCS} bin, the correlations is larger for n_5/s=0.2 and have lower values for n_5/s=0.1 and 0.0 (i.e, correlation decreases with a decrease in the CME signal injection). γ-correlator for SS is negative for top f_{DbCS} bins and for lower f_{DbCS} it is positive showing the normal events toward the lower value of f_{DbCS}. The values of γ-correlator have increased many times than the average value of centrality. The γ (SS and OS) for charge shuffled (γ_{ChS}) background exhibit approximately the same value within each f_{DbCS} bin for all sets of AVFD irrespective of the amount of injected CME-like signal. The γ (SS and OS) for the correlated background is constant across all f_{DbCS} bins for each AVFD set, with higher values observed for n_5/s=0.2. Figure 4.23 and 4.24 depicts the variation of γ-correlator for

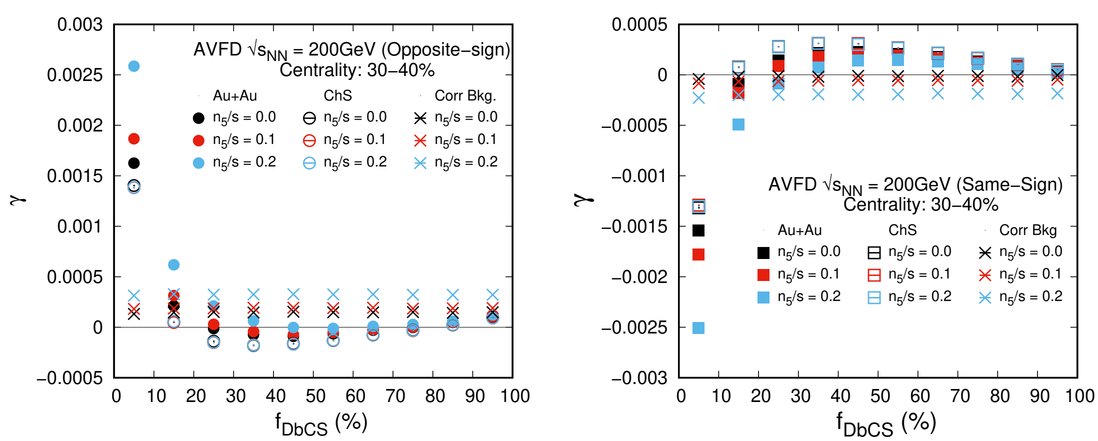

Figure 4.22: Dependence of γ correlator on f_{DbCS} (10 bins) for 30-40% collision centrality for Au+Au, charge shuffle (ChS) and correlated (Corr) backgrounds for three AVFD datasets (i.e., n_5/s=0.0, 0.1, 0.2) at $\sqrt{s_{NN}}$ =200 GeV opposite sign (Left) and same sign (Right) charge pairs.

opposite-sign (Left) and same-sign (Right) charge pairs with respect to f_{DbCS} percentile bins for Ru+Ru and Zr+Zr collisions including the comparison with Charge Shuffle (ChS) and Correlated backgrounds (i.e., *Corr*) for three sets of AVFD with different CME signal injection (i.e., n_5/s=0.0, 0.1, 0.2). The γ-correlator for isobar (Ru+Ru and Zr+Zr) collisions shows higher correlations compared to Au+Au collisions (Fig. 4.22).

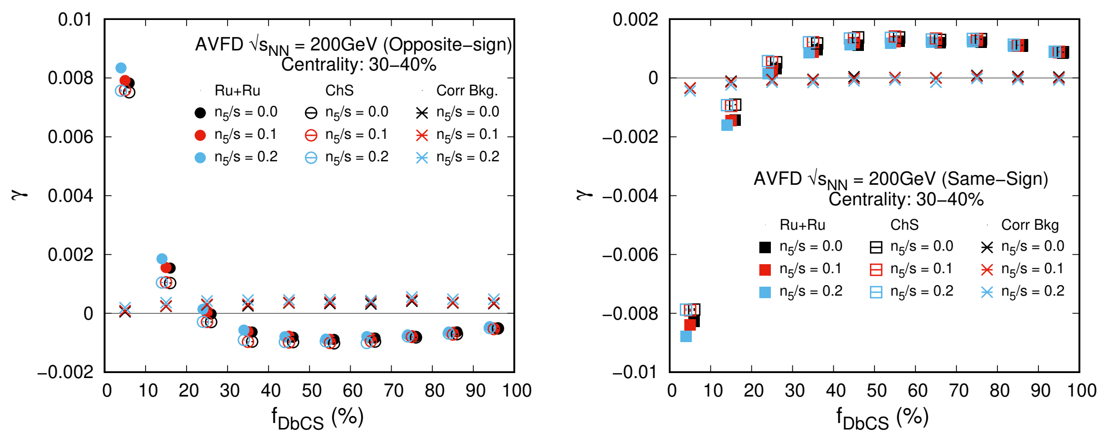

Figure 4.23: Dependence of γ correlator on f_{DbCS} (10 bins) for 30-40% collision centrality for Ru+Ru, charge shuffle (ChS) and correlated (Corr) backgrounds for three AVFD datasets (i.e., n_5/s=0.0, 0.1, 0.2) at $\sqrt{s_{NN}}$ =200 GeV opposite sign (Left) and same sign (Right) charge pairs. The points are shifted for Ru+Ru and ChS for the sake of clarity.

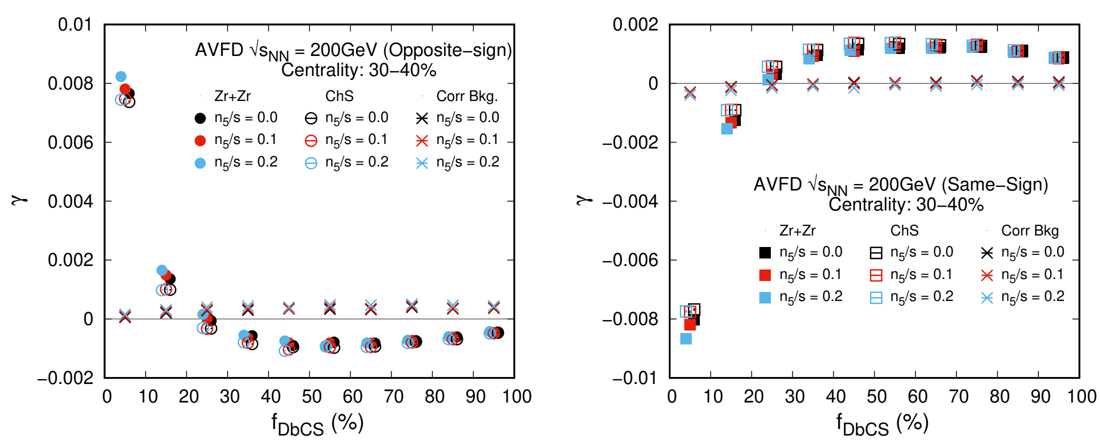

Figure 4.24: Dependence of γ correlator on f_{DbCS} (10 bins) for 30-40% collision centrality for Zr+Zr, charge shuffle (ChS) and correlated (Corr) backgrounds for three AVFD datasets (i.e., n_5/s=0.0, 0.1, 0.2) at $\sqrt{s_{NN}}$ =200 GeV opposite sign (Left) and same sign (Right) charge pairs. The points are shifted for Zr+Zr and ChS for the sake of clarity.

4.7.2.4 $\Delta\gamma$ correlator using SDM

Figure 4.25 displays the $\Delta\gamma$-correlator as a function of f_{DbCS} percentile bins for AVFD generated Au+Au (Top), Ru+Ru (Bottom Left) and Zr+Zr (Bottom Right) collisions at $\sqrt{s_{NN}}$ =200 GeV. Each figure includes AVFD (i.e., Au+Au, Ru+Ru, and Zr+Zr collisions) with different CME injected samples i.e., n_5/s=0.0, 0.1, 0.2 along with their corresponding charge shuffle (ChS) and correlated (Corr) backgrounds. It is seen that with increasing CME signal, the value of $\Delta\gamma$ increases for

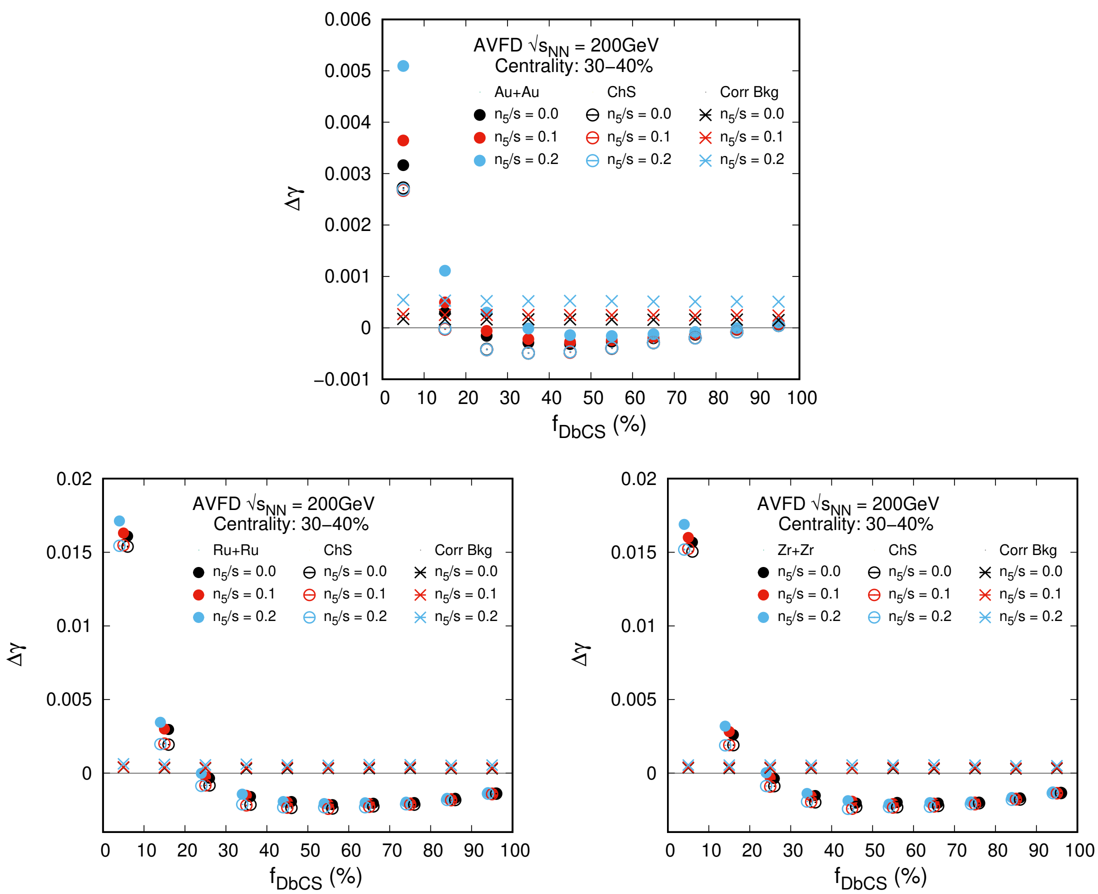

Figure 4.25: Top: The dependence of $\Delta\gamma$ on f_{DbCS} for 30-40% collision centrality for Au+Au, charge shuffle (ChS) and correlated (Corr) background for three AVFD datasets (i.e., n_5/s=0.0, 0.1, 0.2) at $\sqrt{s_{NN}}$ =200 GeV. Bottom Left: Similar plot for Ru+Ru collisions. Bottom Right: Similar plot for Zr+Zr collisions.

all f_{DbCS} bins. The highest values of the $\Delta\gamma$-correlator are observed in the top 10% f_{DbCS} bin, and these values decrease as f_{DbCS} decreases. The $\Delta\gamma$ values for the Charge Shuffle (ChS) backgrounds are approximately the same within the statistical errors for all three sets of AVFD simulations with n_5/s = 0.0, 0.1, and 0.2 while significantly lower than the data (i.e., Au+Au, Ru+Ru, and Zr+Zr). $\Delta\gamma$ values for the correlated backgrounds (Corr) remain constant across all f_{DbCS} bins. However, there are differences between Au+Au and isobaric (Ru+Ru and Zr+Zr) collisions.

4.7.2.5 CME fraction (f_{CME})

Figure 4.26 displays the fraction of CME (f_{CME}) calculated using Eq. 4.7 versus n_5/s (the axial charge per entropy density) for Au+Au, Ru+Ru, and Zr+Zr collisions. The f_{CME} increases with an increase in externally injected CME signals, corresponding to an increase in axial charge per entropy density (n_5/s) from 0.0 to 0.2. It is observed that for Au+Au collisions, f_{CME} increases from approximately

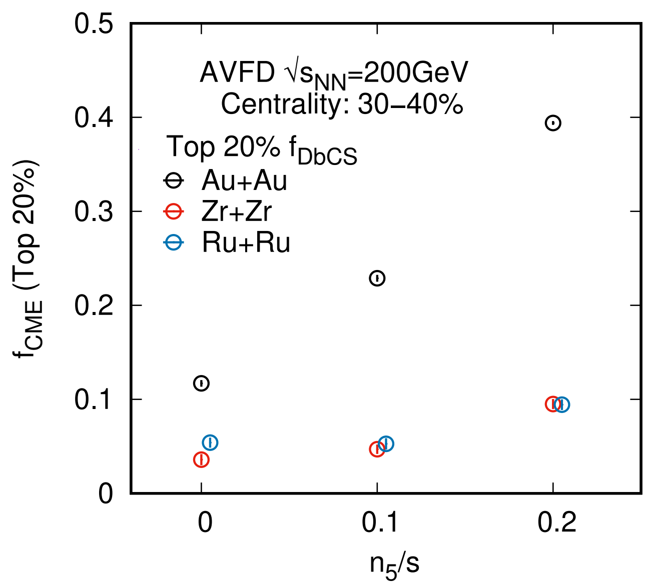

Figure 4.26: The variation of CME fraction (f_{CME}) with n_5/s for AVFD (Au+Au, Ru+Ru, and Zr+Zr) with 33% LCC for 30-40% collision centrality.

11.5% (n_5/s=0.0) to approximately 39% (n_5/s=0.2) considering top 20% f_{DbCS} as displayed in Fig. 4.26. For Ru+Ru (Zr+Zr) collisions, f_{CME} increases from approximately 5% (3.6%) for n_5/s=0.0 to approximately 9.5% (9.4%) for n_5/s=0.2 for top 20% f_{DbCS}. It is worth noting that for the n_5/s=0.0 case, f_{CME} exhibits positive values. The presence of 33% local charge conservation (LCC) in the samples with

n_5/s = 0.0 can explain this observation.

It is observed that for n_5/s = 0.1, f_{CME} value doubles as compared to n_5/s = 0.0, and for n_5/s = 0.2, f_{CME} becomes more than three times as compared to n_5=0.0 for Au+Au collisions. However, in the case of isobaric collisions, the increase is not as significant as in Au+Au collisions. Additionally, the points for Ru+Ru and Zr+Zr collisions agree within errors. This suggests that the increased magnetic field in Ru+Ru collisions compared to Zr+Zr collisions may not be distinguishable, possibly due to the lower multiplicities in these collisions. It is worth noting that even in the presence of local charge conservation (LCC), CME-like signals can still be extracted using the Sliding Dumbbell Method (SDM). This indicates that the SDM is capable of effectively distinguishing the CME signal from the background, allowing for the identification of CME-like effects even in situations where LCC is present.

4.8 Conclusion

The Sliding Dumbbell Method (SDM) is utilized to investigate the Chiral Magnetic Effect (CME) in heavy-ion collisions. SDM examines the event-by-event occurrence of back-to-back charge separation between positive and negative charged particles. To validate the SDM, events generated with the string melting approach in the AMPT model are analyzed. A CME-like signal is externally injected into AMPT-generated events by flipping the charges of particles (called as “CME” sample). The injected signal's percentage varies with collision centrality. Similarly, the AVFD (Anomalous Viscous Fluid Dynamics) model is also utilized to study the CME in heavy-ion collisions. AVFD incorporates anomalous transport phenomena, including the CME and 33% LCC (Local Charge Conservation). The parameter n_5/s, which represents the axial charge per entropy density, is varied to investigate the CME in collisions involving Au+Au and isobaric (Ru+Ru and Zr+Zr) systems.

In AMPT simulations, it has been observed that the value of $\Delta\gamma$ increases as the percentage of externally injected CME signal increases. However, in default AMPT simulations without the injected CME signal, $\Delta\gamma$ remains very small and agrees with the background within statistical uncertainties. When analyzing using the SDM, it has been observed that for the top charge separation (f_{DbCS}) bins, the magnitudes of the γ and δ correlators increase significantly. Additionally, for the same charge pairs, γ is negative while δ is positive, and for opposite charge pairs, δ is negative and γ is positive, which aligns with the expected behavior for CME-like events. Furthermore, both same-sign and opposite-sign charge pairs exhibit out-of-plane correlations due to the back-to-back charge separation. The fraction of CME (f_{CME}) is examined for different f_{DbCS} bins in CME and AMPT simulations for collision centralities ranging from 10% to 60%. It has been observed that the CME fraction is significant, approximately 50%, for the top f_{DbCS} bins in the CME sample. However, for default AMPT simulations, f_{CME} is zero within the uncertainties for all collision centralities. It is worth mentioning that using the SDM, CME-like events corresponding to the top 20% f_{DbCS} bins can be extracted even with a small percentage, approximately 1%, of the CME signal.

The presence of 33% local charge conservation (LCC) in the samples with n_5/s=0 can explain observed CME signal. In the case of Au+Au collisions, it is observed that for n_5/s=0.1, f_{CME} doubles compared to n_5/s=0, and for n_5/s=0.2, f_{CME} becomes more than three times as compared to n_5/s=0. However, in the case of isobaric collisions, the increase is not as significant. Additionally, the points for Ru+Ru and Zr+Zr collisions agree within errors. This suggests that the increased magnetic field in Ru+Ru collisions compared to Zr+Zr collisions may not be distinguishable, possibly due to the lower multiplicities in these collisions.

It is worth noting that even in the presence of local charge conservation (LCC), CME-like signals can still be extracted using the Sliding Dumbbell Method (SDM). This indicates that the SDM is capable of effectively distinguishing the CME signal from the background, allowing for the identification of CME-like effects even in situations where LCC is present.

Bibliography

[1] K. Fukushima *et al.*, “The Chiral Magnetic Effect”, Phys. Rev. D 78, 074033 (2006).

[2] D.E. Kharzeev, “Parity violation in hot QCD: Why it can happen, and how to look for it”, Phys. Lett. B 633, 260 (2006).

[3] D.E. Kharzeev and A. Zhitnitsky, “Charge separation induced by P-odd bubbles in QCD matter”, Nucl. Phys. A 797, 67 (2007).

[4] D. Kharzeev *et al.*, “Possibility of spontaneous parity violation in hot QCD”, Phys. Rev. Lett. 81, 512 (1998).

[5] S.A. Voloshin, “Parity violation in hot QCD: How to detect it”, Phys. Rev. C 70, 057901 (2004).

[6] D. Kharzeev, L.D. McLerran, and H.J. Warringa, “The effects of topological charge change in heavy ion collisions: “Event by event P and CP violation”, Nucl. Phys. A 803, 227 (2008).

[7] A. Bzdak, V. Koch, and J. Liao, “Charge-Dependent Correlations in Relativistic Heavy Ion Collisions and the Chiral Magnetic Effect”, arXiv:1207.7327v1 [nucl- th] (2012).

[8] B. Abelev *et al.*, [STAR Collaboration], “Observation of charge-dependent azimuthal correlations and possible local parity violation in heavy-ion collisions”, Phys. Rev. C 81, 054908 (2010).

[9] L. Adamczyk *et al.*, [STAR Collaboration], "Beam-Energy Dependence of Charge Separation along the Magnetic Field in Au+Au Collisions at RHIC", Phys. Rev. Lett. 113, 052302 (2014).

[10] Abdallah, Mohamed *et al.* [STAR Collaboration], "Search for the chiral magnetic effect with isobar collisions at $\sqrt{s_{NN}} = 200$ GeV by the STAR Collaboration at the BNL Relativistic Heavy Ion Collider", Phys. Rev. C 105, 014901 (2022).

[11] B. Abelev *et al.*, [ALICE collaboration], "Charge separation relative to the re-action plane in Pb-Pb collisions at $\sqrt{s_{NN}} = 2.76$ TeV", Phys. Rev. Lett. 110, 012301 (2013).

[12] S. Acharya *et al.*, [ALICE collaboration], "Constraining the magnitude of the Chiral Magnetic Effect with Event Shape Engineering in Pb-Pb collisions at psNN = 2.76 TeV", Phys. Lett. B 777, 151 (2018).

[13] V. Khachatryan *et al.*, [CMS collaboration], "Observation of charge dependent azimuthal correlations in pPb collisions and its implication for the search for the chiral magnetic effect", Phys. Rev. Lett. 118, 122302 (2014).

[14] R. Baier, A. H. Mueller, D. Schiff, and D. T. Son, "Bottom-up thermalization in heavy ion collisions", Phys. Lett. B502, 51 (2001).

[15] Z. W. Lin, C. M. Ko, B. A. Li *et al.*, "A Multi-phase transport model for relativistic heavy ion collisions", Phys. Rev. C 72, 064901 (2005).

[16] B. Zhang, C. M. Ko, B. A. Li, and Z. W. Lin, "Multiphase transport model for relativistic nuclear collisions", Phys. Rev. C61, 067901 (2000).

[17] B. Zhang, C. M. Ko, B. A. Li, Z. W. Lin, and B. H. Sa, "J/Ψ suppression in ultrarelativistic nuclear collisions" Phys. Rev. C 62, 054905 (2000).

[18] X. N. Wang, "Role of multiple minijets in high-energy hadronic reactions", Phys. Rev. D 43, 104 (1991).

[19] X. N. Wang and M. Gyulassy, "hijing: A Monte Carlo model for multiple jet production in pp, pA, and AA collisions" Phys. Rev. D 44, 3501 (1991).

[20] X. N. Wang and M. Gyulassy, "Systematic study of particle production in $p + p(\bar{p})$ collisions via the HIJING model", Phys. Rev. D 45, 844 (1992).

[21] M. Gyulassy and X. N. Wang, "HIJING 1.0: A Monte Carlo program for parton and particle production in high energy hadronic and nuclear collisions", Comput. Phys. Commun. 83, 307 (1994).

[22] B. Zhang, "ZPC 1.0.1: A Parton cascade for ultrarelativistic heavy ion collisions", Comput. Phys. Commun. 109, 193 (1998).

[23] B. I. Abelev *et al.* [STAR Collaboration], "Azimuthal Charged-Particle Correlations and Possible Local Strong Parity Violation", Phys. Rev. Lett. 103, 251601 (2009).

[24] B. I. Abelev *et al.* [STAR Collaboration], "Observation of charge-dependent azimuthal correlations and possible local strong parity violation in heavy-ion collisions", Phys. Rev. C 81, 054908 (2010).

[25] B. I. Abelev *et al.* [ALICE Collaboration], "Charge separation relative to the reaction plane in Pb-Pb collisions at $\sqrt{s_{NN}} = 2.76$ TeV", Phys. Rev. Lett. 110, 012301 (2013).

[26] Y. Jiang, S. Shi, Y. Yin, and J. Liao, "Quantifying the chiral magnetic effect from anomalous-viscous fluid dynamics", Chin. Phys. C, 42, 011001 (2018).

[27] S. Shi, Y. Jiang, E. Lilleskov, and J. Liao, "Anomalous Chiral Transport in Heavy Ion Collisions from Anomalous-Viscous Fluid Dynamics", Annals. Phys., 394, 50 (2018).

[28] Ulrich W. Heinz, J. Liu, "Pre-equilibrium dynamics and heavy-ion observables", Nucl. Phys. A 956, 549 (2016)

[29] Y. Feng, Y. Lin, J. Zhao, F. Wang. "Revisit the chiral magnetic effect expectation in isobaric collisions at the relativistic heavy ion collider", Phys. Lett. B, 820, 136549 (2021).

[30] S. Shi *et al.*, "Signatures of Chiral Magnetic Effect in the Collisions of Isobars", Phys. Rev. Lett. 125, 242301 (2020).

Chapter 5

Chiral Magnetic Effect in Au+Au collisions at $\sqrt{s_{\mathrm{NN}}} = 200$ GeV using SDM

5.1 Introduction

In Chapter III, the Chiral Magnetic Effect (CME) [1–3] is introduced as the phenomenon of back-to-back charge separation perpendicular to the reaction plane in non-central heavy-ion collisions. The chapter discusses various methods that have been employed by researchers over the past decade to search for the CME and highlights the limitations and uncertainties in obtaining conclusive evidence for its existence. The Sliding Dumbbell Method (SDM) [4–6] is introduced as a new technique specifically designed to detect the back-to-back charge separation associated with the CME. The SDM is explained in detail, and its potential in exploring the CME is discussed.

In Chapter IV, the validation of the SDM is performed using events generated by the A Multi-Phase Transport (AMPT) model for Au+Au collisions. The AMPT events include an externally injected CME-like signal, allowing for the testing and verification of the SDM's sensitivity to the CME. Additionally, the chapter presents results obtained using the Anomalous Viscous Fluid Dynamics (AVFD) model, which incorporates local charge conservation (LCC) along with other factors. This model provides a framework for understanding the interplay between the axial charge current and the bulk medium in heavy-ion collisions.

The purpose of this chapter is to provide a comprehensive analysis of Au+Au collisions data at the center of mass energy per nucleon 200 GeV using the SDM, ensuring a thorough understanding of the concepts and methods used in the analysis. By presenting these details, the chapter aims to contribute to a deeper insight into the Chiral Magnetic Effect.

The investigation of the CME has utilized 2-particle (δ) and 3-particle (γ) correlators [7,8], which are defined as follows:

$$\delta \equiv \langle cos(\phi_\alpha - \phi_\beta)\rangle \tag{5.1}$$

$$\gamma = \langle cos(\phi_\alpha + \phi_\beta - 2\Psi_{RP})\rangle \tag{5.2}$$

Here, ϕ_α, ϕ_β denote the azimuthal angles of the particles "α" and "β", respectively, and Ψ_{RP} is the reaction plane angle. Since the reaction plane angle can not be determined experimentally, Voloshin [8] modified Eq. 5.2 as follows:

$$\gamma = \langle cos(\phi_\alpha + \phi_\beta - 2\phi_c)\rangle / v_{2,c} \tag{5.3}$$

where, $v_{2,c}$ represents the elliptic flow of third particle i.e., "c". Here the averaging $\langle \cdots \rangle$ is performed over all the particles and over the events. The difference ($\Delta\gamma$) between the opposite-sign (OS) and same-sign (SS) γ correlators is considered to get rid of charge-independent correlation backgrounds [9], i.e.,

$$\Delta\gamma = \gamma_{OS} - \gamma_{SS} \tag{5.4}$$

The $\Delta\gamma$ is highly sensitive to the preferential emission of positively and negatively charged particles to opposite sides of the reaction plane. The STAR (Solenoidal Tracker at RHIC) Collaboration has reported their initial measurements of nonzero $\Delta\gamma$ (or γ) in Au+Au and Cu+Cu collisions at $\sqrt{s_{NN}} = 200$ GeV in their studies [8,10]. These publications discuss the possible sources contributing to the observed signals, including expectations from CME-driven effects and flow-induced background arising from resonance decays. The presence of a nonzero $\Delta\gamma$ has been further confirmed through measurements conducted at various energies by the RHIC facility [11] and the LHC experiments [12]. However, accurately quantifying the magnitudes of CME signal in heavy-ion collisions remains a challenging task despite significant theoretical advancements.

In recent years, data-driven approaches and observables have been developed to distinguish the potential signal of the Chiral Magnetic Effect (CME) from background contributions [13–15]. At the LHC, the CMS and ALICE Collaborations have conducted Event-shape Engineering (ESE) investigations, which have yielded results consistent with zero CME-induced charge separation within upper limits of 7% and 26% at the 95% confidence level (CL) respectively [16,17].

Indeed, the weak nature of the Chiral Magnetic Effect (CME) signal and its susceptibility to statistical fluctuations emphasize the importance of conducting the search on an event-by-event basis. By analyzing individual events, it becomes possible to identify and study those events that exhibit a significant back-to-back charge separation, which is a distinct signature of the CME. The Sliding Dumbbell Method (SDM) [4–6] is a novel technique specifically developed to enhance the identification of CME-enriched events within each collision centrality. The SDM involves scanning the azimuthal plane using a dumbbell-shaped window, which allows for the examination of charge separation across the dumbbell. By systematically analyzing the charge distribution within each event, the SDM facilitates the extraction of events that demonstrate localized charge separation associated with the CME. By employing the SDM and examining events on an individual basis, we can effectively isolate and characterize the CME signal from the background and statistical fluctuations. This approach provides a more sensitive and accurate means of studying the CME phenomenon, ultimately leading to a deeper understanding of its properties and underlying physics.

5.2 Data analysis

As discussed in previous chapter III, in the SDM, the azimuthal plane in each event is scanned by sliding the dumbbell of $\Delta\phi = 90^\circ$ in steps of $\delta\phi = 1^\circ$ while calculating Db_{+-} for each region to obtain maximum values of Db_{+-} (Db^{max}_{+-}) in each event with a condition that $\mid Db_{asy} \mid < 0.25$. The quantity Db_{+-}, which is "the sum of the positive charge fraction on one side of the dumbbell and negative charge fraction on the other side of the dumbbell", is defined as:

$$
\begin{aligned}
Db_{+-} &= Db^{a}_{+} + Db^{b}_{-} \\
&= \frac{n^{a}_{+}}{n^{a}_{+} + n^{a}_{-}} + \frac{n^{b}_{-}}{n^{b}_{+} + n^{b}_{-}}
\end{aligned}
\tag{5.5}
$$

where n^a_+ and n^a_- are the number of positive and negative charge particles, respectively, on "a" side of the dumbbell; and n^b_+ and n^b_- are number of positive and negative charge particles, respectively, on "b" side of the dumbbell. To calculate the Db^{max}_{+-}, a condition on the charge excess asymmetry across the dumbbell, $\mid Db_{asy} \mid < 0.25$ is imposed for each event. The Db_{asy} is defined as follows:

$$
Db_{asy} = \frac{Pos^{a}_{ex} - Neg^{b}_{ex}}{Pos^{a}_{ex} + Neg^{b}_{ex}}
\tag{5.6}
$$

where $Pos^a_{ex} = n^a_+ - n^a_-$ is positively charged particle excess on side "a" of the dumbbell and $Neg^b_{ex} = n^b_- - n^b_+$ is negatively charged particle excess on side "b" of the dumbbell. The Db_{asy} is used to select the events which are similar to the CME-like events while rejecting the events having one side charge separation.

The charge separation across the dumbbell (f_{DbCS}) is defined as follows:

$$
f_{DbCS} = Db^{max}_{+-} - 1
\tag{5.7}
$$

In the analysis described, the f_{DbCS} (fractional charge separation across the dumb-bell) is quantified in the range of 0 to 1. A value of $f_{DbCS} = 1$ corresponds to maximum back-to-back charge separation, representing 100% charge separation, while $f_{DbCS} = 0$ corresponds to no back-to-back charge separation. To investigate the relationship between f_{DbCS} and charge correlations, the f_{DbCS} distributions are obtained for each centrality class. These distributions are then subdivided into ten percentile bins, ranging from 0-10% to 90-100%, for each collision centrality. This division allows for a more detailed analysis of the charge separation effects within specific centrality ranges.

After obtaining the f_{DbCS} bins, multi-particle correlators are calculated for different charge combinations. These correlators include 2-particle, 3-particle, and 4-particle correlators. The charge combinations considered are same-sign (+,+ and -,-) and opposite-sign (+,- and -,+). For each f_{DbCS} bin in each centrality and for different samples, the correlators (such as γ, δ, v_2, etc.) are calculated using the Q-cumulant method [18–21], which provides a robust statistical technique for extracting the correlations and characterizing the charge separation effects. By analyzing the correlators in different f_{DbCS} bins and for different charge combinations, we can investigate the relationship between charge separation and the corresponding correlator magnitudes. This analysis helps in understanding the impact of the CME and other effects on the observed charge correlations in heavy-ion collisions.

5.2.1 Data sets

We analyzed the collision data from ${}^{197}_{79}Au$+${}^{197}_{79}Au$ collisions, which was collected by the STAR detector during the year 2011 (Run-11) at a center-of-mass energy per nucleon of 200 GeV. The main subsystems of the STAR detector are the Time Projection Chamber (TPC) [22], the time-of-flight detector (TOF) [23], the zero-degree calorimeters (ZDCs) [24], and the vertex position detectors (VPDs) [25] etc.

The dataset used in our analysis corresponds to the Minimum Bias triggered data (STAR-library: P11id.SL19c) obtained from Run11. It is important to note that we excluded certain bad runs with known issues. The list of these excluded bad runs is provided below.

12113091, 12114007, 12114035, 12114078, 12114092, 12114116, 12115009, 12115014, 12115015, 12115016, 12115018, 12115019, 12115020, 12115022, 12115023, 12115062, 12115073, 12115093, 12115094, 12116012, 12116054, 12117010, 12117016, 12117020, 12117065, 12119040, 12119042, 12120017, 12120026, 12121017, 12121022, 12121034, 12121050, 12121067, 12122019, 12127003, 12127010, 12127011, 12127017, 12127018, 12127032, 12128025, 12132043, 12132061, 12133018, 12134023, 12136005, 12136006, 12136014, 12136017, 12136022, 12136023, 12136024, 12136025, 12136027, 12136028, 12136029, 12136030, 12136031, 12136034, 12136054, 12138005, 12138017, 12138021, 12146004, 12146006, 12146007, 12146008, 12151035, 12153002, 12153004, 12153007, 12153013, 12157038, 12157051, 12158040, 12158041, 12158054, 12158056, 12158057, 12162055, 12162056, 12162057, 12162058, 12164037, 12164078, 12164079, 12166002, 12166003, 12167015, 12167024, 12167052, 12168002, 12168009, 12168022, 12168077, 12170044, 12170045, 12170054, 12170056, 12172050, 12172051, 12172055, 12173030, 12173031, 12173032, 12173033, 12173034, 12174067, 12174085, 12175062, 12175087, 12175113, 12175114, 12175115, 12176001, 12176044, 12176054, 12176071, 12177015, 12177061, 12177092, 12177099, 12177101, 12177106, 12177107, 12177108, 12178003, 12178004, 12178005, 12178006, 12178013, 12178099, 12178120

Details about the event selection cuts, track selection cuts, and collision centralities are given in the following sections.

5.2.1.1 Event selection vertex cuts

In the collisions, TPC is used to reconstruct the primary vertex position i.e., $V_{z,TPC}$ or V_z along the beam direction axis (z-axis). On the primary vertex position, a variety of cuts have been applied to select the good events whereas the events outside the cuts listed in table 5.1 are termed as bad events (not used for the analysis). The events must have a vertex z-coordinate (V_z) within a range of ± 30 cm from the central point of the Time Projection Chamber (TPC), as shown in Fig. 5.1 (Left). We are utilizing the minimum bias (MB) events with MB trigger IDs 350003, 350013, 350023, 350033, and 350043. The Minimum Bias data sample is obtained

Event parameters	Cuts
Vertex cut ($V_{z,TPC}$)	-30 < V_z < 30 cm
$\mid V_{z,VPD}$ - $V_{z,TPC} \mid$	< 4 cm
V_x	$\mid V_x \mid$ < 2.0 cm
V_y	$\mid V_y \mid$ < 2.0 cm
$V_r = \sqrt{V_x^2 + V_y^2}$	< 2.0 cm

Table 5.1: Event selection Cuts for Au+Au at $\sqrt{s_{NN}}$ = 200 GeV collisions.

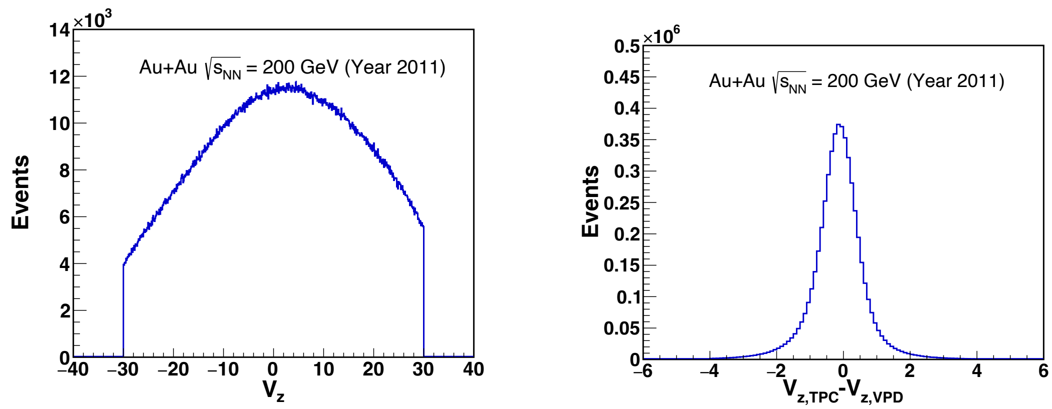

Figure 5.1: (Left) Z-Vertex distribution for Au+Au collisions at $\sqrt{s_{NN}}$ = 200 GeV. (Right) $V_{z,TPC} - V_{z,VPD}$ distribution for Au+Au collisions. Here, $V_{z,VPD}$ is Vz taken from the Vertex Position Detector (VPD) and $V_{z,TPC}$ is Vz taken from the TPC.

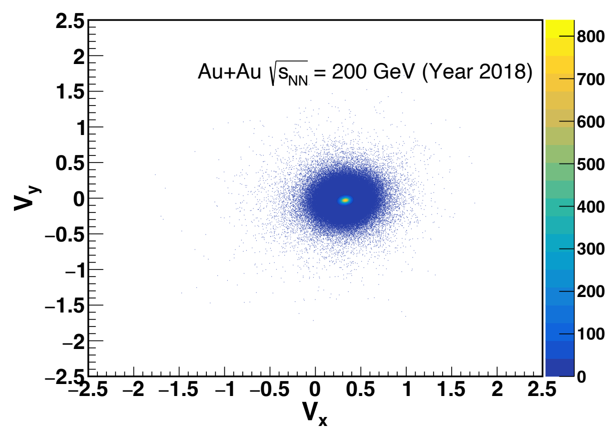

Figure 5.2: V_x vs V_y scatter plot for Au+Au collisions at $\sqrt{s_{NN}}$ = 200 GeV.

through a trigger that relies on information from two VPD detectors. In order to select the good events, an additional condition is imposed on V_z, namely $\mid V_{z,TPC} - V_{z,VPD} \mid < 4$ cm. The corresponding distribution is depicted in Figure 5.1 (Right). Figure 5.2 displays the scatter plot of V_x vs V_y where both V_x and V_y are less

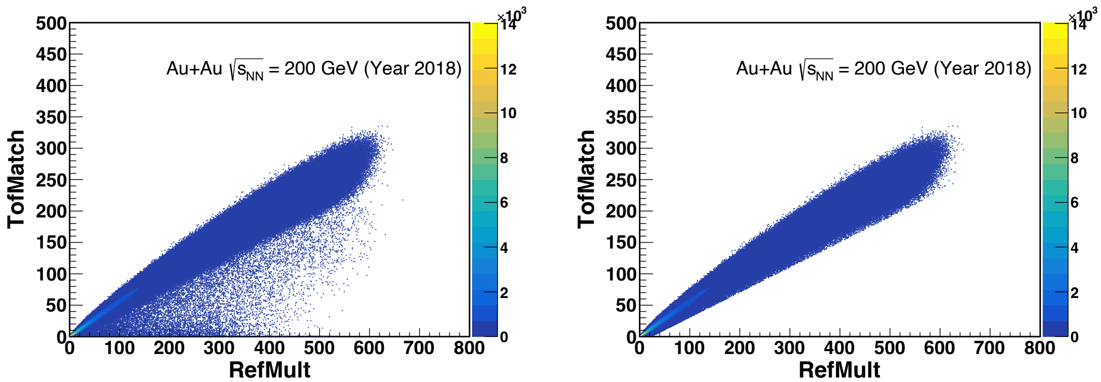

Figure 5.3: (Left) RefMult ($N_{trk}^{offline}$) vs TofMatch with the pile-up events. (Right) RefMult ($N_{trk}^{offline}$) vs TofMatch after removing the pile-up event for Au+Au collisions at $\sqrt{s_{NN}}$=200 GeV.

than 2.0 cm. An offline rejection is required for the pile-up events to get the good events for the analysis. There are a few events which were identified as pile-up and were removed. Figure 5.3 (Left) displays RefMult (uncorrected charged particle multiplicity in TPC within $\mid \eta \mid$<0.5) versus TofMatch (the number of TPC tracks also having a hit in the TOF detector) for Au+Au collisions. To remove the pile-up events in Au+Au collisions the following condition was imposed on TofMatch i.e., "TofMatch > 0.40*RefMult-10" [26]. After imposing the condition on TofMatch, RefMult versus TofMatch is displayed in Fig. 5.3 (Right).

5.2.1.2 Track selection cuts

To reduce contamination from secondary charged particles in heavy-ion collisions, distance of closest approach (DCA) between reconstructed TPC tracks and the primary vertex is taken to be less than 3 cm (as illustrated in Fig.5.4 (a)). Each track must have at least 15 ionization points (N_{fits}) in the TPC, resulting in the N_{hits} distribution as shown in Fig.5.4 (b). The TPC detects charged particles in the pseudo-rapidity range $\mid \eta \mid < 1$, with full azimuthal coverage ($\Phi = 2\pi$) and a transverse momentum lower limit of $p_T > 0.15$ GeV/c. The transverse momentum (p_T) distribution for 2.0 GeV/$c > p_T >$ 0.15 GeV/c is given in the Fig. 5.4 (c) and pseudo-rapidity (η) distribution is shown in Fig. 5.4 (d). These restrictions help in preventing track splitting and merging effects and improve momentum resolution. Table5.2 lists a summary of all the track selection cuts for Au+Au collisions. Additionally, Fig. 5.4 (e) displays the ϕ distribution (in degrees) for the 30-40% collision centrality in Au+Au collisions. The ϕ distribution is not flat due to detector inefficiency. After applying all the event and track selection cuts we get approximately

Track parameters	Cuts
DCA	$\leq$ 3 cm
N_{Hits}	> 14
$N_{HitsFit}/N_{HitsPoss}$	> 0.52
p_T	0.15 GeV/$c < p_T <$ 2.0 GeV/c
$\mid \eta \mid$	< 1.0

Table 5.2: Track selection Cuts for Au+Au collisions at $\sqrt{s_{NN}}$ = 200 GeV.

$\sim$465 Million minimum bias (MB) events for Au+Au collisions at $\sqrt{s_{NN}}$ = 200 GeV.

5.2.1.3 Centrality selection

Centrality label	RefMult2
0-5%	>453
5-10%	>383
10-20%	>268
20-30%	>181
30-40%	>117
40-50%	>71
50-60%	>40
60-70%	>20
70-80%	>9

Table 5.3: Centrality selection from RefMult2 in Au+Au collisions at $\sqrt{s_{NN}}$=200 GeV.

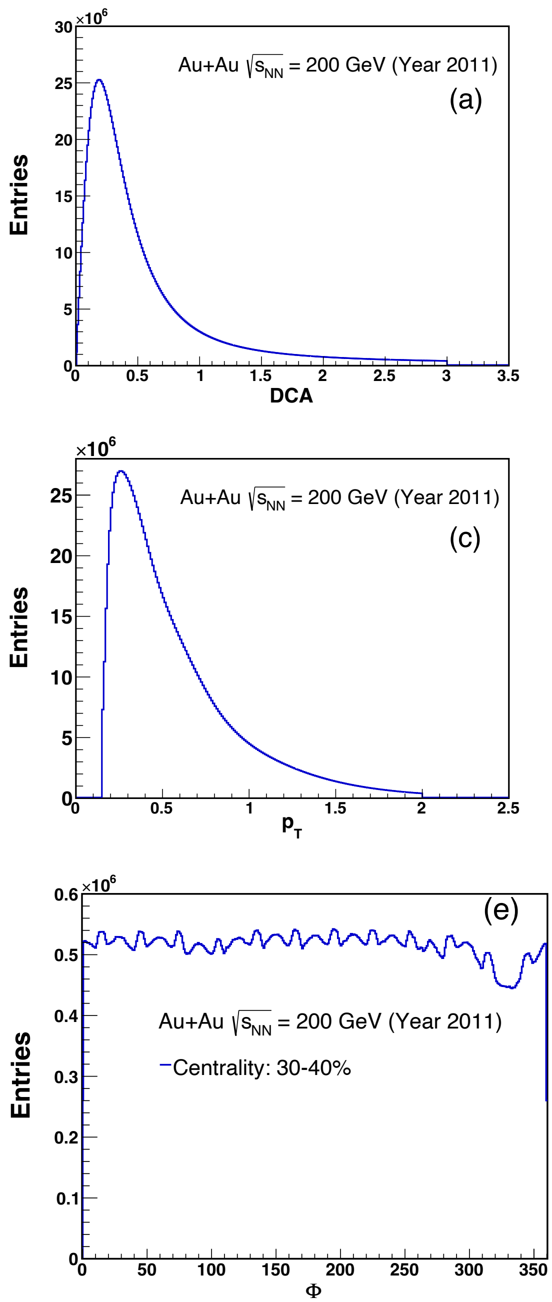

Figure 5.4: Distributions of (a) DCA, (b) N_{hits}, (c) p_T, (d) η, and (e) ϕ (in degrees) distributions for Au+Au collisions at $\sqrt{s_{NN}}$=200 GeV.

The measurement either of the impact parameter or N_{part} in the heavy-ion collision is not feasible. Therefore, the multiplicity of charged particles is employed to determine the centrality classes for the collisions. In the case of the STAR experiment, $N_{trk}^{offline}$ or RefMult is utilized to establish centrality class, which corresponds to the uncorrected multiplicity of charged particles reconstructed within $\mid \eta \mid< 0.5$ for the TPC detector. The centrality information is obtained by dividing RefMult into 10-percentile bins. For this analysis, we used the RefMult2 definition as a reference multiplicity, representing the uncorrected charged particle multiplicity in the TPC region $0.5< \eta < 1.0$. This centrality selection was implemented to reduce the auto-correlation effect among the charged particles. RefMult2 is used to determine the collision centrality. The cuts on RefMult2 for eight centrality bins are listed in table 5.3 [26] wherein the multiplicity gradually decreases with decreasing collision centrality. Figure 5.5 displays the positive and negative charge particle multiplicity distributions which shows good agreement for different collision centralities.

5.3 Uncertainty estimation

5.3.1 Statistical uncertainties

We employed the sub-sampling method in conjunction with standard error propagation to estimate the statistical uncertainties. The dataset was divided into ten sub-samples, following the approach used in simulation studies.

5.3.2 Systematic uncertainties

In order to assess the systematic uncertainties, variations were introduced to the standard event and track cuts used. Each cut was varied independently, and the maximum deviation of a given observable was considered as the systematic uncertainty associated with that cut. Systematic uncertainties from different cuts are added in quadrature. The table 5.4 lists details of the various cuts employed in the

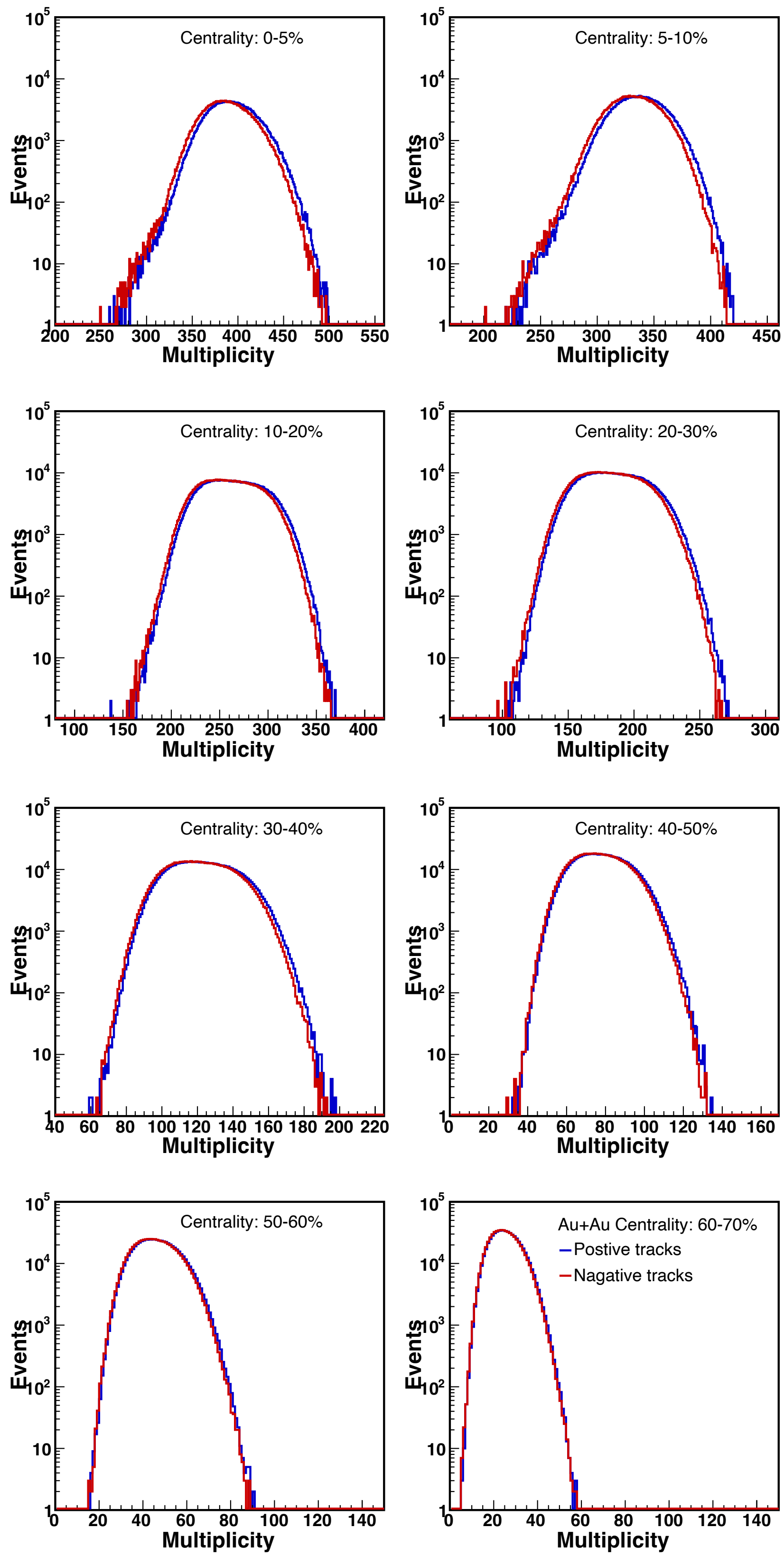

Figure 5.5: Positively and negatively charged particle multiplicity distributions for Au+Au collisions at $\sqrt{s_{NN}}$=200 GeV for different collision centralities.

analysis along with the default values. The default value of elliptic flow (v_2) is calcu-

Sources of uncertainty	Standard Cut	Varied Cut
V_z	-30 < V_z < 30 cm	-30 < V_z < 0 cm
DCA	< 3 cm	< 2 cm
N_{hits}	> 14	> 19

Table 5.4: Various standard cuts and varied systematic cuts to obtain the systematic uncertainties in Au+Au collisions at $\sqrt{s_{NN}}$=200 GeV.

lated as the average of $v_2\{2\}$ and $v_2\{4\}$. The systematic uncertainty is determined by taking half of the difference between $v_2\{2\}$ and $v_2\{4\}$.

5.4 Non-Uniform Acceptance Correction

To account for the effects of detector acceptance, it is necessary to include corrections in the calculations of cumulants from multi-particle correlations. In detectors with uniform acceptance, certain terms in the calculations can be disregarded. However, for detectors that are "almost" perfect but still exhibit small deviations from perfect uniformity, it is important to reintroduce the terms that were previously eliminated [18–21]. The expressions for obtaining the acceptance correction in the calculations are as follows:

- **Generalized 2^{nd} order Q-Cumulant:** In order to take into consideration the non-uniform detector acceptance, the 2^{nd} order cumulant has been modified as follows:

$$c_n\{2\} = \langle\langle \cos n(\phi_1 - \phi_2)\rangle\rangle - \langle\langle \cos n\phi_1\rangle\rangle^2 - \langle\langle \sin n\phi_1\rangle\rangle^2 \tag{5.8}$$

The correction terms in Eq. 5.8 (which are highlighted in red) are intended to cancel out the bias in the two-particle correlation that is caused by the non-uniform acceptance [18–21]. These terms can be decomposed into the real and imaginary parts of the Q-vectors in the following way:

$$\langle\langle\cos n\phi_1\rangle\rangle = \frac{\sum_{i=1}^{N}(\Re e[Q_n])_i}{\sum_{i=1}^{N} M_i} = \frac{\sum_{i=1}^{N}(\langle\cos n\phi\rangle)_i}{\sum_{i=1}^{N} M_i} \tag{5.9}$$

$$\langle\langle\sin n\phi_1\rangle\rangle = \frac{\sum_{i=1}^{N}(\Im m[Q_n])_i}{\sum_{i=1}^{N} M_i} = \frac{\sum_{i=1}^{N}(\langle\sin n\phi\rangle)_i}{\sum_{i=1}^{N} M_i} \tag{5.10}$$

where, “M” represents the multiplicity and “N” is the number of events. The angle brackets denote the average over particles in an event. Thus, generalized 2nd order cumulant can be written as,

$$c_n\{2\} = \langle\langle 2\rangle\rangle_{n|n} - \frac{\sum_{i=1}^{N}(\langle\cos n\phi\rangle)_i}{\sum_{i=1}^{N} M_i} - \frac{\sum_{i=1}^{N}(\langle\sin n\phi\rangle)_i}{\sum_{i=1}^{N} M_i} \tag{5.11}$$

- **Generalized 4^{th} order Q-Cumulant:** The generalized 4^{th} order cumulant in the case of detectors with non-uniform acceptance is corrected as:

$$\begin{aligned}
c_n\{4\} = {} & \langle\langle\cos n(\phi_1 + \phi_2 - \phi_3 - \phi_4)\rangle\rangle - 2\,.\,\langle\langle\cos n(\phi_1 - \phi_2)\rangle\rangle^2 \\
& - 4\,.\,\langle\langle\cos n(\phi_1)\rangle\rangle\,\langle\langle\cos n(\phi_1 - \phi_2 - \phi_3)\rangle\rangle \\
& + 4\,.\,\langle\langle\sin n(\phi_1)\rangle\rangle\,\langle\langle\sin n(\phi_1 - \phi_2 - \phi_3)\rangle\rangle \\
& - \langle\langle\cos n(\phi_1 + \phi_2)\rangle\rangle^2 - \langle\langle\sin n(\phi_1 + \phi_2)\rangle\rangle^2 \\
& + 4\,.\,\langle\langle\cos n(\phi_1 + \phi_2)\rangle\rangle\,[\langle\langle\cos n\phi_1\rangle\rangle^2 - \langle\langle\sin n\phi_1\rangle\rangle^2] \\
& + 8\,.\,\langle\langle\sin n(\phi_1 + \phi_2)\rangle\rangle\langle\langle\sin n\phi_1\rangle\rangle\langle\langle\cos n\phi_1\rangle\rangle \\
& + 8\,.\,\langle\langle\cos n(\phi_1 - \phi_2)\rangle\rangle\,[\langle\langle\cos n\phi_1\rangle\rangle^2 + \langle\langle\sin n\phi_1\rangle\rangle^2] \\
& - 6\,.\,[\langle\langle\cos n\phi_1\rangle\rangle^2 + \langle\langle\sin n\phi_1\rangle\rangle^2]^2
\end{aligned} \tag{5.12}$$

The terms beginning from the second line in Eq. 5.12 counterbalance the bias caused by non-uniform acceptance so that $c_n\{4\}$ is unbiased [18–21]. These terms in red can be decomposed into the real and imaginary parts of Q-vectors, like:

$$\langle\langle\cos n(\phi_1 + \phi_2)\rangle\rangle = \frac{\sum_{i=1}^{N}(\Re e[Q_nQ_n - Q_{2n}])_i}{\sum_{i=1}^{N} M_i(M_i - 1)} \tag{5.13}$$

$$\langle\langle \sin n(\phi_1 + \phi_2)\rangle\rangle = \frac{\sum_{i=1}^{N}(\Im m[Q_nQ_n - Q_{2n}])_i}{\sum_{i=1}^{N} M_i(M_i-1)} \tag{5.14}$$

$$\langle\langle \cos n(\phi_1 - \phi_2 - \phi_3)\rangle\rangle = \frac{\sum_{i=1}^{N}(\Re e\ [Q_nQ_n^*Q_n^* - Q_nQ_{2n}^* - 2(M_i-1)Q_n^*])_i}{\sum_{i=1}^{N} M_i(M_i-1)(M_i-2)} \tag{5.15}$$

$$\langle\langle \sin n(\phi_1 - \phi_2 - \phi_3)\rangle\rangle = \frac{\sum_{i=1}^{N}(\Im m\ [Q_nQ_n^*Q_n^* - Q_nQ_{2n}^* - 2(M_i-1)Q_n^*])_i}{\sum_{i=1}^{N} M_i(M_i-1)(M_i-2)} \tag{5.16}$$

- **Generalized 3^{rd} order Q-Cumulant:** The three particles general formulae for the Cumulant with the acceptance correction [26] is given below:

$$\begin{aligned} QC\{3\} = \langle\langle \cos n(\phi_1 + \phi_2 - 2\phi_3\rangle\rangle \\ &- \ 2\ \langle\langle \cos n(\phi_1 - 2\phi_2)\rangle\rangle\ \langle\langle \cos n\phi_1\rangle\rangle \\ &+ \ \langle\langle \sin n(\phi_1 - 2\phi_2)\rangle\rangle\ \langle\langle \sin n\phi_1\rangle\rangle \\ &- \ \langle\langle \cos n(\phi_1 + \phi_2)\rangle\rangle\ \langle\langle \cos 2\phi_1\rangle\rangle \\ &- \ \langle\langle \sin n(\phi_1 + \phi_2)\rangle\rangle\ \langle\langle \sin 2\phi_1\rangle\rangle \\ &+ \ 2\ \langle\langle \cos 2n\phi_1\rangle\rangle\ [\langle\langle \cos n\phi_1\rangle\rangle^2 - \langle\langle \sin n\phi_1\rangle\rangle^2] \\ &+ \ 4\ \langle\langle \sin 2n\phi_1\rangle\rangle\ [\langle\langle \cos n\phi_1\rangle\rangle\ \langle\langle \sin n\phi_1\rangle\rangle] \end{aligned} \tag{5.17}$$

These terms are decomposed into real and imaginary parts as:

$$\langle\langle \cos n(\phi_1 - 2\phi_2)\rangle\rangle = \frac{\sum_{i=1}^{N}(\Re e\ [Q_nQ_{2n}^* - Q_n^*])_i}{\sum_{i=1}^{N} M_i(M_i-1)} \tag{5.18}$$

$$\langle\langle \sin n(\phi_1 - 2\phi_2)\rangle\rangle = \frac{\sum_{i=1}^{N}(\Im m\ [Q_nQ_{2n}^* - Q_n^*])_i}{\sum_{i=1}^{N} M_i(M_i-1)} \tag{5.19}$$

By including these correction terms in the calculations, one can obtain more accurate results for cumulants and multi-particle correlations, ensuring that the effects of detector non-uniformity are properly accounted for. This approach is particularly important when working with detectors that exhibit small deviations from perfect uniform acceptance, allowing for a more precise analysis of the data and reducing potential biases.

5.5 Background Estimation

In this analysis, two types of background contributions are considered: Charge Shuffle background (ChS) and Correlated background (Corr).

Charge Shuffle background (ChS): It refers to the contribution from random combinations of charges, where the charges of particles are shuffled randomly while keeping their momenta (i.e., θ and ϕ) unchanged. This background estimation helps in understanding the level of charge correlations that can occur purely by chance. The value of γ for the "ChS" events' sample is determined for a specific bin of f_{DbCS} and is referred to as γ_{ChS}.

Correlated background (Corr): This on the other hand, accounts for correlations arising from non-CME effects, such as collective flow or resonance decays. It represents the background signal that is not related to the Chiral Magnetic Effect but can manifest as charge correlations. This is recovered from the corresponding original events in a particular f_{DbCS} bin and termed as correlated background γ_{Corr}.

Thus, the total background contribution to the γ-correlator is given by:

$$\gamma_{Bkg} = \gamma_{ChS} + \gamma_{Corr} \tag{5.20}$$

5.6 Results and Discussion

In the following sections, we present the centrality dependence of 2- (δ) and 3- (γ) particle correlators for different charge combinations (i.e., same charges: + +, - - and opposite charges: + -) along with differences between the opposite and same charge pairs.

5.6.1 δ-correlator

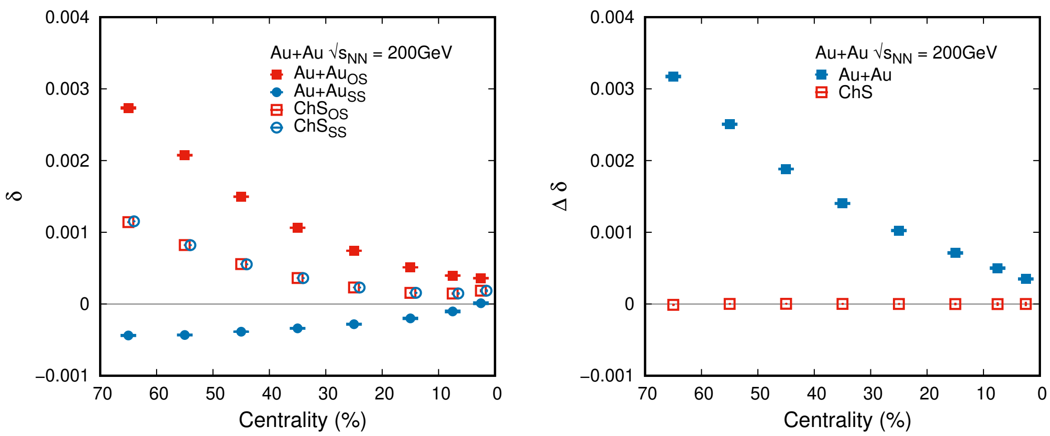

Figure 5.6: (Left) The dependence of δ correlator for opposite sign (OS) and same sign (SS) charge pairs on collision centralities for Au+Au collisions at $\sqrt{s_{NN}} = 200$ GeV and its charge shuffled (ChS) event sample. (Right) Centrality dependence of $\Delta\delta$ correlator for Au+Au collisions and ChS background. The statistical (bars) and systematic (boxes) errors are relatively small, falling within the marker sizes.

The centrality dependence of the 2-particle (δ) correlator is examined for both opposite sign (OS) and same sign (SS) charge pairs for Au+Au collisions at $\sqrt{s_{NN}}$ = 200 GeV and its charge shuffled background (ChS). Additionally, the correlator $\Delta\delta$ (=$\delta_{OS} - \delta_{SS}$) is investigated. The corresponding results are presented in Fig. 5.6. For OS charge pairs (red markers), the 2-particle correlations exhibit positive values that increase with decreasing collision centrality. For SS charge pairs, the correlation values are negative and become more negative with decreasing collision centrality. For the ChS background, both SS and OS charge pairs are positive and agree within uncertainties. Furthermore, these correlations increase with decreasing collision centrality and are useful for the CME investigation as discussed in Chapter 4. Figure 5.6 (Right) exhibits the dependence of the $\Delta\delta$ on collision centrality. It is observed that $\Delta\delta$ is positive and decreases with increasing centrality. The statistical errors are relatively small, falling within the marker sizes, and the systematic errors are shown in boxes. Table 5.5 and table 5.6 presents a summary of the sources of systematic errors and their corresponding fractional values for the opposite sign and same sign δ correlators, respectively, for Au+Au collisions at $\sqrt{s_{NN}} = 200$ GeV.

Sources	Centrality							
	60-70%	50-60%	40-50%	30-40%	20-30%	10-20%	5-10%	0-5%
V_z	0.0017	0.00126	0.0011	0.001	0.00077	0.00082	0.0022	0.0054
DCA	0.00175	0.0013	0.0012	0.00092	0.00012	0.00046	0.00298	0.0056
nHIT	0.0020	0.0011	0.0012	0.00095	0.00059	0.00097	0.0025	0.0053
Total	0.0031	0.00214	0.0020	0.0017	0.00099	0.0014	0.0044	0.0094

Table 5.5: The values of fractional systematic uncertainty for δ-correlator for opposite sign (δ_{OS}) charge pairs in Au+Au collisions at $\sqrt{s_{NN}} = 200$ GeV.

Sources	Centrality							
	60-70%	50-60%	40-50%	30-40%	20-30%	10-20%	5-10%	0-5%
V_z	0.00785	0.0074	0.0016	0.0085	0.013	0.025	0.066	0.60
DCA	0.0098	0.0071	0.0016	0.0092	0.013	0.024	0.065	0.58
nHIT	0.0097	0.0078	0.0015	0.0095	0.014	0.025	0.068	0.62
Total	0.016	0.013	0.0027	0.016	0.023	0.043	0.12	1.05

Table 5.6: The values of fractional systematic uncertainties for δ-correlator for same sign (δ_{SS}) charge pairs in Au+Au collisions at $\sqrt{s_{NN}} = 200$ GeV.

5.6.2 Elliptic flow (v_2)

Figure 5.7 illustrates the centrality dependence of the elliptic flow (v_2) for Au+Au collisions at $\sqrt{s_{NN}} = 200$ GeV. The v_2 values are calculated using the 2-particle ($v_2\{2\}$) and 4-particle ($v_2\{4\}$) Q-cumulant methods. The $v_2\{2\}$ increases as collision centrality decreases and reaches a plateau for centralities between 40-60%. The value of $v_2\{2\}$ is higher compared to $v_2\{4\}$ due to the presence of non-flow effects, which cannot be removed from $v_2\{2\}$. To calculate the three-particle correlations, the average of $v_2\{2\}$ and $v_2\{4\}$ is taken, denoted as $v_2^{mean} = \frac{v_2\{2\}+v_2\{4\}}{2.0}$.

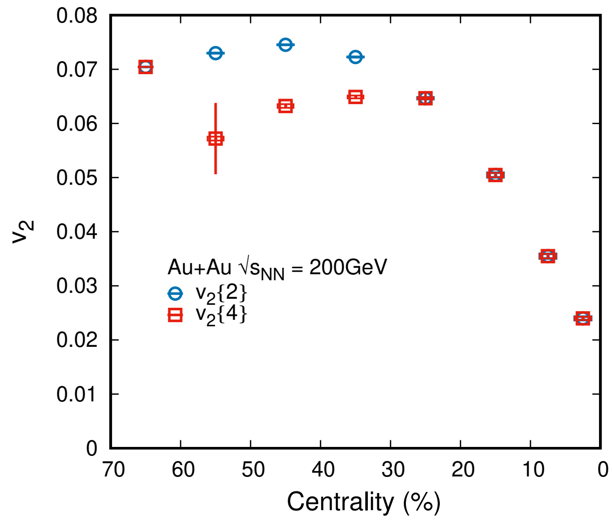

Figure 5.7: Elliptic flow (v_2) measurements using Q-cumulant method in Au+Au collisions at $\sqrt{s_{NN}} = 200$ GeV as a function of collision centrality.

5.6.3 γ-correlator

Figure 5.8 (Left) depicts the centrality dependence of the 3-particle (γ) correlator for different charge combinations, including same-sign (SS: + +, - -) and opposite-sign (OS: + -) charge pairs. The γ-correlator for SS charge pairs exhibits negative correlations, while for OS charge pairs, the correlations are positive. Additionally, the magnitude of correlations is larger for SS charge pairs compared to OS charge pairs within the centrality range of 10-70%. Furthermore, the magnitude of correlations (for both OS and SS) decreases as collision centrality increases. For the ChS background, the correlations are negative for both SS and OS charge pairs and agree within uncertainties. Moreover, the magnitude of correlations increases with decreasing collision centrality for both SS and OS charge pairs.

Figure 5.8 (Right) illustrates the centrality dependence of the $\Delta\gamma$ correlator for Au+Au collisions and the ChS background. For Au+Au collisions, the magnitude of the $\Delta\gamma$ correlator is positive for each centrality and increases as collision centrality decreases. This positive $\Delta\gamma$ correlator is considered as a signal for the Chiral Magnetic Effect (CME). On the other hand, for the ChS background, the $\Delta\gamma$ correlator is approximately zero within the uncertainties for all collision centralities. The

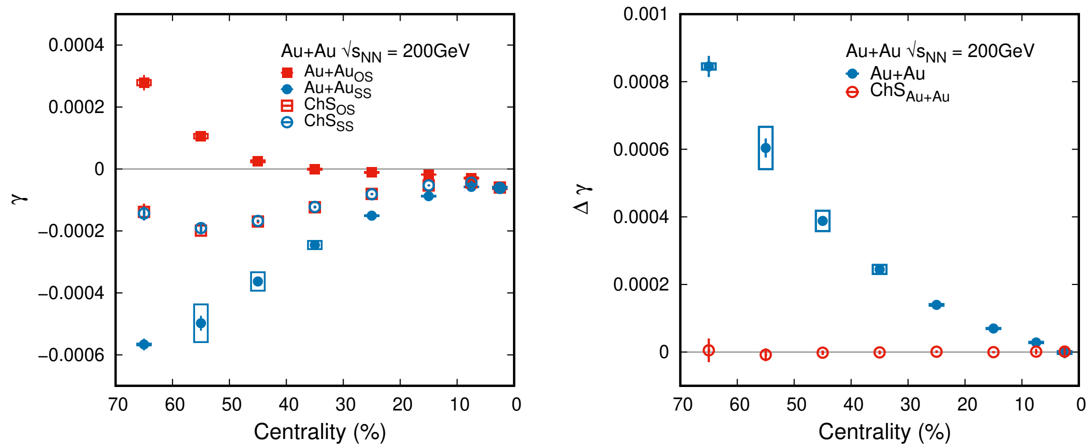

Figure 5.8: (Left) The dependence of γ correlator for opposite sign (OS) and same sign (SS) charge pairs on collision centralities for Au+Au collisions at $\sqrt{s_{NN}} = 200$ GeV and charge shuffled (ChS) background. (Right) The centrality dependence of $\Delta\gamma$ correlator for Au+Au collisions and ChS background.

Sources	Centrality							
	60-70%	50-60%	40-50%	30-40%	20-30%	10-20%	5-10%	0-5%
V_z	0.0178	0.0336	0.0818	1.26	0.079	0.00347	0.0377	0.0345
DCA	0.0206	0.0438	0.0936	1.486	0.096	0.0040	0.030	0.038
nHIT	0.0149	0.046	0.050	1.35	0.084	0.0020	0.033	0.035
v_2	0	0.12	0.08	0.054	0	0	0	0
Total	0.031	0.072	0.13	2.37	0.15	0.0057	0.059	0.062

Table 5.7: The values of fractional systematic uncertainties for γ-correlator for opposite sign (γ_{OS}) charge pairs in Au+Au collisions at $\sqrt{s_{NN}} = 200$ GeV.

Sources	Centrality							
	60-70%	50-60%	40-50%	30-40%	20-30%	10-20%	5-10%	0-5%
V_z	0.0029	0.0055	0.00069	0.0042	0.0044	0.0060	0.0177	0.033
DCA	0.0038	0.0069	0.00061	0.0029	0.0042	0.0034	0.0185	0.035
nHIT	0.00241	0.0070	0.0013	0.0036	0.0051	0.0041	0.0148	0.032
v_2	0	0.12	0.08	0.054	0	0	0	0
Total	0.0054	0.011	0.0016	0.0062	0.0080	0.0080	0.030	0.058

Table 5.8: The values of fractional systematic uncertainties for γ-correlator for same sign (γ_{OS}) charge pairs in Au+Au collisions at $\sqrt{s_{NN}} = 200$ GeV.

statistical errors associated with the measurements are very small and fall within the marker sizes, while the systematic errors are represented as boxes. Table 5.7 and table 5.8 lists the systematic error sources and their associated fractional values for the opposite sign and same sign γ correlators, respectively, across various collision centralities in Au+Au collisions at $\sqrt{s_{NN}}$ = 200 GeV.

5.6.4 In-plane and out-of-plane correlator

The in-plane ($\sim \langle \cos(\Delta\phi_i)\cos(\Delta\phi_j)\rangle$) and out-of-plane ($\sim \langle \sin(\Delta\phi_i)\sin(\Delta\phi_j)\rangle$) correlations can be obtained from δ and γ correlators as:

$$\langle cos\Delta\phi_\alpha cos\Delta\phi_\beta\rangle = \frac{\delta+\gamma}{2} \tag{5.21}$$

$$\langle sin\Delta\phi_\alpha sin\Delta\phi_\beta\rangle = \frac{\delta-\gamma}{2} \tag{5.22}$$

The out-of-plane correlations are sensitive to the CME [27]. Figure 5.9 displays the

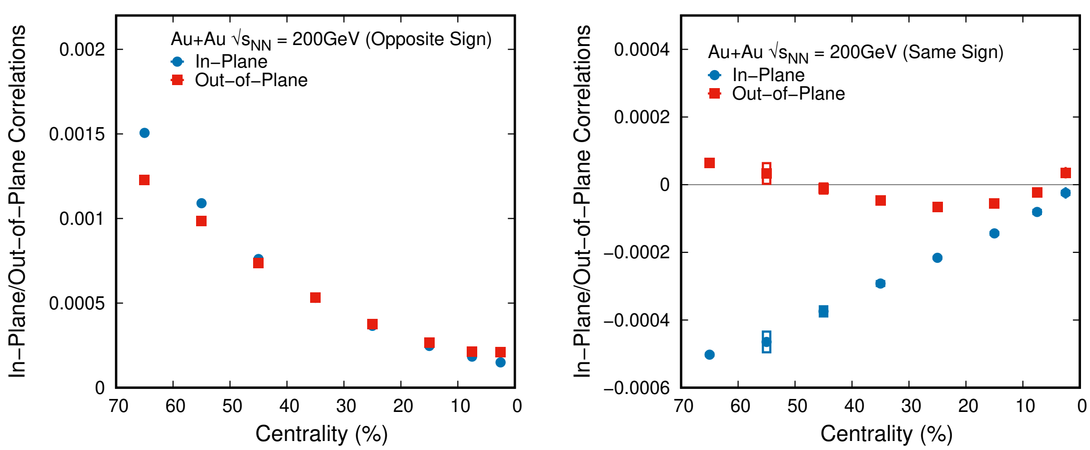

Figure 5.9: Centrality dependence of in-plane and out-of-plane correlator for OS (Left) and SS (Right) charge pairs for Au+Au collisions at $\sqrt{s_{NN}}$=200 GeV.

in-plane (blue circle marker) and out-of-plane (red square marker) correlations for opposite sign (OS) and same sign (SS) charge pairs in Au+Au collisions. For OS charge pairs, the in-plane, and out-of-plane correlations agree within uncertainties for the 0-50% collision centrality range. However, for the 50-70% collision centrality range, the magnitude of the out-of-plane correlations is lower compared to the in-plane correlations. Additionally, it is observed that the correlations increase as the collision centrality decreases. In the case of SS charge pairs, the in-plane correlations are negative, and their magnitude increases and becomes more negative with decreasing collision centrality. On the other hand, the out-of-plane correlations are positive for the 50-70% collision centrality range and negative for higher collision centralities. This indicates that the back-to-back charge separation is in-plane, contrary to the CME expectation where one expects the charge separation perpendicular to the reaction plane in non-central heavy-ion collisions [28]. This charge separation is driven by the interplay between the axial charge current and the external magnetic field.

Further investigations and refinements in the analysis techniques may be necessary to better understand the observed trend and determine the underlying physics responsible for the measured charge correlations.

5.7 Results with SDM

In this section, we will present the findings obtained through the application of the Sliding Dumbbell Method (SDM) [4–6]. The SDM systematically scans the entire azimuthal plane using a dumbbell-shaped region spanning 90 degrees. This method enables us to examine the fractional charge separation across the dumbbell, quantified by the parameter $f_{DbCS} = Db_{+-}^{max} - 1$, as explained in the preceding chapter. When applying the SDM, the charge shuffled background (ChS) is treated in the same manner as the Au+Au data. By employing the SDM and appropriately handling background effects, our analysis aims to discern any potential genuine charge separation signal associated with the phenomenon under investigation. The results obtained through the SDM shed light on the degree of charge separation and its characteristics within the studied system.

5.7.1 f_{DbCS} distributions

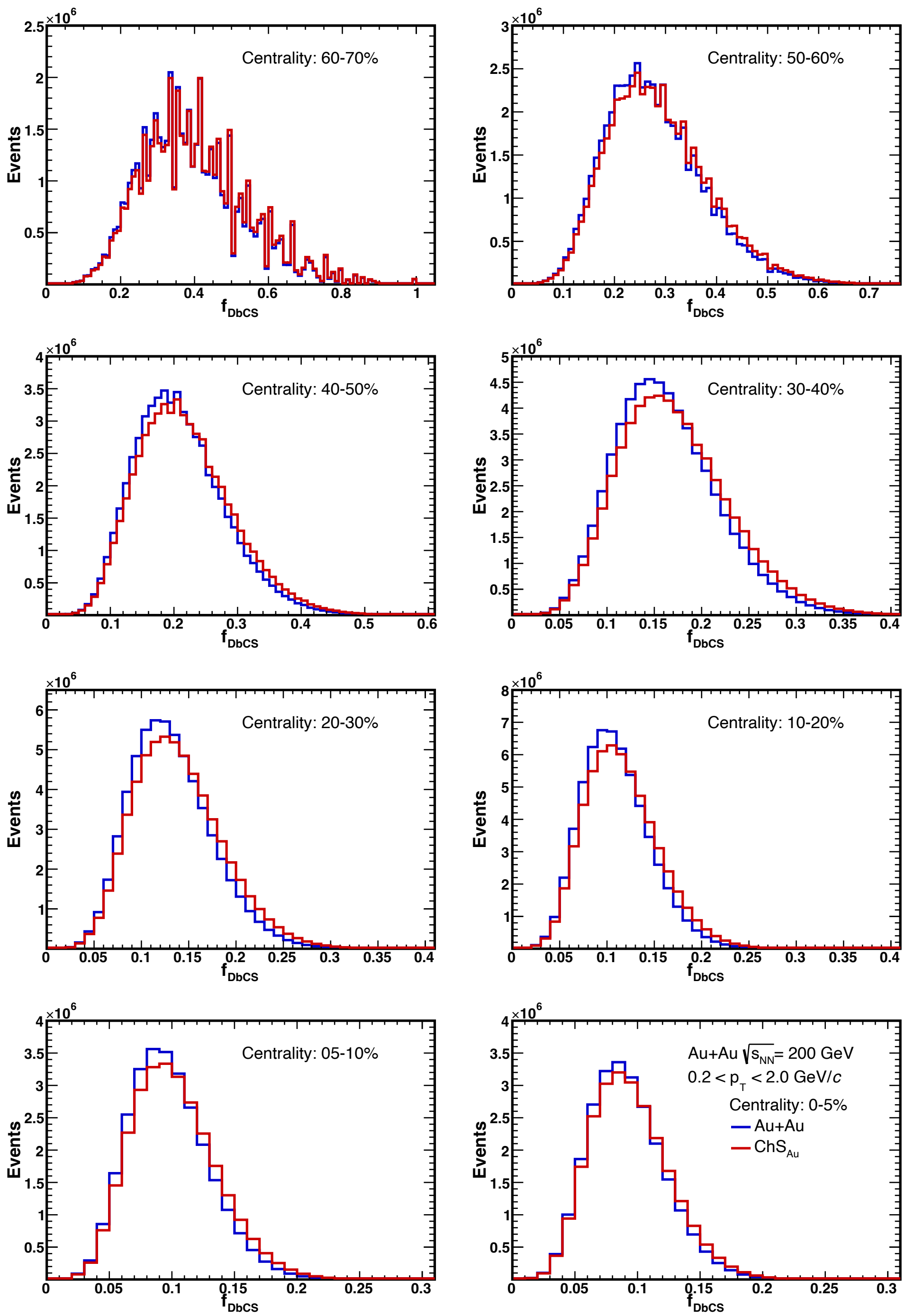

Figure 5.10: Comparison of f_{DbCS}^{Au+Au} distributions with f_{DbCS}^{ChS} for different collision centralities in Au+Au collisions at $\sqrt{s_{NN}}$=200 GeV.

Figure 5.10 depicts the distributions of f_{DbCS} for Au+Au collisions, along with their corresponding f_{DbCS}^{ChS} distributions obtained from charge shuffle background. It is observed that the f_{DbCS}^{ChS} distributions consistently exhibit a little higher values than the f_{DbCS}^{Au+Au} distributions across all collision centralities. Moreover, both the Au+Au data and the ChS background distributions shift towards higher values of f_{DbCS} as the collision centrality decreases.

Figure 5.11 presents the scatter plots for 30-40% (Left) and 50-60% (Right) collision centralities. It is observed that there is no correlation between the f_{DbCS} of the real events (f_{DbCS}^{Au+Au}) and f_{DbCS} of the charge shuffled events (f_{DbCS}^{ChS}).

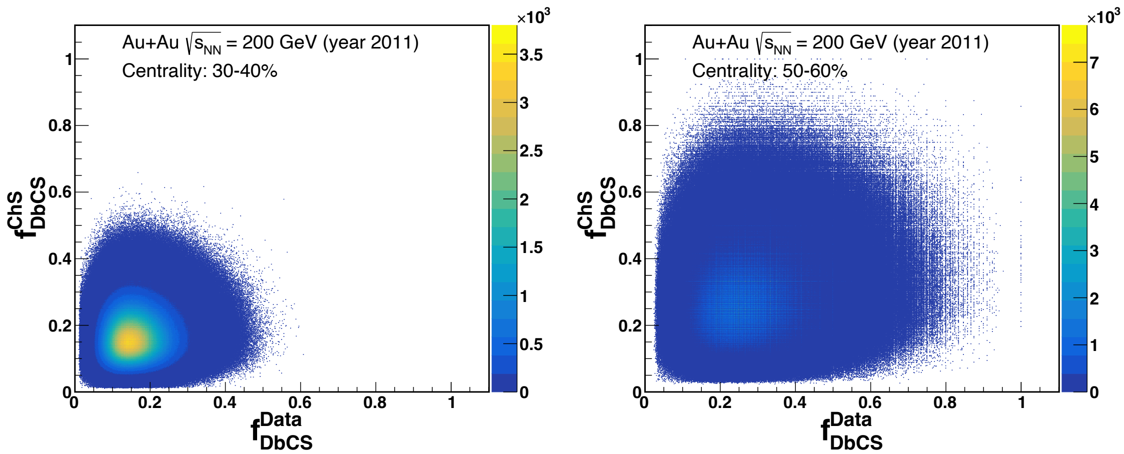

Figure 5.11: Scatter plot of f_{DbCS}^{Au+Au} versus f_{DbCS}^{ChS} for 30-40% (Left) and 50-60% (Right) collision centralities for Au+Au collisions at $\sqrt{s_{NN}}$ = 200 GeV.

In the forthcoming section, we will discuss the dependence of f_{DbCS} on various physics observables for collision centrality range of 0-70%.

5.7.2 v_2 dependence on f_{DbCS}

The dependence of elliptic flow (v_2) on f_{DbCS} for Au+Au collisions in the 0-70% collision centrality range is depicted in Fig. 5.12. The figure illustrates that the top f_{DbCS} bins shows a higher v_2 and it decreases in the lower f_{DbCS} bins. In the 40-60% collision centrality range, the values of $v_2\{4\}$ are lower compared to $v_2\{2\}$ due to the presence of non-flow contributions in $v_2\{2\}$. The statistical uncertainties are indicated by the bars, while the systematic uncertainties are represented by the boxes.

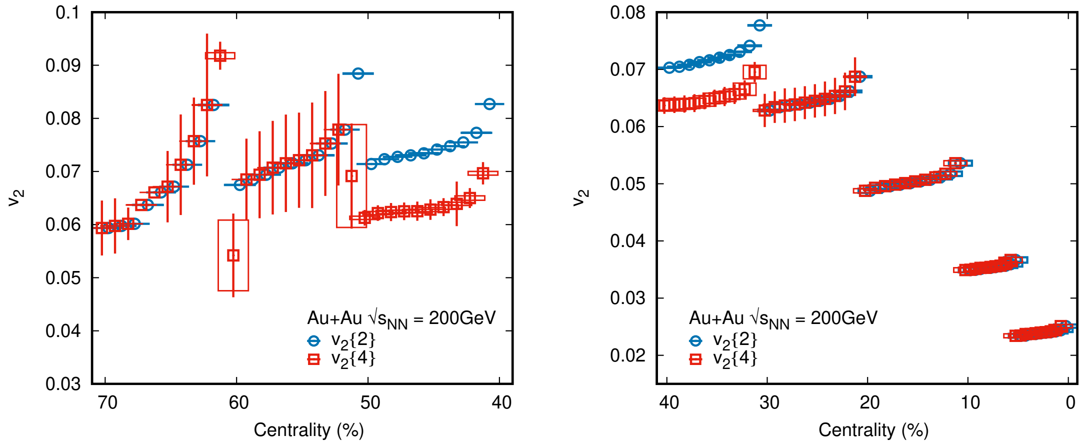

Figure 5.12: The charge separation (f_{DbCS}) dependence of $v_2\{2\}$ and $v_2\{4\}$ for Au+Au collisions at $\sqrt{s_{NN}}$ = 200 GeV. The right column plots are for 0-40% collision centralities and the left column plots for 40-70% centralities and Y-axes for 0-40% collision centralities are magnified for the sake of clarity.

5.7.3 δ-correlator's dependence on f_{DbCS}

Figure 5.13 displays the dependence of the δ-correlator for opposite sign (OS) and same sign (SS) charge pairs on f_{DbCS} for Au+Au collisions at $\sqrt{s_{NN}}$ = 200 GeV in the 0-70% collision centrality range. δ-correlator for OS charge pairs are represented in red color while SS charge pairs are represented in blue color. For OS charge pairs δ-correlator shows negative values for top f_{DbCS} bins while for lower f_{DbCS} bins they become positive. An opposite trend is seen for the same sign charge pairs. δ-correlator values are positive for SS charge pairs in the top f_{DbCS} bins and they become negative in the lower f_{DbCS} bins. This trend is opposite to average values of δ-correlator (Fig. 5.6) where OS charge pairs show positive correlations and SS charge pairs show negative correlations. In the case of CME, we expect δ_{SS} to be positive and δ_{OS} to be negative. It is seen that for 0-70% collision centralities $\delta_{SS} > 0$ for the top f_{DbCS} bins, indicating a CME enriched sample.

5.7.4 γ-correlator's dependence on f_{DbCS}

The charge separation (f_{DbCS}) dependences of γ-correlator for opposite sign and same sign charge pairs are displayed in Fig. 5.14 (OS) and Fig. 5.15 (SS), respec-

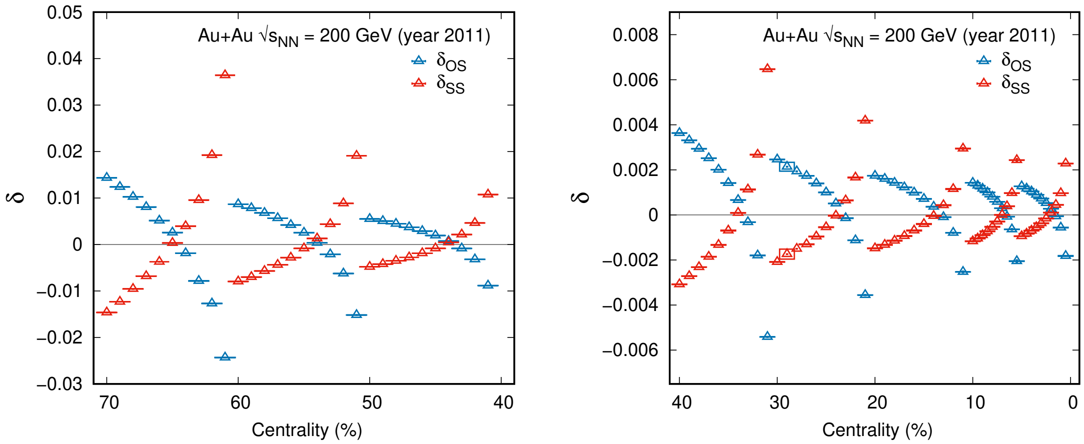

Figure 5.13: The charge separation (f_{DbCS}) dependence of δ-correlator for opposite and same sign charge pairs for Au+Au collisions at $\sqrt{s_{NN}}$ = 200 GeV. The right column plots are for 0-40% collision centralities and the left column plots for 40-70% centralities and Y-axes for 0-40% collision centralities are magnified for the sake of clarity.

tively, for Au+Au collisions at $\sqrt{s_{NN}}$ = 200 GeV. The figures also include the charge shuffled (ChS) and correlated (Corr) backgrounds for 0-70% collision centralities. The right column plots are for 0-40% collision centralities and the left column plots for 40-70% centralities and Y-axes for 0-40% collision centralities are magnified for the sake of clarity. The values of γ's (OS and SS) in the top f_{DbCS}

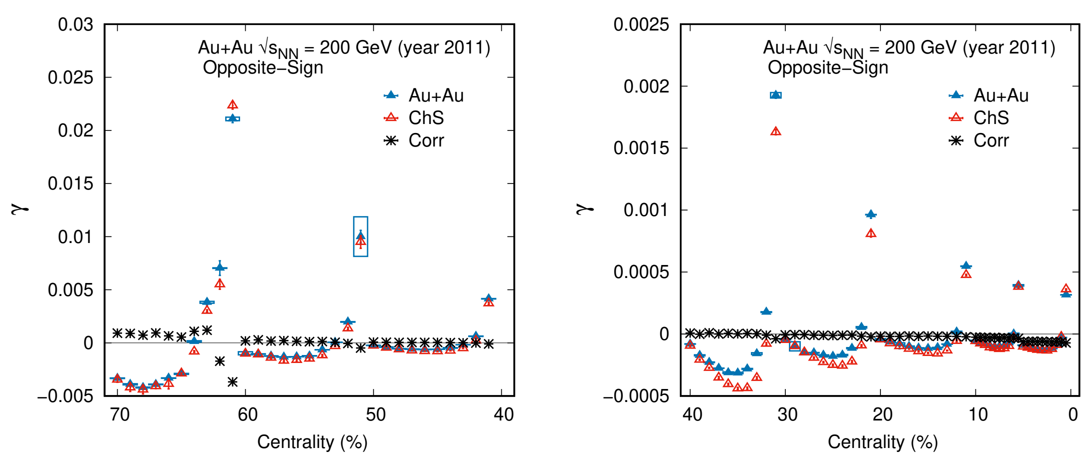

Figure 5.14: The charge separation (f_{DbCS}) dependence of γ-correlator for opposite sign charge pairs for Au+Au collisions at $\sqrt{s_{NN}}$ = 200 GeV. The right column plots are for 0-40% collision centralities and the left column plots for 40-70% centralities and Y-axes for 0-40% collision centralities are magnified for the sake of clarity.

bins exhibit a significant increase compared to the average values shown in Fig. 5.8 (Left). Specifically, it is observed that $\gamma_{OS} > 0$ and $\gamma_{SS} < 0$ corresponding to top f_{DbCS} bins (i.e., for 0-20% (0-30%) f_{DbCS} for 0-60% (60-70%) collision centrality), as expected for CME-like events. Notably, it is observed that $\mid \gamma_{OS} \mid$ is approximately equal to $\mid \gamma_{SS} \mid$ for the top f_{DbCS} bins, representing the highest back-to-back charge separation across the dumbbell. The charge shuffle background also exhibits a sig-

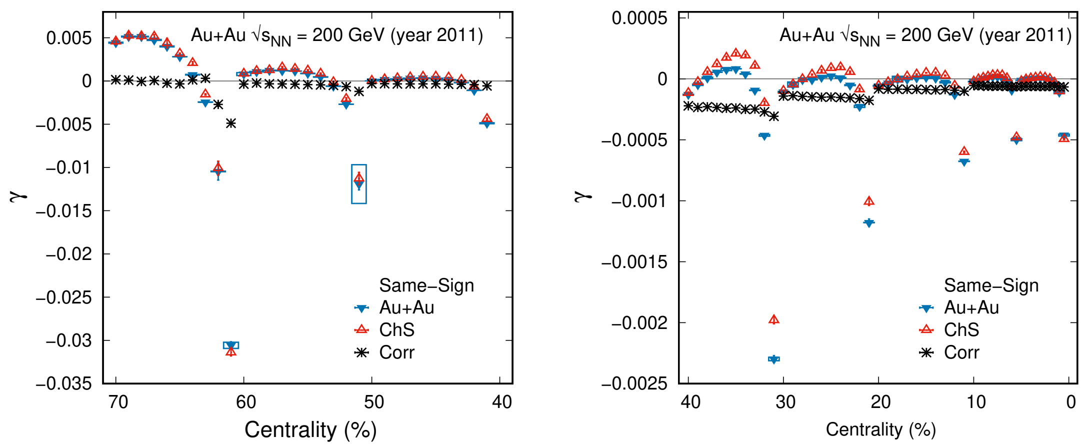

Figure 5.15: The charge separation (f_{DbCS}) dependence of γ-correlator for same sign charge pairs for Au+Au collisions at $\sqrt{s_{NN}} = 200$ GeV. The right column plots are for 0-40% collision centralities and the left column plots for 40-70% centralities and Y-axes for 0-40% collision centralities are magnified for the sake of clarity.

nificantly higher enhancement and follows a similar trend, although its values are lower compared to those of the Au+Au data for the top f_{DbCS} bins across 10-60% collision centralities. The correlated background shows positive correlations for OS charge pairs and negative correlations for SS charge pairs across 10-70% collision centrality. The correlated background values remain approximately constant within uncertainties for all f_{DbCS} bins within each collision centrality, while their magnitude gradually increases with decreasing collision centrality. The systematic uncertainties are represented by boxes, while the statistical uncertainties are indicated by bars. The statistical uncertainties are negligible and fall within the marker sizes.

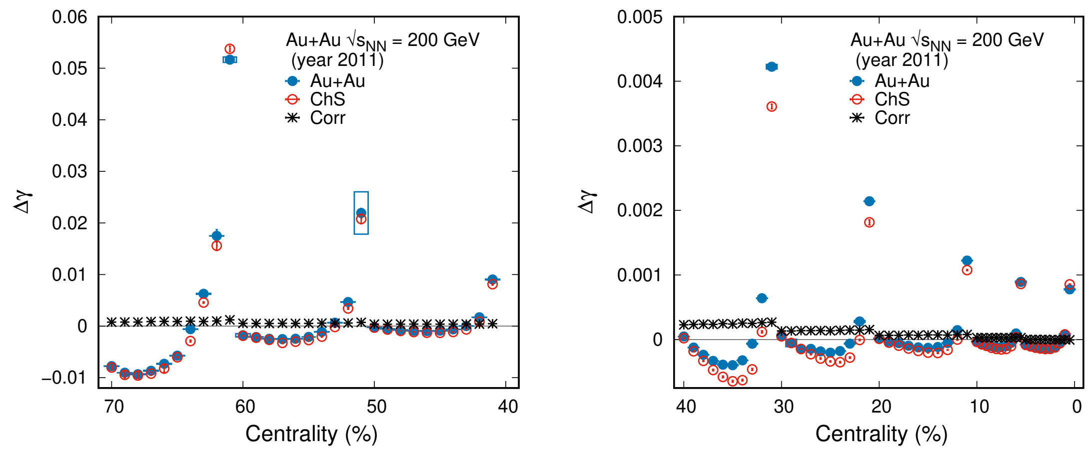

Figure 5.16: The charge separation (f_{DbCS}) dependence of $\Delta\gamma$-correlator ($\Delta\gamma$=$\gamma_{OS} - \gamma_{SS}$) for Au+Au collisions at $\sqrt{s_{NN}}$ = 200 GeV. The right column plots are for 0-40% collision centralities and the left column plots for 40-70% centralities and Y-axes for 0-40% collision centralities are magnified for the sake of clarity.

5.7.5 $\Delta\gamma$-correlator's dependence on f_{DbCS}

Figure 5.16 displays the dependence of $\Delta\gamma$ on f_{DbCS} for 0-70% collision centrality for Au+Au collisions at $\sqrt{s_{NN}}$ = 200 GeV. It is seen that $\Delta\gamma$ is positive for the top 20% (30%) f_{DbCS} bins for 0-60%(60-70%) centralities. The values of $\Delta\gamma$'s in the top f_{DbCS} bins has increased many times higher than the average values shown in Fig. 5.8(Right). Boxes represent the systematic errors while the bars represent the statistical errors. Statistical uncertainties are too small and are within the marker sizes. $\Delta\gamma$-correlator for charge shuffled background (ChS) is represented by red circles while the correlated background is shown by black crosses in Fig. 5.16. $\Delta\gamma_{ChS}$ exhibits the similar trend as Au+Au data while $\Delta\gamma_{Corr}$ has approximately same values for all f_{DbCS} bins within each collision centrality. It is observed that, $\Delta\gamma_{ChS} < \Delta\gamma_{data}$ for the top 20% (30%) f_{DbCS} bins for 10-60% (60-70%) collision centralities. Furthermore, the total background, $\Delta\gamma_{ChS} + \Delta\gamma_{Corr}$, is lower than $\Delta\gamma_{data}$ in the top f_{DbCS} bins, as expected for CME-like events. These observations indicate the presence of a CME-like enriched sample.

The normalized $\Delta\gamma^{Norm}$ defined as $\Delta\gamma^{Norm} = \frac{\Delta\gamma_{(Top10\% f_{DbCS})}}{\Delta\gamma_{(Avg.)}}$ is presented for top 10% f_{DbCS} in Fig. 5.17. It is observed that $\Delta\gamma^{Norm}$ in the top 10% f_{DbCS} bins

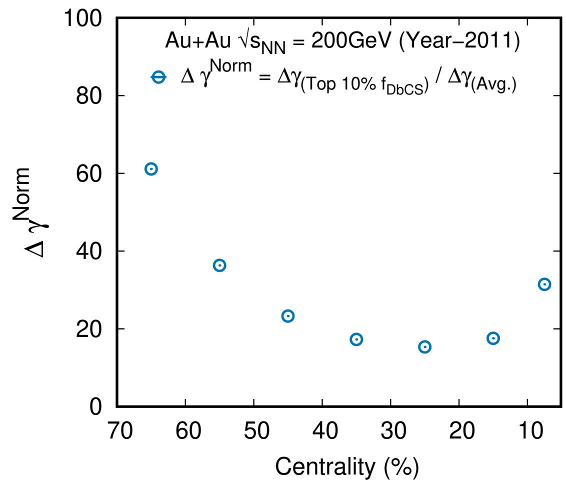

Figure 5.17: $\Delta\gamma^{Norm}$ $(= \frac{\Delta\gamma_{(Top10\% f_{DbCS})}}{\Delta\gamma_{(Avg.)}})$ for different centralities for Au+Au collisions at $\sqrt{s_{NN}} = 200$ GeV.

is more than 15 for all collision centralities indicating a significant enhancement of $\Delta\gamma$ values. This may be due to CME contribution in the top 10% f_{DbCS} bins.

We will use $\Delta\gamma$ for Au+Au data, ChS, and Corr backgrounds to calculate the fraction of CME in the top f_{DbCS} bins where $\Delta\gamma > 0$ in the forthcoming section.

5.7.6 In-plane and out-of-plane correlator's dependence on f_{DbCS}

Figure 5.18 presents the dependence of in-plane (blue markers) and out-of-plane (red markers) correlations on f_{DbCS} for opposite charge combinations for 0-70% collision centralities for Au+Au collisions at $\sqrt{s_{NN}} = 200$ GeV. The out-of-plane correlations are negative for OS charge pairs in the top f_{DbCS} (i.e., top 20-30% f_{DbCS}) bins while the correlations become positive for lower f_{DbCS} bins. Similarly, the dependence of in-plane and out-of-plane correlations on f_{DbCS} for the same charge combinations is shown in Fig. 5.19 for 0-70% collision centralities. The out-of-plane correlations are positive for top f_{DbCS} bins and the trend becomes the opposite for lower f_{DbCS} bins for the same sign charge pairs.

Stronger correlations are seen in out-of-plane for both same-sign and opposite-

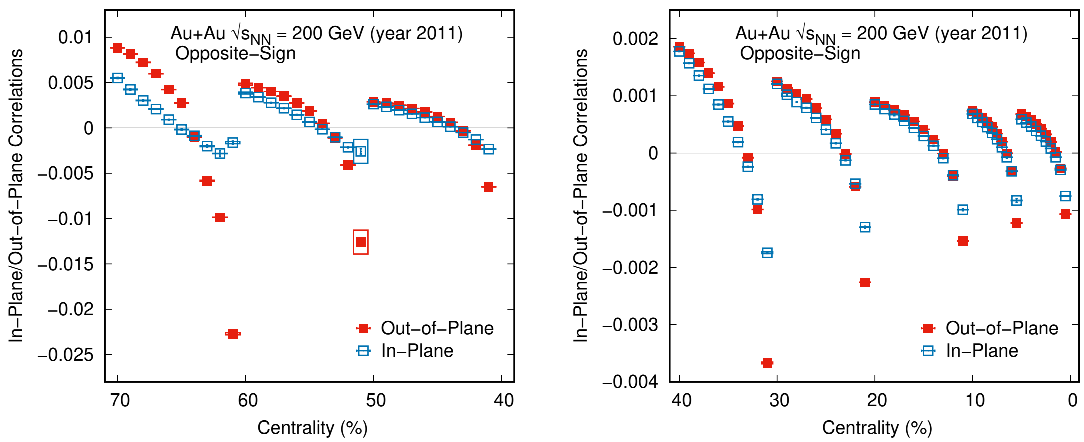

Figure 5.18: The charge separation (f_{DbCS}) dependence of in-plane and out-of-correlator for opposite sign charge pairs for Au+Au collisions at $\sqrt{s_{NN}} = 200$ GeV. The right column plots are for 0-40% collision centralities and the left column plots for 40-70% centralities and Y-axes for 0-40% collision centralities are magnified for the sake of clarity.

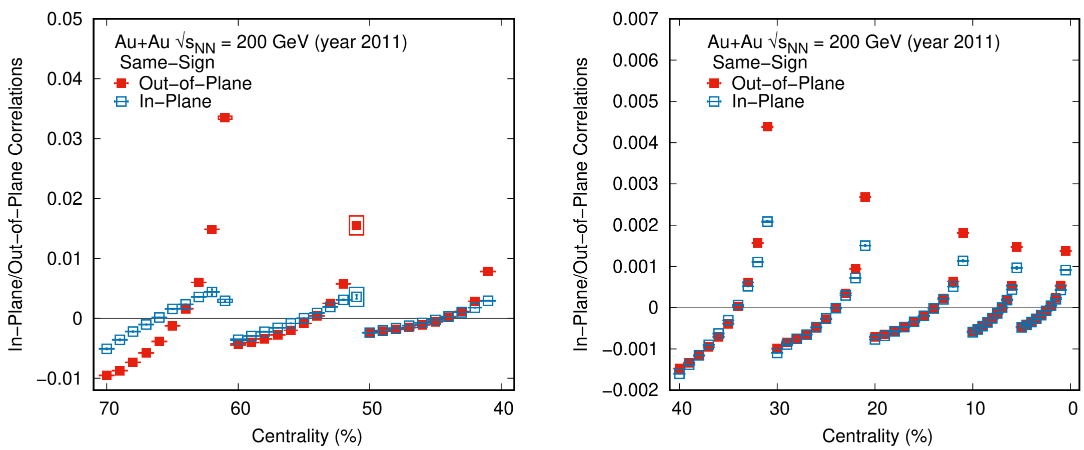

Figure 5.19: The charge separation (f_{DbCS}) dependence of in-plane and out-of-correlator for same sign charge pairs for Au+Au collisions at $\sqrt{s_{NN}} = 200$ GeV. The right column plots are for 0-40% collision centralities and the left column plots for 40-70% centralities and Y-axes for 0-40% collision centralities are magnified for the sake of clarity.

sign charge pairs due to out-of-plane charge separation for Au+Au collisions for top f_{DbCS} bins representing the highest back-to-back charge separation across the dumbbell.

5.7.7 CME fraction (f_{CME})

To calculate the CME fraction(f_{CME}) first we check $\Delta\gamma > 0$ for Au+Au data and get the total background which is the sum of charge shuffle (ChS) and correlated (Corr) backgrounds as shown in Fig. 5.16. The f_{CME} is calculated using the following equation:

$$f_{CME} = 1 - \frac{\Delta\gamma_{Bkg}}{\Delta\gamma_{data}} \\ \Delta\gamma_{Bkg} = \Delta\gamma_{ChS} + \Delta\gamma_{Corr} \tag{5.23}$$

We performed calculations of the f_{CME} values using the top 20% f_{DbCS} bins for

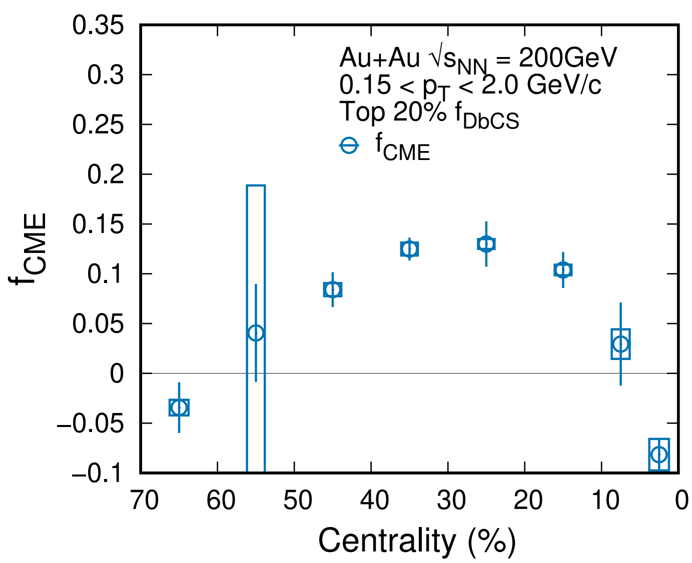

Figure 5.20: f_{CME} for 0-70% collision centralities for Au+Au collisions at $\sqrt{s_{NN}}$ = 200 GeV.

both the Au+Au data and the background events. By utilizing the Sliding Dumbbell Method (SDM), which identifies CME-enriched samples within these top f_{DbCS} bins, we were able to determine the CME fraction specifically for these selected bins using equation 5.23. Figure 5.20 illustrates the obtained f_{CME} results for collision centralities ranging from 0% to 70% in Au+Au collisions at $\sqrt{s_{NN}} = 200$ GeV. The data shows that f_{CME} ranges from approximately 8% to 13% for top 20% f_{DbCS} bins for collision centralities between 10% and 50%. However, for both the most central and peripheral collisions, the f_{CME} values are negative, indicating a lack of significant CME signal in these centrality ranges.

Overall, the analysis suggests that the f_{CME} values are highest in the 10% to 50% collision centrality range, where they range from approximately 8% to 13% for top 20% f_{DbCS} bins. In contrast, the f_{CME} values are negative for most central and peripheral collisions, indicating a different underlying physical mechanism or the absence of a CME signal in these centrality ranges.

5.8 Conclusion

The analysis was conducted on data from ${}^{197}_{79}$Au+${}^{197}_{79}$Au collisions collected by the STAR detector in 2011 at a center-of-mass energy of $\sqrt{s_{NN}} = 200$ GeV. The focus was on studying the dependence of the 2-particle (δ) and 3-particle (γ) correlators on collision centrality. It was observed that the CME-sensitive $\Delta\gamma$ decreased with increasing collision centrality, which was considered as a CME effect. However, it was noted that the correlations of same-sign charge pairs were in-plane, contrary to what is expected for the chiral magnetic effect (CME).

In this work, the Sliding Dumbbell Method (SDM) was employed to specifically search for back-to-back charge separation events on an event-by-event basis within each collision centrality. The correlators mentioned earlier were examined based on the charge separation across the dumbbell (f_{DbCS}) in each centrality. The f_{DbCS} distribution was divided into ten percentile bins to identify potential CME-like events with the highest back-to-back charge separation. To extract the fractional CME signal in the top f_{DbCS} bins, two types of backgrounds were considered. The Charge Shuffle background (ChS) involved random shuffling of charges while keeping their momenta unchanged, providing insight into the level of charge correlations that can occur by chance. The correlated background involved recovering correlations among particles from the original events within a specific f_{DbCS} bin, as discussed in the chapter.

The elliptic flow shows a slight increase in the top f_{DbCS} bins compared to the lower f_{DbCS} bins. The values of δ and γ correlators in the top f_{DbCS} bins showed a significant increase compared to the average values in a given centrality, both for same-sign and opposite-sign charge pairs. In the top f_{DbCS} bins, same-sign charge pairs exhibited negative γ correlators and positive δ correlators, while opposite-sign charge pairs displayed the opposite trend. Interestingly, both same-sign and opposite-sign charge pairs exhibited out-of-plane correlations due to the out-of-plane charge separation. These characteristics indicated that events in the top f_{DbCS} bins were the most potential CME-like events for a given collision centrality. Similar analyses were performed for the charge shuffled events and for correlated backgrounds to determine the fractional CME contribution in the top f_{DbCS} bins. The charge shuffled events also exhibited significant enhancements in both δ and γ correlators, showing similar trends for different charge combinations with reduced magnitudes in the top f_{DbCS} bins. The correlated background showed positive correlations for opposite-sign charge pairs and negative correlations for same-sign charge pairs across 10-70% collision centralities. The values of the correlated background remained approximately constant within uncertainties for all f_{DbCS} bins in each centrality, with their magnitude gradually increasing as collision centrality decreased.

Furthermore, $\Delta\gamma$ was positive for the top 20% (30%) f_{DbCS} bins in 0-60% (60-70%) collision centralities. The values of $\Delta\gamma$ in the top f_{DbCS} bins were significantly higher than the average values. $\Delta\gamma_{ChS}$ exhibited a similar trend as the Au+Au data, while $\Delta\gamma_{Corr}$ had approximately the same values for all f_{DbCS} bins within each centrality. It was observed that $\Delta\gamma_{ChS} < \Delta\gamma_{data}$ for the top 20% (30%) f_{DbCS} bins in 10-60% (60-70%) collision centralities. Moreover, the total background, $\Delta\gamma_{ChS}$ + $\Delta\gamma_{Corr}$, was lower than $\Delta\gamma_{data}$ in the top f_{DbCS} bins, as expected for CME-like events. These observations indicated the presence of a CME-like enriched sample for each collision centrality.

The CME fraction (f_{CME}) was calculated using the CME-sensitive $\Delta\gamma$-correlator in the top 20% f_{DbCS} bins. The f_{CME} ranged from approximately 8% to 13% for top 20% f_{DbCS} bins (obtained using SDM) in 10-50% collision centralities but showed negative values for most central and peripheral collisions. The CME-like events are observed in the top 20% f_{DbCS} bins whereas the rest of the 80% f_{DbCS} bins in a given centrality show no CME-like events. Glimpses of fractional CME were observed in the top 20% charge separation across the dumbbell (f_{DbCS}) in the given centrality range of 10-50% collision centralities.

Bibliography

[1] D. Kharzeev, "Parity violation in hot QCD: Why it can happen, and how to look for it", Phys. Lett. B 633, 260 (2006).

[2] K. Fukushima, D. E. Kharzeev, and H. J. Warringa, "Chiral magnetic effect", Phys. Rev. D 78, 074033 (2008).

[3] D. E. Kharzeev, L. D. McLerran, and H. J. Warringa, "The effects of topological charge change in heavy ion collisions: "Event by event P and CP violation"", Nucl. Phys. A 803, 227 (2008).

[4] Jagbir Singh, "Search for the Chiral Magnetic Effect using Sliding Dumbbell Method in Isobar Collisions ($^{96}_{44}Ru +^{96}_{44} Ru$ and $^{96}_{40}Zr +^{96}_{40} Zr$) at RHIC", Proceedings of the DAE Symp. Nucl. Phys. 66, 1048, (2022).

[5] Jagbir Singh, Anjali Attri, and Madan M. Aggarwal, "Charge dependent azimuthal correlations using Sliding Dumbbell Method to search CME in Au+Au Collisions with AMPT", Proceedings of the DAE Symp. Nucl. Phys. 64, 830, (2019).

[6] Anjali Attri, Jagbir Singh, Madan M. Aggarwal, "Event-by-Event Charge Separation in Au+Au Collisions at $\sqrt{s_{NN}}$ = 200 GeV Using AMPT", Springer Proc. Phys. 261, 1065 (2021).

[7] S. A. Voloshin, "Parity violation in hot QCD: How to detect it", Phys. Rev. C 70, 057901 (2004).

[8] B. I. Abelev *et al.* [STAR Collaboration], "Azimuthal Charged-Particle Correlations and Possible Local Strong Parity Violation", Phys. Rev. Lett. 103, 251601 (2009).

[9] A. Bzdak, V. Koch, and J. Liao, "Azimuthal correlations from transverse momentum conservation and possible local parity violation", Phys. Rev. C 83, 014905 (2011).

[10] B. I. Abelev *et al.* [STAR Collaboration], "Observation of charge-dependent azimuthal correlations and possible local strong parity violation in heavy-ion collisions", Phys. Rev. C 81, 054908 (2010).

[11] L. Adamczyk *et al.* [STAR Collaboration], "Beam-Energy Dependence of Charge Separation along the Magnetic Field in Au+Au Collisions at RHIC" Phys. Rev. Lett. 113, 052302 (2014).

[12] V. Khachatryan *et al.* [CMS Collaboration], "Observation of Charge-Dependent Azimuthal Correlations in p-Pb Collisions and Its Implication for the Search for the Chiral Magnetic Effect", Phys. Rev. Lett. 118, 122301 (2017).

[13] V. Koch *et al.*, "Status of the chiral magnetic effect and collisions of isobars", Chin. Phys. C 41, 072001 (2017).

[14] J. Zhao, H. Li, and F. Wang, "Isolating the chiral magnetic effect from backgrounds by pair invariant mass", Eur. Phys. J. C 79, 168 (2019).

[15] J. Schukraft, A. Timmins, and S. A. Voloshin, "Ultra-relativistic nuclear collisions: event shape engineering", Phys. Lett. B 719, 394 (2013).

[16] A. M. Sirunyan *et al.* [CMS Collaboration], "Constraints on the chiral magnetic effect using charge-dependent azimuthal correlations in *pPb* and PbPb collisions at the CERN Large Hadron Collider" , Phys. Rev. C 97, 044912 (2018).

[17] S. Acharya *et al.* [ALICE Collaboration], "Constraining the magnitude of the Chiral Magnetic Effect with Event Shape Engineering in Pb-Pb collisions at $\sqrt{s_{NN}} = 2.76$ TeV", Phys. Lett. B 777, 151 (2018).

[18] N. Borghini, P. M. Dinh and J. Y. Ollitrault, "A new method for measuring azimuthal distributions in nucleus-nucleus collisions", Phys. Rev. C 63, 054906 (2001) [arXiv:nucl-th/0007063].

[19] N. Borghini, P. M. Dinh and J. Y. Ollitrault, "Flow analysis from multi-particle azimuthal correlations", Phys. Rev. C 64 054901 (2001) [arXiv:nucl-th/0105040].

[20] A. Bilandzic, R. Snellings and S. Voloshin, "Flow analysis with cumulants: direct calculations", Phys. Rev. C 83, 044913 (2011).

[21] R. Kubo, "Generalized Cumulant Expansion Method*", Journal of the Physical Society of Japan, Vol. 17, No. 7 (1962).

[22] M. Anderson *et al.*, "The STAR time projection chamber: a unique tool for studying high multiplicity events at RHIC", Nucl. Instrum. Methods Phys. Res., Sect. A 499, 659 (2003).

[23] W. J. Llope *et al.*, "The TOFp/pVPD time-of-flight system for STAR", Nucl. Instrum. Methods Phys. Res., Sect. A 522, 252 (2004).

[24] C. Adler, A. Denisov, E. Garcia, M. J. Murray, H. Strobele, and S. N. White, "The RHIC Zero Degree Calorimeter", Nucl. Instrum. Methods Phys. Res., Sect. A 470, 488 (2001).

[25] W. J. Llope *et al.*, "The STAR Vertex Position Detector", Nucl. Instrum. Methods Phys. Res., Sect. A 759, 23 (2014).

[26] A. Attri, "Event by event charge separation in heavy ion collisions using star detector at rhic", "https://shodhganga.inflibnet.ac.in:8443/jspui/handle/10603/348065", (2022).

[27] B. I. Abelev *et al.*, [ALICE Collaboration], "Charge separation relative to the reaction plane in Pb-Pb collisions at $\sqrt{s_{NN}} = 2.76$ TeV", Phys. Rev. Lett. 110, 012301 (2013).

[28] A. Bzdak, V. Koch, and J. Liao, "Charge-Dependent Correlations in Relativistic Heavy Ion Collisions and the Chiral Magnetic Effect", Lecture Notes in Physics, 871, 503 (2013) [arXiv:1207.7327v1].

Chapter 6

Chiral Magnetic Effect in isobaric collisions at $\sqrt{s_{\mathrm{NN}}} = 200$ GeV using SDM

6.1 Introduction

The STAR detector at the Relativistic Heavy Ion Collider (RHIC) is specifically designed to study the properties of the QGP and explore the phase diagram of nuclear matter. Isobaric collisions at the STAR experiment provide a unique platform to study intriguing phenomena such as the Chiral Magnetic Effect (CME) [1–3]. Isobaric collisions of ${}^{96}_{44}$Ru+${}^{96}_{44}$Ru and ${}^{96}_{40}$Zr+${}^{96}_{40}$Zr nuclei, have been proposed as a promising approach to address the challenges associated with the detection of the Chiral Magnetic Effect (CME) in heavy-ion collisions [4]. The use of isobaric collisions presents certain advantages due to the anticipated differences in magnetic field strength and similar backgrounds. In particular, the larger atomic number of Ruthenium (${}^{96}_{44}$Ru) compared to Zirconium (${}^{96}_{40}$Zr) leads to an increase of approximately 15% in the squared magnetic field in Ru+Ru collisions [2,5–11]. This enhanced magnetic field is expected to lead to a proportional increase in the CME contribution in Ru+Ru collisions, while the similarity in mass numbers of the colliding nuclei ensures comparable flow-driven backgrounds. While the backgrounds in Ru+Ru and Zr+Zr collisions were predicted to be comparable, it is important to note that they are not identical. Differences in the nuclear deformation of the two isobars result in a background variation of less than 1% in peripheral to mid-central collisions, but can exceed 2% in collisions with a centrality of 0-20% [12]. Hydrodynamic simulations incorporating local charge conservation (LCC) further indicate a 4% distinction in the flow-driven background between the two systems [13]. To enhance the sensitivity to the potentially small Chiral Magnetic Effect (CME) signal, minimizing the background contributions is crucial. Isobar collisions provide an effective approach to achieve this objective by analyzing and comparing various CME-sensitive observables (i.e., δ, γ, $\Delta\gamma$, etc.) [14, 15] in two isobaric systems. These observables were carefully examined and evaluated in the Isobar Blind Analysis.

In an effort to validate the Chiral Magnetic Effect (CME) in isobaric collisions, the STAR experiment at RHIC conducted a dedicated high-statistics run in 2018, accumulating a total of approximately 4 billion events. It was anticipated that the ratio of Ru+Ru to Zr+Zr collisions, of the CME-sensitive $\Delta\gamma$ correlator would be greater than 1, as the backgrounds were expected to be similar in these isobaric systems. However, the experimental results yielded unexpected outcomes. Contrary to expectations, the STAR Collaboration reported that "no CME signature that satisfies the predefined criteria has been observed" [12]. Despite the rigorous data analysis and examination of various CME-sensitive observables, the evidence supporting the presence of the CME in isobaric collisions was not found. This outcome highlights the importance of thorough and meticulous investigations to validate the existence of the CME. The search for the CME continues, and further studies and analyses may be needed to explore its manifestation in different collision systems and energies.

6.2 Analysis Strategy and Data sets

It is recognized that not every heavy-ion collision environment may be conducive to give rise to the Chiral Magnetic Effect (CME). Given the expected weak nature of the CME signal, which can be easily masked by statistical fluctuations, it is crucial to adopt a careful approach to effectively identify the CME signal. Instead of averaging over all events within a collision centrality, it is important to examine each individual event independently. To tackle this challenge, a novel technique known as the Sliding Dumbbell Method (SDM) [16, 17] has been developed. The SDM aims to isolate and extract the events enriched with CME within each collision centrality. By employing the SDM, it becomes possible to identify and study the back-to-back charge separation characteristic of the CME on an event-by-event basis. This approach allows for a more detailed investigation of the CME signal, accounting for statistical fluctuations and enhancing the sensitivity to its occurrence. The SDM provides a valuable tool in the quest to understand and validate the presence of the CME in heavy-ion collisions.

As discussed in previous chapters, in the SDM, the azimuthal plane in each event is scanned by sliding the dumbbell of $\Delta\phi = 90^\circ$ in steps of $\delta\phi = 1^\circ$ while calculating Db_{+-} for each region to obtain maximum values of Db_{+-} (Db_{+-}^{max}) in each event with a condition that $\mid Db_{asy} \mid < 0.25$. The charge separation across the dumbbell (f_{DbCS}) is defined as follows:

$$f_{DbCS} = Db_{+-}^{max} - 1 \tag{6.1}$$

The f_{DbCS} distributions are obtained for each centrality class and subdivided into ten percentile bins, ranging from $0-10\%$ to $90-100\%$ for each collision centrality. The multi-particle (2-, 3-, and 4-particle) [14, 15] correlators are computed for different charge combinations and for each f_{DbCS} bin in each centrality for different samples as explained in Chapters 4 and 5. These correlator (γ, δ, v_2, etc.) are calculated using the Q-cumulants [18].

6.2.1 Isobar data sets

The isobar collisions of $^{96}_{44}$Ru+$^{96}_{44}$Ru and $^{96}_{40}$Zr+$^{96}_{40}$Zr were performed at the RHIC facility in the year 2018. The collision data was taken by STAR (Solenoid tracker at RHIC) detector at the center-of-mass energy per nucleon of 200 GeV. The main subsystems of STAR during isobar data collection were the Time Projection Chamber (TPC) [19], the time-of-flight detector (TOF) [20], the event plane detector (EPD) [21], the zero-degree calorimeters (ZDCs) [22], and the vertex position detectors (VPDs) [23]. High statistics were collected for both the isobars i.e., approximately 2 Billion events for each and ~4 Billion events in total.

The datasets used in this analysis were the Minimum Bias (MB) triggered data (STAR-library: SL18h) from Run18 isobar collisions at $\sqrt{s_{NN}}$ = 200 GeV. Certain bad runs with certain issues were excluded from the analysis, which are listed below.

Bad Run Numbers for Isobar collisions:

19120009, 19102023, 19102054, 19103022, 19083049, 19083050, 19083051, 19083052, 19083053, 19083054, 19083055, 19083056, 19083057, 19083058, 19083059, 19083060, 19083061, 19083062, 19083063, 19083064, 19083065, 19083066, 19083067, 19084001, 19084002, 19084003, 19084004, 19084005, 19084006, 19084007, 19084008, 19084010, 19084011, 19084013, 19084022, 19084024, 19084025, 19084026, 19084027, 19084028, 19084029, 19084030, 19084031, 19084032, 19084033, 19084034, 19084035, 19084036, 19084037, 19084038, 19084039, 19084053, 19084055, 19084057, 19084059, 19084060, 19084061, 19084062, 19084063, 19084064, 19084065, 19084066, 19084067, 19084068, 19084070, 19084071, 19084072, 19085001, 19085002, 19085003, 19085004, 19085005, 19085006, 19085007, 19085008, 19085009, 19085010, 19085011, 19085012, 19085013, 19085014, 19085015, 19085016, 19085017, 19085018, 19085019, 19085020, 19085021, 19085023, 19085024, 19085025, 19085026, 19085058, 19086026, 19086060, 19086061, 19086062, 19086063, 19086064, 19086066, 19086067, 19086069, 19086070, 19086072, 19086073, 19086074, 19086076, 19086077, 19086080, 19087001, 19087012, 19087014, 19087015, 19087016, 19087017, 19087021, 19087022, 19087038, 19087042, 19088051, 19088052, 19088053, 19088055, 19090009, 19090010, 19090011, 19090012, 19090015,

19090016, 19090018, 19090019, 19090021, 19090022, 19090023, 19090024, 19090025, 19090032, 19092051, 19093042, 19093043, 19095061, 19096002, 19096005, 19096006, 19096057, 19097057, 19098017, 19098018, 19098020, 19100045, 19103007, 19103041, 19105024, 19105026, 19106023, 19106034, 19107045, 19110015, 19110039, 19112012, 19112029, 19115020, 19116035, 19120047, 19120048, 19122004, 19122005, 0
Quality assurance (QA) checks in the form of event and track selections have been conducted prior to the analysis to ensure the utilization of high-quality data.

6.2.1.1 Event selection cuts

In the collisions, TPC is used to reconstruct the primary vertex position i.e., $V_{z,TPC}$ or V_z along the beam direction axis (z-axis). The vertex position in each event is considered within -35 < $V_{z,TPC}$ < 25 cm (shown in Fig. 6.1 (a)) where the origin is at the TPC center. The asymmetries in the vertex distribution are a direct result of the online vertex selection during data taking. The asymmetry is caused by a difference in timing between the east and west VPD, which measures the z position of the vertex. Different event selection cuts are given in table 6.1. The Minimum

Event parameters	Cuts
Minimum bias Trigger	600001, 600011, 600021, 600031
Vertex cut ($V_{z,TPC}$)	-35 < V_z < 25 cm
$\mid V_{z,VPD}$ - $V_{z,TPC} \mid$	< 5 cm
V_x and V_y	$\mid V_x \mid$ < 2.0 cm, $\mid V_y \mid$ < 2.0 cm
$V_r = \sqrt{V_x^2 + V_y^2}$	< 2.0 cm

Table 6.1: Event selection Cuts for isobar (Ru+Ru and Zr+Zr) collisions.

Bias (MB) data sample is acquired using a trigger based on the information from two VPD detectors. In order to select the good events, we require the condition that $\mid V_{z,TPC} - V_{z,VPD} \mid < 5$ cm as shown in Fig. 6.1 (b). Figure 6.2 displays the distributions of events after applying the cuts $\sqrt{V_x^2 + V_y^2} < 2.0$ cm and $\mid V_x(V_y) \mid$ < 2.0 cm for Ru+Ru (Left) and Zr+Zr (Right) collisions. Methods for event selection frequently experience an out-of-time pile-up, which requires the use of

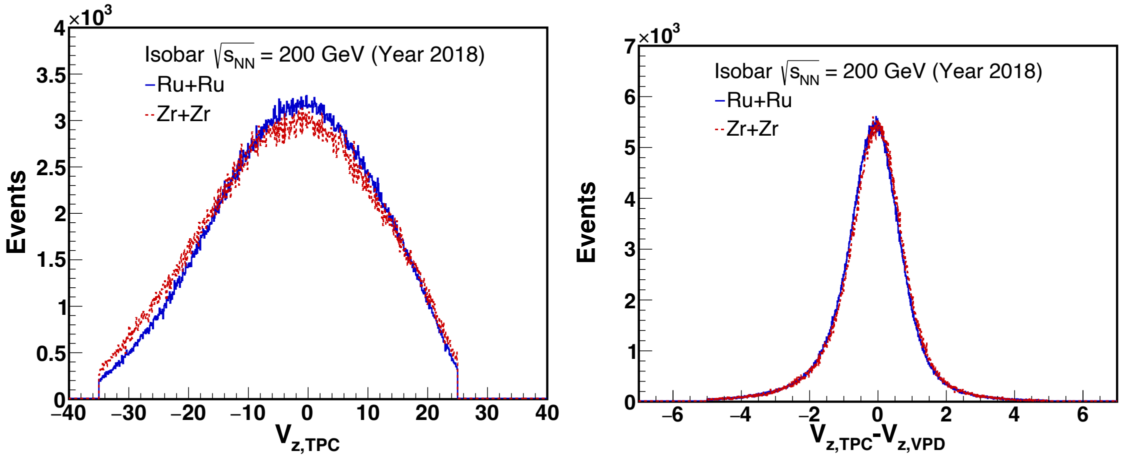

Figure 6.1: (a) Z-Vertex distribution for Ru+Ru and Zr+Zr collisions at $\sqrt{s_{NN}}$=200 GeV. (b) $V_{z,TPC} - V_{z,VPD}$ distribution for Ru+Ru and Zr+Zr collisions.

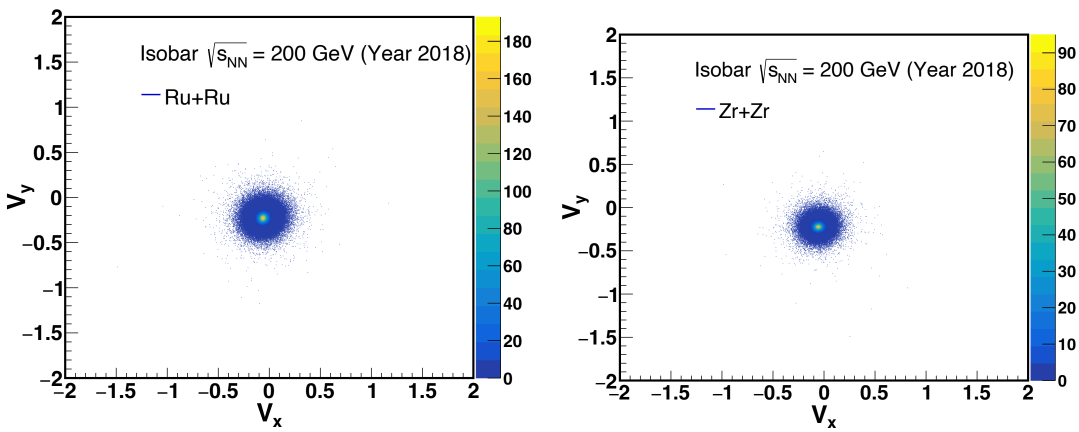

Figure 6.2: V_X vs V_Y distribution for Ru+Ru (Left) and Zr+Zr (Right) collisions at $\sqrt{s_{NN}}$=200 GeV.

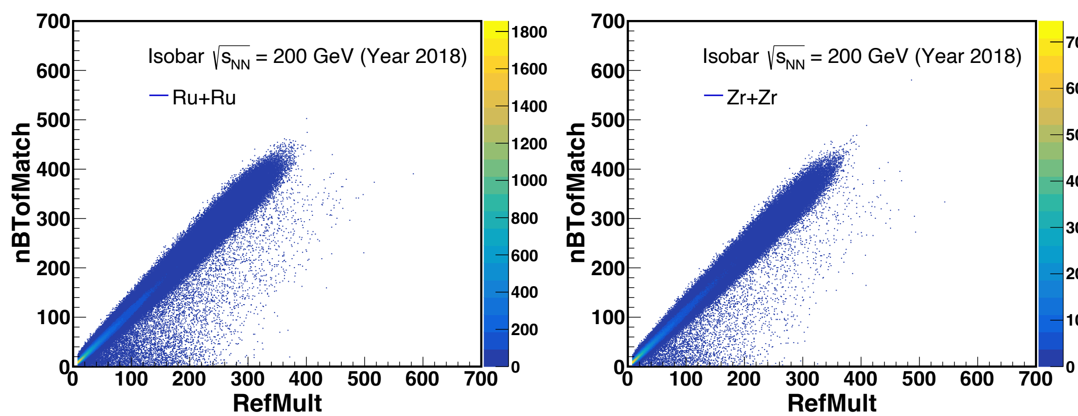

Figure 6.3: RefMult ($N_{trk}^{offline}$) vs TofMatch including the out-of-time pile-up events for Ru+Ru (Left) and Zr+Zr (Right) collisions at $\sqrt{s_{NN}}$=200 GeV.

an offline rejection. Approximately 0.5% of events are identified as pile-up and removed by excluding events in the correlation between the number of TPC tracks and the number of those tracks matching a hit in the TOF detector (the TOF is a fast detector and does not suffer from out-of-time pile-up). While selecting good events, we also need at least one TPC track that matches the TOF [12,24,25]. The Pile-up events are displayed in Fig. 6.3 with a scatter plot of $N_{trk}^{offline}$ (efficiency-uncorrected multiplicity in the TPC within $\mid \eta \mid < 0.5$, often known as RefMult) versus TofMatched hits. Figure 6.4 displays the plots after Pile-up rejection for Ru+Ru and Zr+Zr collisions as suggested in [24,25].

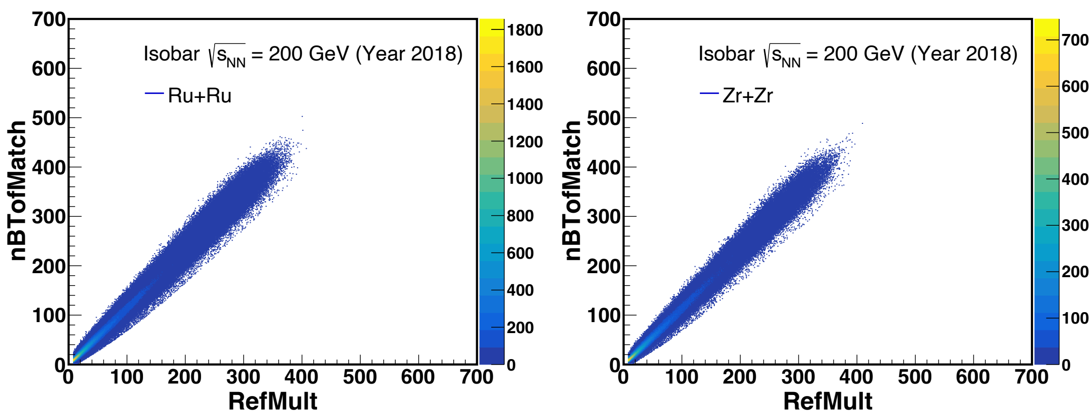

Figure 6.4: RefMult ($N_{trk}^{offline}$) vs TofMatch after removing the pile-up events for Ru+Ru (Left) and Zr+Zr (Right) collisions at $\sqrt{s_{NN}}$=200 GeV.

6.2.1.2 Track selection cuts

The track selection cuts for isobar (Ru+Ru and Zr+Zr) collisions are listed in table 6.2. In order to reduce the contamination from secondary charged particles, we require that the distance of the closest approach (DCA) between reconstructed TPC tracks and the primary vertex be less than 3 cm. DCA distribution is shown in Fig. 6.5 (a). In addition, each track must have at least 16 ionization points (N_{fits}) in the TPC. N_{hits} distribution after applying cut on N_{fits} is shown in Fig. 6.5 (b). The TPC detects charged particles in the pseudo-rapidity range $\mid \eta \mid < 1$ (Fig. 6.5 (c)), with full azimuthal coverage (Fig. 6.5 (d)) and a transverse momentum 0.2 <

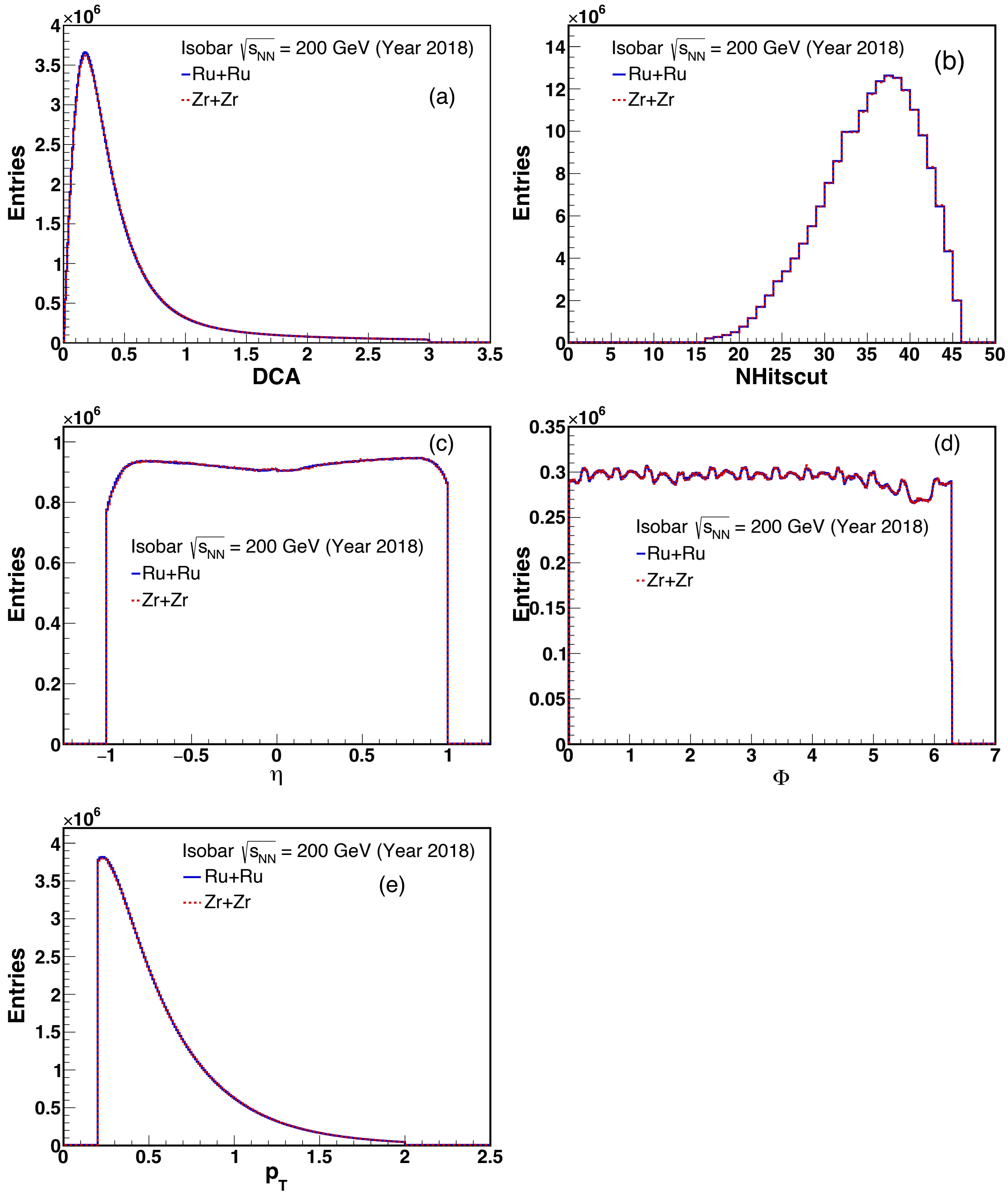

Figure 6.5: Distribution of (a) DCA, (b) N_{hits}, (c) η, (d) ϕ, and (e) p_T for Ru+Ru (blue) and Zr+Zr (red) collisions at $\sqrt{s_{NN}}$=200 GeV.

Track parameters	Cuts
DCA	< 3 cm
N_{Hits}	> 15
$N_{HitsFit}/N_{HitsPoss}$	> 0.52
p_T	0.2 GeV/$c < p_T <$ 2.0 GeV/c
$\mid \eta \mid$	< 1.0

Table 6.2: Track selection Cuts for isobar (Ru+Ru and Zr+Zr) collisions.

$p_T <$ 2.0 GeV/c is displayed in the Fig. 6.5 (e).

After applying all the event and track selection cuts we get approximately ∼1.7 Billion minimum bias (MB) events for both Ru+Ru and Zr+Zr collisions at $\sqrt{s_{NN}}$=200 GeV.

6.2.1.3 Centrality selection

The $N_{trk}^{offline}$ or RefMult distribution is shown in Fig. 6.6 for both Ru+Ru and Zr+Zr collisions at $\sqrt{s_{NN}}$=200 GeV. We get the centrality information from this distribution after slicing this into separate centrality bins. For eight centrality bins the cuts on the $N_{trk}^{offline}$ are given in the table 6.3 [12]. After applying all the event

Centrality label	Ru+Ru $N_{trk}^{offline}$	Zr+Zr $N_{trk}^{offline}$
0-5%	258-500	256-500
5-10%	216-258	213–256
10-20%	151-216	147-213
20-30%	103-151	100-147
30-40%	69-103	65-100
40-50%	44-69	41-63
50-60%	26-44	25-41
60-70%	15-26	14-25
70-80%	8-15	7-14

Table 6.3: Centrality selection from $N_{trk}^{offline}$ in Ru+Ru and Zr+Zr collisions.

and track selection cuts, the multiplicity distribution for each centrality is checked for further analysis. The distribution of positive and negative charged particle's multiplicities are shown for Ru+Ru collisions in Fig. 6.7 and for Zr+Zr collisions in

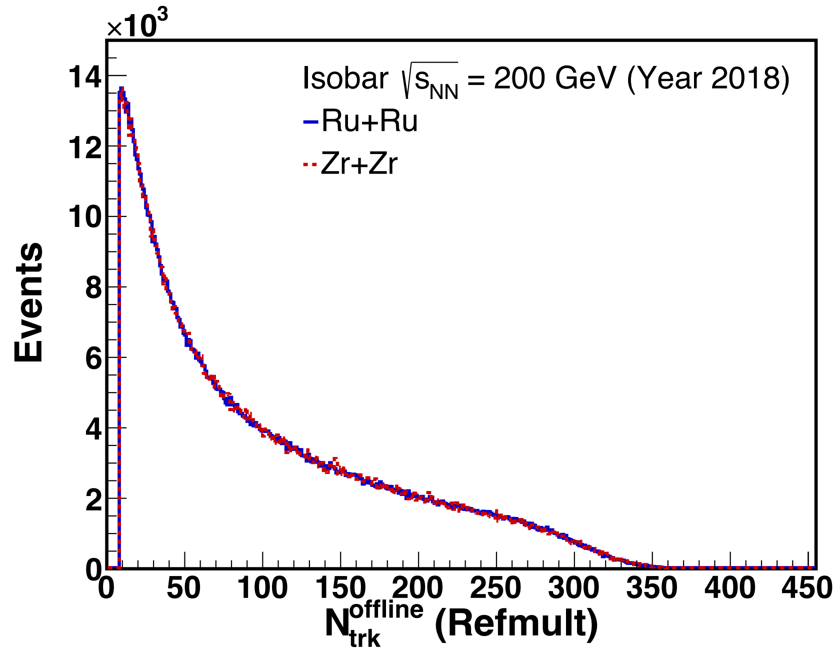

Figure 6.6: $N_{trk}^{offline}$ distributions for Ru+Ru (blue) and Zr+Zr (red) collisions at $\sqrt{s_{NN}}$=200 GeV.

Fig. 6.8. The figures show similar behavior for both positive and negative charged particle's multiplicity distributions.

6.3 Uncertainty estimation

6.3.1 Statistical uncertainties

We used the sub-sampling method along with the standard error propagation to calculate the statistical uncertainties. We divided the data into ten sub-samples as explained in chapter 4.

6.3.2 Systematic uncertainties

In order to evaluate the systematic uncertainties, we first vary the standard events and track cuts which were employed in the analysis. The systematic uncertainty is taken as the maximum deviation of a given observable by varying the cut away

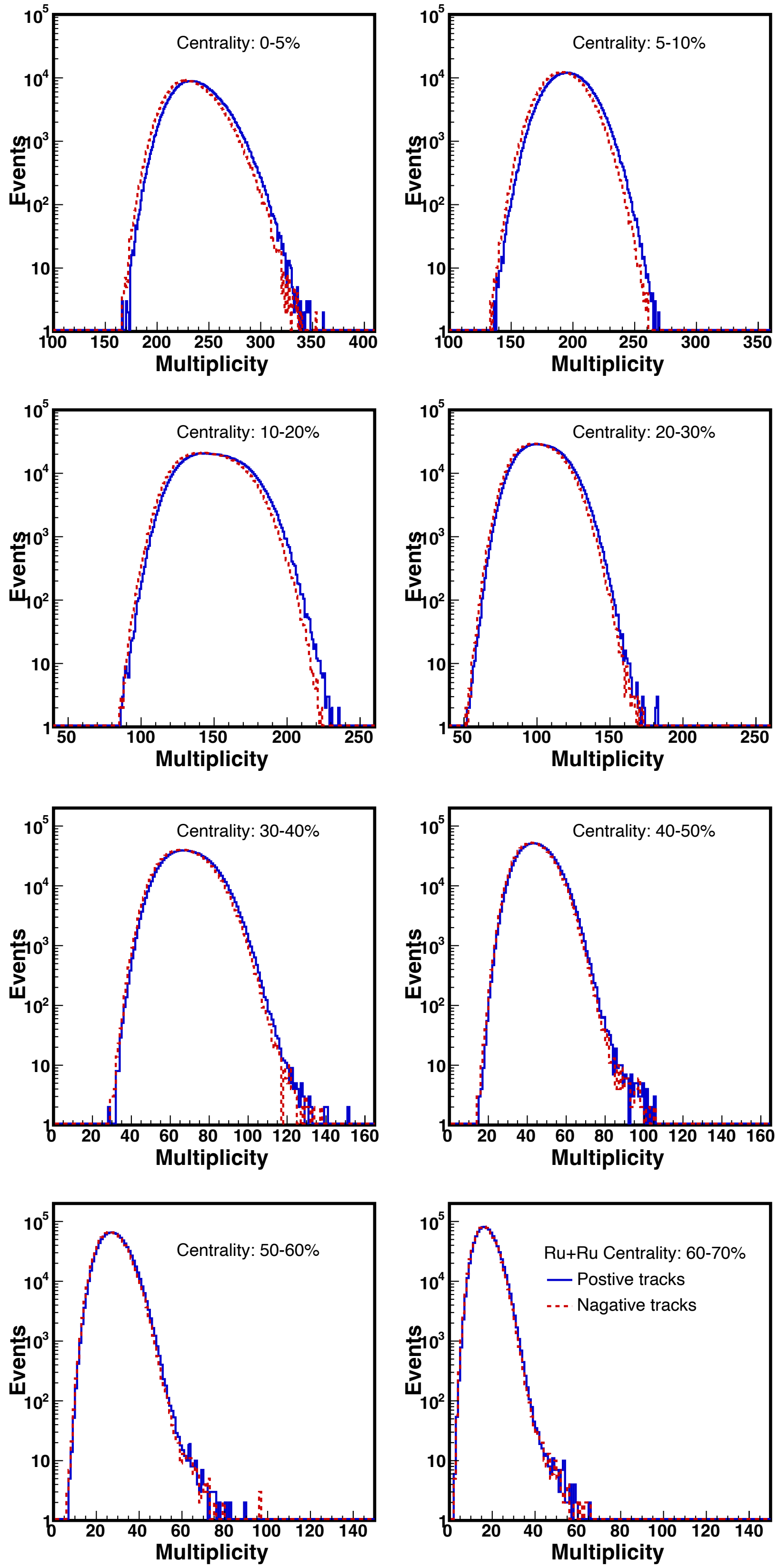

Figure 6.7: Multiplicity distributions for positively and negatively charged particles for Ru+Ru collisions at $\sqrt{s_{NN}}$=200 GeV.

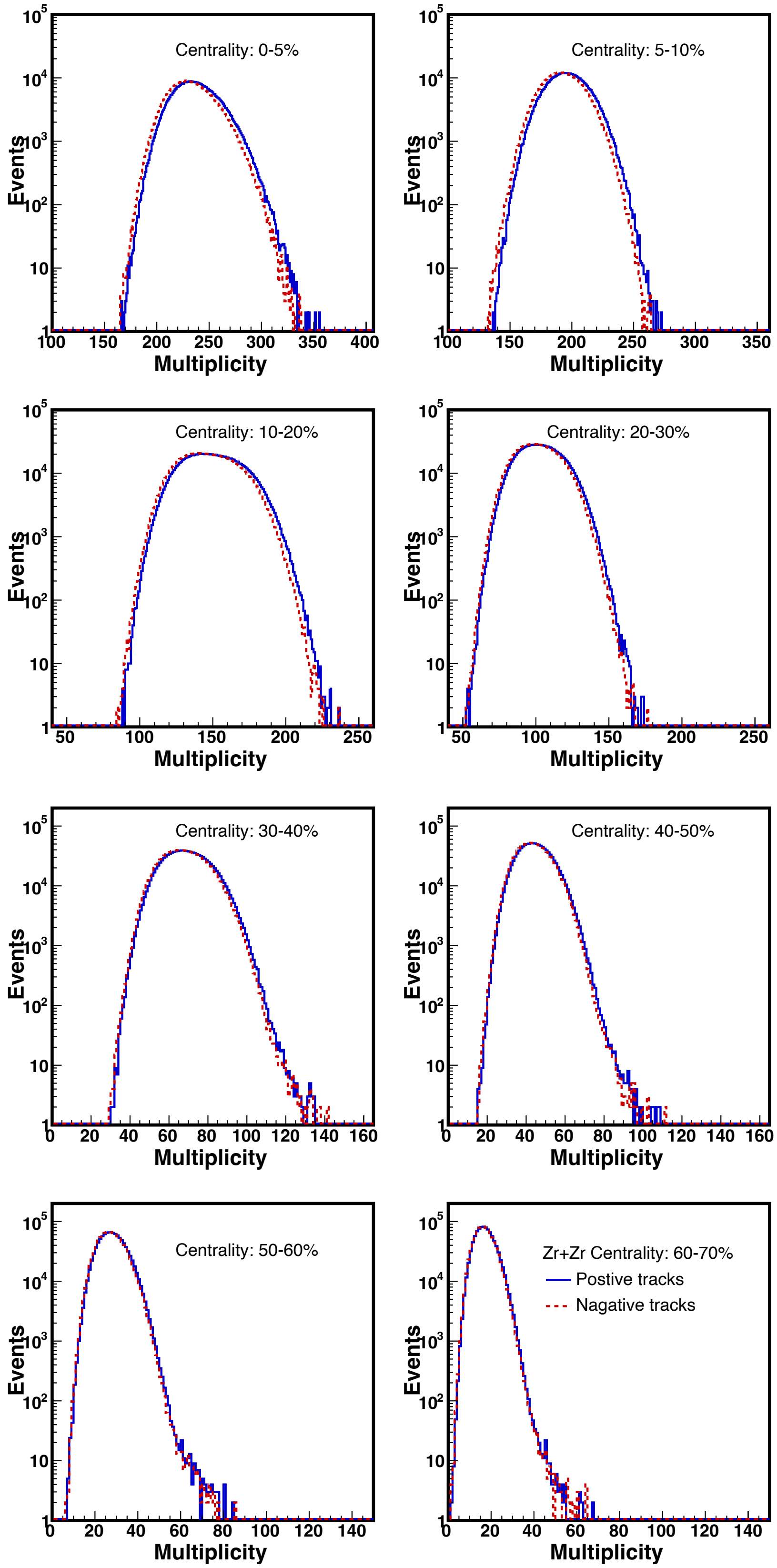

Figure 6.8: Multiplicity distributions for positively and negatively charged particles for Zr+Zr collisions at $\sqrt{s_{NN}}$=200 GeV.

from the default cut. The final estimate of the systematic uncertainty is obtained by adding in quadrature the estimated systematic errors obtained from each variable. For this analysis, we are using the same cuts for systematic uncertainties which were employed by isobar blind analyzers in reference [12] and are given in table 6.4. To

Sources of uncertainty	Standard Cut	Varied Cut
V_z	-35 $< V_z <$ 25 cm	-35 $< V_z <$ 0 cm
DCA	$<$ 3 cm	$<$ 2 cm
N_{hits}	$>$ 15	$>$ 20

Table 6.4: Various standard cuts and varied systematic cuts to obtain the systematic uncertainties in Ru+Ru and Zr+Zr collisions.

estimate the systematic uncertainty resulting from the acceptance dependence on $V_{z,TPC}$, the results using only events within -35 $< V_{z,TPC} <$ 0 cm are compared with those from the entire $V_{z,TPC}$ range. The TPC tracks must have a maximum DCA of 3 cm and a minimum N_{hits} of 16 in order to be utilized in the analysis. For the purpose of evaluating systematic uncertainties, we reduced the maximum DCA from 3 cm to 2 cm and increased the minimum N_{hits} from 16 to 21.

Figure 6.9 explains the flowchart for the calculation of the systematic uncertainties. Here Y_{def} and Y_i are the default values and varied values of the observable (i.e., $\Delta\gamma$). The difference between the default value (Y_{def}) and varied value (Y_i) is $\mid Y_i - Y_{def} \mid$ and the statistical fluctuation on this difference is given by $\sigma_{stat,diff} = \sqrt{\sigma^2_{stat,i} + \sigma^2_{stat,def}}$, where $\sigma_{stat,i}$ and $\sigma_{stat,def}$ are the statistical errors for the two measurements. If $\sigma_{stat,diff}$ is larger than $\mid Y_i - Y_{def} \mid$, no systematic uncertainty is considered for that particular variation on the cut, as the change in the result is consistent with statistical uncertainties. If $\sigma_{stat,diff} < \mid Y_i - Y_{def} \mid$, then the systematic uncertainty is given by $\sigma_{sys,i} = \sqrt{(Y_i - Y_{def})^2 - \sigma^2_{stat,diff}}/\sqrt{12}$. The final systematic uncertainty includes all the varied $\sigma_{sys,i}$ added in quadrature using $\sigma_{Sys} = \sqrt{\sum \sigma^2_{sys,i}}$.

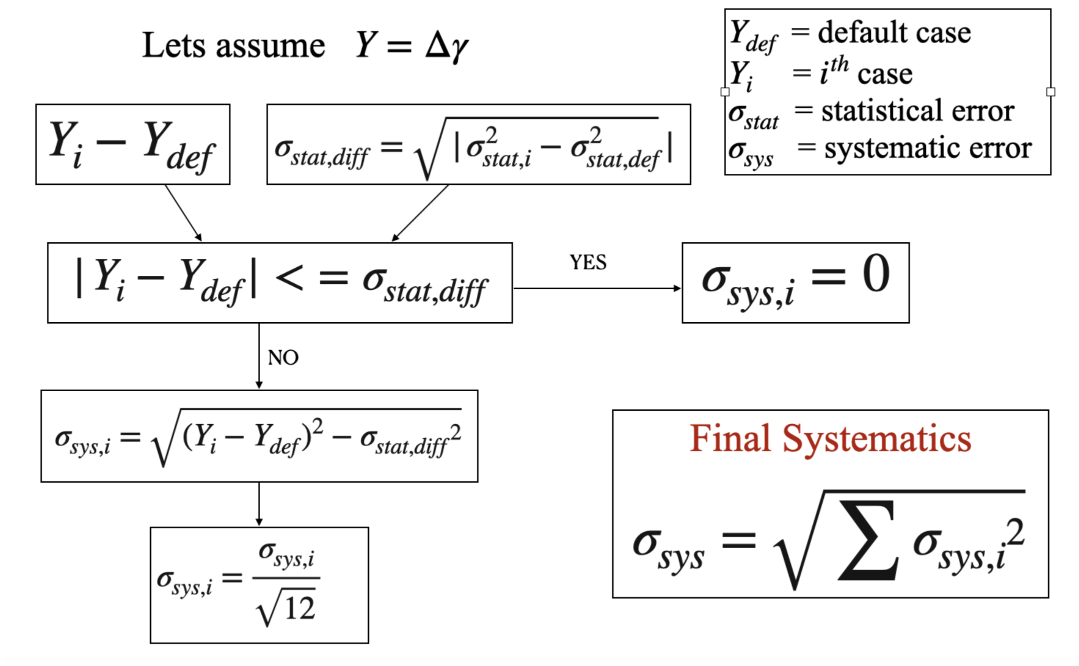

Figure 6.9: A flowchart explaining the approach to calculate the systematic uncertainties.

6.4 Result and Discussion: Dependences of observables on centrality

In this section, we will discuss the centrality dependence of different observables i.e., v_2, δ, γ, etc., and compare them with the published results for consistency check. These observables will be calculated using the Q-cumulant [18] methodology as discussed in previous chapters.

The centrality dependence of Mean Multiplicity and $\langle N_{trk}^{offline} \rangle$ (efficiency-uncorrected mean multiplicity) is shown in Fig. 6.10. It can be seen from the ratios (in the lower panels) that Ru+Ru collisions have more multiplicity than the Zr+Zr collisions. The statistical uncertainties associated with the points are small relative to the size of the markers.

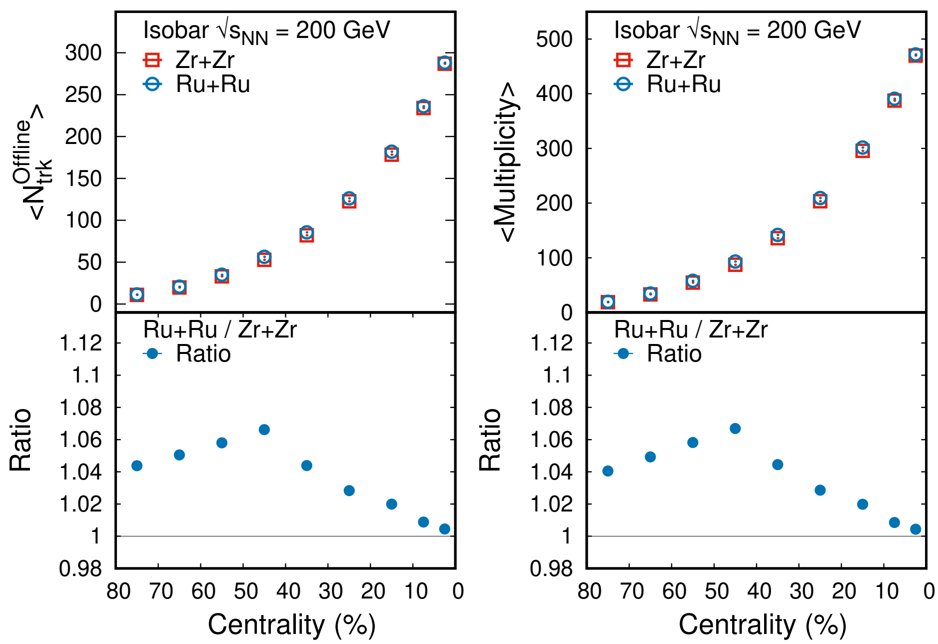

Figure 6.10: (Left) The efficiency-uncorrected mean multiplicity $\langle N_{trk}^{offline} \rangle$ from the TPC within $\eta < 0.5$ as a function of centrality in Ru+Ru and Zr+Zr collisions. (Right) The centrality dependence of Mean multiplicity for Ru+Ru and Zr+Zr collisions and their ratios. The lower panels show the ratios for Ru+Ru over Zr+Zr.

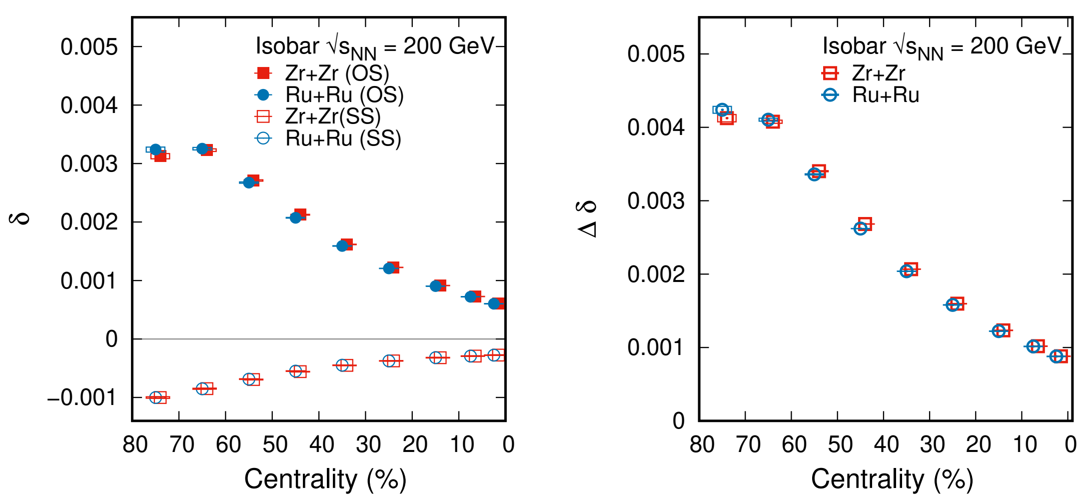

Figure 6.11: (Left) The dependence of δ correlator for opposite sign (OS) and same sign (SS) charge pairs on collision centralities for Ru+Ru and Zr+Zr collisions at $\sqrt{s_{NN}} = 200$ GeV. (Right) The centrality dependence of $\Delta\delta$ correlator for Ru+Ru and Zr+Zr collisions.

6.4.1 Centrality dependence of δ-correlator

The centrality dependence of 2-particle (δ) correlator i.e., $\delta = \langle\cos(\phi_i - \phi_j)\rangle$ for opposite sign (OS) and same sign (SS) charge pairs and $\Delta\delta$ ($= \delta_{OS} - \delta_{SS}$) correlator are shown in Fig. 6.11. The red color represents Zr+Zr whereas the blue color denotes Ru+Ru collisions. It is seen that the OS (solid circles) charge pair correlations for 2-particles are positive and the magnitude is increasing with decreasing collision centrality for both Ru+Ru and Zr+Zr collisions. For SS charge pairs the correlation values are negative and become more negative with decreasing collision centrality. For both SS and OS, the correlation agrees within uncertainties for both Ru+Ru and Zr+Zr collisions. For all collision centralities, two isobar species display similar $\Delta\delta$ values within uncertainties. The fractional systematic uncertainties for

Sources	Centrality							
	60-70%	50-60%	40-50%	30-40%	20-30%	10-20%	5-10%	0-5%
V_z	0	0	0.00032	0.00054	0.00053	0.00068	0.0016	0.0013
DCA	0.0062	0.0038	0.0025	0.0017	0.0013	0.0011	0.0015	0.0016
nHIT	0.0021	0.0018	0.0016	0.0014	0.0013	0.0015	0.0015	0.0018
Total	0.0066	0.0042	0.0030	0.0023	0.0019	0.0020	0.0027	0.0028

Table 6.5: The values of fractional systematic uncertainties for δ-correlator for opposite sign (δ_{OS}) charge pairs in Ru+Ru collisions at $\sqrt{s_{NN}}$ = 200 GeV.

Sources	Centrality							
	60-70%	50-60%	40-50%	30-40%	20-30%	10-20%	5-10%	0-5%
V_z	0	0.0011	0.0011	0.0023	0.0023	0.0023	0.0045	0.0039
DCA	0.00063	0.0043	0.0070	0.0095	0.011	0.0128	0.014	0.014
nHIT	0.0098	0.0077	0.0052	0.0043	0.0034	0.0034	0.0031	0.0035
Total	0.0098	0.0089	0.0088	0.011	0.012	0.0135	0.015	0.015

Table 6.6: The values of fractional systematic uncertainties for δ-correlator for same sign (δ_{SS}) charge pairs in Ru+Ru collisions at $\sqrt{s_{NN}}$ = 200 GeV.

δ-correlator for Ru+Ru collisions are listed in table 6.5 (opposite-sign) and table 6.6 (same-sign). The fractional systematic uncertainties for δ-correlator for Zr+Zr collisions are listed in table 6.7 (opposite-sign) and table 6.8 (same-sign).

Sources	Centrality							
	60-70%	50-60%	40-50%	30-40%	20-30%	10-20%	5-10%	0-5%
V_z	0	0	0	0.00052	0.00051	0.00073	0.0011	0.00057
DCA	0.0067	0.0039	0.0028	0.0018	0.00136	0.0012	0.0014	0.0014
nHIT	0.0020	0.0018	0.0016	0.0014	0.0013	0.0014	0.0014	0.0017
Total	0.0070	0.0043	0.0032	0.0024	0.0019	0.0020	0.0023	0.0024

Table 6.7: The values of fractional systematic uncertainties for δ-correlator for opposite sign (δ_{OS}) charge pairs in Zr+Zr collisions at $\sqrt{s_{NN}}$ = 200 GeV.

Sources	Centrality							
	60-70%	50-60%	40-50%	30-40%	20-30%	10-20%	5-10%	0-5%
V_z	0	0.0019	0.00187	0.0022	0.0013	0.0029	0.0030	0.0035
DCA	0	0.0047	0.0066	0.0094	0.011	0.013	0.0139	0.0142
nHIT	0.010	0.0075	0.0059	0.0044	0.0033	0.0033	0.0030	0.0033
Total	0.010	0.0091	0.0091	0.011	0.012	0.014	0.0146	0.015

Table 6.8: The values of fractional systematic uncertainties for δ-correlator for same sign (δ_{SS}) charge pairs in Zr+Zr collisions at $\sqrt{s_{NN}}$ = 200 GeV.

6.4.2 Centrality dependence of elliptic flow (v_2)

Figure 6.12 demonstrates the elliptic flow v_2 obtained using the 2-particle Q-cumulant method as a function of centrality for both Ru+Ru (represented by blue symbols) and Zr+Zr (represented by red symbols) collisions. The lower panels of the figure display the ratios (Ru/Zr) of the v_2 values. In mid-central collisions, the ratios exhibit values above unity by approximately ∼2%, which is consistent with the findings of the isobar blind analysis [12]. As the collisions move towards peripheral and central centrality ranges, the ratios decrease. However, an exception is observed in the 0-5% centrality class, where the ratio is slightly above unity by a few percent. DFT simulations [26] suggest that the distinct nuclear structures present in the two isobaric systems may account for the above-unity ratios observed in mid-central collisions. The different v_2 ratios indicate that the backgrounds related to the Chiral Magnetic Effect (CME) in the two isobar systems are not similar, contradicting the assumption of comparable CME backgrounds in both types of isobaric collisions. The fractional systematic uncertainties for v_2 are listed in table 6.9 for

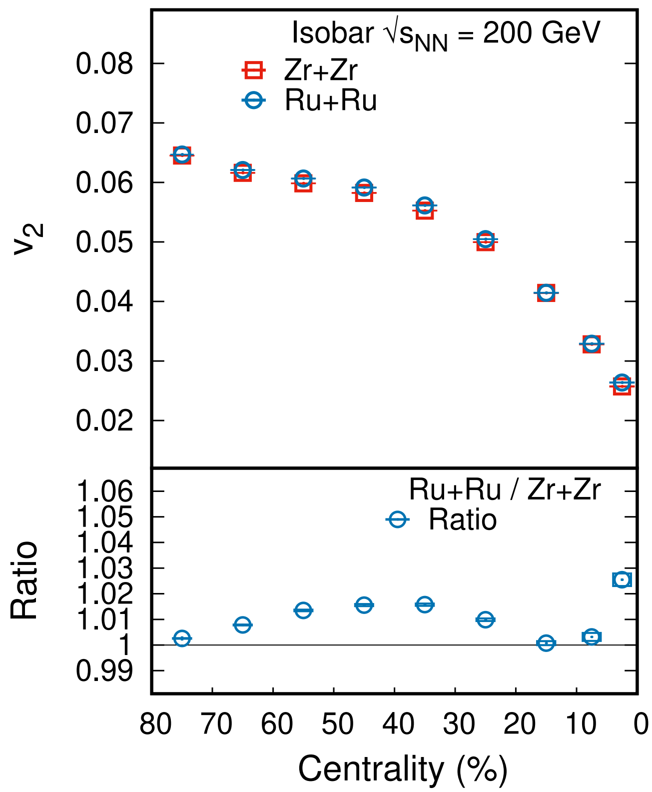

Figure 6.12: Elliptic flow (v_2) measurements using Q-cumulant method in isobar collisions at $\sqrt{s_{NN}}$ = 200 GeV as a function of collision centrality.

Ru+Ru collisions and in table 6.10 for Zr+Zr collisions.

Sources	Centrality							
	60-70%	50-60%	40-50%	30-40%	20-30%	10-20%	5-10%	0-5%
V_z	0	0	0	3.87e-05	9.68e-05	0	0.00038	7.57e-05
DCA	0.00011	0.00020	0.00020	0.00013	6.17e-05	0.00042	0.00096	0.00160
nHIT	0	7.48e-05	0.00019	0.00027	0.00034	0.00038	0.00037	0.00029
Total	0.00011	0.00020	0.00028	0.00032	0.00036	0.00054	0.0011	0.0017

Table 6.9: The values of fractional systematic uncertainties for v_2 in Ru+Ru collisions at $\sqrt{s_{NN}}$ = 200 GeV.

Sources	Centrality							
	60-70%	50-60%	40-50%	30-40%	20-30%	10-20%	5-10%	0-5%
V_z	0	2.91e-05	0	7.61e-05	9.08e-05	0	0.00027	0.00018
DCA	0.00012	0.00020	0.00021	0.000117	5.2e-05	0.00041	0.00099	0.0017
nHIT	0	4.04364e-05	0.00019	0.00029	0.00035	0.00035	0.00040	0.00023
Total	0.00012	0.000204	0.00028	0.00032	0.000364	0.00054	0.0011	0.00174

Table 6.10: The values of fractional systematic uncertainties for v_2 in Zr+Zr collisions at $\sqrt{s_{NN}}$ = 200 GeV.

6.4.3 Centrality dependence of γ-correlator

Figure 6.13 (Left) presents the centrality dependence of the three particle $\gamma-$correlator for various charge combinations i.e., same sign (SS; + +, - -), and opposite sign (OS; + -, - +) charge pairs. The $\gamma-$correlator for SS charge pairs is negative while for OS charge pairs correlations are positive. The correlations for SS charge pairs exhibit larger correlations than OS charge pairs for 0-70% collision centrality. The correlations agree within the uncertainties for both the isobar species. The correlation magnitude (for both OS and SS) decreases with increasing collision centrality.

Figure 6.13 (Right) presents the centrality dependence of $\Delta\gamma$ correlator for Ru+Ru and Zr+Zr collisions which are compared with published results [12]. Some differences seen in the figure are due to the different methods employed in determining the γ-correlator. It is seen that the $\Delta\gamma$ magnitudes are positive for each

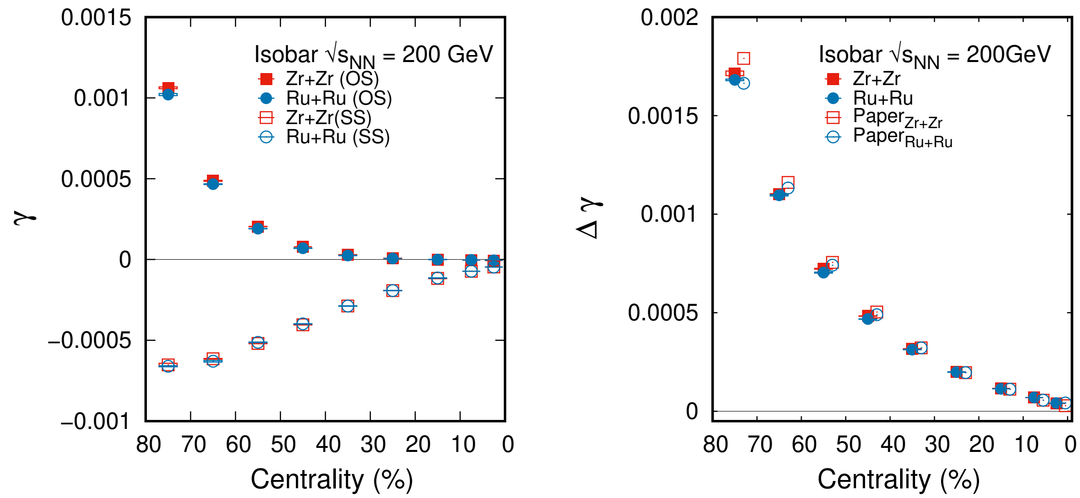

Figure 6.13: (Left) The dependence of γ correlator for opposite sign (OS) and same sign (SS) charge pairs on collision centralities for Ru+Ru and Zr+Zr collisions at $\sqrt{s_{NN}}$ = 200 GeV. (Right) The centrality dependence of $\Delta\gamma$ correlator for Ru+Ru and Zr+Zr collisions. The $\Delta\gamma$ from published paper [12] are shifted horizontally for clarity.

centrality and are increasing with decreasing collision centrality. It is to mention that the two isobar species show approximately the same $\Delta\gamma$ values for all collision centralities. It can be seen that the $\Delta\gamma$ values agree with the published $\Delta\gamma$ results [12]. A positive $\Delta\gamma$ is regarded as the signal for CME. The statistical errors are too small and are within the marker and systematic error is shown in boxes. For Ru+Ru collisions, the fractional systematic uncertainties for γ-correlator are listed in table 6.11 (opposite-sign) and table 6.12 (same-sign).

Sources	Centrality							
	60-70%	50-60%	40-50%	30-40%	20-30%	10-20%	5-10%	0-5%
V_z	0.0034	0.0019	0.017	0	0	0	0	0
DCA	0.0028	0	0.0055	0.0053	0	0.20	0	0
nHIT	0.0018	0.0037	0	0.0082	0	0	0	0
Total	0.0048	0.0042	0.0179	0.0098	0	0.20	0	0

Table 6.11: The values of fractional systematic uncertainties for γ-correlator for opposite sign (γ_{SS}) charge pairs in Ru+Ru collisions at $\sqrt{s_{NN}}$ = 200 GeV.

For Zr+Zr collisions, the fractional systematic uncertainties for γ-correlator are listed in table 6.13 (opposite-sign) and table 6.14 (same-sign).

Sources	Centrality							
	60-70%	50-60%	40-50%	30-40%	20-30%	10-20%	5-10%	0-5%
V_z	0.0074	0.0021	0.00078	0.00043	0	0	0	0
DCA	0	0.0026	0.0024	0.0030	0.00095	0.0013	0	0
nHIT	0.00013	0	0	0	0	0	0	0
Total	0.0075	0.0034	0.0025	0.0030	0.00095	0.0013	0	0

Table 6.12: The values of fractional systematic uncertainties for γ-correlator for same sign (γ_{SS}) charge pairs in Ru+Ru collisions at $\sqrt{s_{NN}}$ = 200 GeV.

Sources	Centrality							
	60-70%	50-60%	40-50%	30-40%	20-30%	10-20%	5-10%	0-5%
V_z	0	0.0037	0	0.012	0	0	0	0
DCA	0.0014	0.0011	0.0027	0.015	0.026	0	0	0
nHIT	0.0060	0.0014	0	0	0	0	0	0
Total	0.0062	0.0042	0.0027	0.0199	0.026	0	0	0

Table 6.13: The values of fractional systematic uncertainties for γ-correlator for opposite sign (γ_{OS}) charge pairs in Zr+Zr collisions at $\sqrt{s_{NN}}$ = 200 GeV.

Sources	Centrality							
	60-70%	50-60%	40-50%	30-40%	20-30%	10-20%	5-10%	0-5%
V_z	0.0027	0.0019	0	0	0	0	0	0
DCA	0.0014	0.0016	0.0022	0.0034	0.0031	0.0013	0	0
nHIT	0.0022	0.00024	0.00014	0	0	0	0	0
Total	0.0038	0.0026	0.0023	0.0034	0.0031	0.0013	0	0

Table 6.14: The values of fractional systematic uncertainties for γ-correlator for same sign (γ_{SS}) charge pairs in Zr+Zr collisions at $\sqrt{s_{NN}}$ = 200 GeV.

6.4.4 In-plane and out-of-plane correlator

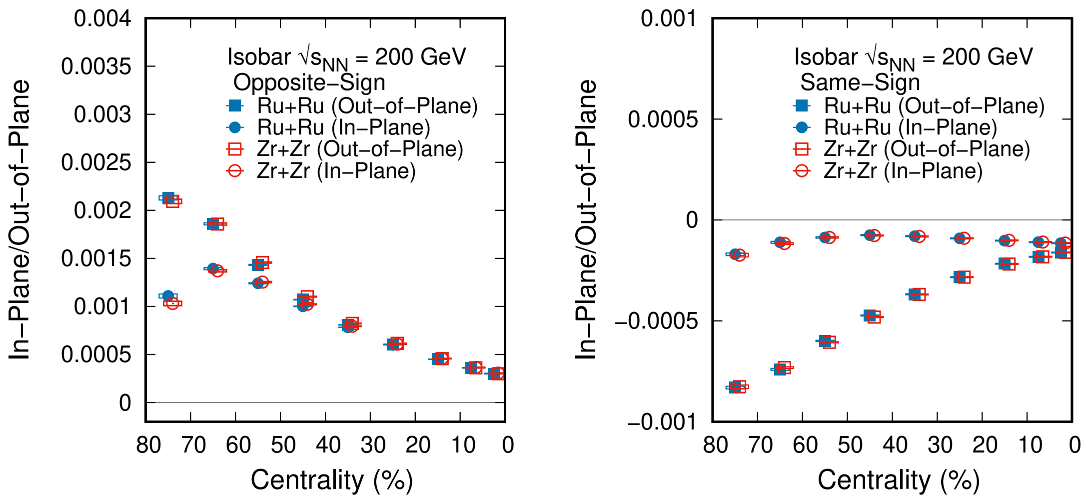

Figure 6.14: Centrality dependence of in-plane and out-of-plane correlators for OS (Left) and SS (Right) charge pairs for Ru+Ru and Zr+Zr collisions at $\sqrt{s_{NN}} = 200$ GeV.

The in-plane ($\sim \langle\cos(\Delta\phi_i)\cos(\Delta\phi_j)\rangle$) and out-of-plane ($\sim \langle\sin(\Delta\phi_i)\sin(\Delta\phi_j)\rangle$) correlations can be obtained from δ and γ correlators. The out-of-plane correlations are sensitive to the CME [27]. Figure 6.14 displays the in-plane correlations (represented by circle markers) and out-of-plane correlations (represented by square markers) for both opposite sign (Left) and same sign (Right) charge pairs in Ru+Ru (blue color) and Zr+Zr (red color) collisions. The in-plane and out-of-plane correlations for different charge combinations agree within errors for both Ru+Ru and Zr+Zr collisions. For OS charge pairs, the in-plane and out-of-plane correlations agree within uncertainties for 0-50% collision centrality, and for 50-80% collision centrality, the magnitude is higher for out-of-plane correlations. It is also noted that the correlations increase with decreasing collision centrality. For SS charge pairs, the out-of-plane correlations increase and become more negative with decreasing collision centrality while the in-plane correlations are independent of the collision centrality.

6.5 Results employing Sliding Dumbbell Method

In this section, we will present the results obtained using the Sliding Dumbbell Method (SDM) [16, 17]. The SDM involves scanning the entire azimuthal plane with a dumbbell shape of 90 degrees, which allows us to observe the fractional charge separation across the dumbbell (referred to as f_{DbCS}, calculated as $Db^{max}_{+-} - 1$), as explained in the previous chapters. In the SDM analysis, the charge shuffled (ChS) background is generated using real events from the data itself, specifically from the Ru+Ru and Zr+Zr collisions, following a similar procedure as discussed in previous chapters.

6.5.1 f_{DbCS} distributions

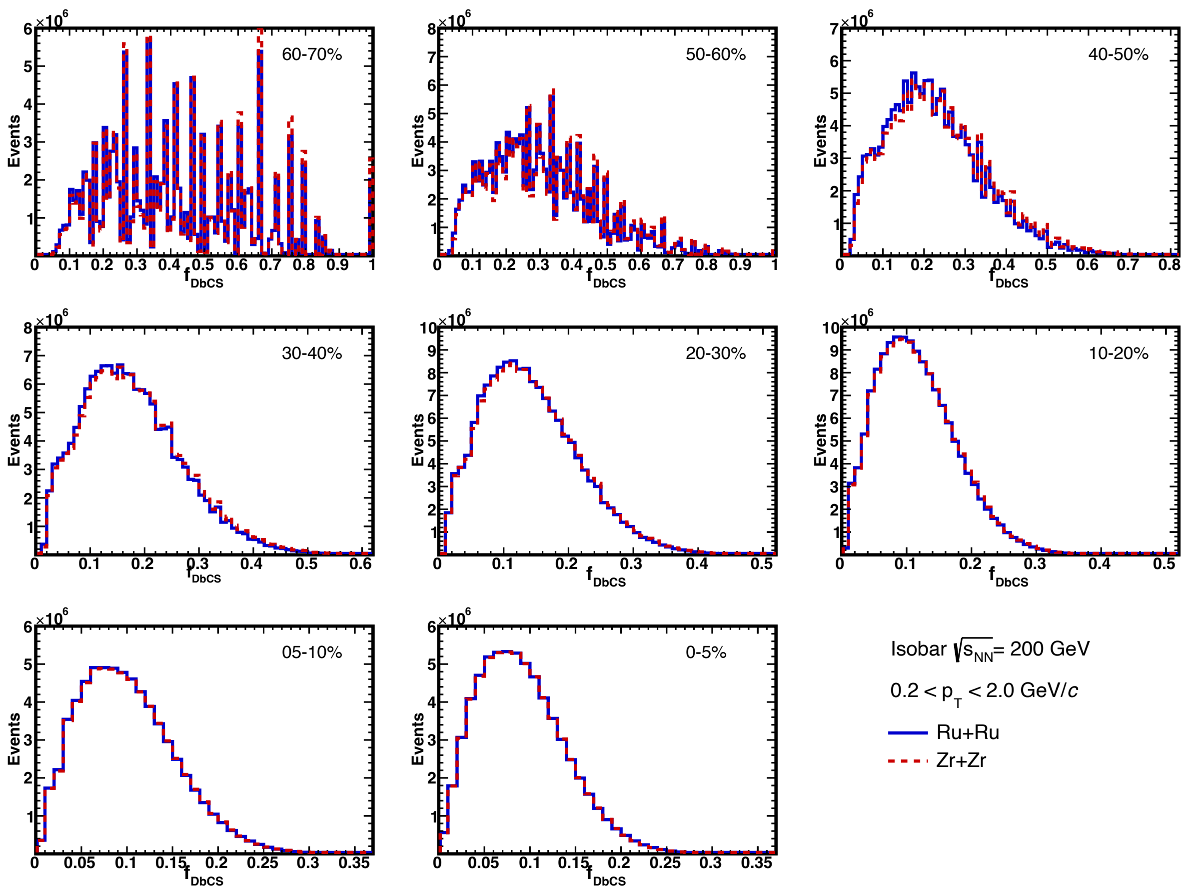

Figure 6.15: Comparison of f_{DbCS} distributions for Ru+Ru and Zr+Zr collisions at $\sqrt{s_{NN}} = 200$ GeV in different collision centralities.

The f_{DbCS} distributions for different collision centralities are compared in Fig. 6.15 for Ru+Ru and Zr+Zr collisions. It can be seen that f_{DbCS}^{Ru+Ru} distribution are almost similar to f_{DbCS}^{Zr+Zr} distribution. Also, the distributions are moving towards higher values of f_{DbCS} with decreasing collision centralities for both Ru+Ru and Zr+Zr collisions. Figure 6.16 and Figure 6.17 compare the f_{DbCS} distributions

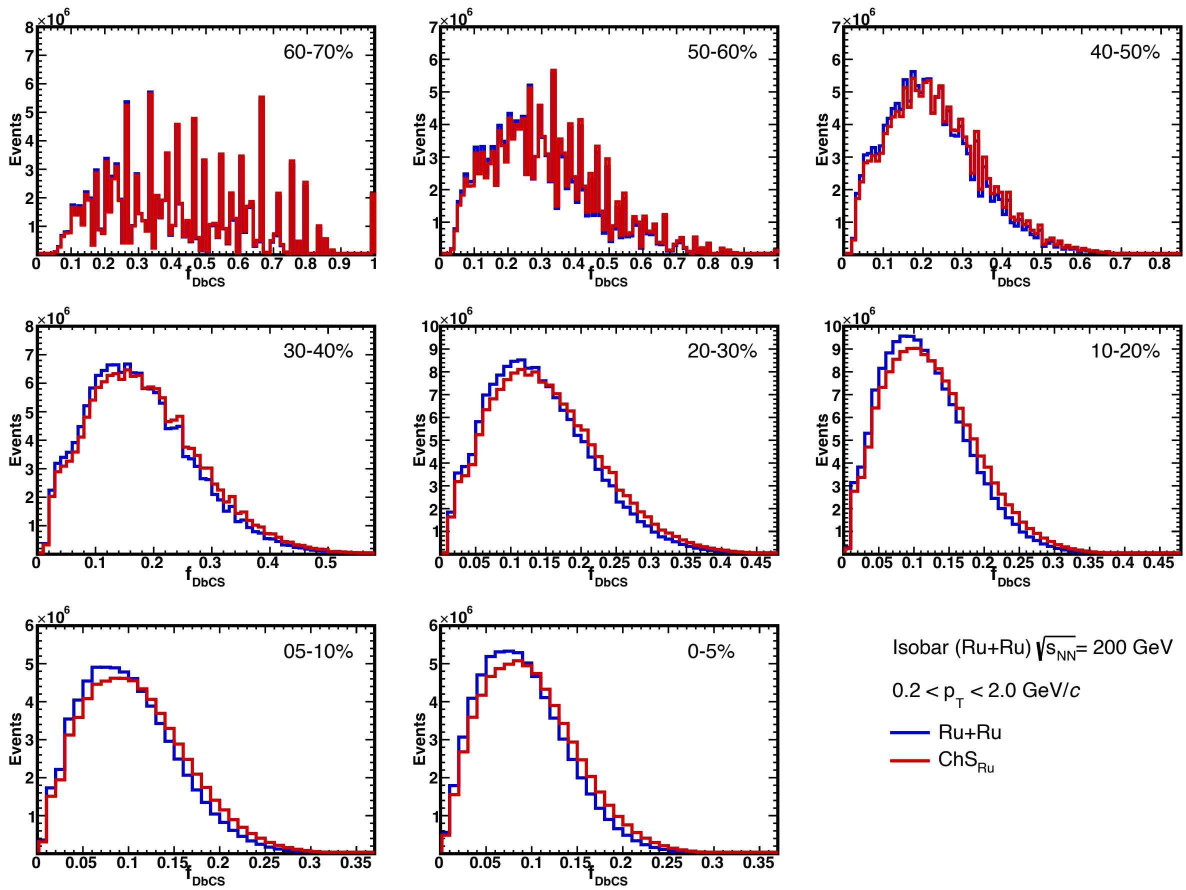

Figure 6.16: Comparison of f_{DbCS}^{Ru+Ru} distributions with f_{DbCS}^{ChS} for different collision centralities.

for Ru+Ru and Zr+Zr collisions, respectively, with the corresponding f_{DbCS}^{ChS}. It can be seen that the f_{DbCS}^{ChS} distributions are ahead of f_{DbCS}^{Ru+Ru} (and f_{DbCS}^{Zr+Zr}) in each collision centrality. f_{DbCS}^{ChS} distributions are also moving towards higher values of f_{DbCS} with decreasing collision centralities for both Ru+Ru and Zr+Zr collisions.

Figure 6.18 (Left) displays the scatter plot for f_{DbCS}^{Ru+Ru} versus f_{DbCS}^{ChS} and Figure 6.18 (Right) displays the scatter plot for f_{DbCS}^{Ru+Ru} versus f_{DbCS}^{ChS} for 30-40% collision

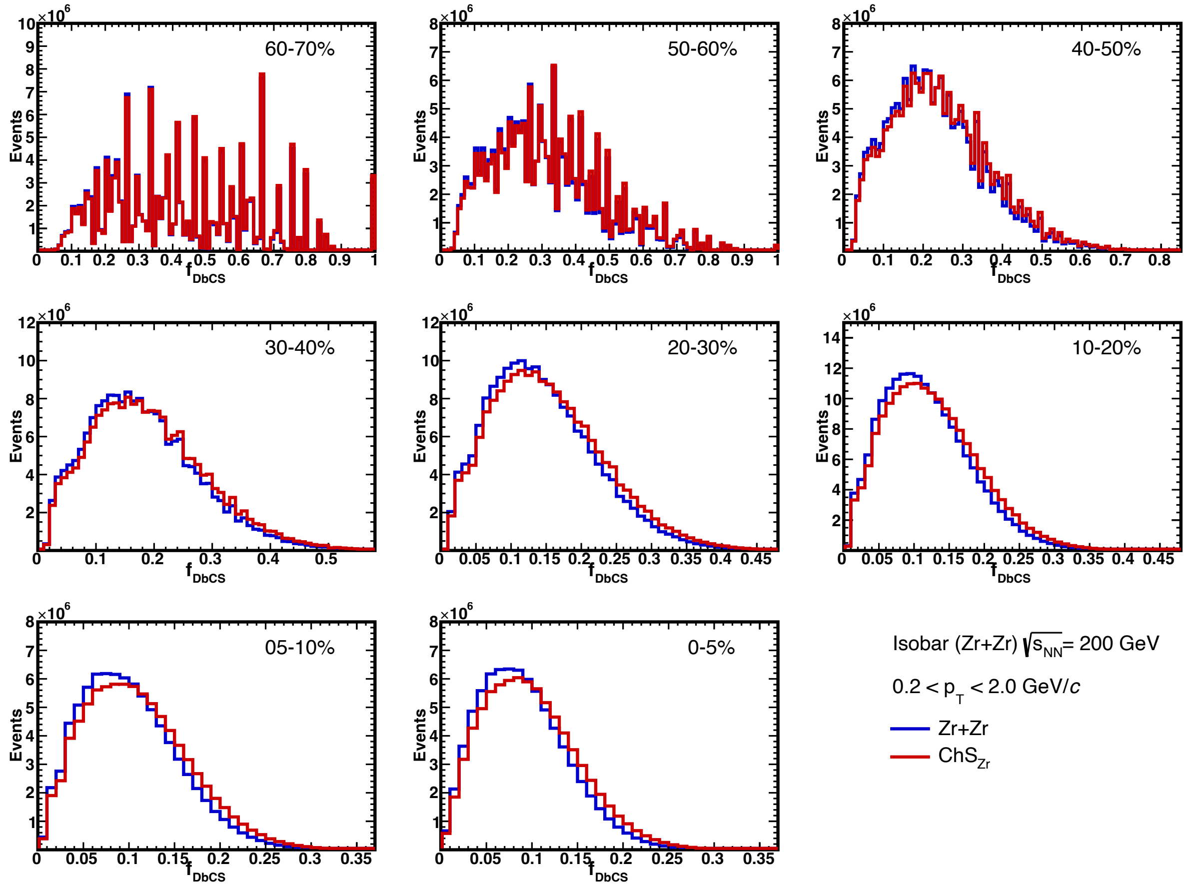

Figure 6.17: Comparison of f_{DbCS}^{Zr+Zr} distributions with f_{DbCS}^{ChS} for different collision centralities.

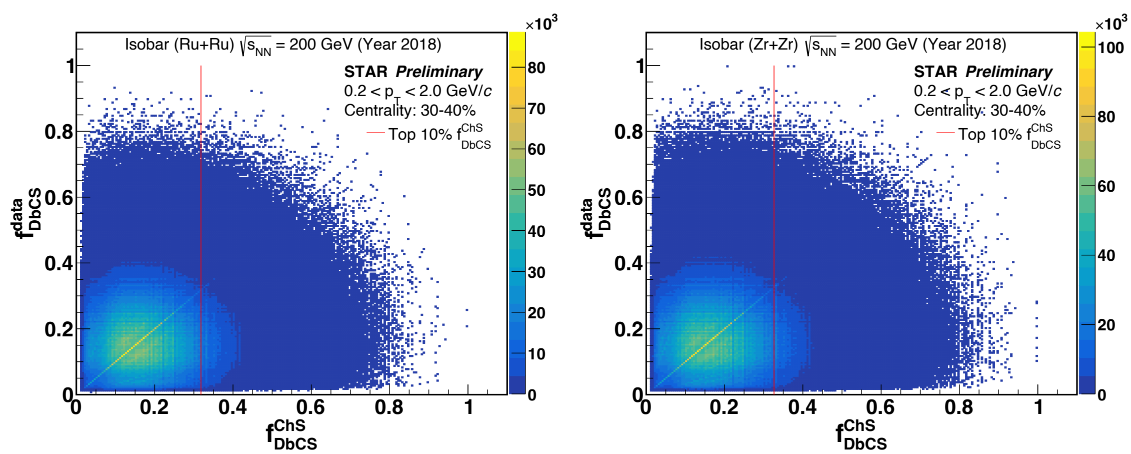

Figure 6.18: Scatter plot of f_{DbCS}^{Ru+Ru} versus f_{DbCS}^{ChS} (Left) and f_{DbCS}^{Zr+Zr} versus f_{DbCS}^{ChS} (Right) for 30-40% collision centrality. The vertical line (red color) is top 10% cut (on the right side) on f_{DbCS}^{ChS}.

centrality. There seems to be no correlation between f_{DbCS} of the charge shuffled event and the f_{DbCS} of the real event for both Ru+Ru and Zr+Zr collisions. For instance the case of top 10% f_{DbCS}^{ChS} on the right side of red lines in Fig. 6.18 are spread over 0-100% for both f_{DbCS}^{Ru+Ru} and f_{DbCS}^{Zr+Zr}. The f_{DbCS} dependence on different physics observables will be discussed for 0-60% collision centrality due to low multiplicity in the lower collision centralities.

6.5.2 Background estimation

As discussed in previous chapters, for the background estimation Charge Shuffle (ChS) and Correlated (Corr) backgrounds are used. The Charge Shuffle background is generated from the data (Ru+Ru and Zr+Zr) itself in which the the charges of particles are shuffled randomly while keeping their momenta (i.e., θ and ϕ) unchanged. This background estimation helps in understanding the level of charge correlations that can occur purely by chance. The γ of the "ChS" events' sample derived for a particular f_{DbCS} bin is denoted as γ_{ChS}. The correlated background, on the other hand, accounts for correlations arising from non-CME effects, such as collective flow or resonance decays. It represents the background signal that is not related to the Chiral Magnetic Effect but can manifest as charge correlations. This is recovered from the corresponding original events in a particular f_{DbCS} bin and termed as correlated background γ_{Corr}. Thus, the total background contribution to the γ-correlator is given by:

$$\gamma_{TotalBkg} = \gamma_{ChS} + \gamma_{Corr} \tag{6.2}$$

6.5.3 Mean multiplicity in f_{DbCS} bins

The dependence of mean multiplicity with f_{DbCS} for each collision centrality (0-60%) is shown in Fig. 6.19. It is seen that the mean multiplicity is lower for top f_{DbCS} bin and increases with decreasing f_{DbCS} values within each collision centrality. Also, the mean multiplicity remains higher for Ru+Ru collision than Zr+Zr collisions for

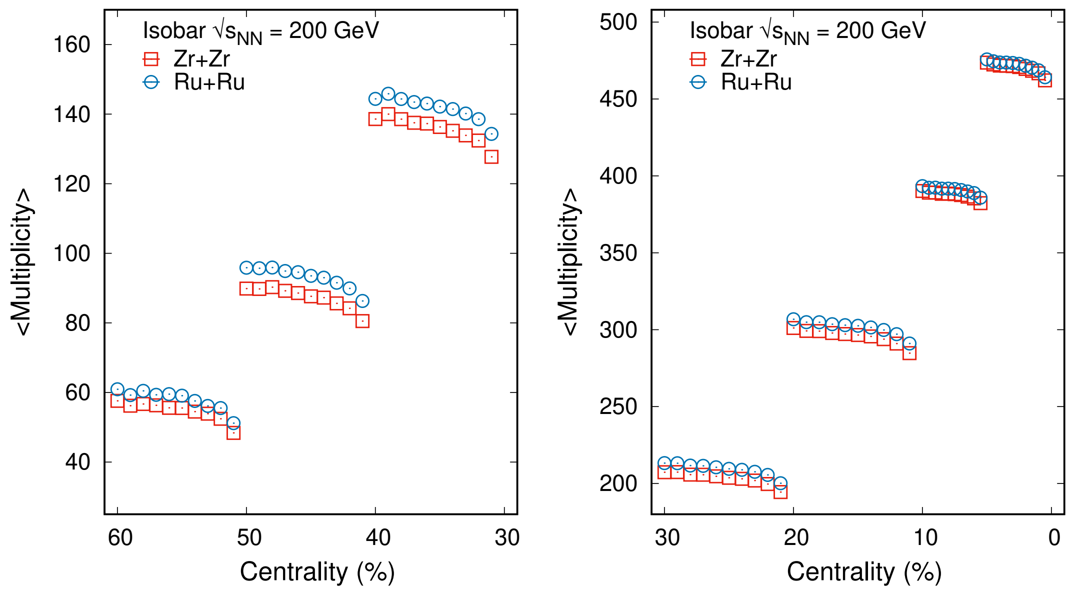

Figure 6.19: The dependence of mean multiplicity on f_{DbCS} for 0-30% (Right) and 30-60% (Left) collision centralities for Ru+Ru and Zr+Zr collisions at $\sqrt{s_{NN}} = 200$ GeV. The rightmost bins represents the top 10% f_{DbCS} and leftmost bins represent 90-100% f_{DbCS} in each collision centrality.

all f_{DbCS} bins.

6.5.4 v_2 dependence on f_{DbCS}

The dependence of elliptic flow (v_2) on f_{DbCS} for 0-60% collision centralities for Ru+Ru and Zr+Zr collisions is shown in Fig. 6.20. It can be seen from the figure that the top f_{DbCS} bins exhibit a higher v_2 and it decreases and becomes approximately the same in the lower f_{DbCS} bins. The spike in v_2 for the top 10% f_{DbCS} is may be due to CME-like events representing a rise in background as well as signal. Also, v_2 in top 10% f_{DbCS} bins is approximately the same for both Ru+Ru and Zr+Zr collisions for 0-50% collision centralities. The statistical uncertainties are given by bars while the systematic uncertainties are represented by boxes. The statistical and systematic uncertainties are too small that they are within the marker size.

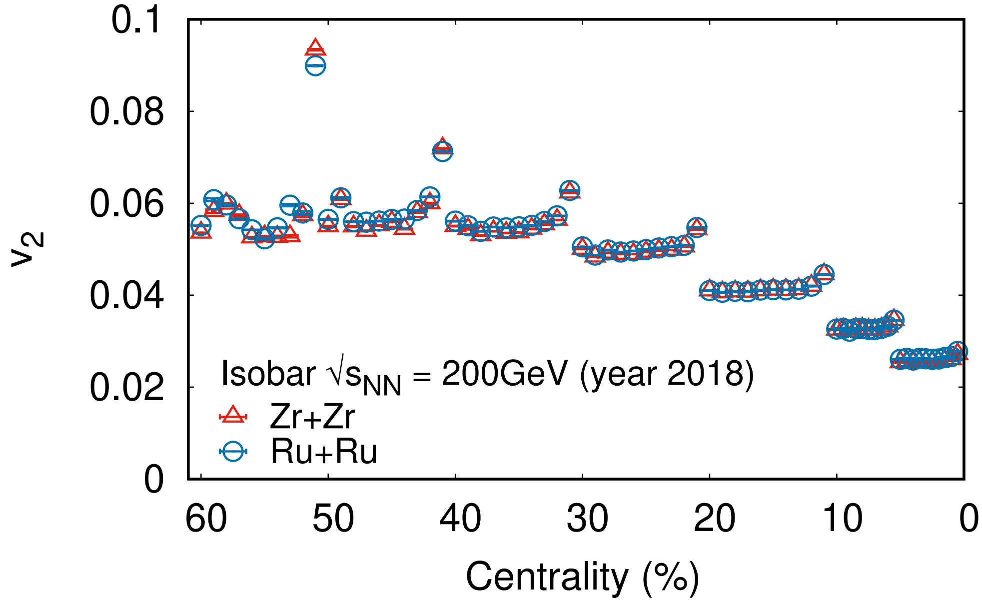

Figure 6.20: v_2 dependence on f_{DbCS} for 0-60% collision centralities for Ru+Ru and Zr+Zr collisions at $\sqrt{s_{NN}}$ = 200 GeV. The rightmost bins represents the top 10% f_{DbCS} and leftmost bins represent 90-100% f_{DbCS} in each collision centrality.

6.5.5 δ-correlator's dependence on f_{DbCS}

The dependence of δ-correlator on f_{DbCS} is displayed in Fig. 6.21 for opposite sign (top panels) and same sign (bottom panels) charge pairs for 0-60% collision centrality for Ru+Ru (blue color) and Zr+Zr (red color) collisions at $\sqrt{s_{NN}}$ = 200 GeV. δ-correlator for OS charge pairs are represented by up-triangles while SS charge pairs are represented by down-triangles. In the case of CME, we expect δ_{SS} to be positive and δ_{OS} to be negative.

In Fig. 6.21, it can be seen that $\delta_{SS} > 0$ (bottom panels) and $\delta_{OS} < 0$ (top panels) for top f_{DbCS} bins (i.e., ∼0-40% f_{DbCS}), while for lower f_{DbCS} bins $\delta_{SS} < 0$ and $\delta_{OS} > 0$. The top f_{DbCS} bins the δ-correlator shows opposite behavior than the average values shown in Fig. 6.11. It is to mention that the magnitude of δ-correlator is a little more for Zr+Zr collisions as compared to Ru+Ru collisions. Y-axes are magnified in the right column plots for 0-30% collision centralities for the sake of clarity.

Figure 6.22 presents the dependence of $\Delta\delta$ (=δ_{OS}-δ_{SS}) on f_{DbCS} for 0-60%

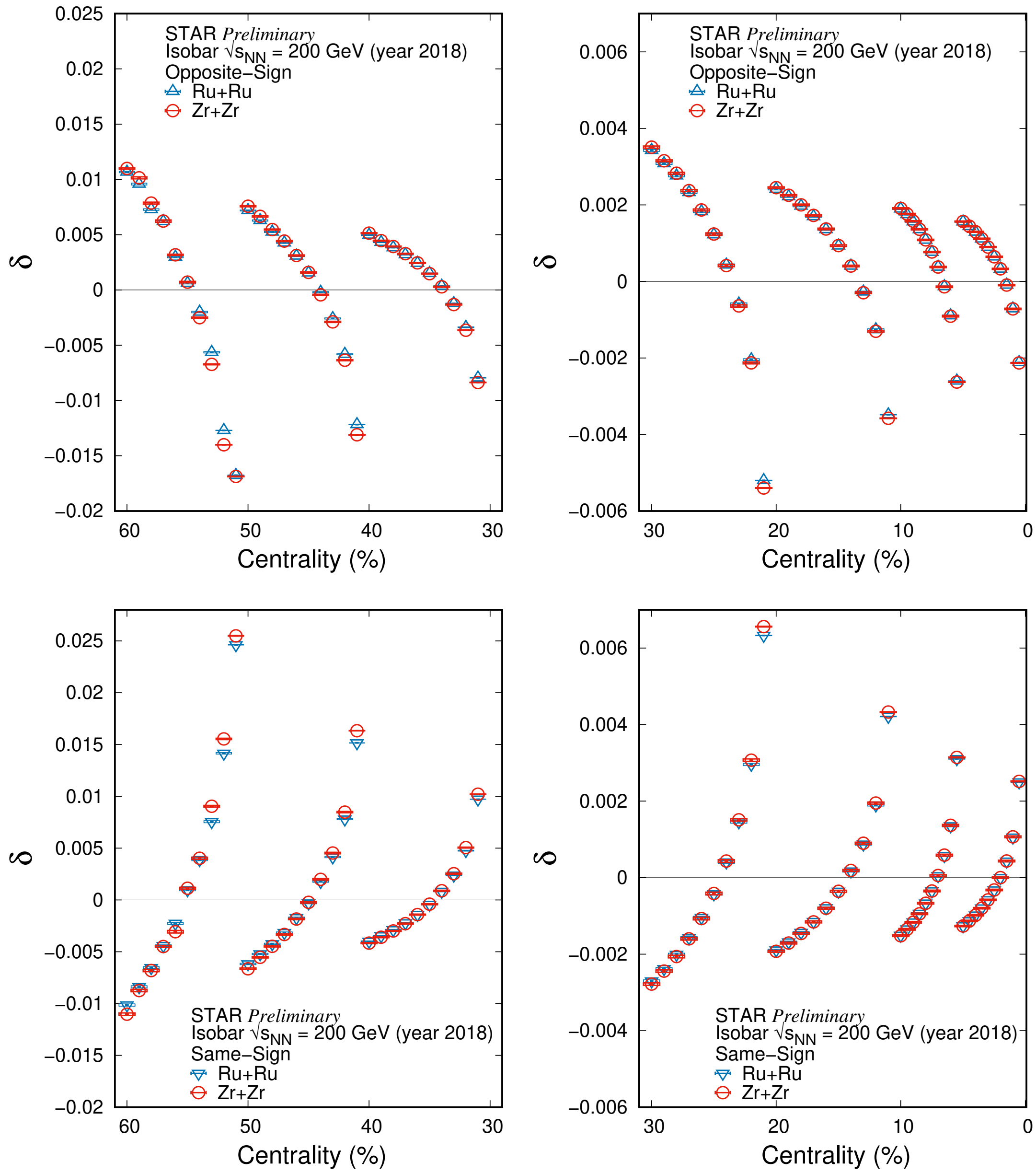

Figure 6.21: δ-correlator dependence on f_{DbCS} for opposite sign (top panels) and same sign (bottom panels) charge pairs for Ru+Ru and Zr+Zr collisions at $\sqrt{s_{NN}}$ = 200 GeV for 0-30% (Right) and 30-60% (Left) collision centralities. The y-axes are magnified in the right panels (for 0-30% collision centralities) for the sake of clarity.

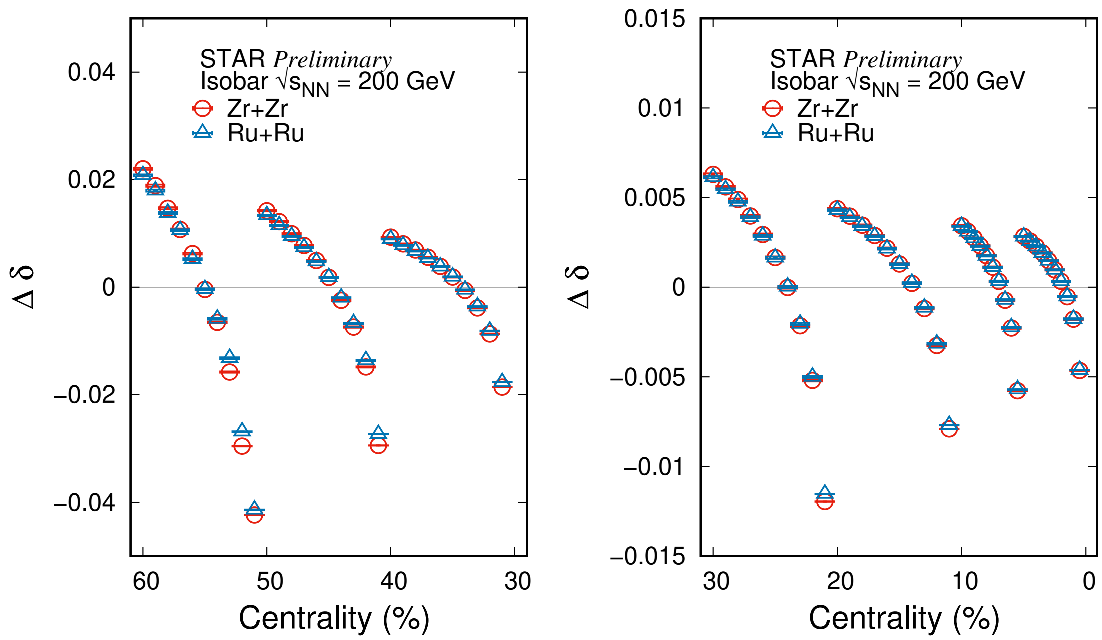

Figure 6.22: $\Delta\delta$-correlator dependence on f_{DbCS} for 0-30% (Right) and 30-60% (Left) collision centralities for Ru+Ru and Zr+Zr collisions at $\sqrt{s_{NN}}$ = 200 GeV. The y-axis is magnified in the right panels (for 0-30% collision centralities) for the sake of clarity.

collision centrality for Ru+Ru (blue color) and Zr+Zr (red color) collisions at $\sqrt{s_{NN}}$ = 200 GeV. $\Delta\delta$ is negative in top f_{DbCS} bins and the correlations become weaker with decreasing f_{DbCS} bins (values) and eventually become positive for lower f_{DbCS} bins. The statistical uncertainties are given by bars while the systematic uncertainties are given by boxes. Statistical uncertainties are too small that they are within the marker size.

6.5.6 γ-correlator's dependence on f_{DbCS}

Figure 6.23 and Fig. 6.24 present the dependence of γ-correlator for OS and SS charge pairs, respectively, on f_{DbCS} for 0-60% collision centralities for Ru+Ru (blue color) and Zr+Zr (red color) collisions at $\sqrt{s_{NN}}$ = 200 GeV. γ-correlator for OS charge pairs are represented by up-triangles while SS charge pairs are represented by down-triangles. The values of γ's (OS and SS) in the top f_{DbCS} bins have increased many times higher than the average values shown in Fig. 6.13 (Left). It can be seen

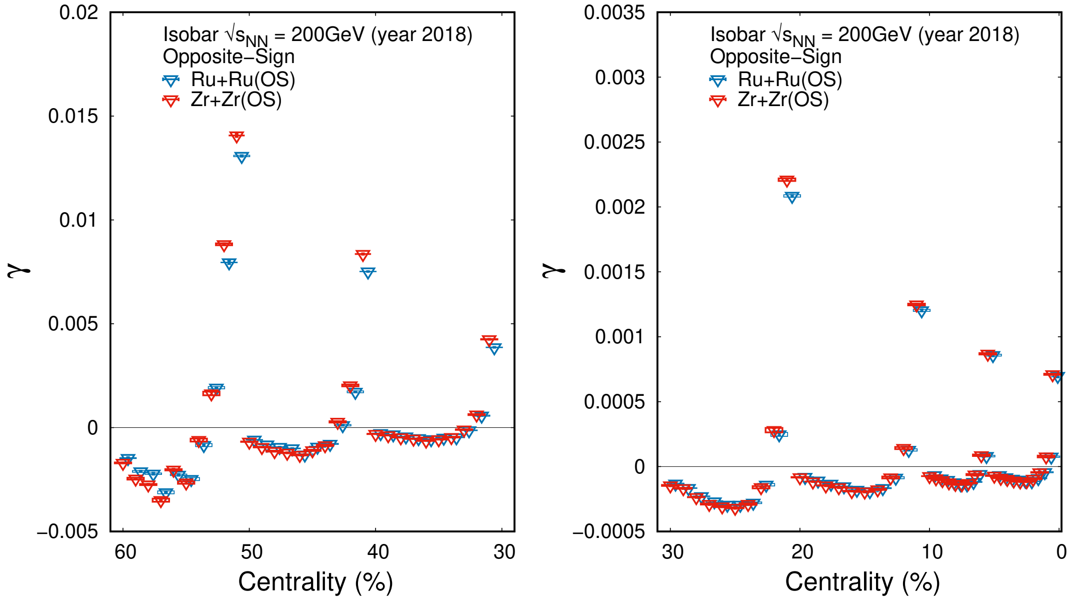

Figure 6.23: The opposite-sign γ-correlator dependence on f_{DbCS} for 0-30% (right) and 30-60% (left) collision centralities for Ru+Ru and Zr+Zr collisions at $\sqrt{s_{NN}}$ = 200 GeV. The y-axis is magnified in the right panels (for 0-30% collision centralities) for the sake of clarity.

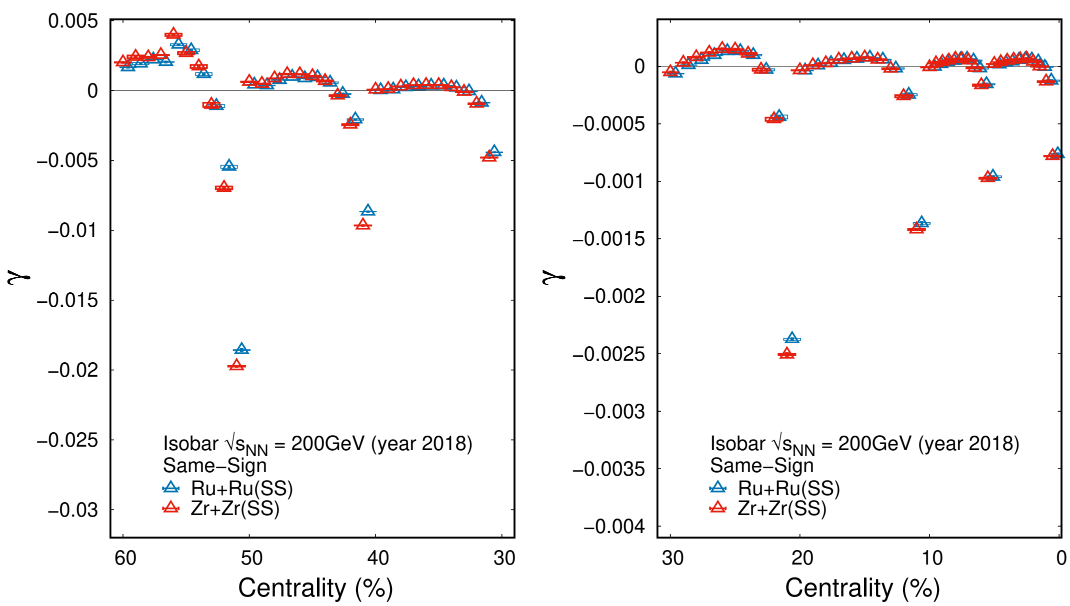

Figure 6.24: The same-sign γ-correlator dependence on f_{DbCS} for 0-30% (right) and 30-60% (left) collision centrality for Ru+Ru and Zr+Zr collisions at $\sqrt{s_{NN}}$ = 200 GeV. The y-axis is magnified in the right panels (for 0-30% collision centralities) for the sake of clarity.

that $\gamma_{OS} > 0$ and $\gamma_{SS} < 0$ for top f_{DbCS} bins (i.e., for 0-20% (0-30%) f_{DbCS} for 0-40% (40-60%) collision centralities), as expected for CME type events. From the figure it is clear that γ's are smaller for Ru+Ru than Zr+Zr collisions in the top 10% (top 20%) f_{DbCS} bins for 20-40% (40-60%) centralities.

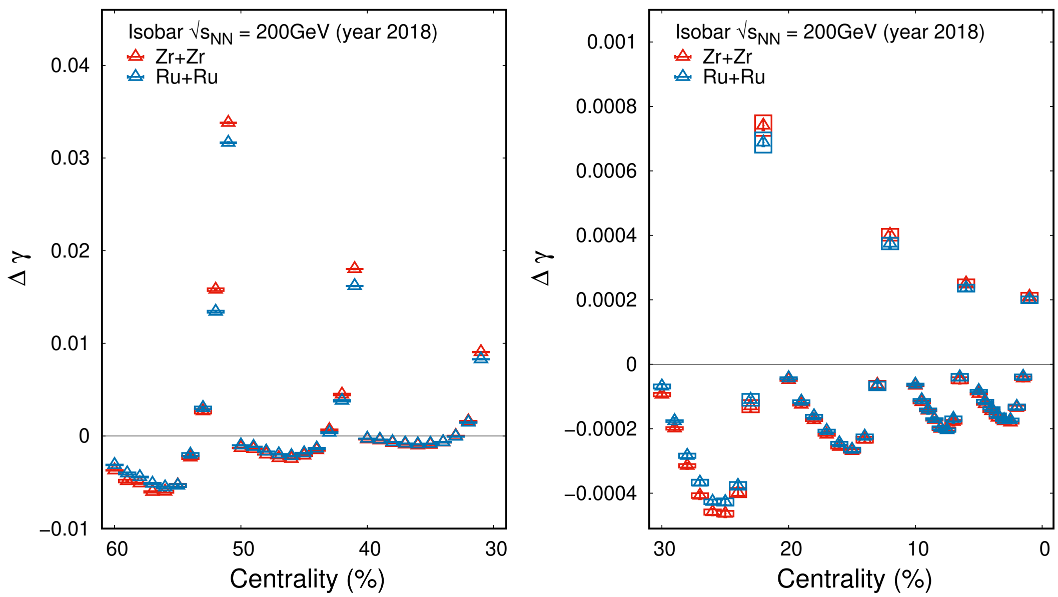

Figure 6.25: The dependence of $\Delta\gamma$ on f_{DbCS} for 0-60% collision centralities for Ru+Ru and Zr+Zr collisions at $\sqrt{s_{NN}}$ = 200 GeV. The y-axis are magnified in the right panels (for 0-30% collision centralities) for the sake of clarity.

Figure 6.25 presents the dependence of $\Delta\gamma$ on f_{DbCS} for 0-60% collision centralities for the isobar (Ru+Ru and Zr+Zr) collisions at $\sqrt{s_{NN}}$ = 200 GeV. It is seen that $\Delta\gamma$ is positive for the top 20% (30%) f_{DbCS} bins for 0-40%(40-60%) centralities. $\Delta\gamma$ is smaller for Ru+Ru than those of Zr+Zr collisions. The values of $\Delta\gamma$'s in the top f_{DbCS} bins have increased many times higher than the average values shown in Fig. 6.13 (Right). Boxes represent the systematic errors while the bars represent the statistical errors. Statistical uncertainties are within the marker size.

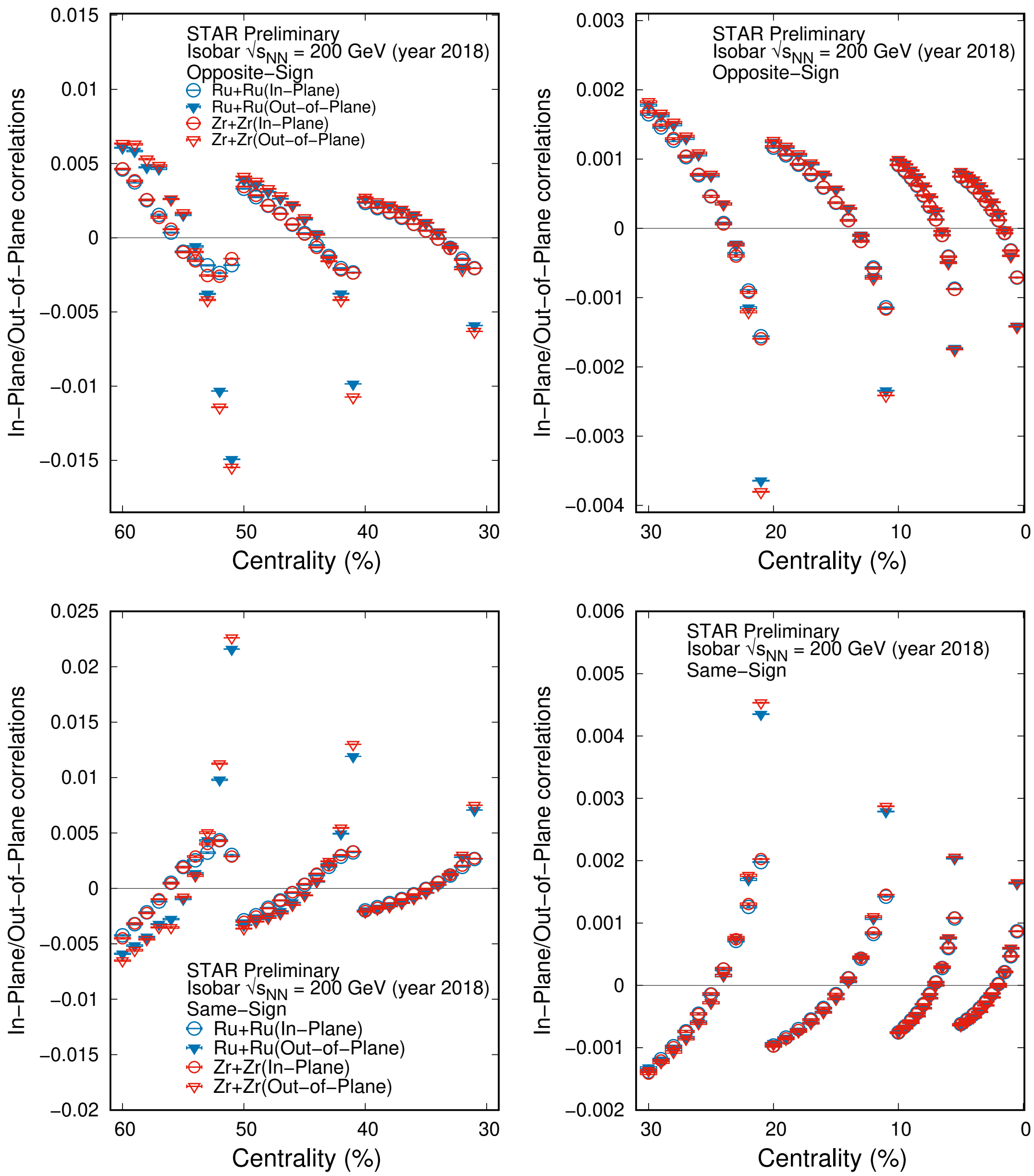

Figure 6.26: The dependence of in-plane and out-of-plane correlations on f_{DbCS} for 0-30% (right) and 30-60% (left) collision centralities for Ru+Ru and Zr+Zr collisions at $\sqrt{s_{NN}} = 200$ GeV for opposite sign (top panels) and same sign (bottom panels) charge pairs. The y-axes are magnified in the right panels (for 0-30% collision centralities) for the sake of clarity.

6.5.7 In-plane and Out-of-plane correlators' dependence on f_{DbCS}

Figure 6.26 presents the dependence of in-plane and out-of-plane correlations on f_{DbCS} for OS (top panels) and SS (bottom panels) charge pairs for 0-60% collision centralities for Ru+Ru and Zr+Zr collisions at $\sqrt{s_{NN}}$ = 200 GeV. The in-plane correlations are represented by circles while out-of-plane correlations are represented by down-triangle. The out-of-plane correlations are negative for OS charge pairs and positive for SS charge pairs for top f_{DbCS} bins. The out-of-plane correlations are higher for Zr+Zr collisions than Ru+Ru collisions. Stronger correlations are seen in out-of-plane for both same-sign and opposite-sign charge pairs due to out-of-plane charge separation for both Ru+Ru and Zr+Zr collisions for top f_{DbCS} bins.

6.5.8 $\Delta\gamma$-correlators and backgrounds dependences on f_{DbCS}

The dependence of $\Delta\gamma$ on f_{DbCS} for Ru+Ru (Zr+Zr) collisions and their respective backgrounds i.e., $ChS_{Ru/Zr}$ and $Corr_{Ru/Zr}$ background, for 0-60% collision centralities is displayed in Fig. 6.27 (and Fig. 6.28). In the figure blue color is for "Ru+Ru" ("Zr+Zr"), red color for "$ChS_{Ru/Zr}$" and black color for "$Corr_{Ru/Zr}$". $\Delta\gamma$ is positive for Ru+Ru (Zr+Zr) for the top 20%/30% bins for 0-40%/40-60% collision centralities. In the lower f_{DbCS} bins the $\Delta\gamma$ becomes negative. A similar trend is seen for charge shuffled $\Delta\gamma$. It is noted that the $\Delta\gamma$ for the correlated background is positive and is independent of the f_{DbCS} bins as its values are approximately the same within each collision centrality. Also, the values of $\Delta\gamma_{Corr}$ increase with decreasing collision centrality.

It can be seen that the $\Delta\gamma$ for Ru+Ru (Zr+Zr) is higher than the $\Delta\gamma_{ChS}$ for the top f_{DbCS} bins (i.e., top 20%/30%). Also the total background i.e., $\Delta\gamma_{ChS} + \Delta\gamma_{Corr}$ is lower than the data (Ru+Ru or Zr+Zr) in the top f_{DbCS} bins. Since a positive $\Delta\gamma$ is considered as signal for CME, thus we need to look for the CME signal in

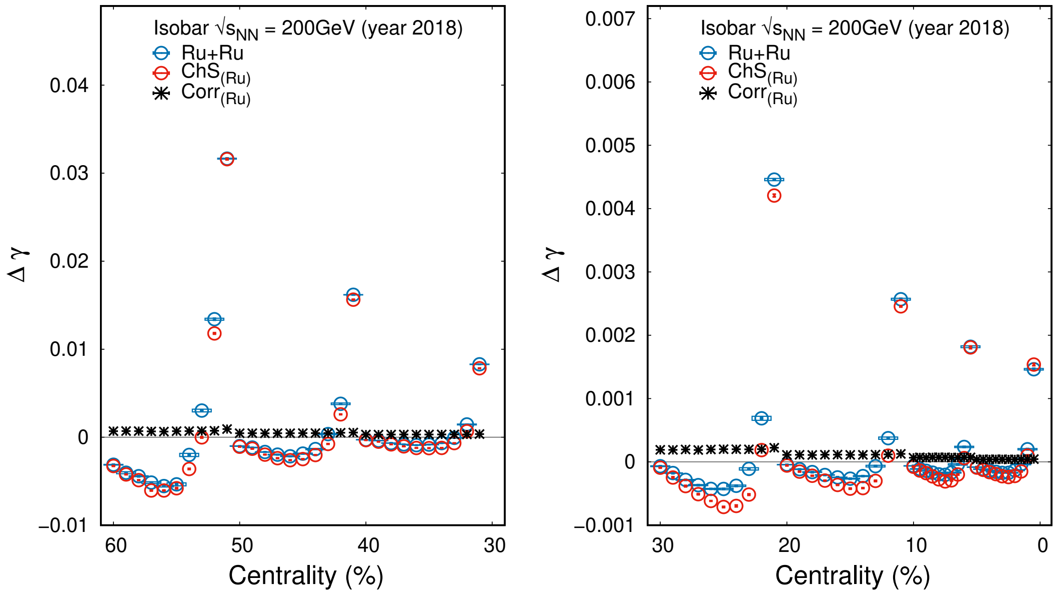

Figure 6.27: f_{DbCS} dependence on $\Delta\gamma$ for Ru+Ru, ChS_{Ru} and $Corr_{Ru}$ background for 0-30% (right) and 30-60% (left) collision centralities.

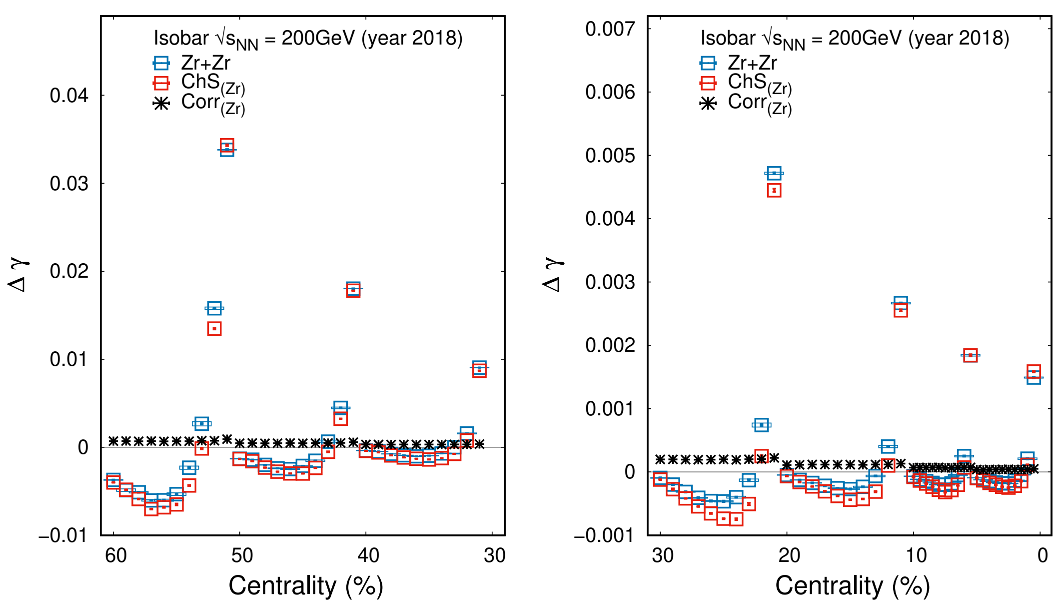

Figure 6.28: f_{DbCS} dependence on $\Delta\gamma$ for Zr+Zr, ChS_{Zr} and $Corr_{Zr}$ background for 0-30% (right) and 30-60% (left) collision centralities.

the top f_{DbCS} bins in which $\Delta\gamma > 0$. Thus the analysis using SDM provides the potential CME-like events in the top 20%/30% f_{DbCS} bins.

6.5.9 $\Delta\gamma_{Data}/\Delta\gamma_{Bkg}$ for Ru+Ru and Zr+Zr

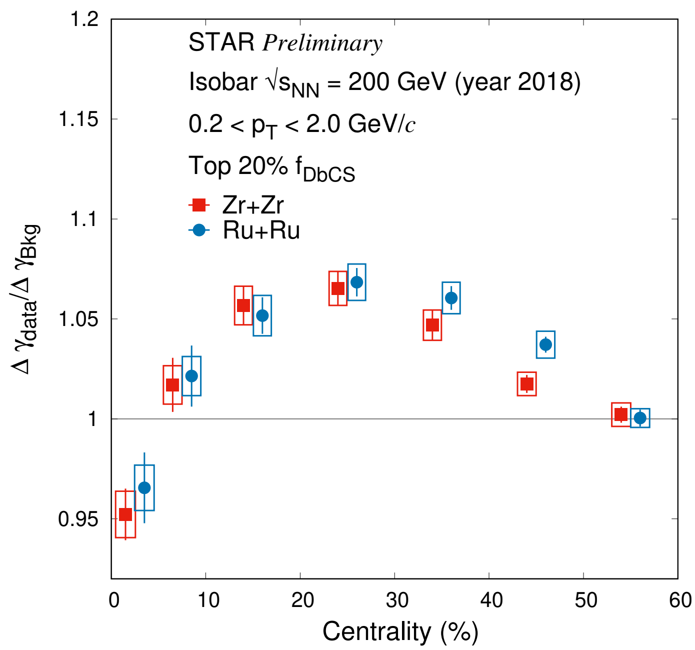

Figure 6.29: $\Delta\gamma_{Data}/\Delta\gamma_{Bkg}$ for Ru+Ru and Zr+Zr collisions at $\sqrt{s_{NN}} = 200$ GeV as a function of collision centrality.

Since it was suggested that there may be a significant excess of the CME signal in Ru+Ru collisions over those in Zr+Zr collisions due to a larger magnetic field in Ru+Ru collisions. We need to check the $\Delta\gamma_{Data}/\Delta\gamma_{Bkg}$ observable for comparison. Here, $\Delta\gamma_{Bkg} = \Delta\gamma_{ChS}+\Delta\gamma_{Corr}$ while $\Delta\gamma_{Data}$ is representing $\Delta\gamma$ for Ru+Ru and Zr+Zr collisions. Figure 6.29 presents $\Delta\gamma_{Data}/\Delta\gamma_{Bkg}$ for Ru+Ru and Zr+Zr collisions. It is seen that the ratio is well over 1 by 2-6% for 10-50% collision centralities. The ratio agrees within uncertainties for Ru+Ru and Zr+Zr collisions. We do not observe any enhancement in the background scaled $\Delta\gamma$ of Ru+Ru over Zr+Zr for the top 20% f_{DbCS}. Figure 6.30 presents the "double ratio" of Ru+Ru to Zr+Zr collisions. The double ratio is computed using eq. 6.3.

$$Double\ Ratio = \frac{(\Delta\gamma_{Data}/\Delta\gamma_{Bkg})_{Ru}}{(\Delta\gamma_{Data}/\Delta\gamma_{Bkg})_{Zr}} \tag{6.3}$$

We have fitted all the points of the double ratio with a "Pol0 Fit" (of a straight

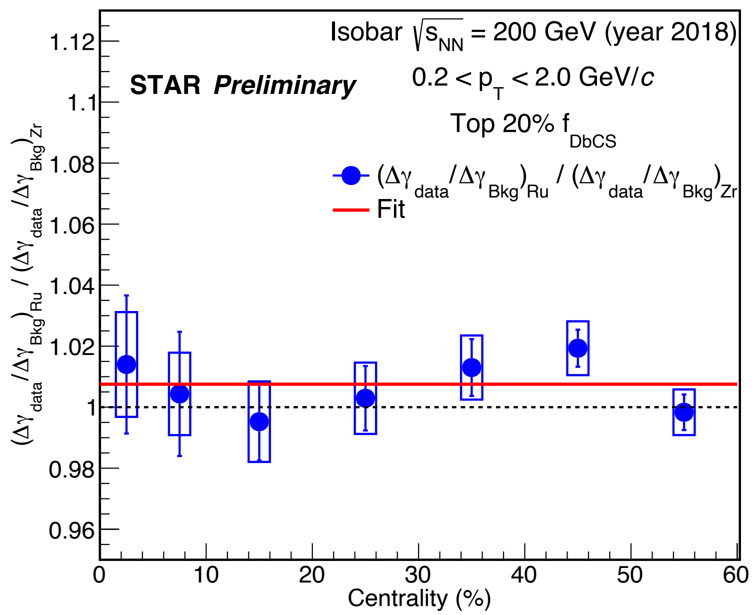

Figure 6.30: Double ratio$(\Delta\gamma_{Data}/\Delta\gamma_{Bkg})_{Ru}/\Delta\gamma_{Data}/\Delta\gamma_{Bkg})_{Zr})$ as a function of collision centrality.

line). The double ratio is 1.007±0.003 (pol0 Fit) for 0-60% centralities. Thus, we see no significant rise of CME signal in Ru+Ru collisions as compared to Zr+Zr collisions contrary to the expectation in isobar collisions as already reported by the STAR [12].

6.6 Conclusion

Isobaric collisions of $^{96}_{44}Ru$+$^{96}_{44}Ru$ and $^{96}_{40}Zr$+$^{96}_{40}Zr$ nuclei were proposed as a promising approach to study the Chiral Magnetic Effect (CME) in heavy-ion collisions. The larger atomic number of Ru compared to Zr was expected to result in a stronger magnetic field in Ru+Ru collisions, potentially enhancing the CME signal. However, a high-statistics run conducted in 2018 did not observe any CME signature that met the predefined criteria, despite rigorous analyses.

In the present work, the isobaric collision data was analyzed using the Sliding Dumbbell method, which searches for back-to-back charge separation across the dumbbell on an event-by-event basis within each collision centrality. Backgrounds in each isobar were calculated using techniques such as the charged shuffled (ChS) background, which explores the correlations that can occur purely by chance, and the correlated (Corr) background, calculated using the individual isobar data itself. These approaches take into account the slightly different elliptic flows and multiplicities of the two isobars in a given collision centrality.

The distribution of the charge separation parameter (f_{DbCS}) shifted towards higher values with decreasing collision centrality, and the mean multiplicity remained higher for Ru+Ru collisions. The elliptic flow shows a slight increase in the top f_{DbCS} bins compared to the lower f_{DbCS} bins, while the mean multiplicity decreases in the top f_{DbCS} bins. The γ and δ correlators exhibit a significant enhancement in the top f_{DbCS} bins compared to the average values for each collision centrality, for both same-sign and opposite-sign charge pairs. The γ-correlators exhibited positive values for opposite-sign (OS) pairs and negative values for same-sign (SS) pairs, while the δ correlator showed the opposite trend. Both SS and OS pairs exhibited out-of-plane correlations in the top f_{DbCS} bins due to the out-of-plane charge separation. These characteristics indicated that the top 20% f_{DbCS} bins represented the most potential CME-like events. Similar trends were observed for the charge shuffled events, but with reduced magnitudes in both isobars. The ratio of $\Delta\gamma_{Data}/\Delta\gamma_{Bkg}$ (using this one can also calculate the fractional CME) was calculated for the top 20% f_{DbCS} bins for each centrality in both isobars.

When comparing the background-scaled $\Delta\gamma$ between Ru+Ru and Zr+Zr collisions, no significant differences were observed. The double ratio $\frac{(\Delta\gamma_{Data}/\Delta\gamma_{Bkg})_{Ru}}{(\Delta\gamma_{Data}/\Delta\gamma_{Bkg})_{Zr}}$ was fitted with a straight line for 0-60% collision centrality, resulting in a value of 1.007±0.003. This indicates that there was no significant enhancement of the CME signal in Ru+Ru collisions compared to Zr+Zr collisions, contrary to initial expectations in isobaric collisions.

Overall, the analyses of isobaric collisions at the STAR experiment did not find evidence of an enhanced CME signal in Ru+Ru collisions compared to Zr+Zr collisions. The experimental results contradicted initial expectations, despite employing various techniques. However, CME-like events are observed in the top 20% f_{DbCS} bins (representing approximately 2-5% CME signal) in both isobars, whereas the rest of the 80% f_{DbCS} bins in a given centrality show no CME-like events. The expected enhancement in Ru+Ru collisions due to the increased magnetic field may not be distinguishable due to the small multiplicities (or not enough increase in the magnetic field) in these isobar systems, as also observed in simulated events generated by the AVFD model mentioned in Chapter 4.

Bibliography

[1] K. Fukushima, D. E. Kharzeev, and H. J. Warringa, “Chiral magnetic effect”, Phys. Rev. D 78, 074033 (2008).

[2] D. E. Kharzeev, L. D. McLerran, and H. J. Warringa, “The effects of topological charge change in heavy ion collisions: “Event by event P and CP violation””, Nucl. Phys. A 803, 227 (2008).

[3] D. Kharzeev, “Parity violation in hot QCD: Why it can happen, and how to look for it”, Phys. Lett. B 633, 260 (2006).

[4] S. A. Voloshin, “Testing the Chiral Magnetic Effect with Central U+U Collisions”, Phys. Rev. Lett. 105, 172301 (2010).

[5] V. Skokov, A. Yu. Illarionov, and V. Toneev, “ESTIMATE OF THE MAGNETIC FIELD STRENGTH IN HEAVY-ION COLLISIONS”, Int. J. Mod. Phys. A 24, 5925 (2009).

[6] A. Bzdak and V. Skokov, “Event-by-event fluctuations of magnetic and electric fields in heavy ion collisions”, Phys. Lett. B 710, 171 (2012).

[7] W. T. Deng and X. G. Huang, “Event-by-event generation of electromagnetic fields in heavy-ion collisions”, Phys. Rev. C 85, 044907 (2012).

[8] J. Bloczynski, X.-G. Huang, X. Zhang, and J. Liao, “Azimuthally fluctuating magnetic field and its impacts on observables in heavy-ion collisions”, Phys. Lett. B 718, 1529 (2013).

[9] J. Bloczynski, X. G. Huang, X. Zhang, and J. Liao, “Charge-dependent azimuthal correlations from AuAu to UU collisions”, Nucl. Phys. A 939, 85 (2015).

[10] L. McLerran and V. Skokov, “Comments about the electromagnetic field in heavy-ion collisions”, Nucl. Phys. A 929, 184 (2014).

[11] Y. Sun, Y. Wang, Q. Li, and F. Wang, “Effect of internal magnetic field on collective flow in heavy ion collisions at intermediate energies”, Phys. Rev. C 99, 064607 (2019).

[12] M. S. Abdallah *et al.* [STAR Collaboration], “Search for the chiral magnetic effect with isobar collisions at $\sqrt{s_{NN}} = 200$ GeV by the STAR Collaboration at the BNL Relativistic Heavy Ion Collider”, Phys. Rev. C 105, 014901 (2022).

[13] B. Schenke, C. Shen, and P. Tribedy, “Multiparticle and charge-dependent azimuthal correlations in heavy-ion collisions at the Relativistic Heavy-Ion Collider”, Phys. Rev. C 99, 044908 (2019).

[14] S. A. Voloshin, “Parity violation in hot QCD: How to detect it”, Phys. Rev. C 70, 057901 (2004).

[15] B. I. Abelev *et al.* [STAR Collaboration], “Azimuthal Charged-Particle Correlations and Possible Local Strong Parity Violation”, Phys. Rev. Lett. 103, 251601 (2009).

[16] Jagbir Singh, “Search for the Chiral Magnetic Effect using Sliding Dumbbell Method in Isobar Collisions ($^{96}_{44}Ru +^{96}_{44} Ru$ and $^{96}_{40}Zr +^{96}_{40} Zr$) at RHIC”, Proceedings of the DAE Symp. Nucl. Phys. 66, 1048, (2022).

[17] Jagbir Singh, Anjali Attri, and Madan M. Aggarwal, “Charge dependent azimuthal correlations using Sliding Dumbbell Method to search CME in Au+Au Collisions with AMPT“, Proceedings of the DAE Symp. Nucl. Phys. 64, 830, (2019).

[18] A. Bilandzic, R. Snellings and S. Voloshin, "Flow analysis with cumulants: direct calculations", Phys. Rev. C 83, 044913 (2011).

[19] M. Anderson *et al.*, "The STAR time projection chamber: a unique tool for studying high multiplicity events at RHIC", Nucl. Instrum. Methods Phys. Res., Sect. A 499, 659 (2003).

[20] W. J. Llope *et al.*, "The TOFp/pVPD time-of-flight system for STAR", Nucl. Instrum. Methods Phys. Res., Sect. A 522, 252 (2004).

[21] J. Adams *et al.*, "The STAR event plane detector", Nucl. Instrum. Methods Phys. Res., Sect. A 968, 163970 (2020).

[22] C. Adler, A. Denisov, E. Garcia, M. J. Murray, H. Strobele, and S. N. White, "The RHIC Zero Degree Calorimeter", Nucl. Instrum. Methods Phys. Res., Sect. A 470, 488 (2001).

[23] W. J. Llope *et al.*, "The STAR Vertex Position Detector", Nucl. Instrum. Methods Phys. Res., Sect. A 759, 23 (2014).

[24] Yu Hu, Subikash Choudhury, Prithwish Tribedy, Analysis Note for Isobar Blind Analysis, "https://drupal.star.bnl.gov/STAR/system/files/isobar_analysis_note_v3.pdf".

[25] Gregory Nigmatkulov, "https://lists.bnl.gov/mailman/private/star-cme-focusgroup-l/attachments/20210517/b4a7f237/attachment-0001.pdf".

[26] H. J. Xu *et al.*, "Importance of Isobar Density Distributions on the Chiral Magnetic Effect Search", Phys. Rev. Lett. 121, 022301 (2018).

[27] B. I. Abelev *et al.* [ALICE Collaboration], "Charge separation relative to the reaction plane in Pb-Pb collisions at $\sqrt{s_{NN}} = 2.76$ TeV", Phys. Rev. Lett. 110, 012301 (2013).

Publications/Conferences

I Papers presented in Conferences, Workshops, Symposiums

1. Jagbir Singh (for the STAR Collaboration), “Chiral Magnetic Effect in isobaric ($^{96}_{44}Ru +^{96}_{44} Ru$ and $^{96}_{40}Zr +^{96}_{40} Zr$) collisions at $\sqrt{s_{\rm NN}}$ = 200 GeV using Sliding Dumbbell Method at RHIC”, International Conference on Physics and Astrophysics of Quark Gluon Plasma, 2023 (to be published).

2. Jagbir Singh (for the STAR Collaboration), “CME search in isobar ($^{96}_{44}Ru +^{96}_{44} Ru$ and $^{96}_{40}Zr +^{96}_{40} Zr$) collisions at $\sqrt{s_{\rm NN}}$ = 200 GeV using SDM at RHIC”, XXV DAE-BRNS HIGH ENERGY PHYSICS SYMPOSIUM, 2022, (to be published).

3. Jagbir Singh (for the STAR Collaboration), “Search for the Chiral Magnetic Effect using Sliding Dumbbell Method in Isobar Collisions ($^{96}_{44}Ru +^{96}_{44} Ru$ and $^{96}_{40}Zr +^{96}_{40} Zr$) at RHIC“, *DAE Symp. Nucl. Phys.* 66, 1048 (2022).

4. Jagbir Singh *et al.*, “Event-by-Event Charge Separation in Au+Au Collisions at $\sqrt{s_{NN}}$ = 200 GeV Using AMPT“, *Springer Proc. Phys.* 261, 1065-1068 (2021).

5. Jagbir Singh *et al.*, “Charge dependent azimuthal correlations using Sliding Dumbbell Method to search CME in Au+Au Collisions with AMPT”, *DAE Symp. Nucl. Phys.* 64, 830-831 (2019).

6. Jagbir Singh *et al.*, "Study of event-by-event charge separation in Au+Au collisons at $\sqrt{s_{NN}}$ = 200 GeV using AMPT", *DAE Symp. Nucl. Phys.* 63, 996-997 (2018).

PUBLICATIONS

1. B. Aboona *et al.* [STAR Collaboration], "Observation of Directed Flow of Hypernuclei ${}^{3}_{\Lambda}$H and ${}^{4}_{\Lambda}$H in $\sqrt{s_{NN}}$ = 3 GeV Au+Au Collisions at RHIC", Phys. Rev. Lett. 130 no.21, 212301 (2023).

2. B. Aboona *et al.* [STAR Collaboration], "Beam energy dependence of the linear and mode-coupled flow harmonics in Au+Au collisions", Phys. Lett. B 839, 137755 (2023).

3. M. S. Abdallah *et al.* [STAR Collaboration], "$K^{*}0$ production in Au+Au collisions at $\sqrt{s_{NN}}$ = 7.7, 11.5, 14.5, 19.6, 27, and 39 GeV from the RHIC beam energy scan", Phys. Rev. C 107 no.3, 034907 (2023).

4. M. S. Abdallah *et al.* [STAR Collaboration], "Higher-order cumulants and correlation functions of proton multiplicity distributions in $\sqrt{s_{NN}}$=3 GeV Au+Au collisions at the RHIC STAR experiment", Phys. Rev. C 107 no.2, 024908 (2023).

5. M. S. Abdallah *et al.* [STAR Collaboration], "Beam Energy Dependence of Triton Production and Yield Ratio ($N_t \times N_p/N_d^2$) in Au+Au Collisions at RHIC", Phys. Rev. Lett. 130, 202301 (2023).

6. B. Aboona *et al.* [STAR Collaboration], "Search for the Chiral Magnetic Effect in Au+Au collisions at $\sqrt{s_{\mathrm{NN}}}$ = 27 GeV with the STAR forward Event Plane Detectors", Phys. Lett. B 839, 137779 (2023).

7. B. Aboona *et al.* [STAR Collaboration], "Beam Energy Dependence of Fifth and Sixth-Order Net-proton Number Fluctuations in Au+Au Collisions at RHIC", Phys. Rev. Lett. 130 no.8, 082301 (2023).

8. B. Aboona *et al.* [STAR Collaboration], "Observation of sequential Υ suppression in Au+Au collisions at $\sqrt{s_{\rm NN}} = 200$ GeV with the STAR experiment", Phys. Rev. Lett. 130 no.11, 112301 (2023).

9. M. S. Abdallah *et al.* [STAR Collaboration], "Azimuthal anisotropy measurement of (multi)strange hadrons in Au+Au collisions at $\sqrt{S_{NN}} = 54.4$ GeV", Phys. Rev. C 107 no.2, 024912 (2023).

10. M. S. Abdallah *et al.* [STAR Collaboration], "Pattern of global spin alignment of ϕ and K^{*0} mesons in heavy-ion collisions", Nature 614 no.7947, 244 (2023).

11. M. Abdallah *et al.* [STAR Collaboration], "Tomography of ultrarelativistic nuclei with polarized photon-gluon collisions", Sci. Adv. 9 no.1 (2023).

12. M. S. Abdallah *et al.* [STAR Collaboration], "Measurement of ${}^4_\Lambda H$ and ${}^4_\Lambda He$ binding energy in Au+Au collisions $\sqrt{s_{NN}}$= 3 GeV", Phys. Lett. B 834, 137449 (2022).

13. M. S. Abdallah *et al.* [STAR Collaboration], "Light nuclei collectivity from $\sqrt{s_{NN}} = 3$ GeV Au+Au collisions at RHIC", Phys. Lett. B 827, 136941 (2022).

14. M. S. Abdallah *et al.* [STAR Collaboration], "Measurements of Proton High Order Cumulants in $\sqrt{s_{\rm NN}} = 3$ GeV Au+Au Collisions and Implications for the QCD Critical Point", Phys. Rev. Lett. 128, no.20, 202303 (2022).

15. M. S. Abdallah *et al.* [STAR Collaboration], "Evidence for Nonlinear Gluon Effects in QCD and Their Mass Number Dependence at STAR", Phys. Rev. Lett. 129, 092501 (2022).

16. M. S. Abdallah *et al.* [STAR Collaboration], "Longitudinal double-spin asymmetry for inclusive jet and dijet production in polarized proton collisions at $\sqrt{s} = 510$ GeV", Phys. Rev. D 105, no.9, 092011 (2022).

17. M. S. Abdallah *et al.* [STAR Collaboration], "Measurements of ${}_{\Lambda}^{3}$H and ${}_{\Lambda}^{4}$H Lifetimes and Yields in Au+Au Collisions in the High Baryon Density Region", Phys. Rev. Lett. 128, no.20, 202301 (2022).

18. M. S. Abdallah *et al.* [STAR Collaboration], "Measurement of cold nuclear matter effects for inclusive J/ψ in p+Au collisions at $\sqrt{s_{NN}}$=200 GeV", Phys. Lett. B 825, 136865 (2022).

19. M. S. Abdallah *et al.* [STAR Collaboration], "Measurement of inclusive electrons from open heavy-flavor hadron decays in p+p collisions at $\sqrt{s}$ = 200 GeV with the STAR detector", Phys. Rev. D 105, no.3, 032007 (2022).

20. M. S. Abdallah *et al.* [STAR Collaboration], "Differential measurements of jet substructure and partonic energy loss in Au+Au collisions at $\sqrt{S_{NN}}$ =200 GeV", Phys. Rev. C 105, no.4, 044906 (2022).

21. M. S. Abdallah *et al.* [STAR Collaboration], "Probing the Gluonic Structure of the Deuteron with J/ψ Photoproduction in d+Au Ultraperipheral Collisions", Phys. Rev. Lett. 128, no.12, 122303 (2022).

22. M. S. Abdallah *et al.* [STAR Collaboration], "Search for the chiral magnetic effect with isobar collisions at $\sqrt{s_{NN}}$=200 GeV by the STAR Collaboration at the BNL Relativistic Heavy Ion Collider", Phys. Rev. C 105, no.1, 014901 (2022).

23. M. S. Abdallah *et al.* [STAR Collaboration], "Disappearance of partonic collectivity in $\sqrt{s_{NN}}$=3 GeV Au+Au collisions at RHIC", Phys. Lett. B 827, 137003 (2022).

24. M. S. Abdallah *et al.* [STAR Collaboration], "Probing strangeness canonical ensemble with K^{-}, ϕ(1020) and Ξ^{-} production in Au+Au collisions at $\sqrt{s_{NN}}$=3 GeV", Phys. Lett. B 831, 137152 (2022).

25. M. S. Abdallah *et al.* [STAR Collaboration], "Global Λ-hyperon polarization in Au+Au collisions at $\sqrt{s_{NN}}$=3 GeV", Phys. Rev. C 104, no.6, L061901

(2021).

26. M. S. Abdallah *et al.* [STAR Collaboration], "Search for the Chiral Magnetic Effect via Charge-Dependent Azimuthal Correlations Relative to Spectator and Participant Planes in Au+Au Collisions at $\sqrt{s_{NN}} = 200$ GeV", Phys. Rev. Lett. 128, no.9, 092301 (2022).

27. M. S. Abdallah *et al.* [STAR Collaboration], "Invariant Jet Mass Measurements in pp Collisions at $\sqrt{s} = 200$ GeV at RHIC", Phys. Rev. D 104, no.5, 052007 (2021).

28. M. S. Abdallah *et al.* [STAR Collaboration], "Azimuthal anisotropy measurements of strange and multistrange hadrons in $U + U$ collisions at $\sqrt{s_{NN}} = 193$ GeV at the BNL Relativistic Heavy Ion Collider", Phys. Rev. C 103, no.6, 064907 (2021).

29. M. S. Abdallah *et al.* [STAR Collaboration], "Longitudinal double-spin asymmetry for inclusive jet and dijet production in polarized proton collisions at $\sqrt{s} = 200$ GeV", Phys. Rev. D 103, no.9, L091103 (2021).

30. M. S. Abdallah *et al.* [STAR Collaboration], "Cumulants and correlation functions of net-proton, proton, and antiproton multiplicity distributions in Au+Au collisions at energies available at the BNL Relativistic Heavy Ion Collider", Phys. Rev. C 104, no.2, 024902 (2021).

31. J. Adam *et al.* [STAR Collaboration], "Global Polarization of Ξ and Ω Hyperons in Au+Au Collisions at $\sqrt{s_{NN}} = 200$ GeV", Phys. Rev. Lett. 126, no.16, 162301 (2021).

32. J. Adam *et al.* [STAR Collaboration], "Measurement of transverse single-spin asymmetries of π^0 and electromagnetic jets at forward rapidity in 200 and 500 GeV transversely polarized proton-proton collisions", Phys. Rev. D 103, no.9, 092009 (2021).

33. J. Adam *et al.* [STAR Collaboration], "Comparison of transverse single-spin asymmetries for forward π^0 production in polarized pp, pAl and pAu collisions at nucleon pair c.m. energy $\sqrt{s_{\mathrm{NN}}} = 200$ GeV", Phys. Rev. D 103, no.7, 072005 (2021).

34. J. Adam *et al.* [STAR Collaboration], "Measurements of W and Z/γ^* cross sections and their ratios in p+p collisions at RHIC", Phys. Rev. D 103, no.1, 012001 (2021).

35. J. Adam *et al.* [STAR Collaboration], "Flow and interferometry results from Au+Au collisions at $\sqrt{s_{NN}} = 4.5$ GeV", Phys. Rev. C 103, no.3, 034908 (2021).

36. J. Adam *et al.* [STAR Collaboration], "Measurement of inclusive J/ψ polarization in $p+p$ collisions at $\sqrt{s}$ =200 GeV by the STAR experiment", Phys. Rev. D 102, no.9, 092009 (2020).

37. J. Adam *et al.* [STAR Collaboration], "Beam-energy dependence of the directed flow of deuterons in Au+Au collisions", Phys. Rev. C 102, no.4, 044906 (2020).

38. J. Adam *et al.* [STAR Collaboration], "Investigation of the linear and mode-coupled flow harmonics in Au+Au collisions at $\sqrt{s_{NN}} = 200$ GeV", Phys. Lett. B 809, 135728 (2020).

39. J. Adam *et al.* [STAR Collaboration], "Measurement of inclusive charged-particle jet production in Au + Au collisions at $\sqrt{s_{NN}}$ =200 GeV", Phys. Rev. C 102, no.5, 054913 (2020).

40. J. Adam *et al.* [STAR Collaboration], "Measurement of the central exclusive production of charged particle pairs in proton-proton collisions at $\sqrt{s} = 200$ GeV with the STAR detector at RHIC", JHEP 07, no.07, 178 (2020).

41. J. Adam *et al.* [STAR Collaboration], "Results on total and elastic cross sections in proton-proton collisions at $\sqrt{s} = 200$ GeV", Phys. Lett. B 808,

135663 (2020).

42. J. Adam *et al.* [STAR Collaboration], "Measurement of groomed jet substructure observables in p+p collisions at $\sqrt{s}$ =200 GeV with STAR", Phys. Lett. B 811, 135846 (2020).

43. J. Adam *et al.* [STAR Collaboration], "Beam energy dependence of net-Λ fluctuations measured by the STAR experiment at the BNL Relativistic Heavy Ion Collider", Phys. Rev. C 102, no.2, 024903 (2020).

44. J. Adam *et al.* [STAR Collaboration], "Nonmonotonic Energy Dependence of Net-Proton Number Fluctuations", Phys. Rev. Lett. 126, no.9, 092301 (2021).

45. J. Adam *et al.* [STAR Collaboration], "Underlying event measurements in $p+p$ collisions at $\sqrt{s} = 200$ GeV at RHIC", Phys. Rev. D 101, no.5, 052004 (2020).

46. J. Adam *et al.* [STAR Collaboration], "Measurement of D^0-meson + hadron two-dimensional angular correlations in Au+Au collisions at $\sqrt{s_{\mathrm{NN}}} = 200$ GeV", Phys. Rev. C 102, no.1, 014905 (2020).

47. J. Adam *et al.* [STAR Collaboration], "Methods for a blind analysis of isobar data collected by the STAR collaboration", Nucl. Sci. Tech. 32, no.5, 48 (2021).

48. J. Adam *et al.* [STAR Collaboration], "First measurement of Λ_c baryon production in Au+Au collisions at $\sqrt{s_{\mathrm{NN}}} = 200$ GeV", Phys. Rev. Lett. 124, no.17, 172301 (2020).

49. J. Adam *et al.* [STAR Collaboration], "Measurement of e^+e^- Momentum and Angular Distributions from Linearly Polarized Photon Collisions", Phys. Rev. Lett. 127, no.5, 052302 (2021).

50. J. Adam *et al.* [STAR Collaboration], "Bulk properties of the system formed in $Au+Au$ collisions at $\sqrt{s_{\rm NN}}$ =14.5 GeV at the BNL STAR detector", Phys. Rev. C 101, no.2, 024905 (2020).

51. J. Adam *et al.* [STAR Collaboration], "Beam-energy dependence of identified two-particle angular correlations in $\sqrt{s_{NN}}$ = 7.7-200 GeV Au+Au collisions", Phys. Rev. C 101, no.1, 014916 (2020).

52. J. Adam *et al.* [STAR Collaboration], "Strange hadron production in Au+Au collisions at $\sqrt{s_{\rm NN}}$ = 7.7, 11.5, 19.6, 27, and 39 GeV", Phys. Rev. C 102, no.3, 034909 (2020).

53. J. Adam *et al.* [STAR Collaboration], "Charge-dependent pair correlations relative to a third particle in p + Au and d+ Au collisions at RHIC", Phys. Lett. B 798, 134975 (2019).

54. J. Adam *et al.* [STAR Collaboration], "Longitudinal double-spin asymmetry for inclusive jet and dijet production in pp collisions at $\sqrt{s}$ = 510 GeV", Phys. Rev. D 100, no.5, 052005 (2019).

55. J. Adam *et al.* [STAR Collaboration], "Measurement of inclusive J/ψ suppression in Au+Au collisions at $\sqrt{s_{NN}}$ = 200 GeV through the dimuon channel at STAR", Phys. Lett. B 797, 134917 (2019).

56. J. Adam *et al.* [STAR Collaboration], "Polarization of Λ ($\bar{\Lambda}$) hyperons along the beam direction in Au+Au collisions at $\sqrt{s_{_{NN}}}$ = 200 GeV", Phys. Rev. Lett. 123, no.13, 132301 (2019).

57. J. Adam *et al.* [STAR Collaboration], "Measurements of the transverse-momentum-dependent cross sections of J/ψ production at mid-rapidity in proton+proton collisions at $\sqrt{s}$ = 510 and 500 GeV with the STAR detector", Phys. Rev. D 100, no.5, 052009 (2019).

58. J. Adam *et al.* [STAR Collaboration], "First Observation of the Directed Flow of D^0 and $\overline{D^0}$ in Au+Au Collisions at $\sqrt{s_{\rm NN}}$ = 200 GeV", Phys. Rev. Lett.

123, no.16, 162301 (2019).

59. J. Adam *et al.* [STAR Collaboration], "Measurement of the mass difference and the binding energy of the hypertriton and antihypertriton", Nature Phys. 16, no.4, 409-412 (2020).

60. J. Adam *et al.* [STAR Collaboration], "Beam energy dependence of (anti-)deuteron production in Au + Au collisions at the BNL Relativistic Heavy Ion Collider", Phys. Rev. C 99, no.6, 064905 (2019).

61. J. Adam *et al.* [STAR Collaboration], "Collision-energy dependence of second-order off-diagonal and diagonal cumulants of net-charge, net-proton, and net-kaon multiplicity distributions in Au + Au collisions", Phys. Rev. C 100, no.1, 014902 (2019).

62. J. Adam *et al.* [STAR Collaboration], "Azimuthal Harmonics in Small and Large Collision Systems at RHIC Top Energies", Phys. Rev. Lett. 122, no.17, 172301 (2019).

63. J. Adam *et al.* [STAR Collaboration], "Collision-energy dependence of p_t correlations in Au + Au collisions at energies available at the BNL Relativistic Heavy Ion Collider", Phys. Rev. C 99, no.4, 044918 (2019).

64. J. Adam *et al.* [STAR Collaboration], "Centrality and transverse momentum dependence of D^0-meson production at mid-rapidity in Au+Au collisions at $\sqrt{s_{\mathrm{NN}}} = 200$ GeV", Phys. Rev. C 99, no.3, 034908 (2019).

65. J. Adam *et al.* [STAR Collaboration], "Measurement of the longitudinal spin asymmetries for weak boson production in proton-proton collisions at $\sqrt{s} = 510$ GeV", Phys. Rev. D 99, no.5, 051102 (2019).

66. J. Adam *et al.* [STAR Collaboration], "Improved measurement of the longitudinal spin transfer to Λ and $\bar{\Lambda}$ hyperons in polarized proton-proton collisions at $\sqrt{s} = 200$ GeV", Phys. Rev. D 98, no.11, 112009 (2018).

67. J. Adam *et al.* [STAR Collaboration], "Transverse spin transfer to Λ and $\bar{\Lambda}$ hyperons in polarized proton-proton collisions at $\sqrt{s} = 200$ GeV", Phys. Rev. D 98, no.9, 091103 (2018).

II Conference, Schools, Symposiums and Workshops Attended

1. 2023, February 7-10, **International Conference on Physics and Astrophysics of Quark Gluon Plasma (ICPAQGP-2023)**, Puri, Odisha, India (Oral Presentation).

2. 2022, December 12 - 16, **XXV DAE-BRNS HIGH ENERGY PHYSICS SYMPOSIUM 2022**, IISER, Mohali, India (Oral Presentation).

3. 2022, December 01 - 05, **66^{th} DAE SYMPOSIUM ON NUCLEAR PHYSICS**, Cotton University, Guwahati, Assam, India.

4. 2022, July 11-22, **The 2022 CFNS Summer School on the Physics of the Electron-Ion Collider (ONLINE)**, Stony Brook University, USA.

5. 2022, April 4-10, **Quark Matter 2022 (XXIXth International Conference on Ultra-relativistic Nucleus-Nucleus Collisions)**, Krakow, Poland.

6. 2021, September 5-16, **MCnet-CTEQ Summer School 2021 (VIRTUAL)**, Dresden.

7. 2021, January 21, **3rd Shivalik HEPCATS Meeting (Winter 2020)**, IISER, Mohali, Punjab, INDIA.

8. 2020, December 14-18, **XXIV DAE-BRNS HIGH ENERGY PHYSICS SYMPOSIUM 2020**, NISER, Jatni, Odisha, INDIA.

9. 2020, November 5-20, **3rd ALICE-INDIA school on Quark-Gluon Plasma, Indian Institute of Technology**, Indore, INDIA.

10. 2019, December 23-27, **64th DAE BRNS Symposium on nuclear physics**, Lucknow, Uttar Pradesh, INDIA.

11. 2019, November 2-9, **Quark Matter 2019 (XXVIIIth International Conference on Ultra-relativistic Nucleus-Nucleus Collisions)**, Wuhan, China.

12. 2018, December 10-14, **XXIII DAE-BRNS HIGH ENERGY PHYSICS SYMPOSIUM**, IIT Madras, Chennai, Tamilnadu, INDIA.

13. 2018, December 9-14, **63rd DAE BRNS Symposium on nuclear physics**, BARC, Mumbai, Maharastra, INDIA, December 9-14, 2018.

14. 2017, November 7-27, **XI SERC School on Experimental High Energy Physics**, School of Physical Science, NISER, Jatni, Odisha, India.